



Etude et modélisation des couplages inter-composants pour la conception des filtres : Application aux filtres du domaine automobile

Marine Stojanovic

► To cite this version:

Marine Stojanovic. Etude et modélisation des couplages inter-composants pour la conception des filtres : Application aux filtres du domaine automobile. Electronique. INSA de Rennes, 2018. Français. NNT : 2018ISAR0014 . tel-01996999

HAL Id: tel-01996999

<https://theses.hal.science/tel-01996999>

Submitted on 28 Jan 2019

HAL is a multi-disciplinary open access archive for the deposit and dissemination of scientific research documents, whether they are published or not. The documents may come from teaching and research institutions in France or abroad, or from public or private research centers.

L'archive ouverte pluridisciplinaire **HAL**, est destinée au dépôt et à la diffusion de documents scientifiques de niveau recherche, publiés ou non, émanant des établissements d'enseignement et de recherche français ou étrangers, des laboratoires publics ou privés.

THESE DE DOCTORAT DE

L'INSA RENNES

COMUE UNIVERSITE BRETAGNE LOIRE

ECOLE DOCTORALE N° 601

*Mathématiques et Sciences et Technologies
de l'Information et de la Communication*

Spécialité : Electronique

Par

Marine STOJANOVIC

Study and Modeling of Inter-Component Coupling for Filter Design

Application to Automotive EMI filters

Thèse présentée et soutenue à Angers, le 14 Septembre 2018

Unité de recherche : IETR

Thèse N° : 18ISAR 15 / D18 – 15

Rapporteurs avant soutenance :

Geneviève DUCHAMP

Professeur des Universités
Université de Bordeaux

Christian VOLLAIRE

Professeur des Universités
Ecole Centrale de Lyon

Composition du Jury :

Président

Philippe BESNIER

Directeur de Recherche CNRS

IETR – INSA de Rennes

Geneviève DUCHAMP

Professeur des Universités

Université de Bordeaux

Christian VOLLAIRE

Professeur des Universités

Ecole Centrale de Lyon

Alain REINEIX

Directeur de Recherche CNRS

XLIM – Université de Limoges

Olivier MAURICE

Expert CEM (HDR) – Ariane Group

Directeur de thèse

Richard PERDRIAU

Enseignant-Chercheur HDR

IETR – ESEO

Co-directeur de thèse

Frédéric LAFON

Master Expert CEM (HDR) – Valeo

Co-encadrant de thèse

Mohamed RAMDANI

Enseignant-Chercheur HDR

IETR – ESEO

Invités

Guillaume DEVAUCHELLE Vice-président Groupe Innovation et
Développement Scientifique – Valeo

Jean-Luc LEVANT

Senior Expert CEM – Microchip

François DE DARAN

Senior Expert CEM

SAFRAN A. S. Group

Xavier BUNLON

Expert CEM – Renault

Intitulé de la thèse :

Study and Modeling of Inter-Component Coupling for Filter Design

Application to Automotive EMI filters

Marine STOJANOVIC

En partenariat avec :



Document protégé par les droits d'auteur

Résumé en Français

Introduction

Les véhicules hybrides et électriques connaissent un essor considérable ces dernières années. De ce fait, de plus en plus d'électroniques et plus particulièrement des électroniques de puissance, sont utilisées dans nos véhicules. Face à cette densification de l'électronique dans un espace toujours aussi restreint, les problèmes de compatibilité électromagnétique (CEM) s'accroissent. En effet, les systèmes d'électronique de puissance sont des sources typiques d'interférences électromagnétiques. Ainsi, afin de réduire ces perturbations électromagnétiques, des filtres doivent être implémentés dans le but de les atténuer et, de ce fait, rendre conforme un équipement, selon les normes qui régissent la CEM.

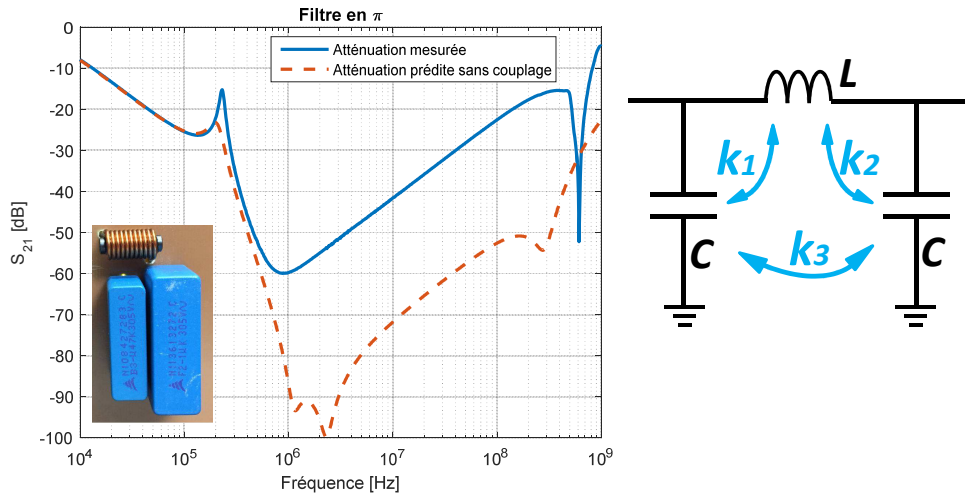


FIGURE 1 – Comparaison entre l'atténuation mesurée et l'atténuation prédite sans tenir compte des couplages

Les filtres pour la CEM, sont généralement constitués de composants passifs tels que les condensateurs, les inductances et les tores de mode commun (TMCs). Ces filtres doivent être dimensionnés au cas par cas, selon l'application et l'atténuation requise. Cependant, de nombreux paramètres peuvent avoir une influence non négligeable sur les performances d'un filtre. Parmi ces paramètres influents, le routage ou bien la mécanique peuvent fortement dégrader les performances du filtre. Afin de prendre en compte ces éléments, la simulation électromagnétique 3D est une bonne solution. Effectivement, les modèles 3D sont souvent déjà existants et peu d'informations sont requises

pour effectuer ce type de simulations.

Un paramètre qui influe également sur la performance d'un filtre, est la proximité des composants les uns par rapport aux autres, ou autrement dit les couplages inter-composants. En effet, la Fig. 1 présente la différence qu'il existe entre l'atténuation mesurée et l'atténuation prédite sans tenir compte des couplages inter-composants. L'écart est significatif (30dB à 10MHz) et une telle erreur de prédiction peut entraîner d'importants problèmes de design car le filtre sera sous-dimensionné pour l'application.

La plupart des travaux menés jusqu'ici sont basés sur des simulations électromagnétiques 3D et le désavantage de ces simulations est qu'elles prennent un temps considérable à la fois pour la construction des modèles mais également pour la résolution. De ce fait, à chaque modification de design, le calcul doit de nouveau être lancé, ceci jusqu'à trouver une solution satisfaisante, et donc cette méthode peut prendre plusieurs jours. De plus, un grand nombre d'informations sont nécessaires sur les composants, tels que la géométrie exacte ou bien les propriétés des matériaux. En règle générale, ces informations sont difficiles à obtenir et donc les modèles 3D sont compliqués à construire.

L'objectif qui émane de cette problématique est le besoin de développer une méthode simplifiée et rapide qui permettent de prédire les performances d'un filtre en tenant compte de son implémentation et quelle que soit sa structure.

Expression analytique simplifiée d'un couplage magnétique

Afin de déterminer une inductance mutuelle, ou bien de façon plus générale, un couplage magnétique, le principe est le suivant (Fig. 2) : lorsqu'un courant i circule dans un composant, un champ magnétique B est généré et est couplé par le second composant à travers sa surface équivalente de couplage S . Le lien qu'il existe entre ces deux composants est appelé une mutuelle inductance M (Eq. 1).

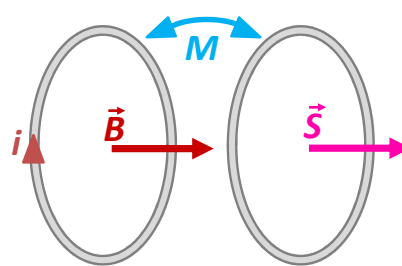
$$\vec{B} \cdot \vec{S} = M.i \quad (1)$$


FIGURE 2 – Principe pour déterminer une inductance mutuelle

De cette équation découlent donc les différentes thématiques de la thèse qui sont la détermination d'une surface équivalente de couplage, le calcul du champ magnétique généré par un composant passif, dans le but de prédire une inductance mutuelle entre deux composants. Finalement, l'ensemble des inductances mutuelles entre les composants d'un même filtre devront être prises en compte pour prédire les performances du filtre.

Détermination de surface équivalente de couplage pour les composants passifs

Une surface équivalente de couplage permet de représenter la sensibilité au champ magnétique d'un composant, autant en ce qui concerne le niveau de sensibilité que sa direction privilégiée. Pour déterminer cette surface équivalente, une méthode utilisant des mesures en cellule TEM a été développée. En effet, lorsque la cellule TEM (Fig. 3) est alimentée via une source RF (radio-fréquence) tel qu'un VNA (Analyseur de réseaux vectoriel), un champ électromagnétique uniforme est généré en cette cellule. De ce fait, il est possible de connaître la valeur, le sens et la direction du champ magnétique dans la cellule. Ainsi, la sensibilité des composants passifs sous des conditions de champ magnétique maîtrisées peut être étudiée. Finalement, une surface équivalente de couplage pour chaque composant pourra être extraite afin de réutiliser ce type de caractérisation.

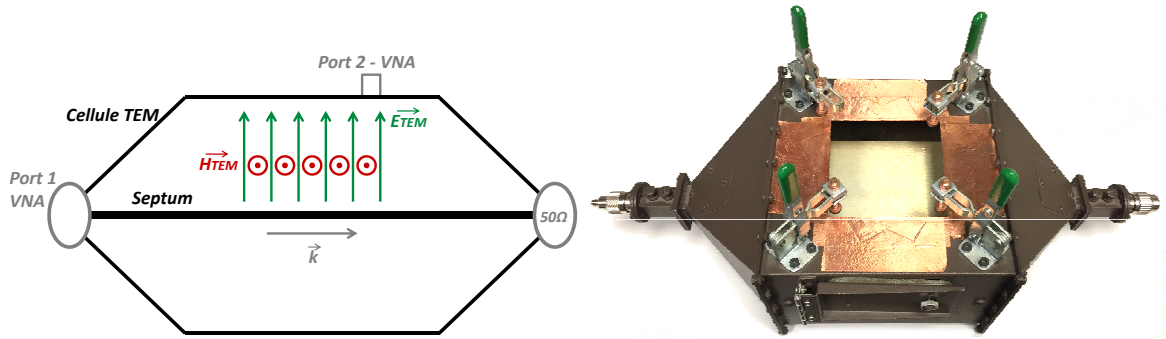


FIGURE 3 – Cellule TEM

Surface équivalente de couplage d'un condensateur

Pour déterminer la surface équivalente de couplage d'un condensateur, il est nécessaire de caractériser le composant pour ses deux orientations privilégiées : lorsque la surface de couplage et le champ magnétique sont colinéaires et dans le même sens, et la seconde lorsqu'ils sont dans des sens opposés. Ces deux mesures sont nécessaires afin de pouvoir supprimer la contribution du champ électrique. En effet, un fort champ électrique est présent en cellule TEM et son influence doit donc être supprimée, par calcul, pour se focaliser uniquement sur l'influence du champ magnétique.

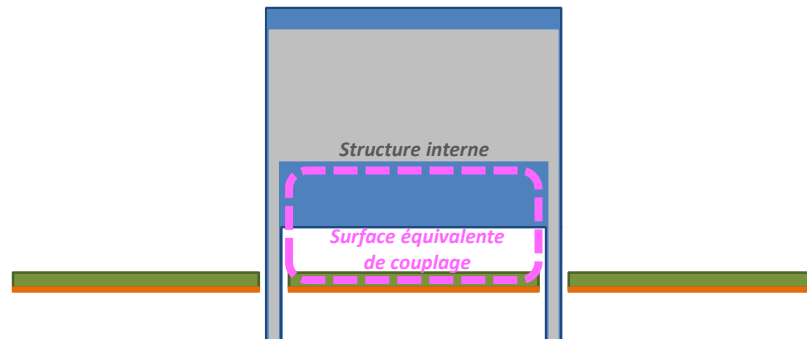


FIGURE 4 – Surface équivalente de couplage d'un condensateur

La direction privilégiée de couplage pour le condensateur est déterminée en effectuant des mesures tout autour du composant. Il s'est avéré que la surface de couplage d'un condensateur est localisée entre ses deux pins, le plan de masse et sa structure interne (Fig. 4).

De ce fait, à moins de connaître la structure interne du condensateur, la meilleure façon pour déterminer sa surface équivalente de couplage est d'effectuer des mesures en cellule TEM.

Surface équivalente de couplage d'une inductance

Pour les inductances, le principe est le même que pour les condensateurs. Deux mesures sont nécessaires, pour les deux directions privilégiées du couplage au champ magnétique. Il a ainsi été déduit que la surface équivalente de couplage d'une inductance est orientée comme ses spires (Fig. 5).

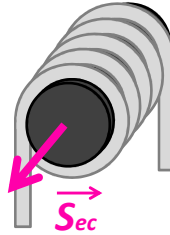


FIGURE 5 – Direction de la surface équivalente de couplage d'une inductance

A partir des mesures en cellule TEM, sur de nombreuses inductances, les paramètres dimensionnant la surface équivalente de couplage d'une inductance ont été identifiés, à savoir : le nombre de spires N , la surface d'une spire S_{spire} et la perméabilité du matériau magnétique μ_r (Eq. 2).

$$S_{ec} = N \cdot S_{spire} \cdot \mu_r \quad (2)$$

Pour une inductance verticale, le principe reste le même. Celle-ci doit être caractérisée de telle sorte à ce que sa surface équivalente de couplage et le champ magnétique soient colinéaires.

Finalement, à moins de connaître ou de pouvoir estimer la perméabilité du matériau magnétique, les mesures en cellule TEM restent la meilleure solution pour déterminer une surface de couplage.

Surfaces équivalentes de couplage d'un TMC

Quant aux TMCs, le principe est un peu plus complexe, du fait de sa géométrie et du fait qu'ils possèdent deux bobines distinctes. Une étude préliminaire a d'ailleurs été effectuée pour les deux modes de fonctionnement d'un TMC : le mode commun (MC) et le mode différentiel (MD). Pour ce faire, la caractérisation s'effectue tout autour du composant. La Fig. 6 présente les résultats des forces électromotrices générées au TMC en MC et en MD selon l'orientation du composant dans la cellule TEM. Il est alors clairement identifiable que le couplage lorsque le TMC est connecté en MC est bien plus faible et n'a pas de direction privilégiée comparée au MD. Il peut donc en être déduit, qu'un modèle représentant uniquement le MD, est suffisant pour modéliser un TMC.

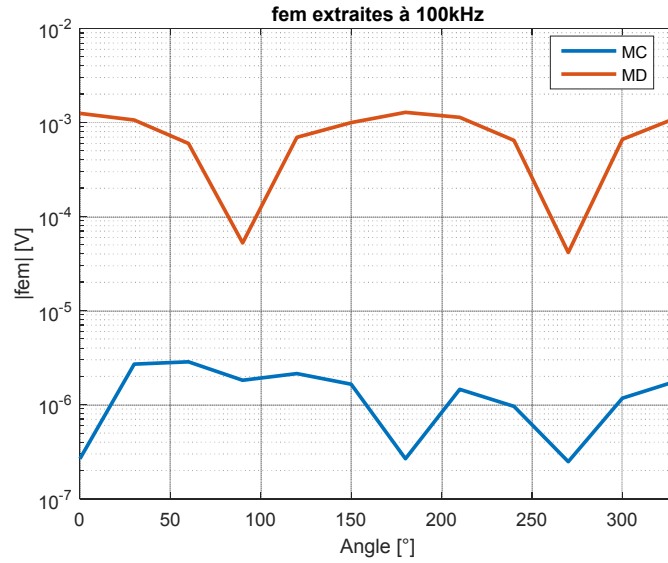


FIGURE 6 – Forces électromotrices générées à un TMC à 100kHz pour le MC et le MD

Afin de modéliser finement le TMC en MD, dix surfaces équivalentes de couplage (cinq par bobinage) vont être prises en compte (Fig. 7). Ces dix surfaces ont une position et direction fixes et ainsi, il ne reste qu'à déterminer l'amplitude des surfaces de couplage. De ce fait, douze mesures en cellule TEM sont nécessaires (à douze orientations différentes en cellule TEM), afin de déterminer les dix surfaces de couplages (deux mesures pour la suppression de l'influence du champ électrique et les dix autres pour la détermination des surfaces de couplage).

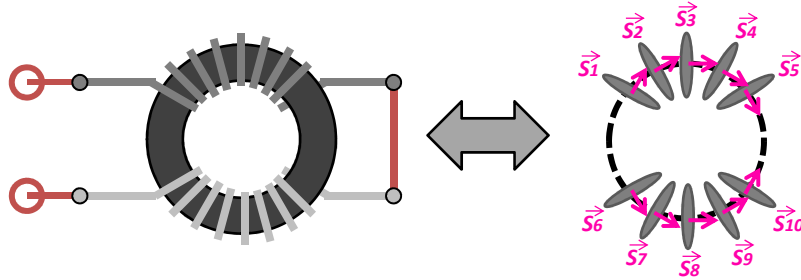


FIGURE 7 – Modèle de couplage équivalent d'un TMC en MD

Calcul analytique de champ magnétique généré par un composant passif

Maintenant qu'une méthode a été définie pour déterminer une surface équivalente de couplage, la deuxième étape est de pouvoir estimer la valeur du champ magnétique généré par un composant passif. Pour ce faire, le modèle équivalent de couplage peut être réutilisé en tant que modèle d'émission, grâce au théorème de réciprocité.

Afin de calculer le champ magnétique généré par un composant passif, la loi de Biot et Savart semble être une bonne approche. En effet, son application est simple d'usage et permet de considérer

n'importe quel type de contour (Eq. 3). Le calcul du champ magnétique avec la loi de Biot et Savart restera valide tant que le courant peut être considéré constant. Cette condition dépend de la valeur de la vitesse de propagation et ainsi que des matériaux (magnétiques, diélectriques).

$$d\vec{B} = \frac{\mu}{4\pi} \frac{\hat{r}}{r^2} I d\vec{S} \quad (3)$$

De plus, afin de correctement prédire le champ magnétique généré par un composant, il est indispensable de prendre en compte l'influence du plan de masse (si tel est le cas). De ce fait, la théorie des images doit être appliquée afin de pouvoir prendre en compte l'influence d'un plan de masse.

Pour chaque type de composant passif (condensateurs, inductances horizontales et verticales, tores de mode commun horizontaux et verticaux), les surfaces équivalentes de couplages sont alors réutilisées pour déterminer la valeur du champ magnétique qu'il génère. La Fig. 8 présente différents exemples de champs magnétiques générés par un condensateur, une inductance et un TMC. L'ensemble de ces calculs ont été validés par des mesures à l'aide d'un scanner champ proche.

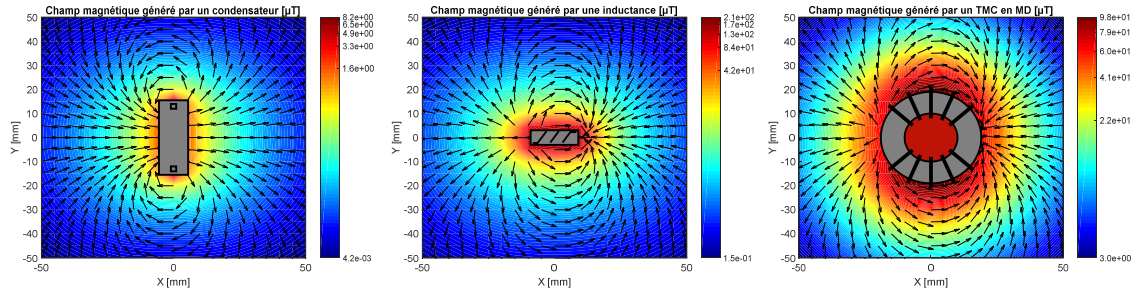


FIGURE 8 – Champs magnétiques générés par un condensateur, une inductance et un TMC en MD

Il est important de remarquer que le champ magnétique d'un TMC n'est calculé que pour le MD. En effet, comme le TMC en MC ne permet que peu de couplage magnétique comparé au MD, le TMC en MC génèrera donc peu de champ magnétique (théorème de réciprocité).

Calcul d'une mutuelle inductance entre deux composants passifs

Avec les deux thématiques précédentes (surface équivalente de couplage et champ magnétique généré par un composant passif), il est désormais possible de calculer une inductance mutuelle entre deux composants, quelle que soit leur position et leur orientation. En effet, l'Eq. 1 peut être appliquée directement.

Prenons l'exemple d'un cas très simple de calcul d'une mutuelle inductance entre une inductance et un condensateur, espacés de 25mm l'un de l'autre (Fig. 9).

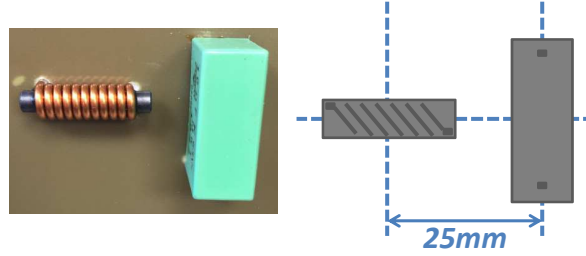


FIGURE 9 – Exemple d’une inductance et d’un condensateur espacés de 25mm

Chacun des composants est caractérisé au préalable, en termes d’impédance et en cellule TEM. Ainsi, le champ magnétique généré par l’inductance est calculé au niveau de la surface de couplage du condensateur (Fig. 10). Le cheminement inverse donnera le même résultat, en accord avec le théorème de réciprocité.

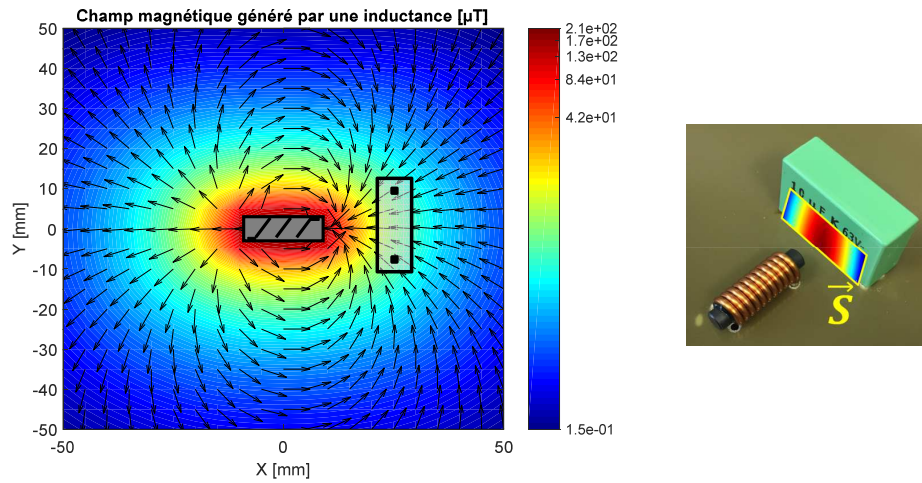


FIGURE 10 – Champ magnétique de l’inductance sur la surface de couplage du condensateur

De cette manière, une valeur constante de la mutuelle qui existe entre ces deux composants peut être extraite. Cette valeur sera alors valable tant que les conditions de la magnéto-statique sont respectés. La Fig. 11 présente la comparaison entre cette valeur d’inductance mutuelle extraite par le calcul et celle extraite par la mesure. Ce type de comparaison a été effectuée pour de nombreux composants passifs, et ainsi la méthode de calcul de mutuelles est validée.

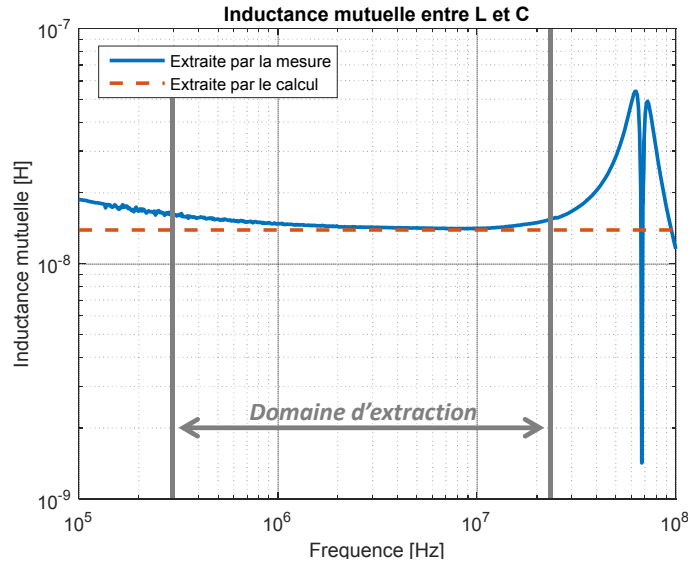


FIGURE 11 – Comparaison entre l'inductance mutuelle extraite par la mesure et par le calcul

Prédiction de l'atténuation d'un filtre quelle que soit sa structure et sa topologie

Désormais, quelle que soit la position des composants les uns par rapport aux autres, il est possible de calculer les mutuelles inductances entre eux, deux par deux. Le grand avantage de cette méthode est que, une fois les composants caractérisés, le calcul de couplage entre les composants est direct et très rapide.

La méthode qui a été choisie pour le calcul d'atténuation d'un filtre, est la MKME (Méthode de Kron Modifiée pour la Compatibilité Électromagnétique). Cette méthode, basée sur l'analyse tensorielle des réseaux est très puissante et permet de décrire n'importe quel système quelle que soit sa complexité. L'avantage majeur de la méthode de Kron est que la filtre peut être décrit en distinguant bien les paramètres intrinsèques au filtre (les composants et leurs éléments parasites) et les paramètres modifiables (les couplages entre les composants). De plus, il existe une infinité de structures et de topologies possibles pour les filtres. De ce fait, un algorithme générique de création de graphe pour le calcul d'atténuation. De cette manière, il est possible de calculer l'atténuation d'un filtre, en MC et MD, quelle que soit sa structure, quelle que soit sa topologie. L'intérêt d'avoir développer une méthode générique est que l'ensemble de cette méthode est capitalisée en un seul outil permettant la prédiction de performance d'un filtre. Cet outil est opérationnel et actuellement utilisé par les ingénieurs design pour l'intégration des filtres.

Afin d'illustrer cette méthode, reprenons l'exemple de l'introduction (Fig. 1) d'un filtre en Pi, composé d'un condensateur, suivi d'une inductance puis d'un second condensateur. L'analyse ayant été effectuée, il est alors possible de prédire les performances de façon très précise (Fig. 12).

Ce simple exemple illustre bien les possibilités de calcul de cette méthode. Des cas bien plus complexes ont été traités et validés, tels que des filtres composés de plusieurs centaines d'inductances mutuelles.

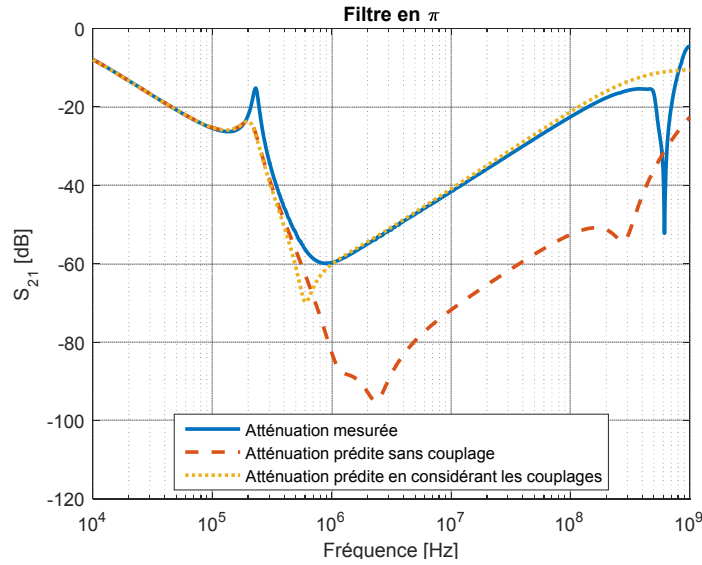


FIGURE 12 – Prédiction des performances du filtre en Pi

Conclusion

L'objectif principal de cette thèse était de développer une méthode analytique afin de prédire les performances d'un filtre en tenant compte de sa topologie. Pour ce faire, le travail a été divisé en quatre grandes étapes : la détermination de surfaces équivalentes de couplage des composants passifs constituant le filtre, le champ magnétique qu'ils génèrent pour finalement prédire un couplage magnétique entre deux composants. La dernière étape a été de développer un algorithme générique permettant le calcul d'atténuation d'un filtre, en considérant les couplages entre les composants, quelle que soit sa structure. Finalement, cette méthode a été appliquée et validée sur de nombreux cas d'applications.

L'ensemble de la méthode a été capitalisée via un outil nommé GFD (Global Filter Design), présenté en Fig. 13. Cet outil permet le calcul d'une simple mutuelle inductance entre deux composants, ou bien la prédiction d'atténuation d'un filtre.

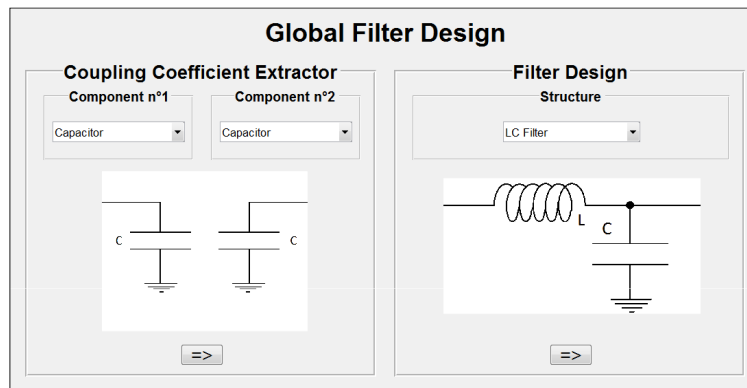


FIGURE 13 – Global Filter Design

Contents

Résumé en Français	1
Introduction	19
1 Main concept of EMI filter design	27
1.1 Introduction to the main concept of EMI filter design	28
1.2 EMI noise sources	28
1.3 EMI filters	30
1.3.1 Filter attenuation signification	30
1.3.1.1 Analytical calculation	31
1.3.1.2 Attenuation measurement	33
1.3.2 Filter structures	34
1.3.2.1 Filter structures dedicated to low input and output impedances of the system regarding the filter position	34
1.3.2.2 Filter structures dedicated to low input and high output impedances of the system regarding the filter position	35
1.3.2.3 Filter structures dedicated to high input and low output impedances of the system regarding the filter position	35
1.3.2.4 Filter structures dedicated to high input and output impedances of the system regarding the filter position	36
1.3.3 Influence of input and output impedances on filter attenuation	36
1.4 Modeling of passive components	39
1.4.1 Impedance measurement	39
1.4.2 Capacitor	41
1.4.3 Inductor	43
1.4.4 Common mode choke	47
1.4.4.1 Classic model	48
1.4.4.2 Multi-resonance model	50
1.4.4.3 Dispersion model	51
1.5 Conclusion	54
2 Equivalent coupling models of passive components	55
2.1 Introduction to the equivalent coupling model principle	56
2.2 The TEM cell	56
2.2.1 Analytical calculation of the magnetic field inside the TEM cell	58

2.2.2	Magnetic field measurement in the TEM cell	58
2.3	DUT measurements in the TEM cell	61
2.3.1	Definition of the normal to the coupling surface	61
2.3.2	Measurements to be carried out on the DUT	63
2.4	Extraction of the equivalent coupling surface	64
2.4.1	Subtraction of the electric field contribution	64
2.4.2	Integration of the impedance of the DUT	65
2.4.3	Extraction of the equivalent coupling surface	66
2.5	Application case: the capacitor	68
2.5.1	Measurements performed on the DUT	68
2.5.2	Measurement post-processing	68
2.5.3	Geometrical approximation	69
2.5.4	Validation of the coupling model with a uniform magnetic field	70
2.5.5	Particular case of MLCC capacitors	71
2.6	Application case: the inductor	72
2.6.1	Measurements performed on the DUT	73
2.6.2	Measurements post-processing	73
2.6.3	Geometrical approximation	74
2.6.4	Extraction of the magnetic permeability	75
2.6.5	Validation of the coupling model with a uniform magnetic field	76
2.6.6	Vertical inductor	77
2.7	Application case: the common mode choke	77
2.7.1	Differential mode analysis	78
2.7.2	Common mode analysis	80
2.7.3	Comparison between DM and CM analyze	81
2.7.4	DM coupling model of a CMC	82
2.7.4.1	Coupling model definition	82
2.7.4.2	Extraction of the DM permeability of a toroidal core	84
2.7.4.3	Extraction of the coupling model at a fixed frequency	84
2.7.4.4	Extraction of the coupling model over frequency	84
2.7.5	Validation of the coupling model with a uniform magnetic field	85
2.7.6	Vertical common mode choke	86
2.8	Conclusion	87
3	Estimation of the mutual inductance between two passive components	89
3.1	Introduction to the mutual inductance estimation	90
3.2	Magnetic field calculation principle	90
3.2.1	Biot & Savart Law	90
3.2.2	Reciprocity principle	91
3.2.3	Image theory	92
3.2.4	Scope of application	93
3.2.5	Application case : the capacitor	94
3.2.6	Application case : the inductor	96
3.2.6.1	Horizontal inductor	96
3.2.6.2	Vertical inductor	98

3.2.7	Application case : the common mode choke	99
3.2.7.1	Horizontal common mode choke	100
3.2.7.2	Vertical common mode choke	100
3.3	Prediction of mutual inductance	101
3.3.1	Between two capacitors	101
3.3.2	Between two inductors	104
3.3.3	Between two CMCs in DM	105
3.3.4	Conclusion	107
3.4	Extension of the method to self-inductance prediction	108
3.4.1	Introduction to the self-inductance prediction	108
3.4.2	Straight coil	108
3.4.2.1	Analytical formulation	110
3.4.2.2	Validation by measurements	111
3.4.3	Toroidal coil	112
3.4.3.1	Analytical formulation	113
3.4.3.2	Validation by measurements	113
3.5	Conclusion	114
4	Prediction of the filter attenuation considering inter-component coupling	117
4.1	Introduction to the prediction of the filter attenuation considering inter-components coupling	118
4.2	Modified Kron's Method applied to EMC (MKME)	118
4.2.1	Graph construction	118
4.2.2	Calculation of tensors and matrices	121
4.2.3	Resolution	122
4.3	Generic Kron's graph development	123
4.3.1	Global parameters	124
4.3.2	Determination of the number of nodes	124
4.3.2.1	Number of nodes in DM	125
4.3.2.2	Number of nodes in CM	126
4.3.3	Determination of the number of edges	127
4.3.4	Definition of the impedance tensor	128
4.3.4.1	Intrinsic impedance tensor	128
4.3.4.2	Coupling tensor	129
4.3.5	Definition of the source tensor	130
4.3.6	Definition of the connectivity matrix : the transfer matrix between the edge and the mesh space	130
4.3.6.1	Determination of meshes and connectivity matrix in DM	131
4.3.6.2	Determination of meshes and connectivity matrix in CM	132
4.3.7	Transformation and attenuation calculation	134
4.4	Application case : attenuation of a LC filter and its optimization	135
4.5	Application case : Pi filter on a LED driver for a DC/DC converter	140
4.6	Application case : OBC (On Board Charger) H filter	141
4.7	Application case : Power filter application	145
4.8	Conclusion	147

Contents	14
Synthesis and conclusions	149
Bibliography	151
A Tools development	157
A.1 Equivalent Surface Extractor - Measurement bench	157
A.2 Global Filter Design	161
A.2.1 Component menus	162
A.2.2 Component connections	165
A.2.3 Calculation of filter performance	165
B Magnetostatic field calculation	167
B.1 Application case: Capacitor	167
B.2 Application case: horizontal inductor	169
B.3 Application case: vertical inductor	170
B.4 Application case: horizontal common mode choke	171
B.5 Application case: vertical common mode choke	172
List of Publications during PhD	173

Remerciements

Je tiens à remercier tous les membres du jury, Geneviève Duchamp, Christian Vollaire, Alain Reineix, Olivier Maurice, Philippe Besnier, Guillaume Devauchelle, Jean-Luc Levant, François De Daran et Xavier Bunlon pour tout l'intérêt que vous avez porté à mon travail. Merci particulièrement à Geneviève Duchamp et Christian Vollaire d'avoir accepté d'en être rapporteur ainsi que de m'avoir permis de soutenir ma thèse.

Ces trois années ont été très riches. J'ai beaucoup appris, en CEM bien évidemment, mais également et surtout sur moi-même. Je suis profondément convaincue que ce qui nous caractérise en tant que personne, autant professionnellement que personnellement, ne vient pas que de nos aptitudes ou de notre caractère. Les personnes que nous rencontrons et qui nous accompagnent au quotidien dimensionnent cette image que nous renvoie le miroir. Et dans cette aventure, je pense avoir eu beaucoup de chance. Beaucoup de chance de rencontrer, d'être accompagnée et entourée par les bonnes personnes.

Frédéric, tu es sans aucun doute celui à qui je pense en premier. Tu m'as fait confiance, m'as donnée ma chance, m'as guidée et accompagnée durant ces trois ans. Tu m'as également poussée dans mes retranchements pour que je donne le meilleur de moi-même, et je t'en suis profondément reconnaissante. Je suis certaine que ces trois années ne sont qu'une préface.

Mohamed et Richard, merci à vous deux de m'avoir si bien guidée, pour votre disponibilité et votre rigueur. Vous aurez été tous les deux, de très bons guides. J'espère que nous continuerons à travailler ensemble.

Merci à mes chers collègues Candice, Priscila, David et Van pour tous ces moments de partage, de complicité et de franche rigolade. Merci à tous mes collègues du laboratoire CEM, qui rendent le quotidien agréable, par leur bonne humeur et leur envie d'avancer ensemble.

Je pense également aux belles rencontres que j'ai pu faire pendant les conférences. Merci à ceux en qui on se retrouve et avec qui on partage la même passion de la recherche.

Enfin, je ne saurais concevoir ces remerciements sans y inclure ceux qui sont si chers à mes yeux.

Merci à mes chers amis, avec qui je partage toujours des moments inoubliables. Merci à ma Luna, mon réconfort. Merci à ma famille, mon indéniable soutien. Merci à mes beaux-parents, Catherine et Jean-Louis, ma belle-soeur, Mélissa, mon beau-frère, Gauthier. Un grand merci à ma grande-tante, Françoise, pour tous ces moments partagés, telle une grand-mère et sa petite fille. Merci à Isa, à mes grands-parents, Negosava et Dusan, mes chers cousins, Johanna et Guillaume, Rémy et Silvia, Alexandre et Célia, mes oncles et tantes, Slavica, William, Goran.

Et pour finir... Les derniers cités mais sans aucun doute les plus chers à mon coeur. Merci ma Soeur, mon soleil. Toi qui m'as fait tant rire en pensant que je pourrais te faire des ordonnances une fois docteur. Merci mon Frère, mon alter-ego. Ton soutien et notre complicité sont ma force.

Merci Papa, mon sourire. Toujours le mot pour rire. Il aura fallu quelques temps avant que la CEM ne soit plus un acronyme inconnu pour toi! Merci Maman, mon modèle. Toi qui m'accompagne. La femme à qui j'aimerais ressembler un jour. Et pour finir, mon Guillaume, mon pilier. Merci... Merci pour tout, pour ton soutien, ta force, ta patience et pour tout le bonheur que tu me donnes en partageant ma vie.

A mes Parents, mon Frère, ma Sœur,

A mon Guillaume.

Introduction

Context of the study

With the continuous progress of hybrid and electrical vehicles, power electronics are becoming widely used in the automotive domain. Power electronics are typical sources of electromagnetic interferences (EMI) and, therefore, well designed filters are required to reduce all those emissions. The main role of a filter is to attenuate disturbances in order to comply with international standards and, therefore, to obtain an EMC-compliant equipment, and particularly a CISPR25-compliant system for automotive domain [1].

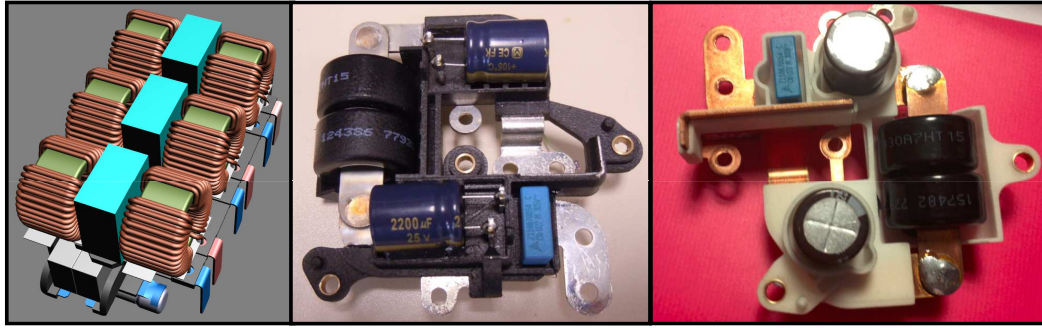


Figure 14: EMI filter examples in power electronics

All filters are different and are designed case per case according to the specific needs. However, there are several parameters that can influence the filter performance.

One of those parameters is the coupling between the traces. Actually, that parameter has an influence on the final filter performance as described in [2]. It can be dealt with 3D electromagnetic simulation as presented in Fig. 15.

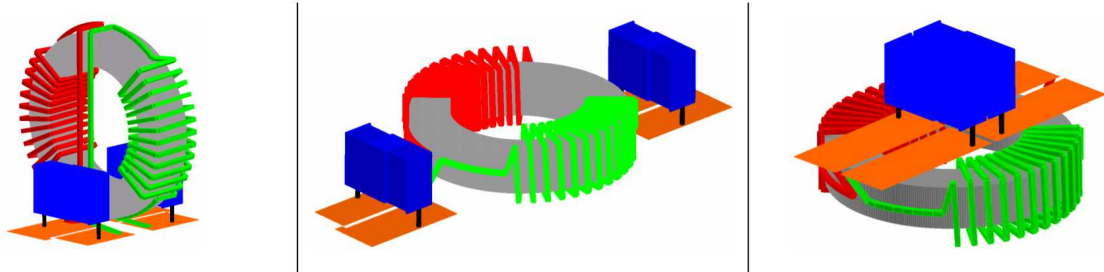


Figure 15: Different filter topologies for a structure, considering PCB traces [2]

Another parameter that have an influence on filter performance is the mechanical structure that can enclose the filter. This part can also be studied with 3D simulation. Actually, it does not require a lot of information on the component or on the material properties. It just requires the 3D geometry coming from other study, like CAD (Computed-Aided Design) design. Fig. 16 presents an example of the 3D model considering the PCB traces and also the housing.

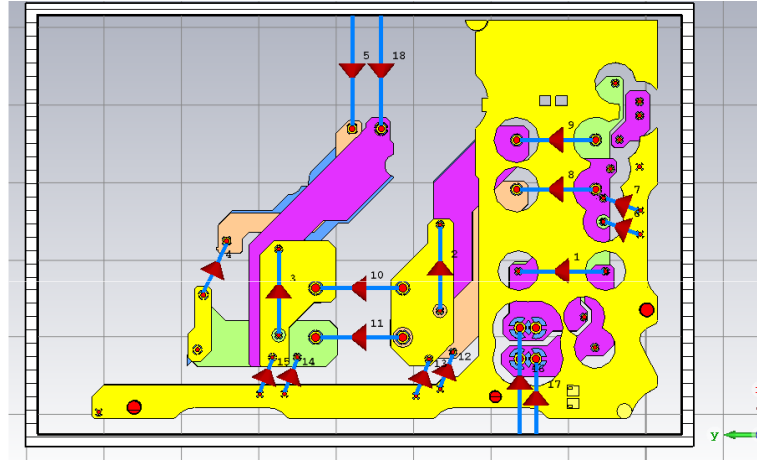


Figure 16: Example of 3D modeling including PCB traces and housing for an AC filter

Then, one of the most destructive parameter, in terms of filter performance, is the inter-component coupling as presented in [3, 4, 5, 6, 7]. Actually, it is presented in Fig. 14 different filter examples where it is clearly identifiable that the components are very close from each other. This proximity induces magnetic coupling between components and has a big influence on the final filter performance. Let's take the example from Fig. 17 which presents the difference between the predicted attenuation without considering those inter-components coupling and the measurement.

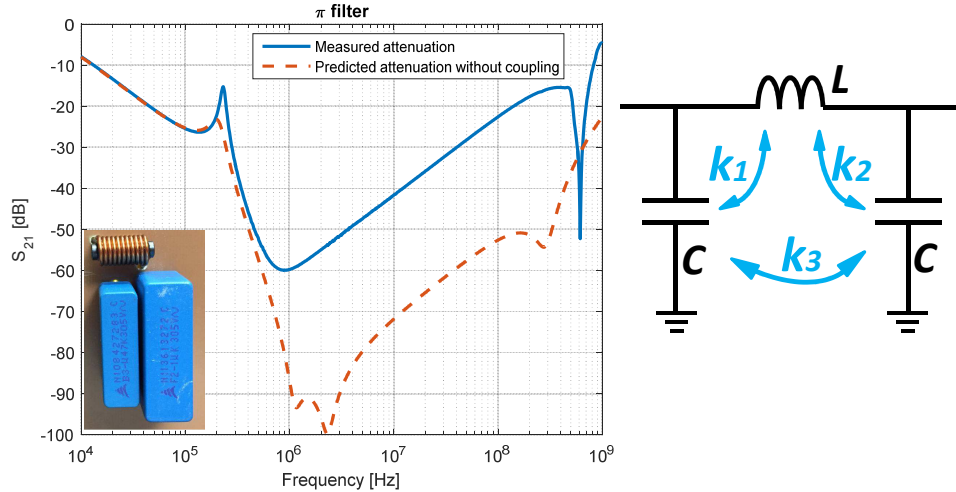


Figure 17: Comparison between the predicted attenuation without considering inter-component coupling and the measured attenuation of a Pi filter

The difference between the predicted attenuation without coupling and the measured attenuation is significant. Thus, a filter which is designed without considering the components proximity, can be finally insufficient to reduce the EMI noises. In such case, additional work must be performed like layout modification or mechanical enclosure. Therefore, in order to avoid those kind of additional works, the integration and the components placement must be considered to have a good prediction of filter performance.

The majority of studies done on inter-component coupling is based on 3D electromagnetic simulation like in [4, 8, 9, 10, 11, 12, 13, 14, 15, 16, 17, 18]. This methodology can be very accurate, but is time consuming for model construction and solving. Furthermore, this kind of simulation requires too much information on the components to build a 3D model.

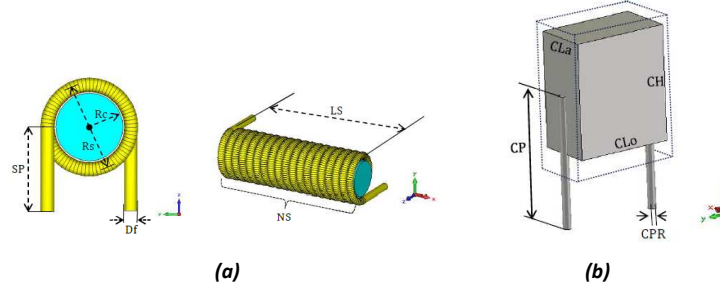


Figure 18: 3D model of a- inductor b- capacitor [4]

A lot of information on components is required and the model must be very accurate regarding actual components (Fig. 18). All the components must be modeled in detail, going through geometry but also the properties, internal structure etc.

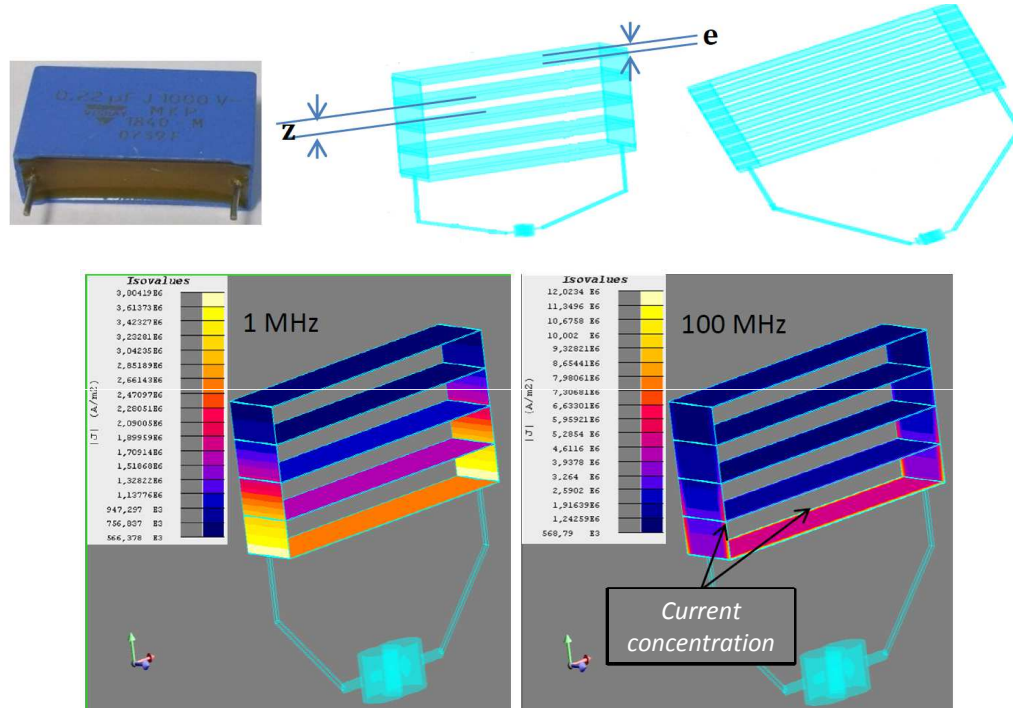


Figure 19: Multilayer capacitor model for 3D electromagnetic simulation [4]

Fig. 19 presents an example that shows the high level of accuracy which is required in terms of modeling in order to obtain good results. All this kind of work is difficult to establish and time consuming. Furthermore, all the filters must be studied case per case and there is no generic methodology for filter design.

The objective that arises from all of those works is the need of developing an analytical and

simplified method for filter design, not based on 3D modeling and generic enough to deal with any kind of structures and topologies.

Inter-component coupling in filter design

Inter-component coupling in a filter design plays a major role on filter performance. Then, in order to model a complete filter, the equivalent electrical models of passive components must be considered, but it is not sufficient. The magnetic couplings between the components are mandatory in order to have a good prediction of filter performance.

Actually, the mutual inductance M (Eq. 4), or more generally a coupling coefficient k , is a link between two inductances L_1 and L_2 , which represents a magnetic coupling.

$$M = k\sqrt{L_1.L_2} \quad (4)$$

A mutual inductance between two inductances can be represented as in Fig. 20-a. Actually, a magnetic coupling can also be represented as an electromotive force generated to the components (Fig. 20-b).

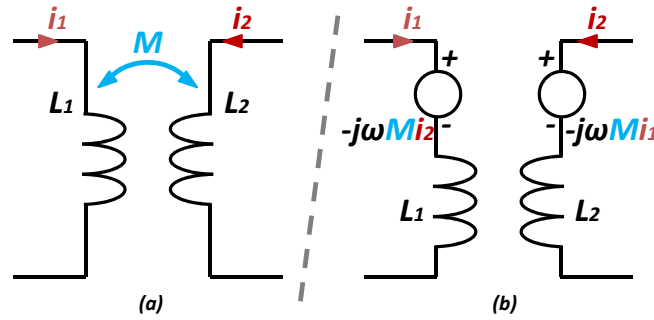


Figure 20: Two different ways to represent a mutual inductance

Those mutual inductances have a high influence on the filter attenuation as highlighted in Fig. 17 and, therefore, they must be considered.

Coupling minimization

The first idea, in order to avoid the degradation coming from the magnetic coupling between components, is to reduce couplings. To minimize those couplings, the first step is to understand how the components radiate and how the components couple the magnetic field. Each type of component has a preferred orientation (or several) in emission and by reciprocity in coupling [19]. A first example for two capacitors in Fig. 21 is presented.

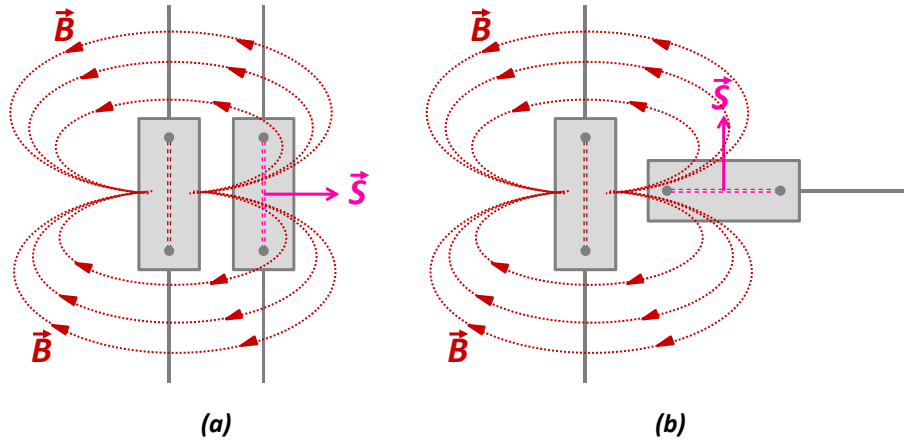


Figure 21: a- High b- Low coupling between two capacitors

When two capacitors are face to face as in Fig. 21-a, the magnetic field generated by the first component is coupled to the second one, through its equivalent coupling surface. Thus, the magnetic coupling between both components is high. However, when both components are perpendicular like in Fig. 21-b, the majority of the magnetic field generated by the first component does not pass through the coupling surface and, therefore, the magnetic coupling is significantly reduced.

For an inductor and a CMC in DM, the principle is the same as for capacitors. The preferred orientation of the magnetic field generated by the first component and the preferred orientation of the coupling to the second component are determined, as presented in Fig. 22 and Fig. 23. The coupling for CMC is only considered in DM because CM does not allow a high coupling compared to DM. This point will be detailed in Sect. 2.7 dedicated to the determination of the equivalent coupling model of a CMC.

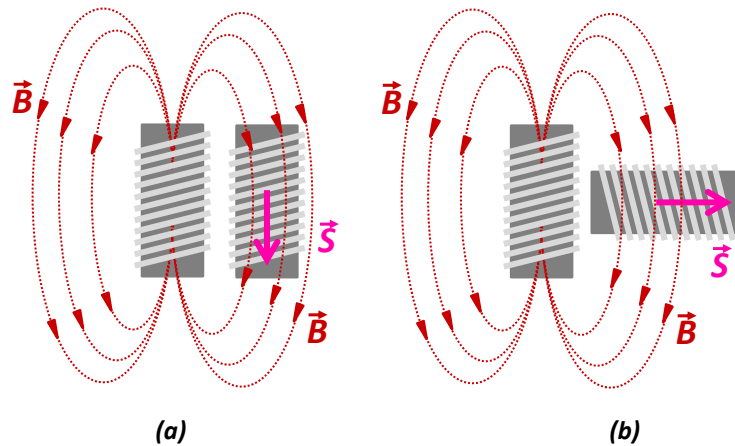


Figure 22: a- High b- Low coupling between two inductors

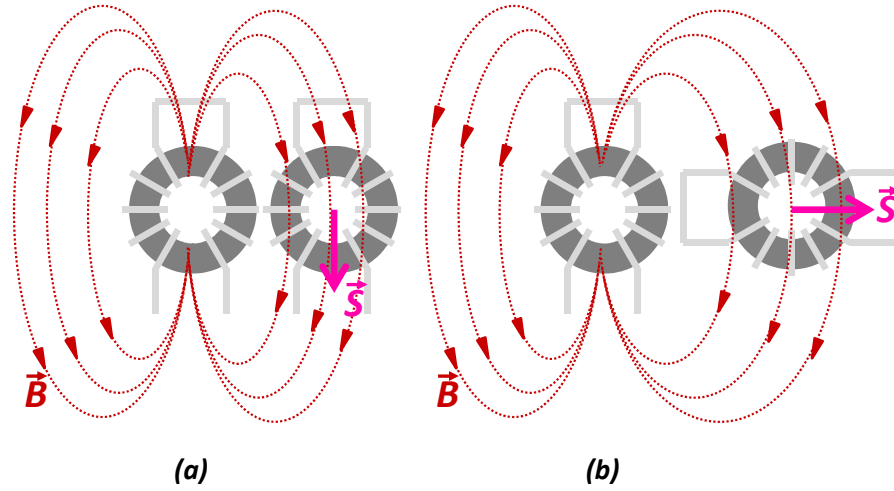


Figure 23: a- High b- Low coupling between two CMCs in DM

As for capacitors, in order to minimize the coupling between two inductors or two CMCs, the component can be turned by 90° as presented in the two previous figures. This reasoning can also be applied for coupling minimization between a capacitor and an inductor, a capacitor and a CMC, etc. This comes from the knowledge of emission direction and coupling direction as presented in [19].

In filter design, to avoid the degradation coming from inter-component coupling, a first step can be the minimization of coupling. This methodology can be applied when there are only two or three components. However, in a real world application, with significant room constraints, this minimization cannot be applied systematically. Indeed, the filter must be designed by considering inter-component coupling and by understanding and knowing which couplings are destructive or not.

Objectives of research studies

The objective of this thesis is to simplify coupling phenomena and to base reasoning only on analytical calculations and exploitation of measurements.

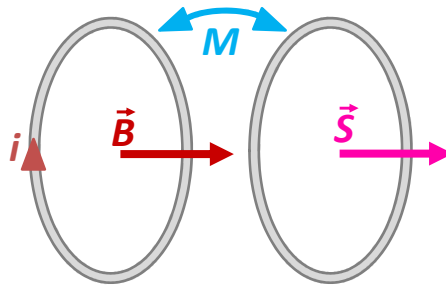


Figure 24: Principle to determine a mutual inductance

The principle which is going to be used is based on Eq. 5 and 6, where the mutual inductance M can be expressed in Eq. 7, considering that p is the complex variable coming from the Laplace transform. Actually, the mutual inductance can be estimated from the magnetic field created by the first component and the equivalent coupling surface of the second component. The flux ϕ created by the magnetic field B on the equivalent surface S are linked to the current by the mutual inductance M (Fig. 24). Eq. 7 clearly describes the different topics (Fig. 25).

$$d\phi = \vec{B} \cdot d\vec{S} \implies \phi = \vec{B} \cdot \vec{S} \quad (5)$$

$$\frac{d\phi}{dt} = M \frac{di}{dt} \implies \phi \cdot p = M \cdot i \cdot p \quad (6)$$

$$\vec{B} \cdot \vec{S} = M \cdot i \quad (7)$$

Coming from Eq. 7, the main steps of the thesis work can be described.

The first chapter deals with the determination of an equivalent coupling surface or, more generally, an equivalent coupling model. Actually, all types of components can have one, several or even no preferred orientation regarding magnetic field coupling. The second chapter is then dedicated to the magnetic field generated by passive components. A mutual inductance can be estimated using both previous topics and will be presented in Chapter 3. Finally, filter performance prediction considering magnetic coupling, with MKME (Modified Kron's Method applied to Electromagnetic compatibility), will be presented in the last chapter. The methodology will be validated under different examples, through real world applications.

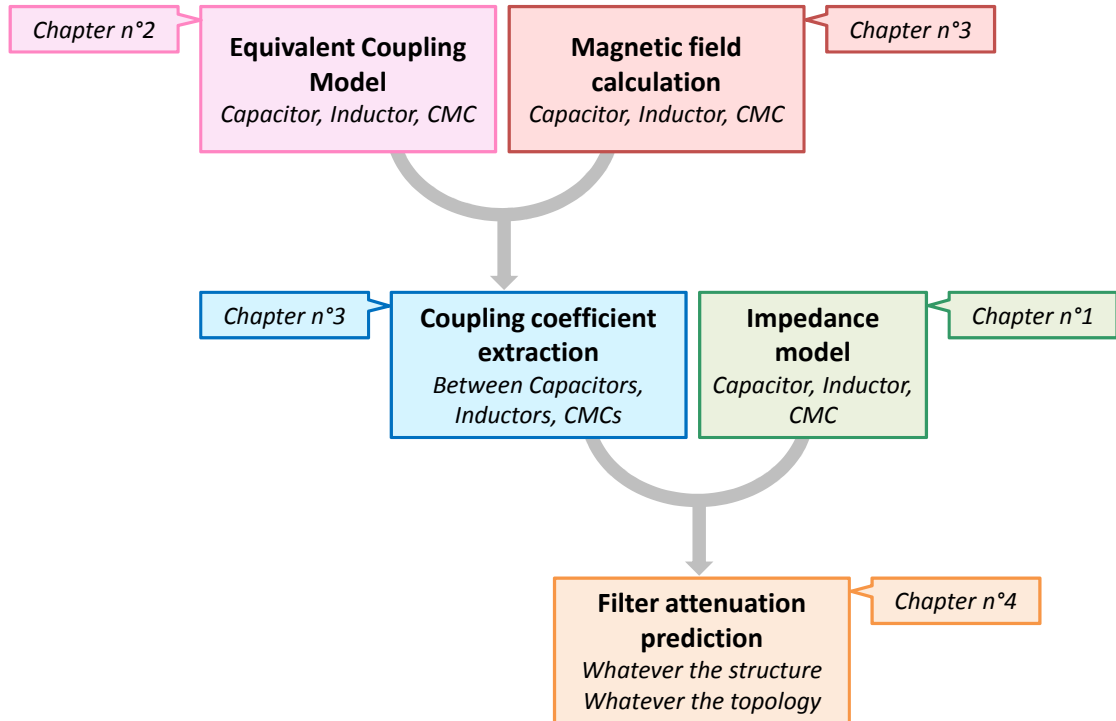
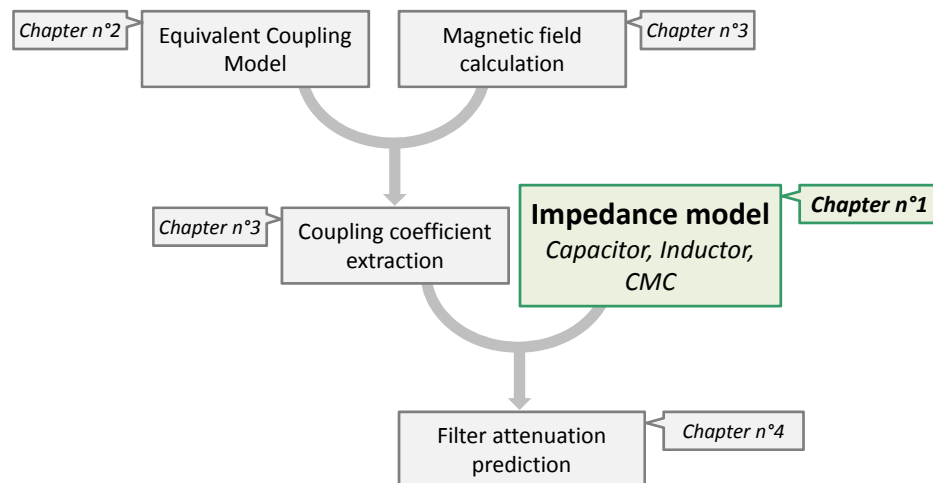


Figure 25: Organization of the different topics

Chapter 1

Main concept of EMI filter design



1.1 Introduction to the main concept of EMI filter design

The design of EMI filters is a key point for EMC (electromagnetic compatibility). Actually, those filters are needed in order to reduce the EMI (electromagnetic interferences) that come from EMI sources. Different structures of filter exist and, therefore, it must be designed case per case considering the required noise attenuation. Finally, in order to build up filters, a good knowledge of passive components in terms of impedance is mandatory.

Therefore, in this first chapter, some general and well-known basics of EMC are presented, such as EMI sources, EMI filters and passive components modeling.

1.2 EMI noise sources

There are two main types of noise sources: natural and artificial sources, as described in [20]. Natural sources gather the earth's magnetic field, lightning or electrostatic discharge for example. Artificial sources can be intentional, such as radar, radio communication, television or medical equipment. There are also unintended sources coming from electronic devices that generate parasitic emissions or from power electronics, with motor control for example. Here, only the unintended artificial noise sources are considered and, more particularly, noise sources coming from electronic and electric equipments.

There are two types of noise propagation that must be distinguished, differential mode (DM) and common mode (CM).

DM noise generally comes from power supply or switching cells. This mode is called the “normal” mode because functional signals are mostly defined in that mode. DM is characterized by currents flowing in the opposite direction for a pair (Fig. 1.1).

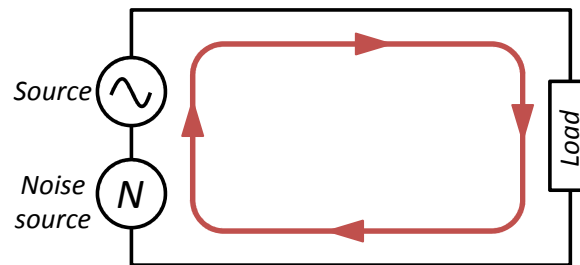


Figure 1.1: DM propagation noise

As far as CM noise is concerned, it appears generally in high frequencies (beyond MHz). CM noise comes from parasitic capacitances between the equipment and its ground reference, as presented in Fig. 1.2. CM noise is commonly named parallel mode because currents are in the same direction for a pair and flow back through the reference.

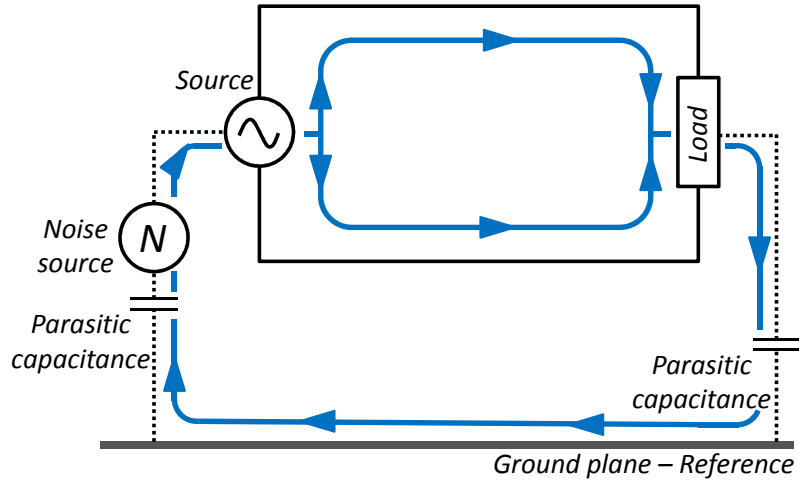


Figure 1.2: CM propagation noise

Therefore, the filter structure must be chosen depending on the mode that requires to be filtered.

Actually, in order to identify the different noise sources and their level, SPICE (Simulation Program with Integrated Circuit Emphasis) simulation is a good solution. By considering parasitic elements, switching cells etc. it is possible to determine which noise is dominant and, therefore, identify the required filtering.

Let us take the example of the noise prediction of a buck converter. In order to perform that, Fig. 1.3 presents the block diagram of the simulation. It includes the different elements for conducted emission simulations which are widely developed in [21, 22, 23, 24, 25]. This block diagram is composed of a battery, two LISNs (for conducted emissions measurements), a filter, a buck converter, a load (which is in this case a resistor) and finally a CM impedance.

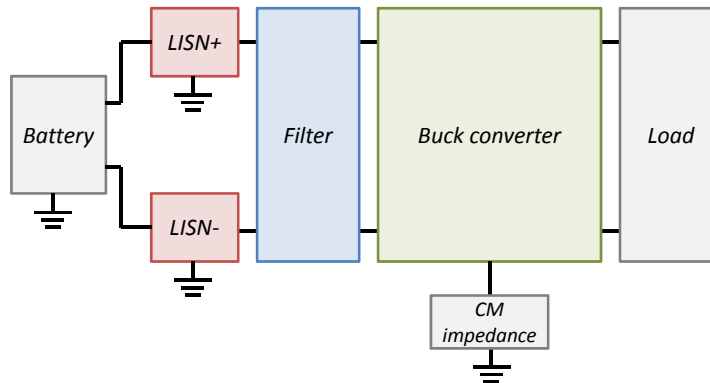


Figure 1.3: Block diagram of noise perturbation estimation for a buck converter

A first step can be to estimate the conducted emissions coming from the buck converter without filtering. Thus, the voltages measured at LISNs level are directly the noise coming from the converter.

Therefore, those voltages are used to extract the related DM and CM noises as presented in Fig. 1.4.

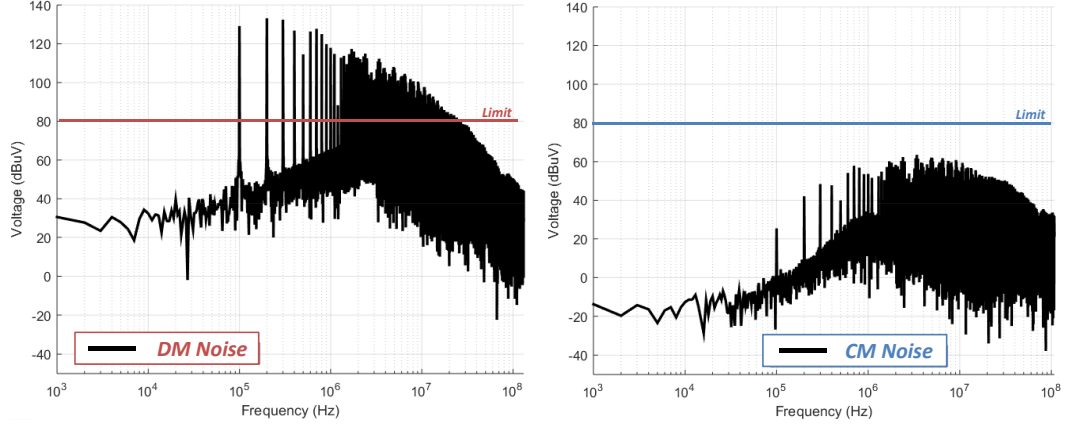


Figure 1.4: DM and CM noise coming from a Buck converter

It clearly appears that, for this particular example, the DM noise is dominant compared to the CM one. Actually, it comes from the switching cell of the converter. Nevertheless, the CM noise is not negligible and it mainly comes from the CM impedance. The limits that are presented in Fig. 1.4 are totally arbitrary and just allow to illustrate the filter design principle.

Actually, it appears that the DM noise overtakes the limit in the frequency band coming from 100kHz to 30MHz and must be reduced by at least 30dB at 200kHz. For the CM noise, it does not overtake the limit and, therefore, a filter more dedicated to DM attenuation must be integrated to the system. This filter must have an operational frequency band coming from 100kHz to 30MHz, and a minimum of 30dB attenuation at 200kHz.

Through this example, it was presented a methodology for CM and DM noises estimation. Considering the limits, the required filter performance is defined and, so, the filter will be designed in consequence. Therefore, the inter-components coupling, that have an influence on filter attenuation, must be considered in order to finally predict the real performances.

The main objective of the thesis work is to ensure that the implemented filter will provide the required attenuation on the correct frequency band.

1.3 EMI filters

1.3.1 Filter attenuation signification

The parameter that characterizes a filter is its attenuation in decibels (dB) and is measurable through its S_{21} parameter. This parameter corresponds to the transmission coefficient between the input and the output of the filter. The S parameters matrix can be defined as the ratio between the incident wave a_i (Eq. 1.1), and reflected wave (Eq. 1.2), as it is described in Eq. 1.3 with $k \neq j$.

$$a_i = \frac{V_i + Z_0 I_i}{2\sqrt{Z_0}} \quad (1.1)$$

$$b_i = \frac{V_i - Z_0 I_i}{2\sqrt{Z_0}} \quad (1.2)$$

$$S_{ij} = \frac{b_i}{a_j} \big|_{a_k=0} \quad (1.3)$$

These S parameters for a two-port network can be presented as in Fig. 1.5 by considering E as an AC voltage and Z_0 the characteristic impedance with $Z_0 = Z_1 = Z_2 = 50\Omega$. S_{ii} parameter is the reflection coefficient of port i when all the other ports are terminated by characteristic impedances. The S_{ij} parameter is the transmission coefficient from port j to port i considering that all the other ports are terminated by characteristic impedances.

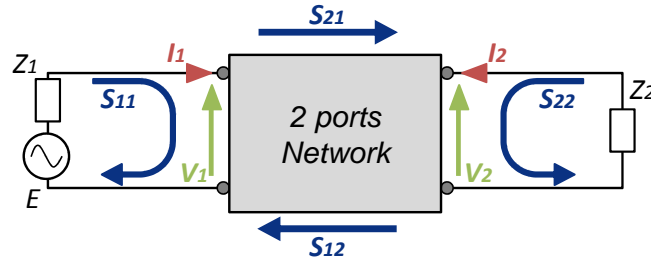


Figure 1.5: S parameters of a two-port network

It must be noticed that it is mandatory to know input and output impedances in order to correctly build the filter. Those impedances have a major influence on filter attenuation as presented in Sect. 1.3.3. It is necessary to characterize the filter under characteristic impedances, so $Z_0 = Z_1 = Z_2 = 50\Omega$, but it is also necessary to predict the filter attenuation considering the real impedances, by simulation or calculation.

1.3.1.1 Analytical calculation

S parameters can be expressed as a function of currents and voltages presented in Fig. 1.5. Eq. 1.1, 1.2 and 1.3 can be summarized and applied to the two ports network.

- $S_{11} = \frac{b_1}{a_1} \big|_{a_2=0}$, it can be considered that $a_2 = 0 \Leftrightarrow V_2 + Z_0 I_2 = 0$ and considering Kirchhoff law, $E = V_1 + Z_0 I_1 \Rightarrow S_{11} = \frac{2V_1}{E} - 1$
- $S_{12} = \frac{b_1}{a_2} \big|_{a_1=0}$, it can be considered that $a_1 = 0 \Leftrightarrow V_1 + Z_0 I_1 = 0$ and considering Kirchhoff law, $E = V_2 + Z_0 I_2 \Rightarrow S_{12} = \frac{2V_1}{E}$
- $S_{21} = \frac{b_2}{a_1} \big|_{a_2=0}$, it can be considered that $a_2 = 0 \Leftrightarrow V_2 + Z_0 I_2 = 0$ and considering Kirchhoff law, $E = V_1 + Z_0 I_1 \Rightarrow S_{21} = \frac{2V_2}{E}$
- $S_{22} = \frac{b_2}{a_2} \big|_{a_1=0}$, it can be considered that $a_1 = 0 \Leftrightarrow V_1 + Z_0 I_1 = 0$ and considering Kirchhoff law, $E = V_2 + Z_0 I_2 \Rightarrow S_{22} = \frac{2V_2}{E} - 1$

In order to simplify all these equations, the AC voltage E can be fixed at $E = 2V$. Indeed, the S parameters matrix can be presented as in Eq. 1.4.

$$[S] = \begin{pmatrix} S_{11} & S_{12} \\ S_{21} & S_{22} \end{pmatrix} = \begin{pmatrix} V_1 - 1 & V_1 \\ V_2 & V_2 - 1 \end{pmatrix} \quad (1.4)$$

The output voltage of the two-port network is then the image of filter attenuation . It must be noticed that the result is a voltage ratio and is dimensionless.

There are two types of noise and so two types of filter. Indeed, the filter must be connected in order to induce a DM or CM current, to extract its performance.

For the first case dedicated to DM noise, the filter must be connected in DM in order to extract its performance in the presence of a DM current. Fig. 1.6 shows how it can be done by using Fig. 1.5 and considering the two-port network as the filter.

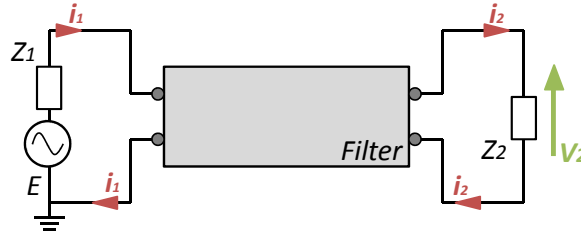


Figure 1.6: DM attenuation calculation

The AC source voltage $E = 2V$ and the characteristic impedance $Z_1 = 50\Omega$ are located between both inputs and a characteristic impedance $Z_2 = 50\Omega$ is located between both outputs, in order to extract V_2 , the image of the DM attenuation.

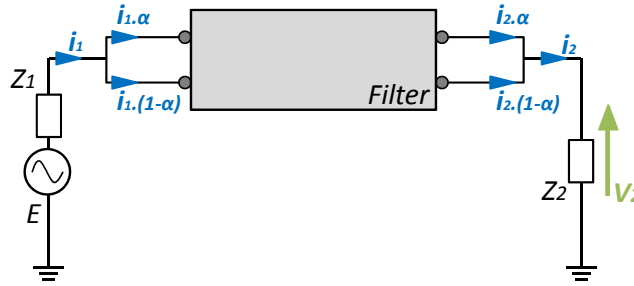


Figure 1.7: CM attenuation calculation

For the second case, the filter must be connected in CM in order to extract its performance in the presence of CM current. Indeed, both inputs are shorted and connected to a characteristic impedance $Z_1 = 50\Omega$ and the AC source voltage $E = 2V$. Outputs are also shorted and connected to a characteristic impedance $Z_2 = 50\Omega$, as presented in Fig. 1.7. A CM current flows through the filter and, therefore, the voltage V_2 is the image of the CM attenuation considering that $0 < \alpha < 1$ the proportion of the current going on each edge (depending on impedances).

This kind of calculation can be performed with nodal analysis such as in a SPICE simulator, or using a modal analysis such as MKME. The choice here is to use a modal analysis as in [26, 27, 28], which is very practical in terms of speed of calculation and genericity [29].

Another advantage of MKME is that everything is configurable and all parameters are grouped and classified into two different categories: the intrinsic parameters and the modifiable ones. This point is very important because the difference is clearly made between all the fixed parameters (filter components and their parasitic elements) and all the modifiable ones (the coupling between the components).

Finally, it must be noticed that all the reasoning that will be presented is capitalized in a unique generic tool and, therefore, speed of calculation and genericity are mandatory.

Indeed, MKME appears as a good choice to study filter attenuation considering inter-component coupling. Consequently, it will be presented in detail in Chapter 4.

1.3.1.2 Attenuation measurement

The attenuation of a filter is measurable through its S_{21} parameter. The dedicated device is the VNA (Vector Network Analyzer) that can measure S parameters in magnitude and phase. The principle is to connect the filter input to the first port and the filter output to the second port and, thus, measure the corresponding S parameters (Fig. 1.8).

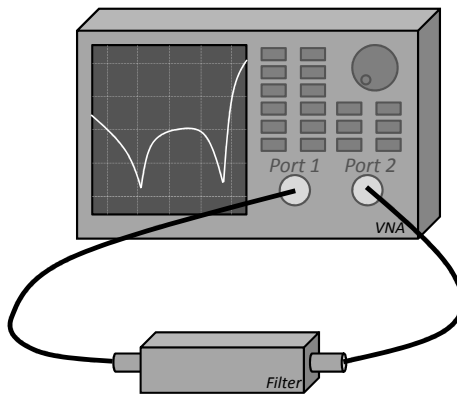


Figure 1.8: Filter attenuation measurement with a VNA

S_{11} parameter is thus the reflection coefficient of the first port, S_{21} the transmission coefficient from the first port to the second one, S_{12} the transmission coefficient from the second port to the first one and finally, S_{22} is the reflection coefficient of the second port.

Before performing any measurement, a VNA calibration must be done in order to compensate wire and connector effects. Indeed, the reference plane is located at the input and output of the filter in order to only measure the S parameters of the filter and not the filter including connections.

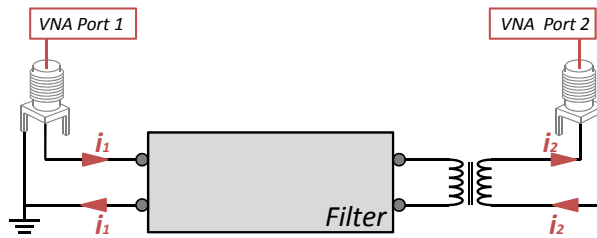


Figure 1.9: DM filter attenuation measurement

Both modes must be measured separately and Fig. 1.9 can be considered as a filter attenuation measurement in DM. Actually, this configuration induces a DM current to the filter and, therefore, its performance for a DM noise can be extracted. It must be noticed that a transformer is necessary at the filter output. Its role is to insulate both ground ports of the VNA, in order not to short

a part of the filter. Actually, the grounds of the two ports of the VNA are connected together and, thus, the transformer is mandatory to extract the real DM filter attenuation with the S_{21} parameter and not only a part of the filter.



Figure 1.10: CM filter attenuation measurement

The CM filter attenuation measurement is based on the same principle as in the previous subsection, the filter must be connected in order to induce a CM current. Fig. 1.10 presents this kind of measurement, both inputs are shorted and connected to the first port of the VNA, and both outputs are shorted and connected to the second port. Finally the S_{21} parameter represents the CM filter attenuation considering that $0 < \alpha < 1$ the proportion of the current going on each edge (depending on impedances).

Examples here are for SMA connectors making the link between the filter and the VNA.

1.3.2 Filter structures

The main objective of a filter is to attenuate the disturbances generated by electronic equipment. To do so, the idea is to introduce an impedance discontinuity. For example, if the input and output impedances of the system, regarding the filter position, are low (regarding 50Ω), the goal is to integrate a filter with a high impedance. Typically, inductances and common mode chokes (CMCs) present high impedances whereas capacitors present low impedances.

Regarding the mode of the perturbation, the filter must be adapted for DM or CM or both. All the structures that are presented in the following subsections can be used on their own or by mixing them together. The structure has to be chosen according to the required attenuation. The higher the number of filter cells in cascade, the higher the filter order and, therefore, the better the filter performance. For instance, a single LC filter presents an ideal behavior of $-40dB/decade$ whereas a double LC filter in cascade presents an ideal behavior of $-80dB/decade$.

In the following subsections, different filter structures are presented but are not exhaustive.

1.3.2.1 Filter structures dedicated to low input and output impedances of the system regarding the filter position

The objective of a filter is to introduce an impedance discontinuity. The system presents low input and output impedances, regarding the filter position. Indeed, the filter should present high input and output impedances (Fig. 1.11).

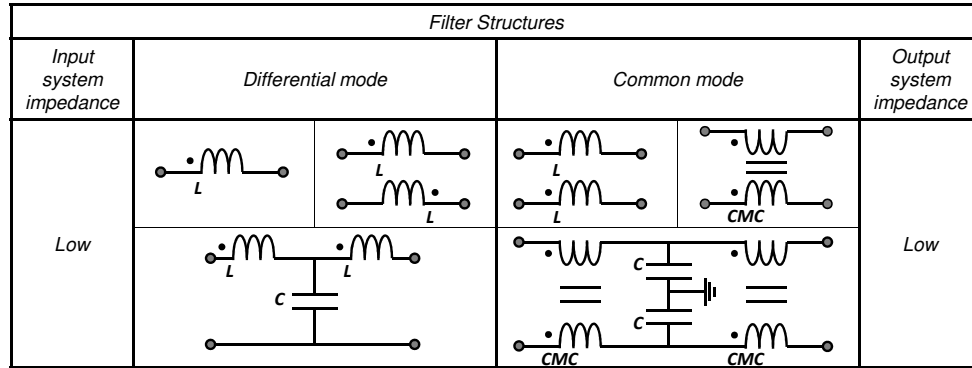


Figure 1.11: Example of structures for low input and output impedances of the system regarding the filter position

The idea is, thus, to present a high impedance and to respect the current path. It must be noticed that a differential mode choke (DMC) can also be used for DM filter structure. This component is based on the same principle as CMC but dedicated for DM attenuation.

1.3.2.2 Filter structures dedicated to low input and high output impedances of the system regarding the filter position

For this case, the system presents low input and high output impedances, regarding the filter position. Indeed, the filter should present a high input impedance and a low output impedance (Fig. 1.12).

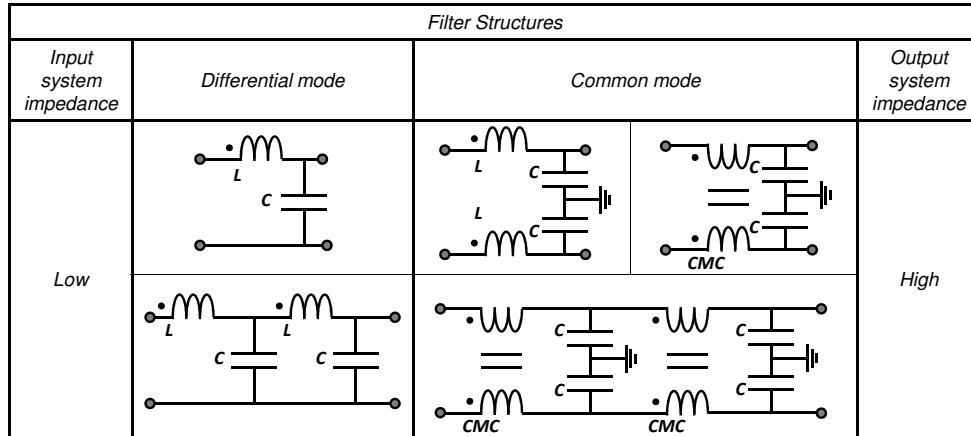


Figure 1.12: Example of structures for low input and high output impedances of the system regarding the filter position

1.3.2.3 Filter structures dedicated to high input and low output impedances of the system regarding the filter position

Now, the system presents high input and low output impedances, regarding the filter position. Indeed, the filter should present a low input impedance and a high output impedance (Fig. 1.13).

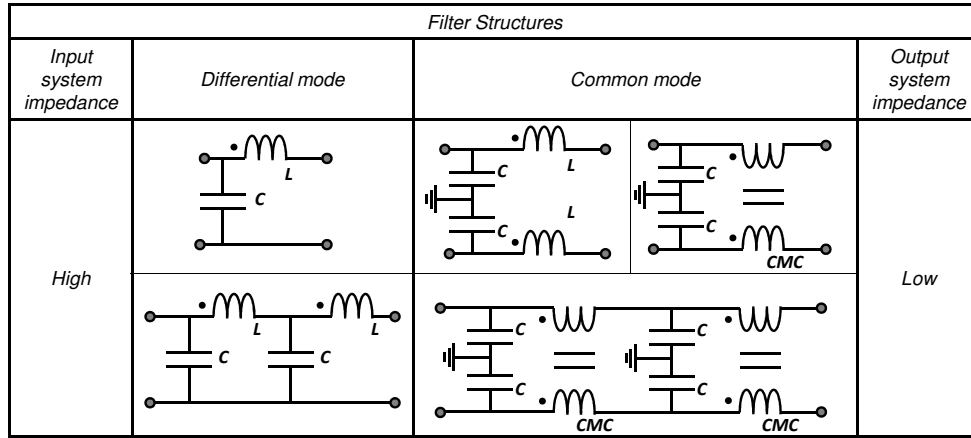


Figure 1.13: Example of structures for high input and low output impedances of the system regarding the filter position

1.3.2.4 Filter structures dedicated to high input and output impedances of the system regarding the filter position

Finally, for the case when the system presents high input and output impedances, regarding the filter position, the filter should present low input and output impedances (Fig. 1.14).

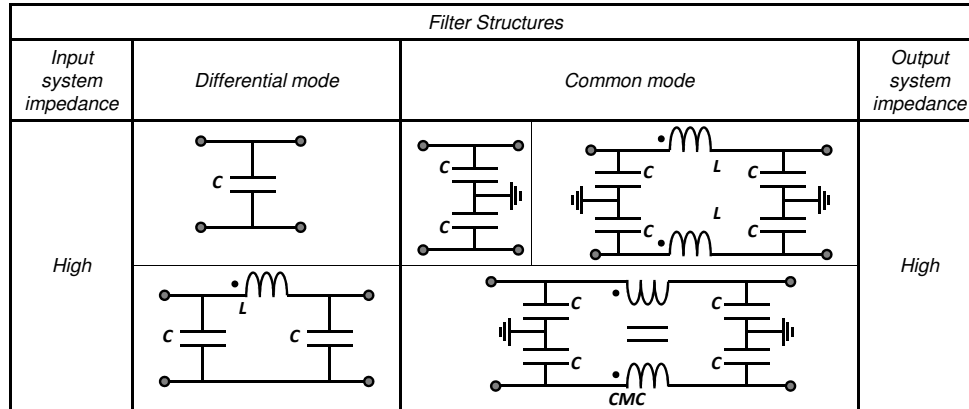


Figure 1.14: Example of structures for high input and output impedances of the system regarding the filter position

1.3.3 Influence of input and output impedances on filter attenuation

Until then, input and output impedances, in order to characterize the filter, are considered as matched impedances such as $Z_0 = Z_1 = Z_2 = 50\Omega$. However, those impedances are rarely matched on a real application. Then, the filter will not have the same performance as the one predicted.

In order to illustrate this influence, let us take a first example presented in Fig. 1.15 of the attenuation calculation of a simple capacitor. The capacitor model is composed of the self-capacitance in series with its parasitic resistance ESR and inductance ESL . This model is presented in detail in Sect. 1.4.2.

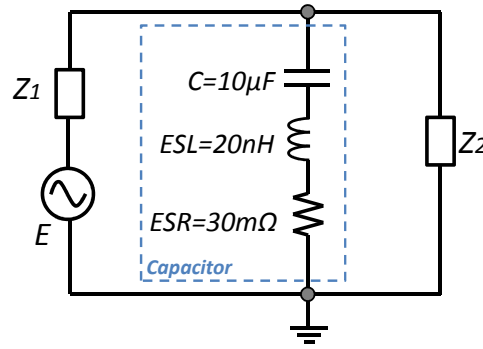


Figure 1.15: Attenuation calculation for a 10μF capacitor

Thus, in order to calculate the filter attenuation, $E = 2V$ and $Z_1 = Z_2 = 50\Omega$ are considered. The final attenuation in Fig. 1.16-a presents an efficient attenuation from 10kHz to 400MHz. Actually, it comes from the impedance ratio in Fig. 1.16-b which confirms the frequency band of attenuation.

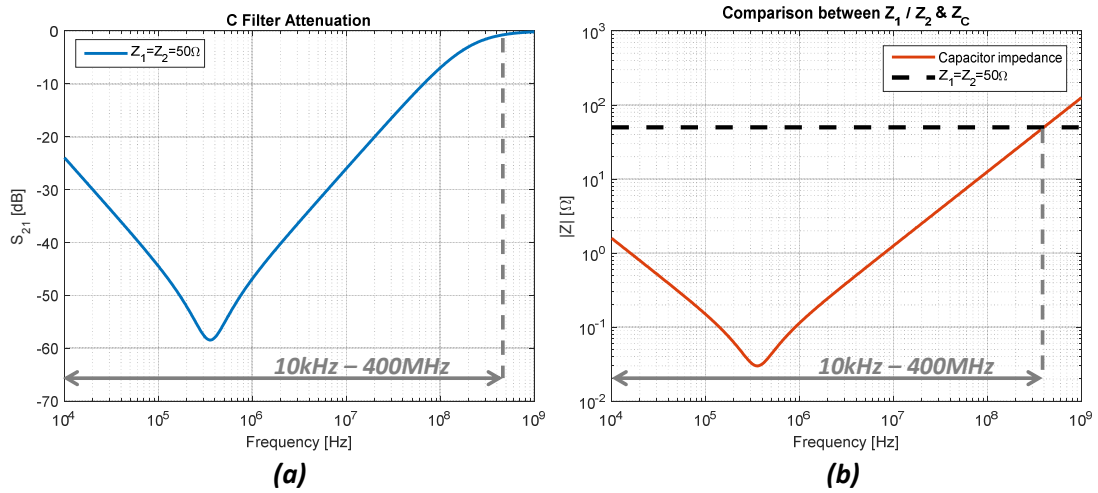


Figure 1.16: a- C Filter attenuation under matched impedances b- Impedances comparison

However, if the system presents a low impedance at the filter input (for example $Z_1 = 1\Omega$), the final filter attenuation is degraded (Fig. 1.17-a) because the impedance ratio is not so high (Fig. 1.17-b). Thus, filter performance and frequency band are clearly reduced. This example shows the importance of the good knowledge of system impedances.

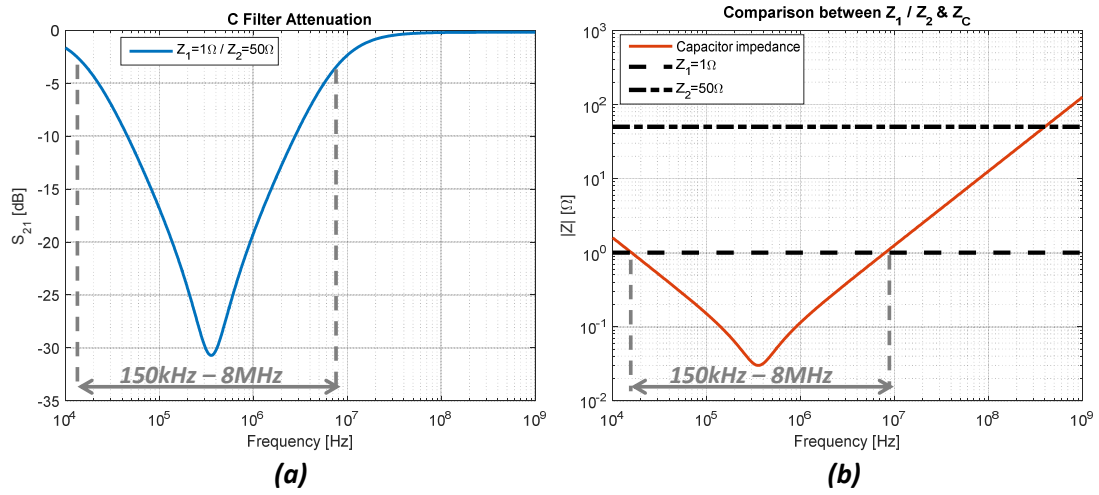


Figure 1.17: a- C Filter attenuation under non-matched impedances b- Impedances comparison

Another phenomenon that can come from the poor knowledge of impedances is the bad attenuation of self-resonances. For a single LC filter, there is only one self-resonance (two components and so one resonance) which is located at $f_s = \frac{1}{2\pi\sqrt{LC}}$. Generally, when impedances are matched, this resonance is damped thanks to the 50 Ω terminations. However, when impedances are unmatched, this self-resonance is no more damped. Then, the filter can amplify instead of attenuating. Let take the example of the filter in Fig. 1.18 with a 10 μ H inductor (the equivalent model is presented in Sect. 1.4.3) and a 1 μ F capacitor. The self-resonance is thus located at 50kHz.

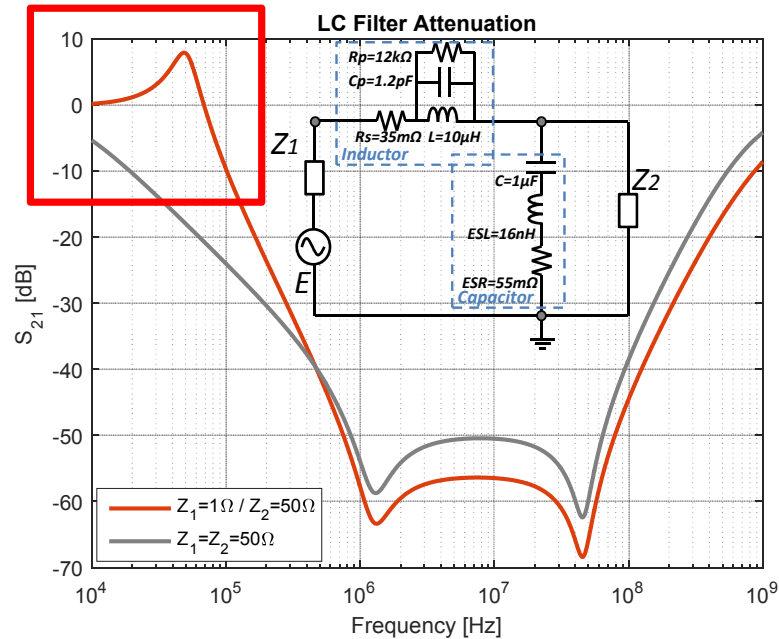


Figure 1.18: LC filter attenuation with matched and unmatched impedances

This kind of problems must be taken into account to avoid the amplification of signals that

are supposed to be attenuated. A damping network must be integrated after the filter [30]. The rule of thumb to design such damping network is to use a capacitor $C_{shunt} = 4.C$ and a resistor $R_{shunt} = \sqrt{L/C}$. For the present example, it gives $C_{shunt} = 4\mu F$ and $R_{shunt} = 3\Omega$ as the damping circuit, and provides good results, as presented in Fig. 1.19.

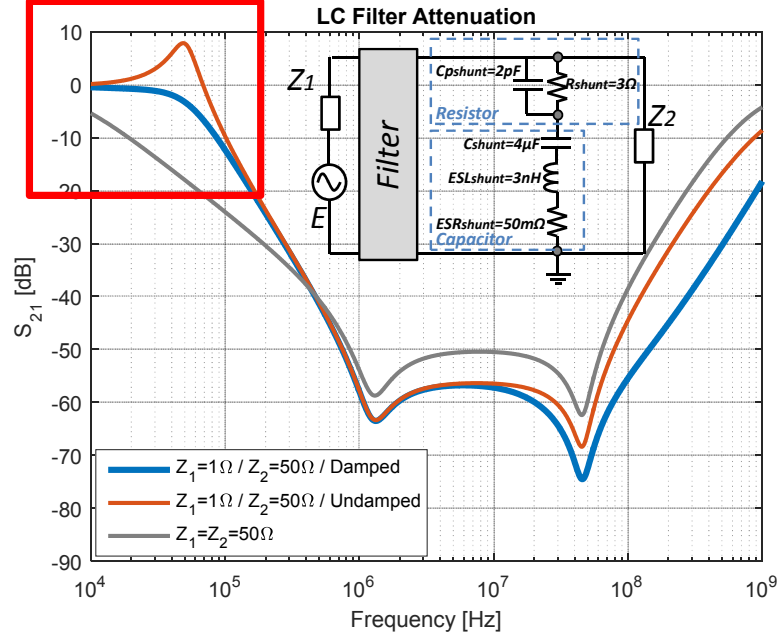


Figure 1.19: LC filter attenuation with matched and unmatched impedances, with and without damping

1.4 Modeling of passive components

1.4.1 Impedance measurement

For the purpose of building model, for filter structures presented in Sect. 1.3.2, it has been mentioned briefly in Sect. 1.3.3, that a passive component has parasitic elements. Actually, a capacitor is not a pure capacitance, as an inductor does not present a purely inductive behavior. Passive components have a frequency behavior which must be characterized and transposed to an equivalent electrical model, in order to correctly predict a filter attenuation for the frequency range dedicated to the conducted emission tests (from 150kHz to 108MHz). However, the validity of the models that are going to be presented can be extended to a wider frequency range.

All equivalent models are based on impedances extracted from measurements with the aim of identifying parasitic elements. Different measurements can be performed to extract an equivalent model.

The first one, which is the more direct one, is to use an impedance analyzer. The working principle for an impedance analyzer is simple: a voltage is applied to the component and the current flowing through the component is measured. This way, the extraction of the impedance is direct thanks to Ohm's law.

The second one is to use a VNA and by converting the S parameters to Z parameters, it is

possible to extract the impedance.

For the VNA, the extraction is indirect because the impedance must be extracted from the S parameters that are measured. Before any measurement, a first guess is necessary on the impedance level which is going to be measured. According to the chosen measurement, S_{21} series, S_{21} parallel or S_{11} (Fig. 1.20), the accuracy is not the same regarding the measured impedance [20, 31, 32, 33].

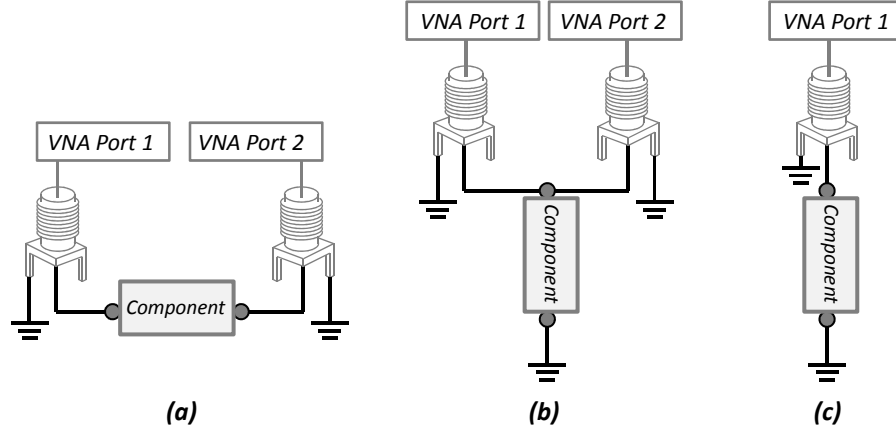


Figure 1.20: a- S_{21} series b- S_{21} parallel c- S_{11} measurements

The S_{21} series measurement is more dedicated to components that present high impedance, that is greater than 50Ω . This measurement is thus more dedicated to inductors or CMC. To calculate an impedance from the measured series S_{21} , Eq. 1.5 can be used, considering that $Z_0 = 50\Omega$ is the VNA impedance.

$$Z = 2 \cdot Z_0 \frac{1 - S_{21series}}{S_{21series}} \quad (1.5)$$

The S_{21} parallel measurement is more dedicated to component with a low impedance, such as capacitors. To calculate an impedance from the measured parallel S_{21} , Eq. 1.6 can be used.

$$Z = Z_0 \frac{S_{21parallel}}{2 \cdot (1 - S_{21parallel})} \quad (1.6)$$

The S_{11} measurement is dedicated to component with an impedance near 50Ω . To calculate an impedance from the measured S_{11} , Eq. 1.7 can be used.

$$Z = Z_0 \frac{1 + S_{11}}{1 - S_{11}} \quad (1.7)$$

Whether with the VNA or impedance analyzer, a calibration phase is mandatory in order to compensate for wire and connector effects.

The point that determines the measurement method is the frequency range and the required accuracy. Actually, the impedance analyzer can measure an impedance from a tenth of Hz until some MHz, whereas the VNA can perform a measurement until a few GHz. However, the impedance analyzer measurement is very accurate from tenths of $m\Omega$ until hundreds of $k\Omega$ (Fig. 1.21) whereas the VNA measurements are much more limited [20].

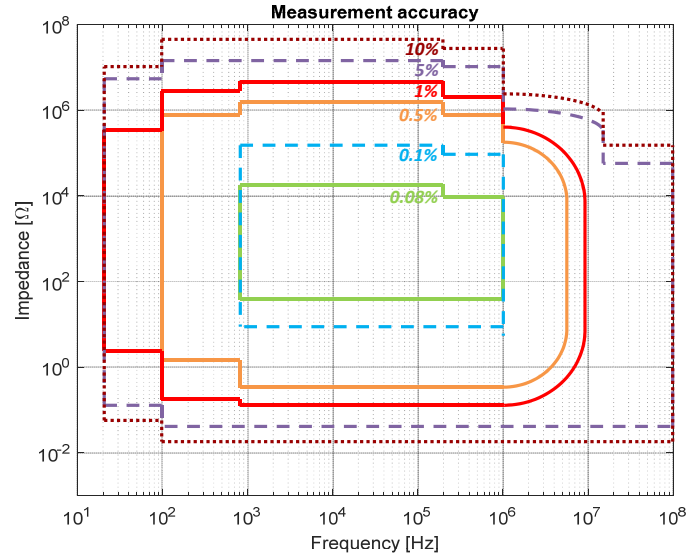


Figure 1.21: Measurement accuracy for impedance analyzer measurements [34]

1.4.2 Capacitor

A capacitor is a two-port passive component, widely used in filter structures. There are a lot of different technologies of capacitors, such as:

- Ceramic capacitors: very stable in temperature and can work at high frequencies thanks to their small size and small capacitance value (from $1pF$ until $10\mu F$),
- Film capacitors: from $1nF$ until $10\mu F$, very stable in temperature and frequency,
- Electrolytic capacitors: polarized and generally used at low frequency because of their high capacitance value (from $1\mu F$ until $10mF$). The performance of electrolytic capacitor highly depends on temperature.

Actually, each capacitor presents the same profile over frequency in terms of impedance. Fig. 1.23 presents the typical behavior of a $10\mu F$ capacitor.

The used impedance analyzer has an operational frequency band from 20Hz until 30MHz and thus limits the model to this frequency band. To go farther, it is possible to perform a measurement with the VNA and, therefore, widen the frequency band in which the model is valid.

Different models for capacitor exist like in [35, 36] but the model that combines simplicity and accuracy is composed of a capacitance C (the self-capacitance of the capacitor), a parasitic inductance ESL and a parasitic resistance ESR (Fig. 1.22).



Figure 1.22: Equivalent model of a capacitor

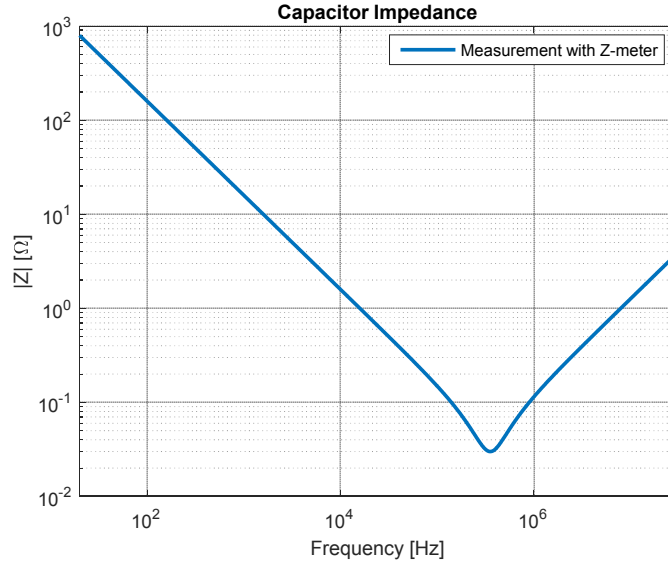


Figure 1.23: Impedance of a 10μF capacitor

From Fig. 1.23, the three types of behavior can be identified:

- At low frequency, the capacitive behavior is dominant. From 20Hz until hundreds of kHz, it is clearly identifiable with its $-20dB/decade$ negative slope. In order to extract the capacitance value, the idea is to choose a frequency where the slope is constant and apply the impedance relation $Z_C = \frac{1}{jC\omega}$. For example, at 1kHz, the impedance can be extracted ($Z_C = 15.6\Omega$) and finally gives a capacitance value of $C = 10\mu F$.
- Then, the resonance appears, which marks the transition from the capacitive to inductive behavior. At this particular frequency, both behaviors compensate for each other, thus the resistive behavior is dominant. In the present example, the resonance appears at 350kHz, the impedance value is about 30mΩ, which provides the *ESR*.
- Finally, the inductive behavior appears and is clearly identifiable thanks to the $+20dB/decade$ slope. This inductance is called the equivalent series inductance and corresponds to the capacitor connections. Consequently, the bigger the capacitor (in size), the higher the *ESL*. In order to extract the inductance value, the idea is to choose a frequency where the slope is constant and apply the impedance relation $Z_L = jL\omega$. For example, at 10MHz, the impedance can be extracted ($Z_{ESL} = 1.26\Omega$) and finally gives an inductance value of $ESL = 20nH$. Another possibility to determine the inductance value is to use the resonance frequency. Actually, at the resonance frequency, the capacitive and inductive behaviors compensate for each other. Thus, $Z_{ESL} = Z_C$ and, consequently, $ESL = \frac{1}{4\pi^2 f_{res}^2 C}$ that gives a value of $ESL = 20nH$.

Particular case of electrolytic capacitors:

As explained at the beginning of this section, electrolytic capacitors are widely used when a high value of capacitance is required. However, the main drawback is that the frequency band where the equivalent series resistances *ESR* is dominant is wide and, therefore, its variation is visible [37].

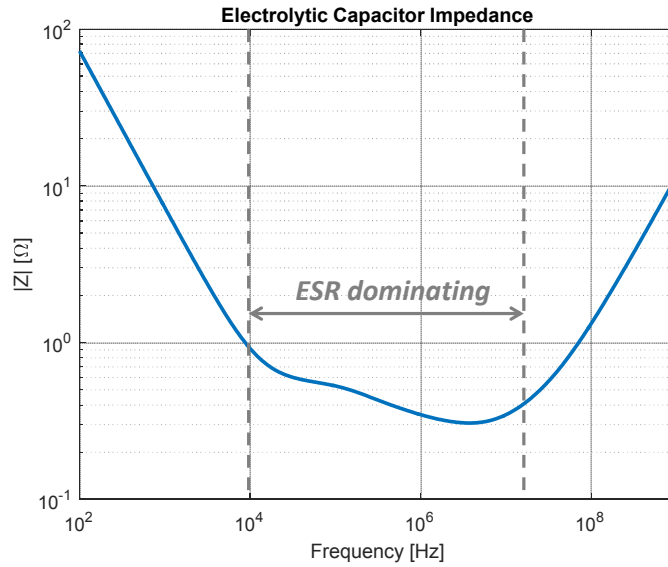
Figure 1.24: Impedance of a 22 μ F electrolytic capacitor

Fig. 1.24 clearly shows that the capacitive and inductive behaviors are still easily identifiable whereas the resistive part is hard to determine because of its variation. Consequently, it is not possible to simply use the RLC in series model for an electrolytic capacitor. The model in Fig. 1.25 can be used to reproduce this particular behavior. The methodology to determine each cell of the model is described in [38] and more generally in [20].

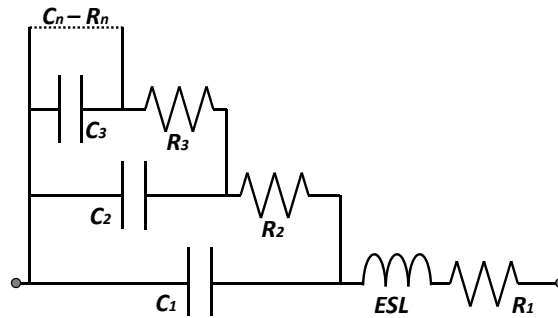


Figure 1.25: Equivalent model of an electrolytic capacitor

1.4.3 Inductor

An inductor is a two-port component, generally composed of a coil wound on a magnetic material. The objective of an inductor is to present a high impedance, so that, when a current flows through the component, the magnetic material increases the impedance and finally improve the filtering. There are several types of inductors: the horizontal inductor, the vertical one or the toroid inductor (Fig. 1.26).

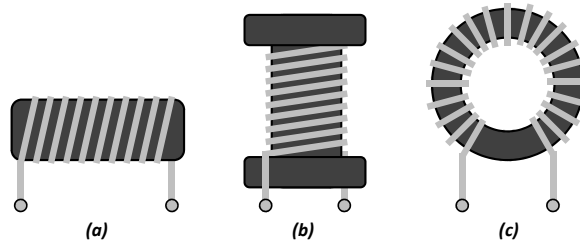


Figure 1.26: a- Horizontal b- Vertical c- Toroid inductors

The typical frequency behavior of an inductor is presented in Fig. 1.27.

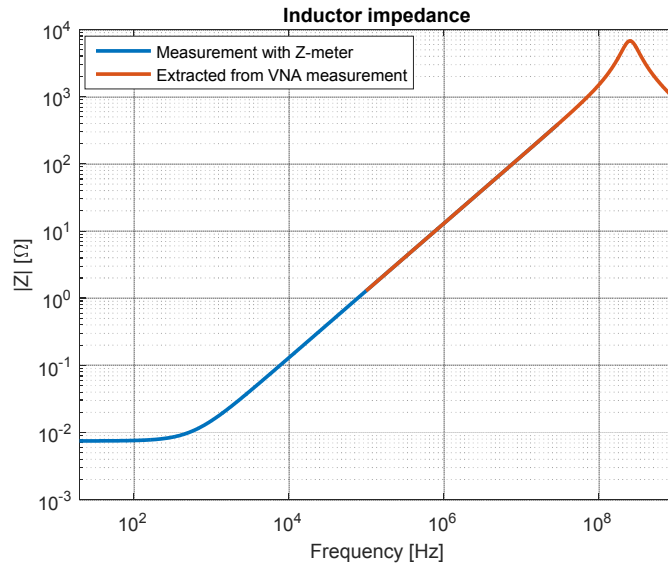
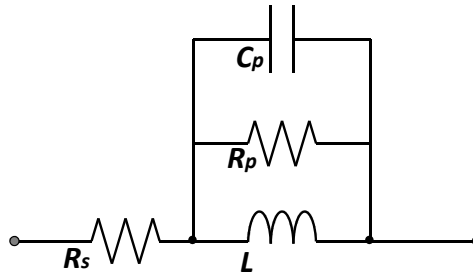
Figure 1.27: Impedance of a $2\mu\text{H}$ inductor

Figure 1.28: Equivalent model of an inductor

Different models exist to describe an inductor behavior like in [35, 39]. Here, Fig. 1.27 presents a typical behavior and it begins by a resistance R_s which is related to the resistance of the wire. Then the inductive behavior appears, which is characterized by L , the self-inductance of the component. The resonance appears, where the parallel parasitic resistance R_p is related to losses

in the magnetic material. Finally, the capacitive behavior characterized by C_p is related to the capacitance between each turn and also between both ports.

The measurement has been performed in two steps as can be seen in Fig. 1.27. Actually, the measurement with the impedance analyzer does not provide enough information on the inductor to have a complete model. Moreover, to obtain the entire typical behavior of an inductor, the first measurement is completed with an impedance extracted from a VNA measurement. The four steps of behaviors can be determined:

- At low frequency, the series resistance R_s is clearly identifiable and $R_s = 75m\Omega$,
- Then, the inductive behavior appears, this part is recognized by the $+20dB/decade$ slope. In order to determine the inductance value, the method used to extract the parasitic inductance of a capacitor can be used. For example, at $1MHz$ the impedance can be extracted and $Z_L = 12.6\Omega$. It gives an inductance value of $L = 2\mu H$.
- The resonance appears and the parallel parasitic resistance R_p can be extracted: $R_p = 6.8k\Omega$.
- Finally, the capacitive behavior is identifiable with its $-20dB/decade$ negative slope. The capacitance value can be extracted in the same manner as for a capacitor. However in this case, the capacitive behavior is not totally stable. Indeed, the resonance frequency is used to extract the capacitance value such as $C_p = \frac{1}{4\pi^2 f_{res}^2 L}$ and it gives for the present case a value of $C_p = 0.2pF$.

Particular case of multi-resonance phenomena:

On power electronics, the components that composed the filter can have a relative big size. Therefore, propagation effects can appear on the frequency range of interest (below 108MHz) and can induce multi-resonances phenomenon (Fig. 1.29). Thus, the classic model, only composed of a series resistance and an RLC in parallel, is not sufficient to reproduce this kind of behavior.

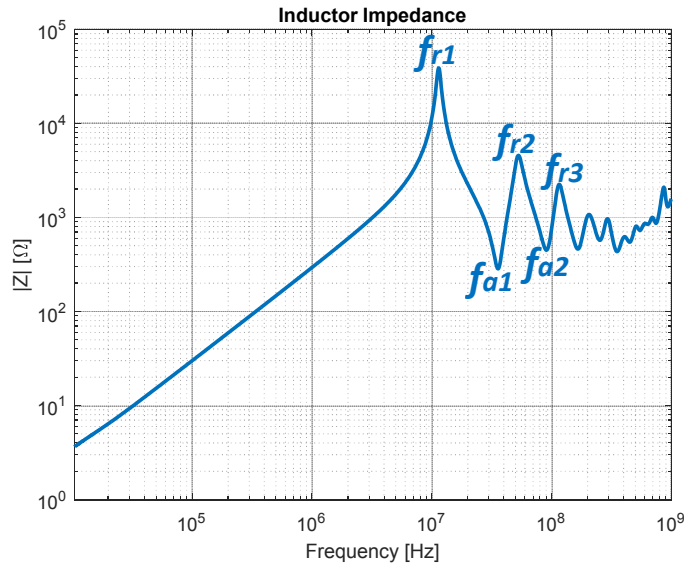


Figure 1.29: Impedance of a 24 μ H inductor

Consequently, it is sometimes necessary to use a more complete model to have a good representation of the reality. The multi-resonance model presented in Fig. 1.30 is based on cascaded parallel RLC cells. All those cells are calculated from resonance frequencies (f_r) and anti-resonance frequencies (f_a).

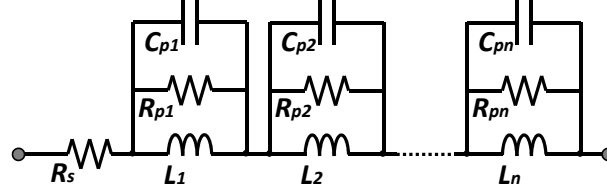


Figure 1.30: Equivalent model of an inductor with multi-resonances

The model in Fig. 1.30 comes from [40] and is derived to be applied to inductors. The first step of the model definition is to determine the first cell: same methodology as for a classic inductor. Then, in order to determine the next cells, the calculation is based on previous cells, resonance and anti-resonance frequencies:

$$L_{i+1} = L_i \frac{1 - \frac{f_{ai}^2}{f_{ri+1}^2}}{\frac{f_{ai}^2}{f_{ri}^2} - 1} \quad (1.8)$$

$$C_{pi+1} = C_{pi} \frac{1 - \frac{f_{ri}^2}{f_{ai}^2}}{\frac{f_{ri+1}^2}{f_{ai}^2} - 1} \quad (1.9)$$

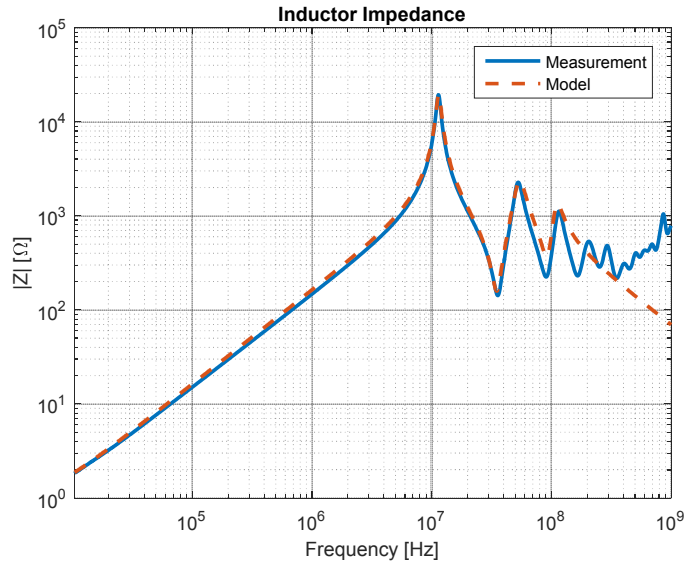


Figure 1.31: Three cells multi-resonance model for a 24μH inductor

The resistance values are determined at the resonance frequency as presented for a classic inductor. Then, Fig. 1.31 presents the model for the 24μH inductor; three cells were required in

order to have a good model from 150kHz to 108MHz, the frequency range of interest.

1.4.4 Common mode choke

A common mode choke (CMC) is a four-port component, made of two coils wound on the same magnetic toroid core. Both coils can face each other (Fig. 1.32-a) or be wound together (Fig. 1.32-b).

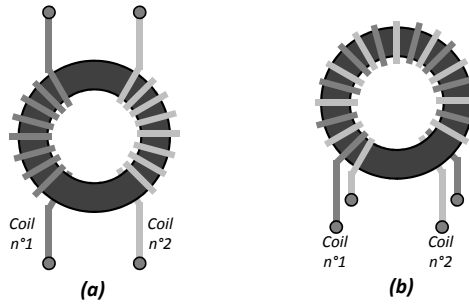


Figure 1.32: CMC windings a- facing each other b- wound together

It must be noticed that a CMC has its two windings in the same direction. This way, when a CM current goes through the component, a magnetic field is generated inside the core, increasing the impedance and, finally, the CMC can play its filtering role. A differential mode choke (DMC) has its two windings in the opposite direction to play its filtering role when a DM current goes through the component. Here, only the CMC model is presented. Nevertheless, it is possible to use this method to build a model for a DMC, simply by inverting the two measurements.

There are two predominant modes for a CMC and, therefore, two measurements are required to build the CMC model:

- A CM measurement, to apply a CM current to the CMC (Fig. 1.33-a),
- A DM measurement, to apply a DM current to the CMC (Fig. 1.33-b).

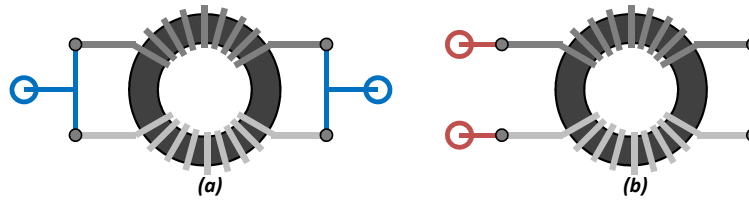


Figure 1.33: a- CM b- DM measurements

Therefore, the self-inductance properties of the choke are extracted from the CM measurement, whereas its leakage properties are extracted from the DM measurement. Typical DM and CM measurements are presented in Fig. 1.34.

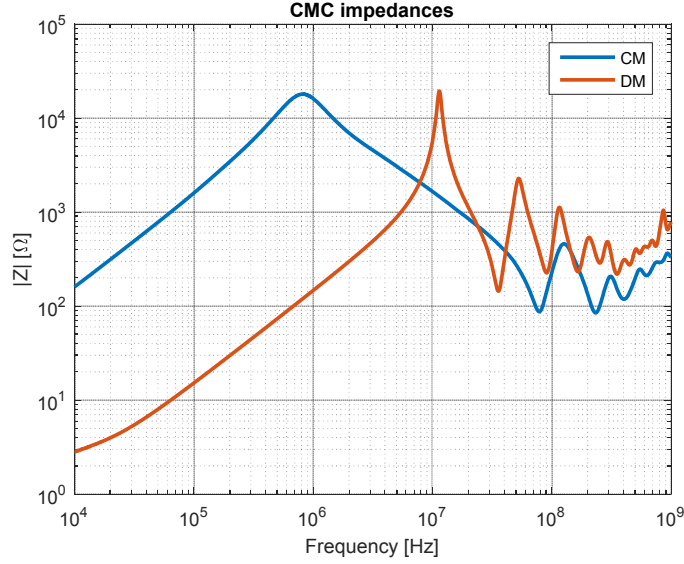


Figure 1.34: DM and CM impedances of a 2.5mH CMC

Different models exist in the literature, like in [41, 42], but are generally limited, in terms of behavior representation or frequency. Furthermore, in the majority of the existing models, two different models exist for the CMC, one for DM and one for CM. Therefore, we developed a model that can represent different typical behaviors of CMC, that can be valid until high frequency and that can group DM and CM in a same model.

The objective here is to present the three different models that were developed for three different types of behaviors. Those models consider both CM and DM of CMCs. The first model is the simplest one and consists of single parallel-RLC based circuits. This model is sufficient if there is no multi-resonance in the frequency range of interest (like for inductors) and if the permeability of the magnetic material is constant as a function of frequency. Then, a model of a CMC inspired from [40] will be explained. The proposed model will be applied to several different CMCs and its validity will be shown. The last model is based on a methodology which makes it possible to approximate an inductive slope different from $+20\text{dB/decade}$. This model enables to build a representative model for all types of CMCs, regardless the steadiness of the permeability in frequency.

1.4.4.1 Classic model

In this model, each winding of the CMC is considered as a simple inductor and is modeled by using the classic model of an inductor with its parasitic resistance and capacitance (Fig. 1.35). The left part is dedicated to CM and the right part to DM. The self-inductances L_s are coupled by a coupling coefficient $k_s = +1$ in order to have an impact only on CM. Moreover, the leakage inductances L_l are coupled by a coupling coefficient $k_l = -1$ in order to have an impact only on DM.

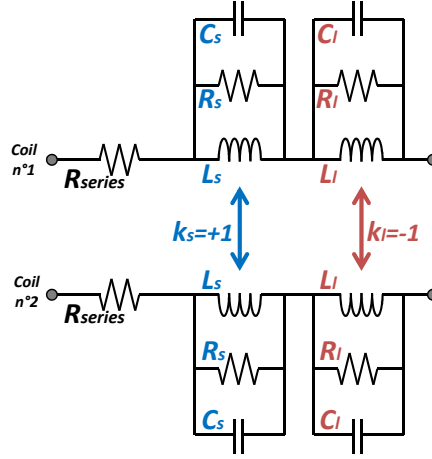


Figure 1.35: Classic CMC model

The R_{series} element is the parasitic series resistance and comes from the wire resistance of each winding. This element is not part of CM or DM but can be visible in CM, DM or both. It can be clearly identified with its resistive behavior at low frequency. Eq. 1.10 can be used to extract this value from CM and DM measurements with $R_{seriesDM}$ the extracted resistance in DM and $R_{seriesCM}$ the extracted resistance in CM.

$$R_{series} = \frac{R_{seriesDM}}{2} = 2.R_{seriesCM} \quad (1.10)$$

Common mode:

In order to identify L_s , C_s and R_s , the first step is to extract L_{CM} , C_{CM} and R_{CM} directly coming from the measurement presented in Fig. 1.33. The methodology to extract those values is the same as for a simple inductor. In the present case, it gives $L_{CM} = 2.5mH$, $C_{CM} = 15.6pF$ and $R_{CM} = 18k\Omega$. To go from CM impedance to self-impedance, Eq. 1.11, 1.12 and 1.13 are used.

$$L_s = L_{CM} \quad (1.11)$$

$$C_s = C_{CM}/2 \quad (1.12)$$

$$R_s = 2.R_{CM} \quad (1.13)$$

Finally, it gives for the present case $L_s = 2.5mH$, $C_s = 7.8pF$ and $R_s = 36k\Omega$.

Differential mode:

As far as the leakage is concerned, the first step is to extract L_{DM} , C_{DM} and R_{DM} directly coming from the measurement presented in Fig. 1.33. In the present case, it gives $L_{DM} = 23.4\mu H$, $C_{DM} = 8.2pF$ and $R_{DM} = 19.4k\Omega$. To go from DM impedance to leakage impedance, Eq. 1.14, 1.15 and 1.16 are used.

$$L_l = L_{DM}/4 \quad (1.14)$$

$$C_l = 2.C_{DM} \quad (1.15)$$

$$R_l = R_{DM}/2 \quad (1.16)$$

Finally, it gives for the present case $L_l = 5.85\mu H$, $C_l = 16.4pF$ and $R_l = 9.7k\Omega$.

Fig. 1.36 presents the comparison between DM and CM measurements and their models. There is a good agreement but in order to extend the valid frequency band, the multi-resonance model can be used.

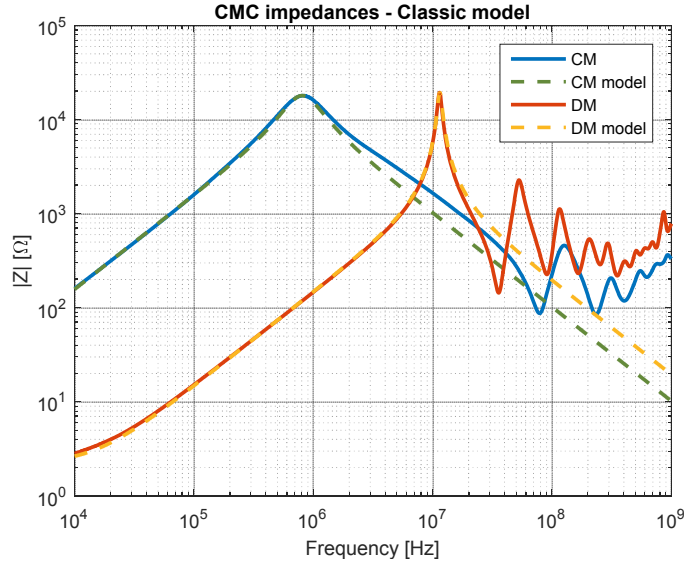


Figure 1.36: Classic model of a 2.5mH CMC

1.4.4.2 Multi-resonance model

The multi-resonance model for CMC, like multi-resonance model for inductors, is based on [40]. The model is presented in Fig. 1.37 and the cells calculation is based on the same equations as in Sect. 1.4.3. The indices n and m refer to the sufficient number of cells to model the CMC. Actually, the sufficient number is equal to the number of resonances that must be represented.

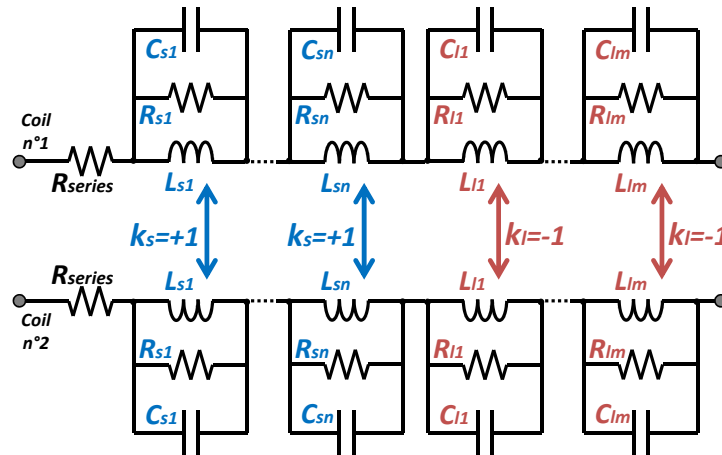


Figure 1.37: Multi-resonance CMC model

For the present case, in order to have a representative model until at least 108MHz, two resonances in CM must be represented and three in DM. Indeed, it gives $n = 2$ cells in CM and $m = 3$ cells in DM. Thanks to Eq. 1.8 applied to CMC for DM and CM, it gives an equivalent model with a result presented in Fig. 1.38. Finally, the model is valid and representative in the current frequency range of interest but can also be extended by using additional cells.

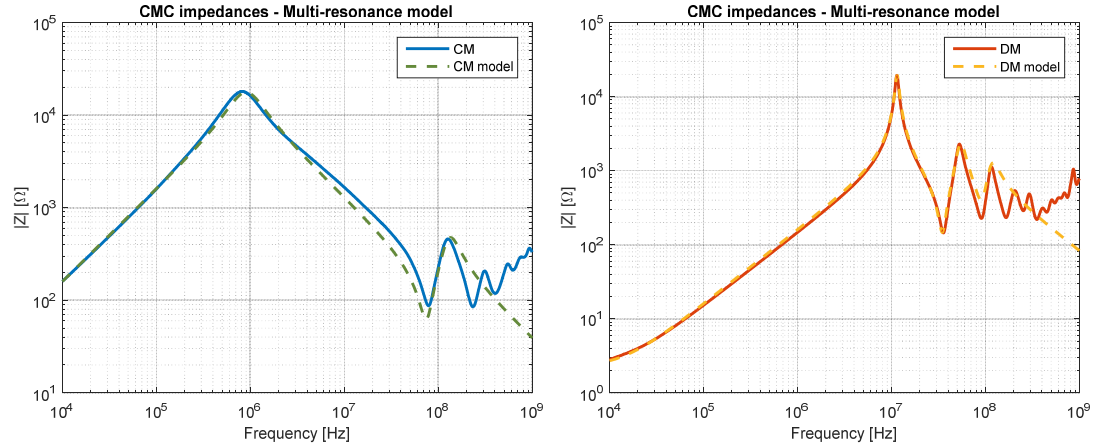


Figure 1.38: Multi-resonance model of a 2.5mH CMC

1.4.4.3 Dispersion model

The dispersion model comes from a real need to build model for all types of CMC. Dispersion can be identified when the inductive slope is lower than $+20dB/decade$. It comes from the decrease of magnetic permeability of the closed material constituting the CMC. Actually, the higher the permeability, the lower the cut off frequency as presented in Fig. 1.39. It presents an example of the evolution of the magnetic permeability over frequency for nanophy cores [43]. Those materials present very high permeability and, therefore, the dispersion is clearly visible at low frequency.

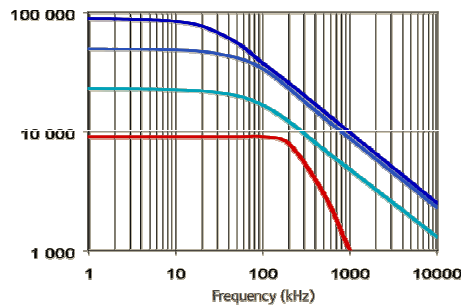


Figure 1.39: Example of permeability over frequency for nanophy core [43]

In most cases, the permeability of the magnetic material is assumed constant with frequency. However, it must be noticed that it is actually impossible to have a magnetic material with constant permeability, but this variation often occurs in high frequencies. Nevertheless, some magnetic materials present this feature at low frequency, which has an influence on the impedance.

For this type of magnetic material, the classic model, which is a simple parallel RLC, is not

sufficient. The main characteristic of a dispersive material is that the inductive part is not identifiable with a constant $+20\text{dB/decade}$ slope. The slope is positive but lower than $+20\text{dB/decade}$. In [44], a methodology which uses multiple parallel-RL cells in order to reproduce the behavior of this kind of CMC is introduced. However, it is said that the approximated values of R and L are empirically determined. A method is defined in order to calculate those cells which are effective to reproduce such behavior. The general structure of the dispersion model is presented in Fig. 1.40. This model is only applicable to CM because the dispersion can only be visible in CM. Actually, in CM, the magnetic material presents a high permeability and, therefore, the permeability decrease can easily be visible. However, in DM, the relative permeability is very low and, thus, that decrease cannot be visible.

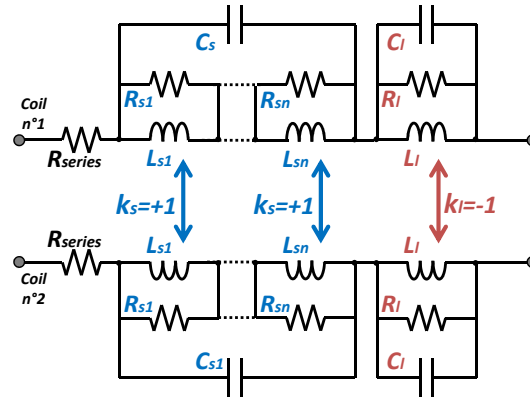


Figure 1.40: Dispersion CMC model

In order to explain how to calculate those cascaded RL cells, a simple example for a $+6\text{dB/decade}$ slope between 1MHz and 10MHz is used. The first step is to define the number of cells that are required to reproduce that kind of behavior. The first studies show that three cells for each decade are sufficient (Fig. 1.41). The objective for those cells is to spread their cut-off frequencies over the defined frequency range from 1MHz to 10MHz .

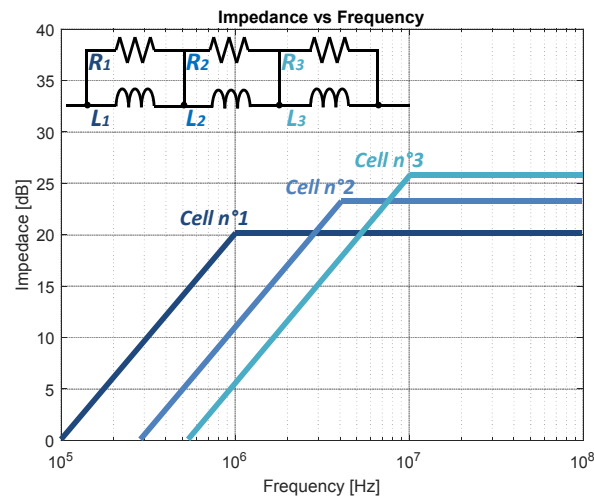


Figure 1.41: Three cascaded RL cells

It must be noticed that the amplitude of the impedance cells are totally arbitrary in Fig. 1.41. The important point is the location of their cut-off frequencies which are spread over the decade. In the case of three cells, there are two components per cell: one resistance and one inductor. Indeed, there are six unknowns and, therefore, six equations are required to calculate all the elements. The method is to define six points at which the total impedance is going to be calculated in order to determine all parameters.

For example, at 2MHz the measurement level can be written as $Z_{m_{2MHz}}$. With the three defined cells, the total impedance can be expressed as the sum of those three cells:

$$Z_{m_{2MHz}} = Z_{cell1} + Z_{cell2} + Z_{cell3} \quad (1.17)$$

However, this equation can be reduced thanks to the distribution of the cut-off frequencies over the frequency range.

$$Z_{m_{2MHz}} = R_1 + j(L_2 + L_3)\omega_{2MHz} \quad (1.18)$$

Using the same reasoning, a system with six equations and six unknowns can be built as follows:

$$\begin{pmatrix} Z_{m_{1MHz}} \\ Z_{m_{1MHz}} \\ Z_{m_{2MHz}} \\ Z_{m_{3MHz}} \\ Z_{m_{6MHz}} \\ Z_{m_{10MHz}} \end{pmatrix} = \begin{pmatrix} 0 & 0 & 0 & j\omega_{1MHz} & j\omega_{1MHz} & j\omega_{1MHz} \\ 1 & 0 & 0 & 0 & j\omega_{1MHz} & j\omega_{1MHz} \\ 1 & 0 & 0 & 0 & j\omega_{2MHz} & j\omega_{2MHz} \\ 1 & 1 & 0 & 0 & 0 & j\omega_{3MHz} \\ 1 & 1 & 0 & 0 & 0 & j\omega_{6MHz} \\ 1 & 1 & 1 & 0 & 0 & 0 \end{pmatrix} \cdot \begin{pmatrix} R_1 \\ R_2 \\ R_3 \\ L_1 \\ L_2 \\ L_3 \end{pmatrix} \quad (1.19)$$

The last step is to invert the matrix to finally obtain the components of each cell. In order to illustrate this example, Fig. 1.42 presents a curve with a slope of $+6dB/decade$ and the impedance of our model with three cascaded RL cells. The model provides a behavior really close to the measurement and enables to validate the methodology. The relative error does not exceed 2%.

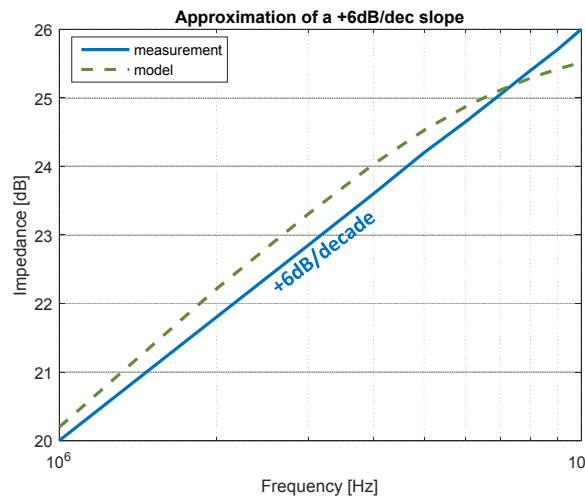


Figure 1.42: Impedance of three cascaded RL cells compared to measurements

This methodology can be applied to a real dispersive CMC as in Fig. 1.43.

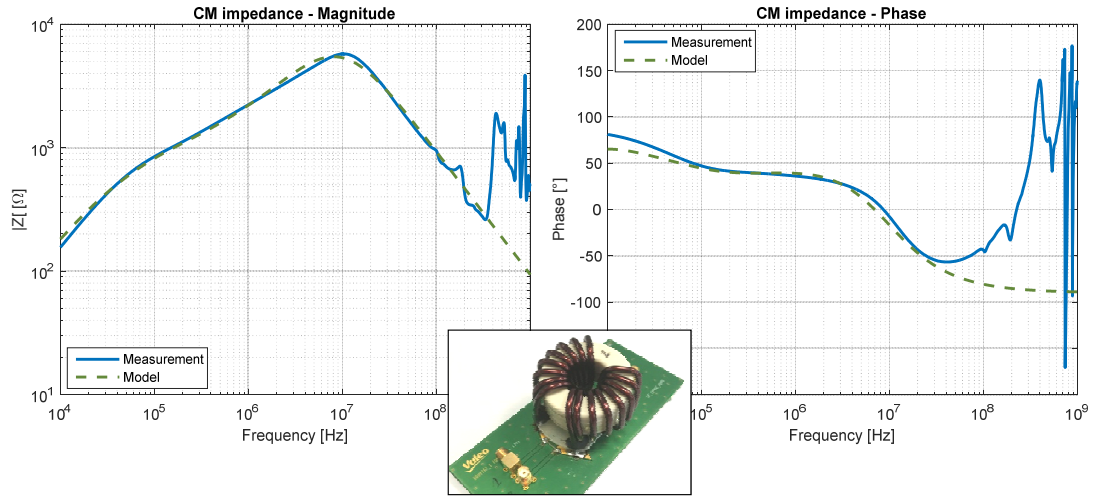


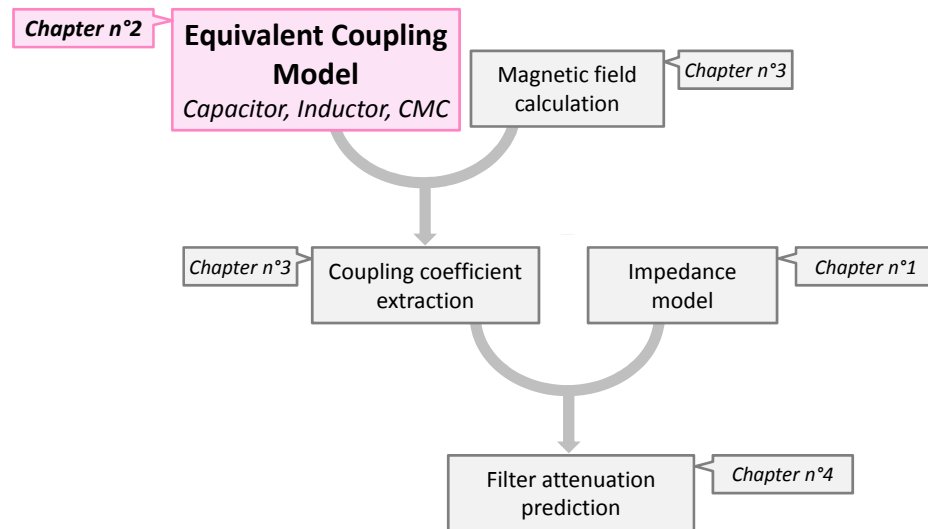
Figure 1.43: Dispersion model of a 2.4mH CMC

1.5 Conclusion

In this chapter, the main concept of EMI filter design were presented. The different EMI noise sources were introduced, such as DM noise source coming from power supply or switching cells and CM noise sources coming parasitic capacitances between an equipment and its reference. Therefore, in order to reduce those noises, different possibility of filter structures were presented. Then, equivalent electrical models of passive components building up the filter are presented. For capacitors and inductors, existing electrical models were presented. As long as CMCs were concerned, different models were developed for three different types of behaviors.

Chapter 2

Equivalent coupling models of passive components



2.1 Introduction to the equivalent coupling model principle

In order to determine a mutual inductance between two passive components, the equivalent coupling model of each component must be known. For some components like capacitors or inductors, their equivalent coupling model can be reduced to a simple surface, thanks to their geometrical properties. However, for more complex components, such as CMCs, several surfaces must be considered to correctly model it.

It must be noticed that the equivalent coupling surface is not a physical surface: it is a model that simplifies and represents the magnetic sensitivity of a passive component. The equivalent coupling model is then fixed for each component and can represent a coupling level whatever the orientation of the component, while considering the skin effect, the proximity effect (with PCB ground plane) or the presence of a magnetic material.

The idea is to characterize the component under a uniform well-known magnetic field and determine if the component has a preferred orientation and if it is sensitive to that magnetic field. Indeed, the equivalent coupling surface is determined considering a uniform magnetic field using the TEM (Transverse ElectroMagnetic) cell.

The following section presents the TEM cell, its main properties and how to determine the magnetic field level inside the cell. Then, the measurements with the TEM cell are presented, when the direction of the surfaces can be determined a priori or not. The methodology to extract the equivalent coupling model is presented and finally applied to capacitors, inductors and CMCs.

2.2 The TEM cell

A TEM cell (Fig. 2.1) is based on a 50Ω transmission line principle, built with three conductors: two ground planes and the center conductor called the “septum” [45, 46, 47]. The TEM cell used for experiments is the one dedicated to integrated circuit characterization [48, 49].

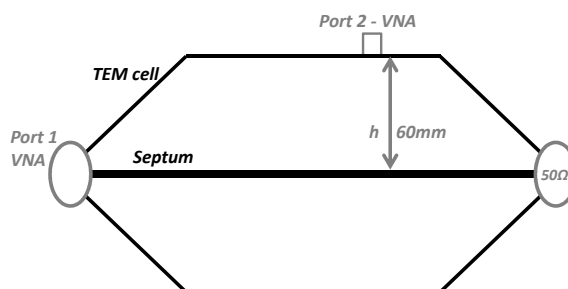


Figure 2.1: The TEM cell

The cell is powered by an RF source, a VNA in our case. This way, a quasi-uniform electromagnetic field is generated inside the cell [50, 51, 52, 53]. The field is considered uniform [48, 54] as long as the width of the cell is lower than half a wavelength. Considering the dimensions presented in Fig. 2.2 and Eq. 2.1, it gives a frequency limit of 833MHz for that TEM cell.

$$\lambda = c/f \quad (2.1)$$

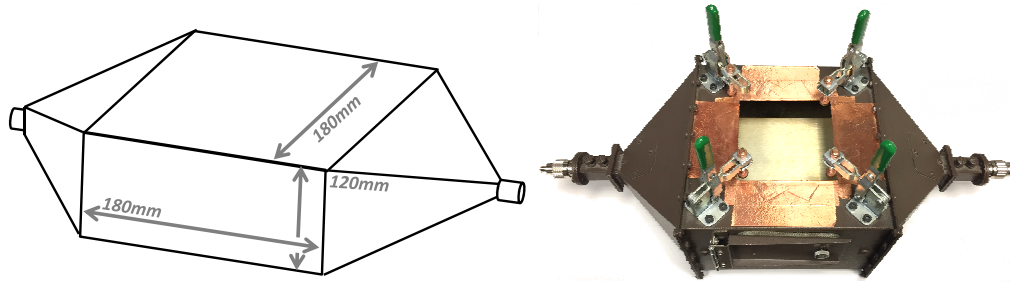


Figure 2.2: TEM cell dimensions

The field value generated inside the cell depends on injected power [45, 55]. The TEM cell is powered by the first port of the VNA. The second port of the VNA is connected to the DUT (Device Under Test) installed in the cell ceiling. The S_{21} parameter thus quantifies the transfer of the uniform electromagnetic field to the DUT.

Before operating the TEM cell, it is essential to know the magnetic field generated inside the cell. The induced wave inside the TEM cell is considered a plane wave. The wave vector \vec{k} is constant and parallel to the septum. The electric and magnetic field components of the wave, \vec{E}_{TEM} and \vec{H}_{TEM} , are located in the plane perpendicular to the propagation direction, and can be represented as in Fig. 2.3.

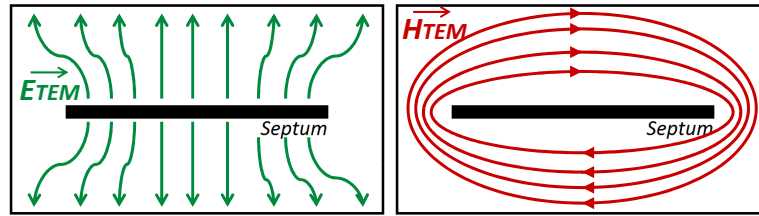


Figure 2.3: Electric and magnetic fields in the plane perpendicular to the propagation direction

Considering that the size of the DUT is small compared to the one of the cell and that the DUT is located in the middle of the cell ceiling, the field vectors \vec{E}_{TEM} and \vec{H}_{TEM} can be represented as in Fig 2.4.

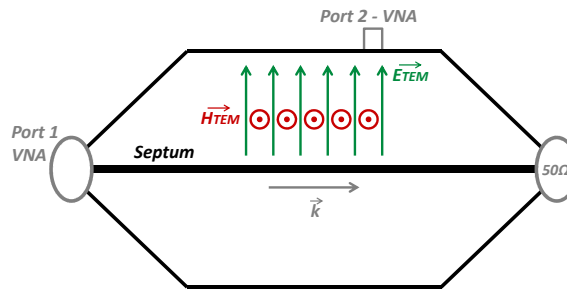


Figure 2.4: Magnetic and electric field vectors considered in the TEM cell

2.2.1 Analytical calculation of the magnetic field inside the TEM cell

First of all, let us consider Eq. 2.2 to establish a link between the magnitude of the electric field $||\overrightarrow{E_{TEM}}||$ and the one of the magnetic field $||\overrightarrow{H_{TEM}}||$ taking into account the impedance of the propagation medium $\eta_0 = 120\pi$.

$$||\overrightarrow{E_{TEM}}|| = \eta_0 ||\overrightarrow{H_{TEM}}|| \quad (2.2)$$

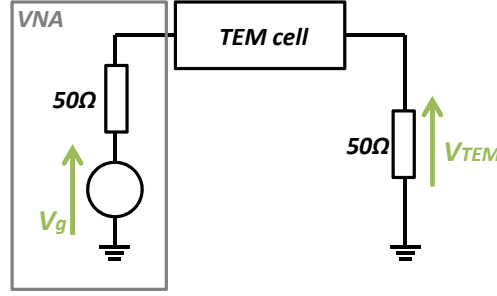


Figure 2.5: Equivalent circuit of the TEM cell measurement

Using the equivalent circuit in Fig. 2.5, the electric field inside the TEM cell can be calculated:

$$V_{TEM} = V_g/2$$

$$P_{in} = \frac{1}{2} \frac{V_{TEM}^2}{Z_0} = \frac{1}{8} \frac{V_g^2}{Z_0} \Leftrightarrow V_g = \sqrt{8P_{in}Z_0}$$

$$||\overrightarrow{E_{TEM}}|| = \frac{V_g}{h} = \frac{\sqrt{8P_{in}Z_0}}{h} \quad (2.3)$$

with P_{in} the power injected into the first port, Z_0 the characteristic impedance of the cell and h the distance between the septum and the ground plane. Using Eq. 2.2 and Eq. 2.3, the magnetic field inside the TEM cell can be expressed:

$$||\overrightarrow{H_{TEM}}|| = \frac{\sqrt{8P_{in}Z_0}}{h\eta_0} \quad (2.4)$$

giving for a 10dBm injected power, a theoretical value of 88mA/m for the magnitude of the magnetic field.

2.2.2 Magnetic field measurement in the TEM cell

Using a magnetic field probe, the field inside the TEM cell is measured in order to confirm the calculation. To do so, a calibrated magnetic field probe is placed inside the cell so that the normal to the surface of the probe is in the same direction as the magnetic field (Fig. 2.6).

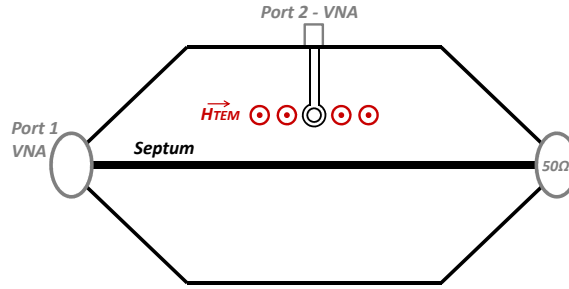
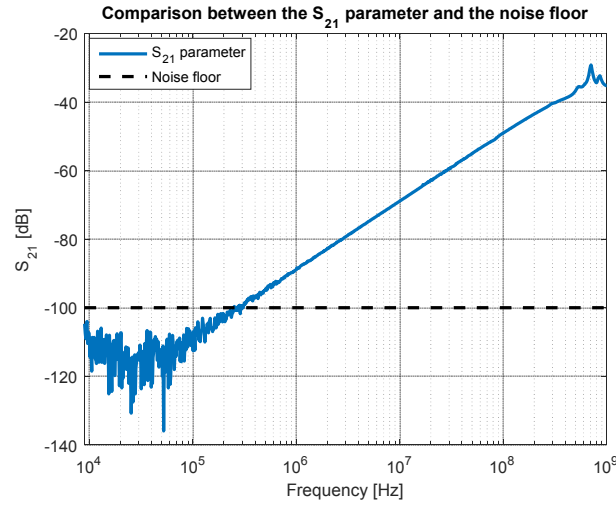


Figure 2.6: Magnetic field measurement in the TEM cell

The TEM cell is powered by the first port of the VNA and the S_{21} parameter measured at the second port, connected to the probe, represents the magnetic field inside the cell. Fig. 2.7 presents this S_{21} parameter extracted from measurements. The noise observed at low frequencies is due to the limitation of the VNA measurement dynamics. Thus, Fig. 2.7 compares the measured S_{21} parameter with the typical dynamic range of a VNA (about 100dB). It is then clear that, below 300kHz, no valid measurement can be extracted.

Figure 2.7: S_{21} parameter measurement

Furthermore, another parameter which must be checked is the standing wave ratio (SWR) as presented in Fig. 2.8. In fact, beyond 800MHz, the SWR starts deviating significantly from 1 and therefore no valid measurement can be extracted hereafter (when $SWR > 1.2$).

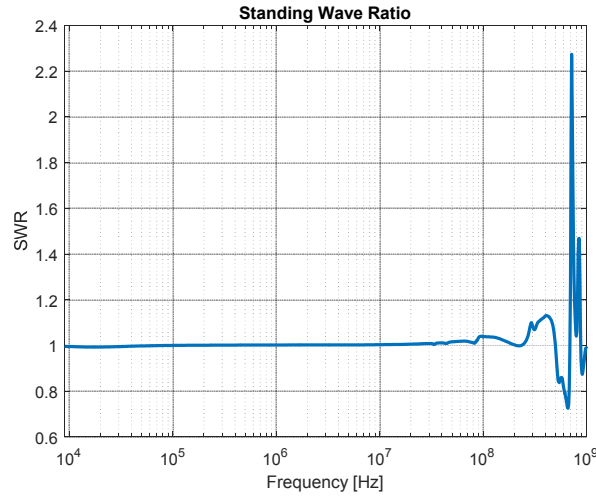


Figure 2.8: Standing Wave Ratio inside the cell

Those two parameters give a valid frequency band going from 300kHz to 800MHz. Then, after extracting all S parameters and determining the valid frequency range, the S_{21} parameter is converted to an emf (electromotive force) induced to the probe:

$$emf_{probe} = \sqrt{2Z_0|S_{21}|^2P_{in}}e^{j\phi_{S_{21}}} \quad (2.5)$$

The magnetic field can be calculated using the antenna factor AF and using Eq. 2.6.

$$||\vec{H_{TEM}}|| = emf_{probe}.AF \quad (2.6)$$

The antenna factor depends on the used magnetic field probe. For the used one presented in Fig. 2.9, the diameter is of 10mm and its associated antenna factor changes with frequency.

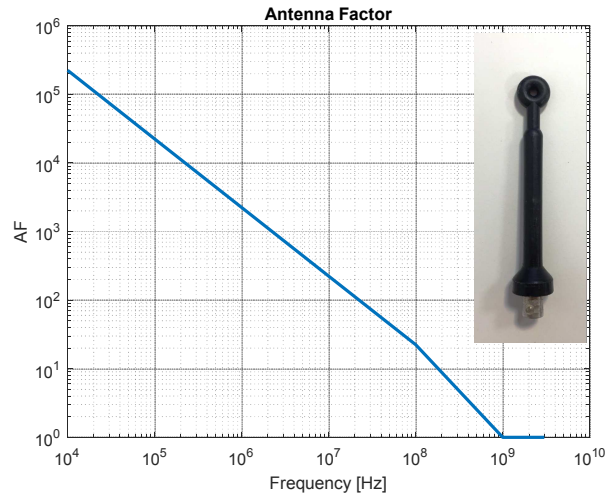


Figure 2.9: Magnetic field probe - Antenna Factor

Finally, Fig. 2.10 provides the evolution of the magnetic field over frequency :

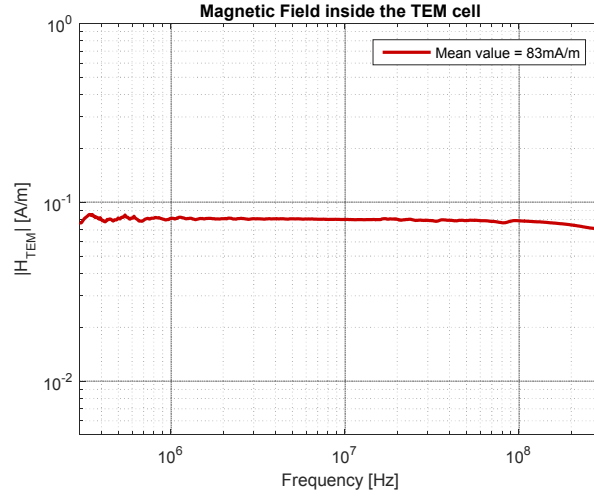


Figure 2.10: Magnetic field inside the TEM cell, extracted from S parameters measurement

As can be seen in Fig. 2.10, the extracted value of the magnetic field is quite constant from 300kHz until 300MHz (83mA/m for $P_{in} = 10dBm$), which is very close to the one calculated in Sect. 2.2.1. It can be noticed that, in the following sections, that evolution of the magnetic field will be used to obtain the most representative value.

2.3 DUT measurements in the TEM cell

2.3.1 Definition of the normal to the coupling surface

The first measurement to be carried out is the determination of the direction of the coupling surface, i.e. the orientation for which the induced electromotive force is the highest. According to Eq. 2.7, it is possible to calculate an electromotive force generated to the DUT from the measured S_{21} parameter.

$$emf = \sqrt{2Z_0|S_{21}|^2P_{in}}e^{j\phi_{S_{21}}} \quad (2.7)$$

This step also makes it possible to determine if only one equivalent surface is necessary for the model. Thus, using the following measurements, it is determined if there is one or more preferred orientations and, consequently, one or more coupling surfaces. To do so, the orientation of the coupling surface of a simple loop can be determined by performing different measurements (Fig. 2.11) corresponding to different orientations.

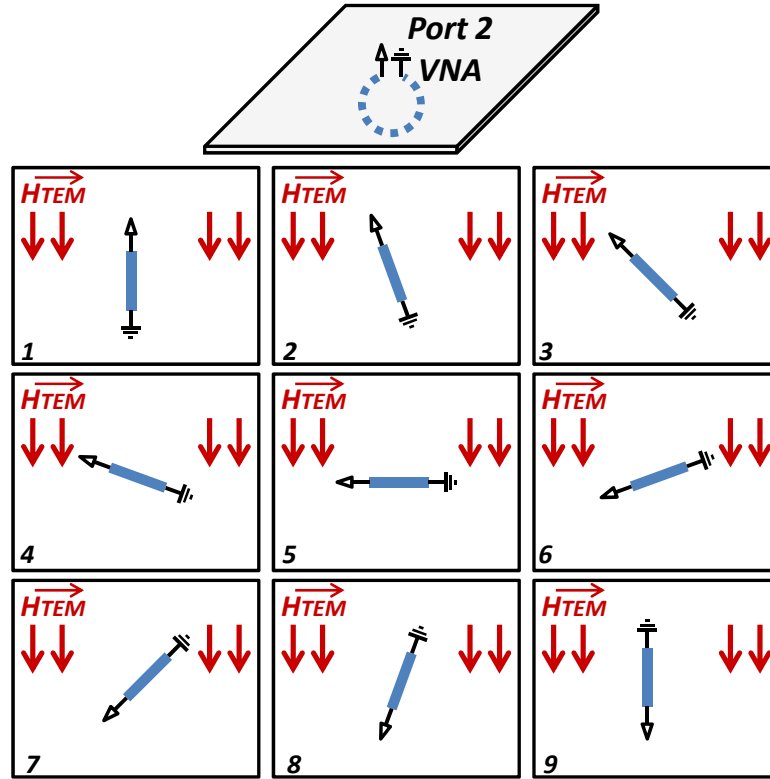
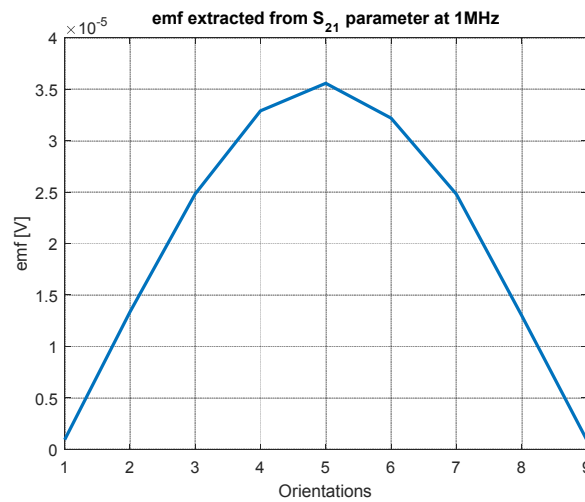


Figure 2.11: Measurements to determine the direction of the coupling surface

Using the nine measurements presented in Fig. 2.11, it is possible to extract the associated *emf* at a fixed frequency to compare the orientations. The result is presented in Fig. 2.12 and it clearly appears that orientation n°5 is the preferred one.

Figure 2.12: Electromotive forces extracted from S_{21} parameter at 1MHz.

It can be concluded that there is only one preferred orientation and, therefore only one equiv-

alent coupling surface. Then, the sensitivity of the loop can be modeled as one simple loop.

That measurement is called from now the measurement at $\theta = 0^\circ$, which means the coupling surface of the DUT and the field crossing this surface are collinear. Furthermore the direction of the coupling surface is determined by the right hand rule (Fig. 2.13).

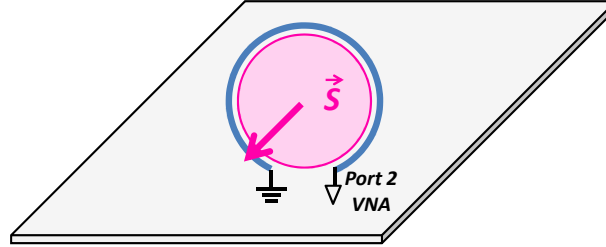


Figure 2.13: Orientation and direction of the coupling surface for a loop

This step is mandatory when the direction of the coupling surface cannot be determined a priori.

2.3.2 Measurements to be carried out on the DUT

Once the orientation of the coupling surface of the loop is known, two measurements must then be carried out, the first for $\theta = 0^\circ$ where the coupling surface and the field are collinear and in the same direction, the second for $\theta = 180^\circ$ where both vectors are collinear but in the opposite direction (Fig. 2.14). These two measurements are needed in order to cancel the electric field contribution; it will be described in Sect. 2.4.1.

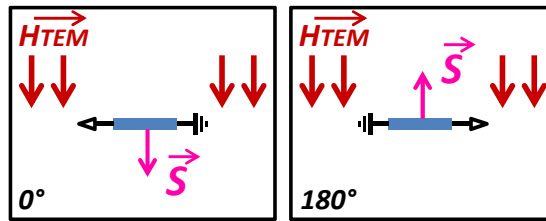


Figure 2.14: Measurements at $\theta = 0^\circ$ and $\theta = 180^\circ$ on a loop

Fig. 2.15 plots the electromotive forces obtained from both measurements. Those measurements are valid from 300kHz because of the measurement dynamics and up to 100MHz due to the matching of the TEM cell.

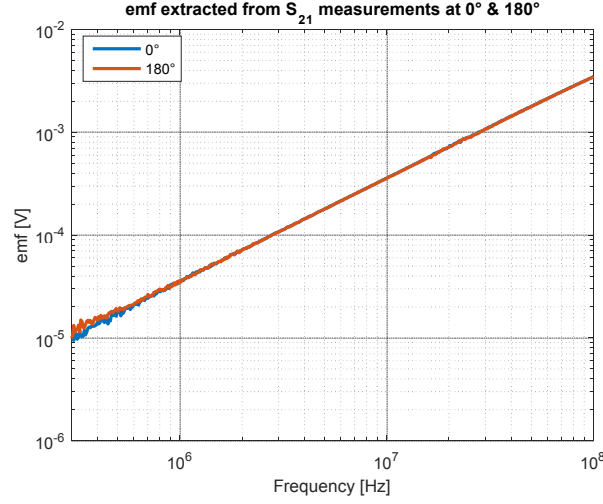


Figure 2.15: emf extracted from S parameter measurements at $\theta = 0^\circ$ and $\theta = 180^\circ$

2.4 Extraction of the equivalent coupling surface

Once the electromotive forces are extracted, three operations must be carried out in order to extract the equivalent coupling surface:

- The first step consists in removing the electric field contribution to consider only the contribution of the magnetic field,
- Then, the second step takes into account the influence of the DUT impedance,
- Finally, the third step determines the equivalent coupling surface of the component.

2.4.1 Subtraction of the electric field contribution

This part re-uses the measurements performed in Sect. 2.3.2. These electromotive forces, emf_{0° and emf_{180° , can be decomposed into two parts in Eq. 2.8 and Eq. 2.9. The first one is dedicated to the magnetic field contribution $\widehat{emf_H}$ and the second one is dedicated to the electric field contribution $\widehat{emf_E}$.

$$emf_{0^\circ} = \widehat{emf_H} + \widehat{emf_E} \quad (2.8)$$

$$emf_{180^\circ} = -\widehat{emf_H} + \widehat{emf_E} \quad (2.9)$$

This makes it possible to use only the contribution due to the magnetic field (Eq. 2.10):

$$\widehat{emf_H} = \frac{emf_{0^\circ} - emf_{180^\circ}}{2} \quad (2.10)$$

$$\widehat{emf_E} = \frac{emf_{0^\circ} + emf_{180^\circ}}{2} \quad (2.11)$$

Fig. 2.16 depicts the evolution of the electromotive forces due to the two different contributions. It can be noticed that the magnetic field contribution is higher than the one of the electric field on the whole frequency band.

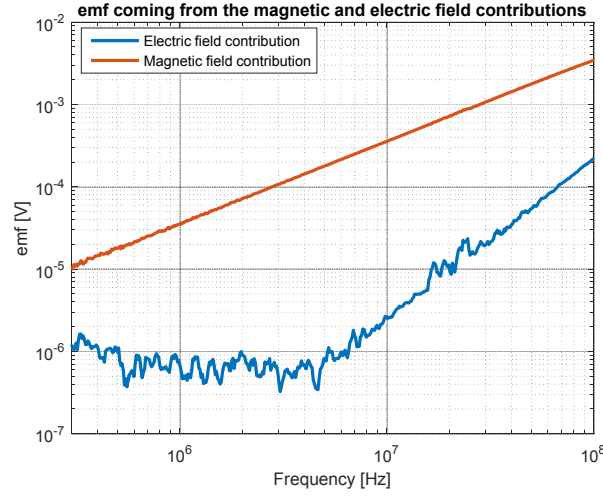


Figure 2.16: Electromotive forces coming from the magnetic and electric field contributions

2.4.2 Integration of the impedance of the DUT

The next measurement is carried out on the DUT using an impedance analyzer [20], with the aim of canceling its influence on the measurement.

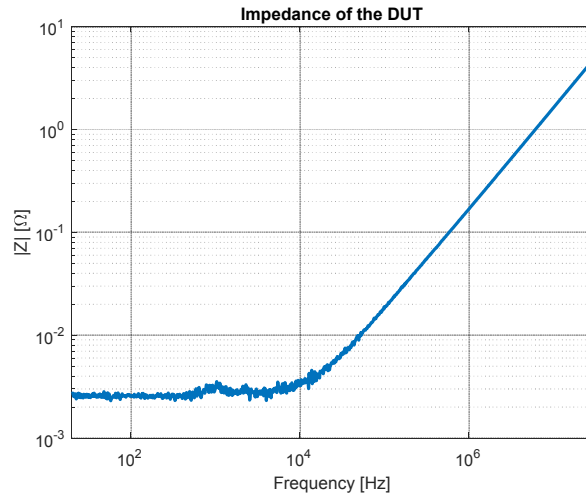


Figure 2.17: Impedance of the DUT

The DUT can be modeled by a simple RL circuit in series with $R_{DUT} = 2.7m\Omega$ and $L_{DUT} = 27nH$. It must be noticed that, as it is presented in Sect. 1.4.1, the extracted value of the resistance presents more than 10% of uncertainty. However, it does not have an influence on the final result as long as this impedance is inferior to 50Ω . Actually, in order to include the impedance influence

and correct the extracted electromotive force, the following equivalent circuit can be considered (Fig. 2.18).

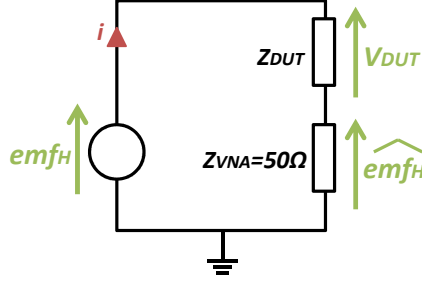


Figure 2.18: Equivalent circuit of the measurement

with $\widehat{emf_H}$ the part of the measured electromotive force coming from the magnetic field contribution, $Z_{VNA} = 50\Omega$ the impedance of the VNA, Z_{DUT} the impedance of the DUT, V_{DUT} its associated voltage, i the current through the loop, emf_H the corrected emf which is finally used to calculate the coupling surface of the DUT.

Consequently, Eq. 2.12 can be established to calculate emf_H (Fig. 2.19). That equation validates the fact that, if the DUT impedance is very small regarding 50Ω , it does not have an influence on the final results.

$$emf_H = V_{DUT} + \widehat{emf_H} = \widehat{emf_H} \left(\frac{Z_{DUT} + Z_{VNA}}{Z_{VNA}} \right) \quad (2.12)$$

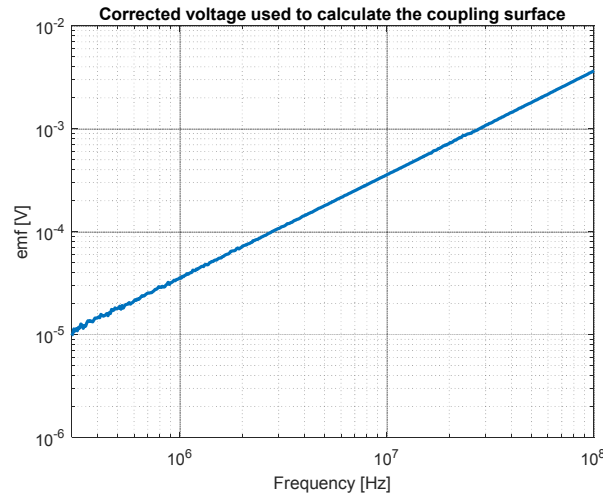


Figure 2.19: Corrected voltage used to calculate the coupling surface

2.4.3 Extraction of the equivalent coupling surface

Using the final corrected electromotive force, it is now possible to calculate the equivalent coupling surface using the following formula:

$$\begin{aligned}
emf_H &= -j\omega \overrightarrow{B_{TEM}} \cdot \overrightarrow{S_{ec}} = -j\omega\mu_0 ||\overrightarrow{H_{TEM}}|| \cdot ||\overrightarrow{S_{ec}}|| \cos\theta \\
&\equiv \\
||\overrightarrow{S_{ec}}|| &= \frac{emf_H}{-j\omega\mu_0 ||\overrightarrow{H_{TEM}}|| \cos\theta}
\end{aligned} \tag{2.13}$$

with $\theta = 0^\circ$ the orientation of the DUT inside the TEM cell (Sect. 2.3.2) and S_{ec} the equivalent coupling surface of the DUT. As illustrated in Fig. 2.20, the equivalent coupling surface is relatively constant over frequency and equal to $S_{ec} = 55mm^2$ at 1MHz.

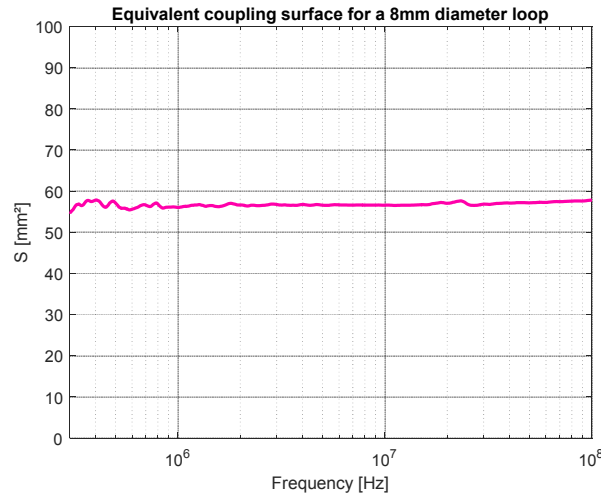


Figure 2.20: Equivalent coupling surface for a 8mm diameter loop

This value can also be determined using the dimension of the loop. It is directly linked to the surface of the loop $S_{loop} = \pi(d/2)^2 = 50mm^2$. Furthermore, the loop ends on the bottom face of the FR4-PCB, having 1mm thickness, as shown in Fig. 2.21. Therefore, an additional surface $S_{additional} = 5mm^2$ can be added to S_{loop} , which gives a total surface determined by geometrical parameters: $S_{total} = 55mm^2$. It can be concluded that the equivalent coupling surface for a simple loop is basically its physical surface.

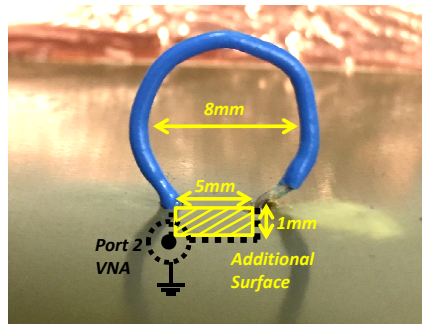


Figure 2.21: 8mm diameter loop

2.5 Application case: the capacitor

All the steps defined in the previous part are now applied to the particular case of a capacitor. For this example, the $10\mu\text{F}$ capacitor presented in Fig. 2.22 will be used.



Figure 2.22: Application case: $10\mu\text{F}$ capacitor

2.5.1 Measurements performed on the DUT

In the same way as for the simple loop (Sect. 2.3), different measurements are performed to determine the preferred orientation. It turns out that the coupling surface is located and oriented like the surface delimited by both pins. Thus, the two measurements presented in Fig. 2.23 will be used for the next steps.

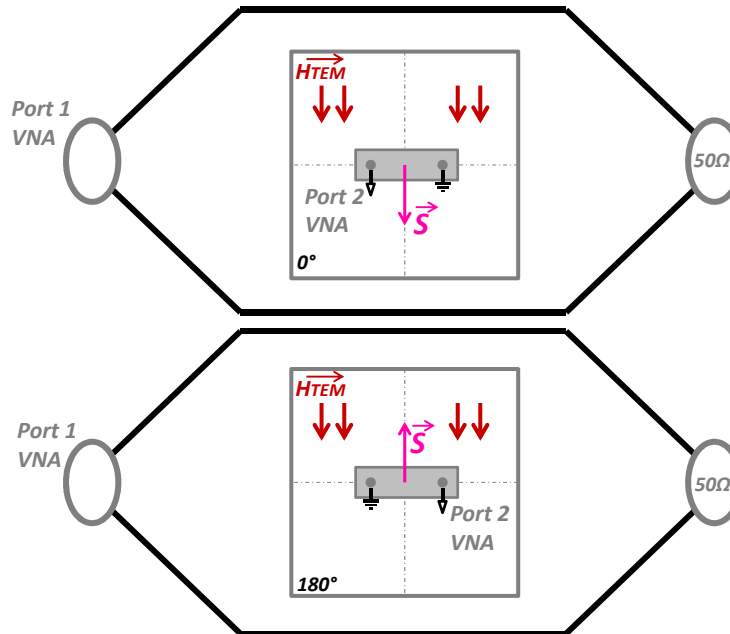


Figure 2.23: Measurements at $\theta = 0^\circ$ and $\theta = 180^\circ$ on a $10\mu\text{F}$ capacitor

2.5.2 Measurement post-processing

As presented in the first case for a loop, three steps are needed to extract the equivalent coupling surface:

- Remove the electric field contribution to only use the magnetic field contribution,
- Include the influence of the capacitor impedance (Sect. 1.4.2),
- Extract the equivalent coupling surface over frequency (Fig. 2.24).

The measurements are valid from 130kHz to 100MHz because of the measurement dynamics and the SWR . Furthermore, to extract a valid equivalent coupling surface, the slope of the impedance has to be checked. The impedance has to present an inductive behavior, i.e. a +20dB/decade slope. For this example, the first resonance frequency of the capacitor is located at 39kHz and so, from 130kHz to 100MHz, the impedance has indeed a +20dB/decade slope.

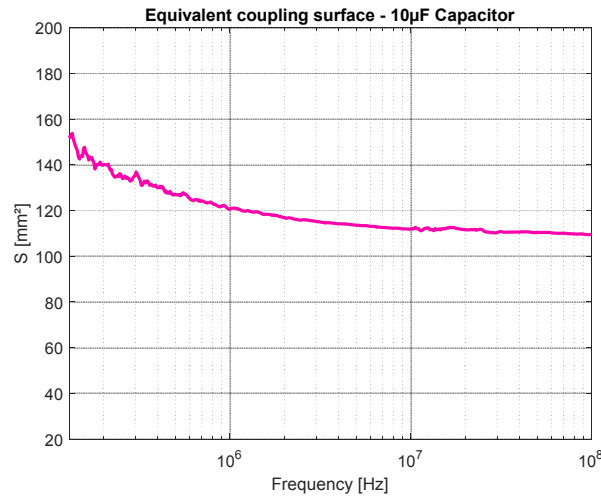


Figure 2.24: Equivalent coupling surface on a 10µF capacitor

A value of $S_{ec} = 112mm^2$ can be extracted at 10MHz. This value is relatively constant from 1MHz to 100MHz, but slightly decreases when frequency increases. This comes from skin and proximity effects with the PCB ground plane: the current tends to flow on facing surfaces and, consequently, the equivalent coupling surface will decrease as observed and discussed in [4].

2.5.3 Geometrical approximation

A capacitor can be geometrically approximated as a simple loop; the equivalent coupling surface is located between the pins of the component, the ground plane and the internal structure (Fig. 2.25). It is thus possible to calculate a value of $S_{ec} = 113mm^2$.

This makes up for a good approximation, but the internal structure of the component has to be known, and it does not provide evolution with frequency. Therefore, such an approximation requires the component to be broken up or to be analyzed by Xray. The geometrical approximation provides a good tendency for design, but it is difficult to set up. As a result, the best way to determine the equivalent coupling surface of a capacitor is a measurement with the TEM cell.

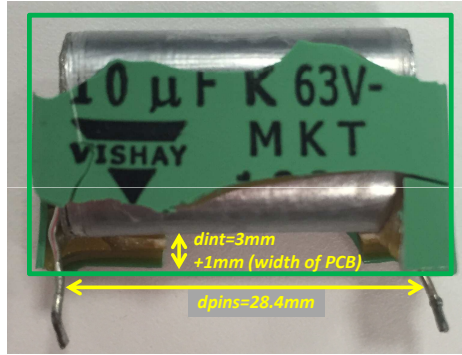


Figure 2.25: Internal structure of a capacitor

2.5.4 Validation of the coupling model with a uniform magnetic field

The aim of this section is to validate the coupling model using a uniform magnetic field and by calculating the electromotive force to be compared with measurements. The example in Fig. 2.26 can be considered, which corresponds to a measurement with $\theta = 30^\circ$.

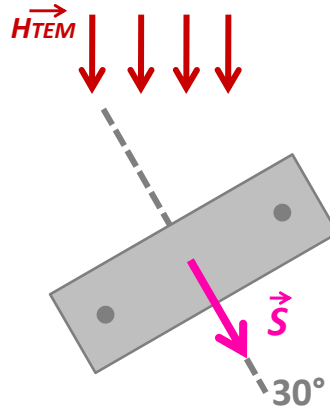


Figure 2.26: Example of validation of the coupling model for a capacitor

Eq. 2.13 can be recalled and applied to this case, where $\theta = 30^\circ$ and the equivalent coupling surface is considered constant.

$$emf_{H_{30^\circ}} = -j\omega\mu_0 ||\overrightarrow{H_{TEM}}|| \cdot ||\overrightarrow{S_{ec}}|| \cdot \cos(30^\circ) \quad (2.14)$$

considering that $||\overrightarrow{H_{TEM}}||$ is the magnetic measured inside the cell (Sect. 2.2.2) and $||\overrightarrow{S_{ec}}||$ the surface of the capacitor extracted from measurements in the TEM cell (Sect. 2.5.2).

Fig. 2.27 depicts the electromotive force calculated from the coupling surface and a measurement at $\theta = 30^\circ$. It can be concluded that the model really fits with the electromotive force extracted from measurements.

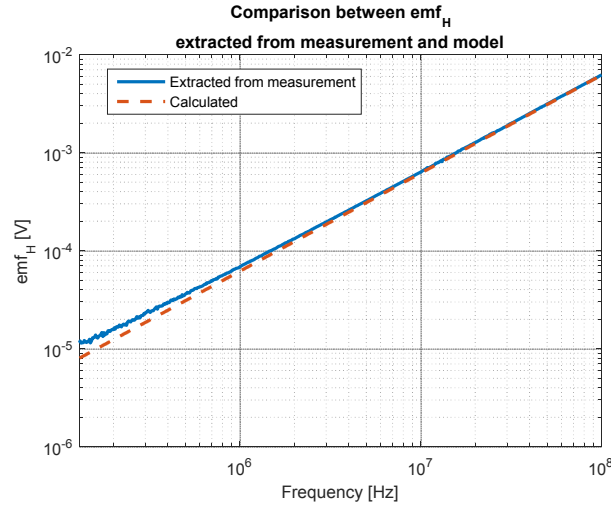


Figure 2.27: Comparison between emf_H extracted from measurement and model

2.5.5 Particular case of MLCC capacitors

As far as MLCC capacitors are concerned, the principle remains the same as for bigger capacitor. The component is characterized in the TEM cell for its two preferred orientations of magnetic coupling. Then, using both measurements, the electric field contribution is removed, in order to only consider the magnetic field contribution. The impedance is then considered as in [20] by using abacus that gives the parasitic elements values depending on the technology and the housing of the MLCC capacitor. Finally, the surface is extracted.



Figure 2.28: MLCC capacitors

In order to have a global view of the equivalent coupling surface of MLCC capacitors, two different packages are tested: 0603 capacitors and 0805 capacitors each with five different capacitance values: 100pF, 1nF, 10nF, 100nF and 1μF. According to Sect. 2.5.3, the equivalent coupling surface is located between the two pins of the component and the ground plane and the internal structure. Therefore, for the MLCC capacitor, it depends on the length of the capacitor, 1.6mm for 0603 and 2mm for 0805, and on the distance between the internal structure and the ground plane. In [4], it is demonstrated that the metallic internal structure is spread in layers on the whole structure. Therefore, theoretically, the surface only depends on the package length and on the distance between the bottom of the component and the ground plane.

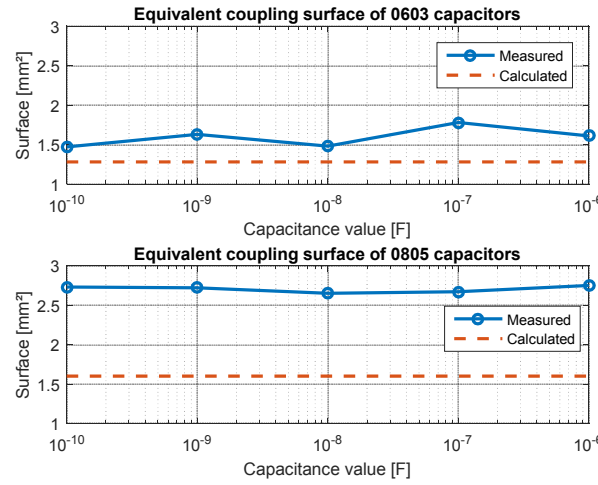


Figure 2.29: Equivalent coupling surfaces for 0603 and 0805 MLCC capacitors

Fig. 2.29 presents the comparison between the measured surfaces and the one calculated from geometrical properties (the component is located at 0.8mm from the ground plane). It can be said that the surface is generally underestimated and it comes from the uncertainty on the soldering, as presented in Fig. 2.30.

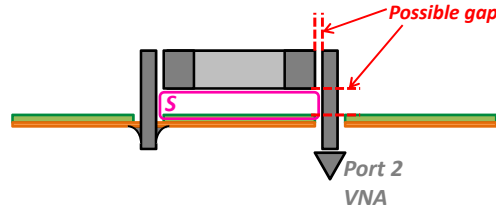


Figure 2.30: Possible gap in capacitor soldering

Finally, as we have more confidence in the geometrical parameters than in manual soldering, the theoretical surface values will be used. Furthermore, the use of the theoretical value of the equivalent coupling surface for MLCC capacitors will be validated in Sect. 4.5, through an application case.

2.6 Application case: the inductor

For this example, the 2 μ H inductor presented in Fig. 2.31 is used.

Figure 2.31: Application case: 2 μ H inductor

2.6.1 Measurements performed on the DUT

In the same way as for the simple loop (Sect. 2.3), different measurements were performed in order to determine the preferred orientation. It turns out that the coupling surface is oriented like the turns of the inductor, parallel to the windings. Thus, the two measurements presented in Fig. 2.32 are used for the next steps.

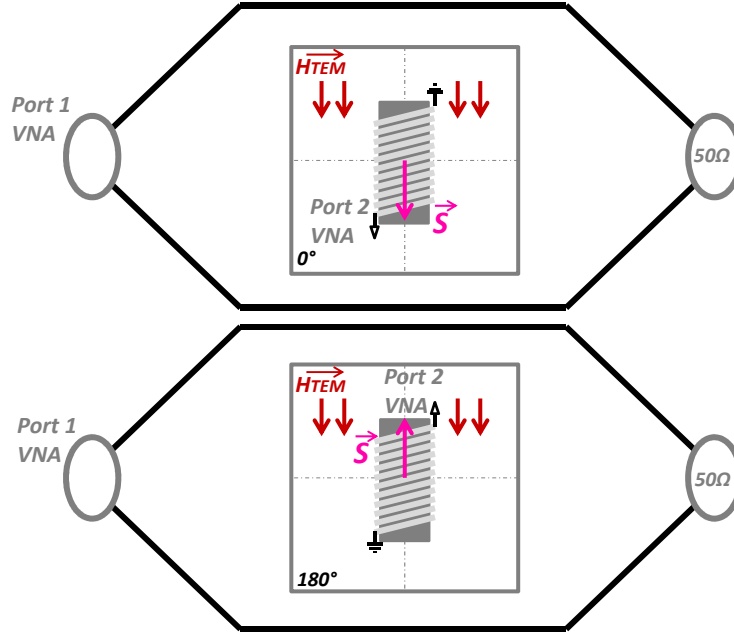


Figure 2.32: Measurements at $\theta = 0^\circ$ and $\theta = 180^\circ$ on a $2\mu\text{H}$ inductor

2.6.2 Measurements post-processing

As presented in the first case for a loop, three steps are needed to extract the equivalent coupling surface:

- Remove the electric field contribution to only use the magnetic field contribution,
- Include the influence of the inductor impedance (Sect. 1.4.3),
- Extract the equivalent coupling surface over frequency, taking into account the magnetic material within the inductor (Fig. 2.24).

The measurements are valid from 80kHz to 100MHz because of the measurement dynamics and the SWR . Furthermore, to extract a valid equivalent coupling surface, the slope of the impedance has to be checked. The impedance must present an inductive behavior, i.e. a $+20\text{dB/decade}$ slope. For this example, the first resonance frequency of the inductor is located at 360MHz and so, from 80kHz to 100MHz, the impedance has indeed a $+20\text{dB/decade}$ slope.

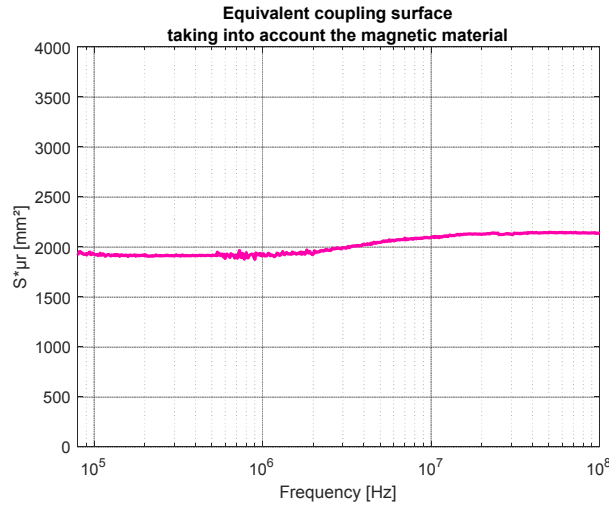


Figure 2.33: Equivalent coupling surface taking into account the magnetic permeability of the material

For mutual inductance calculations that are going to be presented in the following Chapter, it is not necessary to separate the surface and the magnetic permeability. Actually, the total surface, including the influence of the material is used. Indeed, the calculations are simplified.

However, to only extract the coupling surface of the inductor, the result in Fig. 2.33 can be divided by an estimation of the magnetic permeability μ_r . An approximation can be made by calculating the air core coil L_{air} :

$$L_{air} = \frac{\mu_0 N^2 S_{loop}}{l} \quad (2.15)$$

with N the number of turns of the inductor, S_{loop} the surface of one turn and l the length of the inductor. A more accurate methodology to extract the air core coil has been developed by considering the internal couplings between each turn. This principle is presented in Sect. 3.4.2.

Thus, with the impedance measurement carried out in Sect. 2.6.1, it is possible to calculate the magnetic permeability such as $\mu_r = L_{measured}/L_{air}$. Finally, the equivalent coupling surface can be extracted at 1MHz: $S_{ec} = 238mm^2$.

2.6.3 Geometrical approximation

An inductor can be approximated as a succession of N loops. The equivalent coupling surface of an inductor can be calculated as presented in Fig. 2.34: the product of the number of turns by the internal surface of a loop. It gives a value of $S_{ec} = 234mm^2$ for the present case. A little difference is observed between the one calculated from geometrical approximation and from the measurement; this difference comes from the uncertainty on geometrical parameters and on the magnetic material properties.

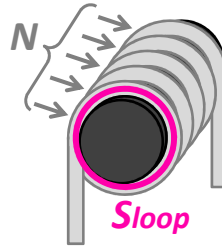


Figure 2.34: Equivalent coupling surface of an inductor

This yields a good approximation but does not give its evolution with frequency. Furthermore, the influence of the magnetic material is not considered, and some approximations have to be made to obtain an estimation. Whereas the geometrical approximation can provide a good tendency for design, the best way to determine the equivalent coupling surface of an inductor is the measurement with a TEM cell.

2.6.4 Extraction of the magnetic permeability

Another possibility is to use the TEM cell measurement to extract the magnetic permeability of a magnetic material. Actually, as it is presented in Sect. 2.6.2, the extracted surface from TEM cell measurements is enhanced by the permeability of the material constituting as expressed in Eq. 2.16 considering that $\theta = 0^\circ$.

$$emf_H = -j\omega\mu_0\mu_r \|\vec{H}_{TEM}\| \cdot \|\vec{S}_{ec}\| \Leftrightarrow \mu_r \|\vec{S}_{ec}\| = \frac{-emf_H}{j\omega\mu_0 \|\vec{H}_{TEM}\|} \quad (2.16)$$

Furthermore, it was presented in Sect. 2.6.3 that the surface, without considering the permeability, can be calculated from geometrical parameters. Therefore, the surface including the material influence can be divided by the physical surface (Sect. 2.6.3) in order to only extract the magnetic permeability seen by the coil (Fig. 2.35)

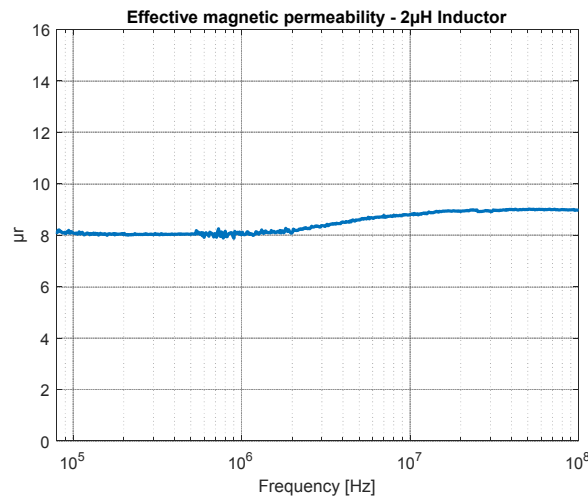


Figure 2.35: Effective permeability - 2μH Inductor

This permeability is generally called the “effective” magnetic permeability because that is seen by the coil and highly depends on the geometry of the coil. This point will be presented in Sect. 3.4.

2.6.5 Validation of the coupling model with a uniform magnetic field

In order to validate this coupling model, the electromotive force generated to the component by a uniform magnetic is calculated and then compared to measurement. The example in Fig. 2.36 can be considered, which corresponds to a measurement with $\theta = 30^\circ$.

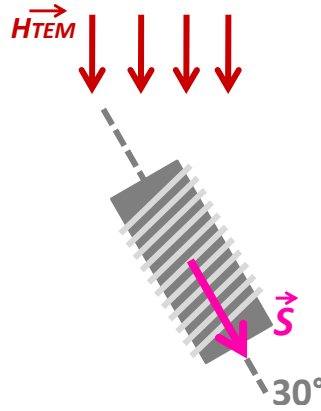


Figure 2.36: Example of validation of the coupling model for a horizontal inductor

Eq. 2.13 can be recalled and applied to this case, where $\theta = 30^\circ$.

$$emf_{H_{30^\circ}} = -j\omega\mu_0\mu_r ||\vec{H}_{TEM}|| \cdot ||\vec{S}_{ec}|| \cdot \cos(30^\circ) \quad (2.17)$$

considering that $||\vec{H}_{TEM}||$ is the magnetic measured inside the cell (Sect. 2.2.2) and $||\vec{S}_{ec}||$ the surface of the inductor extracted from measurements in the TEM cell (Sect. 2.6.2).

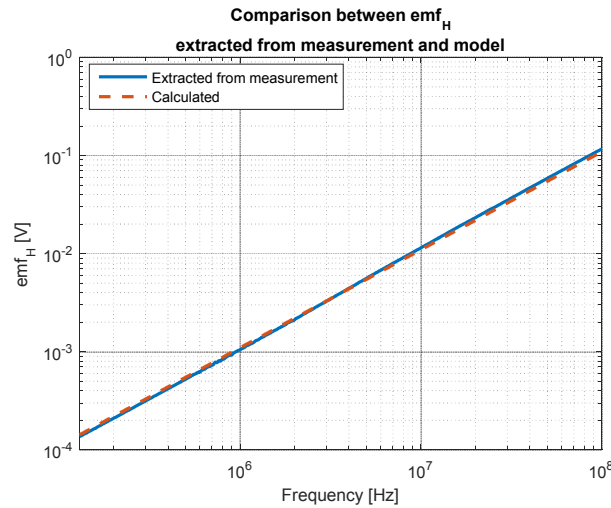


Figure 2.37: Comparison between emf_H extracted from measurement and model

Fig. 2.37 depicts the electromotive force calculated from the coupling surface and a measurement at $\theta = 30^\circ$. It can be concluded that the model really fits with the electromotive force extracted from measurements.

2.6.6 Vertical inductor

For the vertical inductor (Fig. 2.38), the principle is the same but the component must be turned on its side so the turns are oriented like the magnetic field inside the TEM cell. This way, the whole magnetic field can be coupled to the inductor and so the equivalent coupling surface taking into account the magnetic material can be extracted.

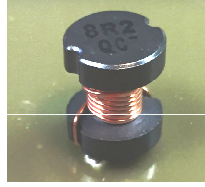


Figure 2.38: 8.4 μ H vertical inductor

2.7 Application case: the common mode choke

A CMC (Fig. 2.39) is a four-port component composed of two windings which are in the same direction. Its main objective is to filter and remove the common mode using a magnetic material. Consequently, two modes are predominant as presented in Sect. 1.4.4: the DM and the CM.

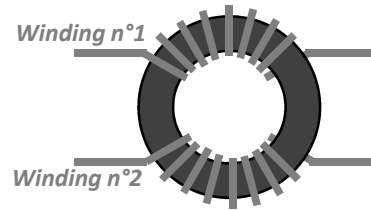


Figure 2.39: Common mode choke

As a result, two kinds of coupling models must be defined: one for CM and one for DM. The first step is to determine whether one of the modes is predominant or not. For this purpose, a CMC was characterized using the TEM cell for both modes. The 6.8mH CMC presented in Fig. 2.40 will illustrate the methodology.

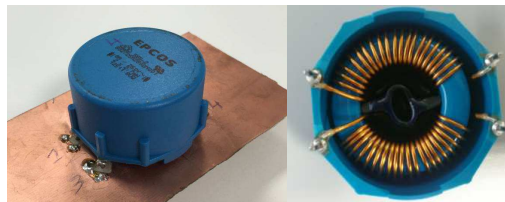


Figure 2.40: 6.8mH CMC

The component is characterized in CM by connecting both windings to reproduce the circuit as seen by a CM current (Fig. 2.41-a). For DM, the outputs of the two windings are connected together and the measurement is done between the inputs (Fig. 2.41-b).

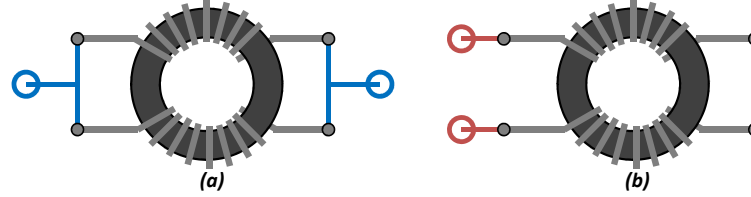


Figure 2.41: a- CM b- DM measurements

A sufficient number of measurements with the TEM cell must be made to determine whether there are preferred orientations and a predominant mode.

2.7.1 Differential mode analysis

The differential mode is the remaining inductance of the CMC when the flux inside the magnetic material is canceled. The TEM cell is then powered through the first port of the VNA, and the second port on the CMC is installed in the cell ceiling. Therefore, the S_{21} parameter represents the transfer of the uniform electromagnetic field to the CMC.

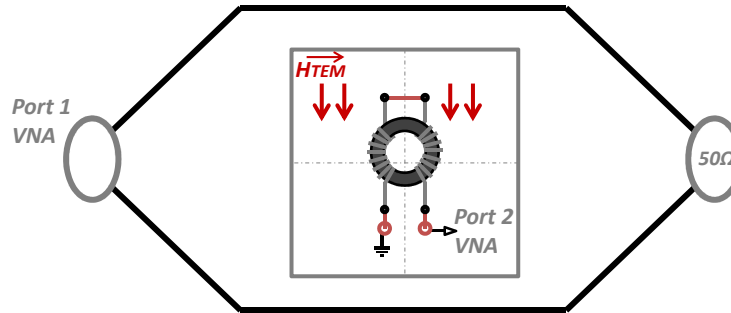
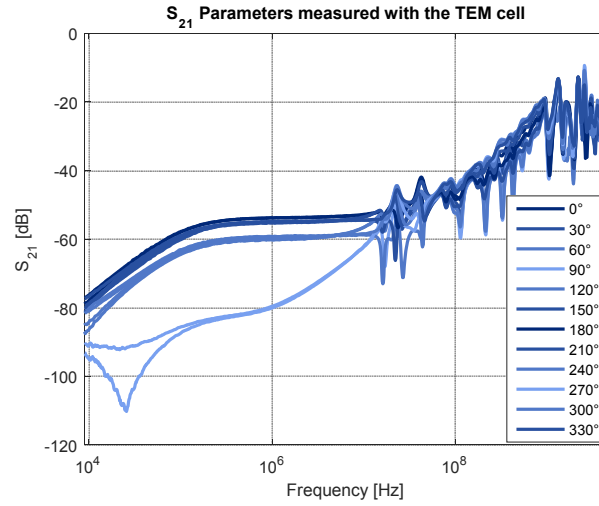


Figure 2.42: DM measurement on a CMC

The aim of this part is to compare electromotive forces generated to the CMC in DM for different orientations. S parameter measurements every 30° from 0° to 360° thus provide a good overview of the coupling level according to the direction of magnetic field. The idea is to re-use the methodology presented in Sect. 2.3.1 to determine the orientations of the surfaces because they cannot be identified a priori.

Fig. 2.43 plots the results of the S_{21} parameters measured from the CMC for different orientations. It is clear that the transfer of the uniform electromagnetic field to the CMC highly depends on the orientation of the component.

Figure 2.43: S_{21} parameters measured with the TEM cell

The measurements are valid from 50kHz to 100MHz because of the measurement dynamics and the SWR . Furthermore, to extract a valid equivalent coupling surface, the slope of the impedance has to be checked. The impedance has to present an inductive behavior (+20dB/decade slope). For this example, the first resonance frequency of the CMC in DM is located at 5.2MHz (Fig. 2.44). Therefore, the valid frequency range has to be reduced to 50kHz to 1.5MHz to extract a coupling model.

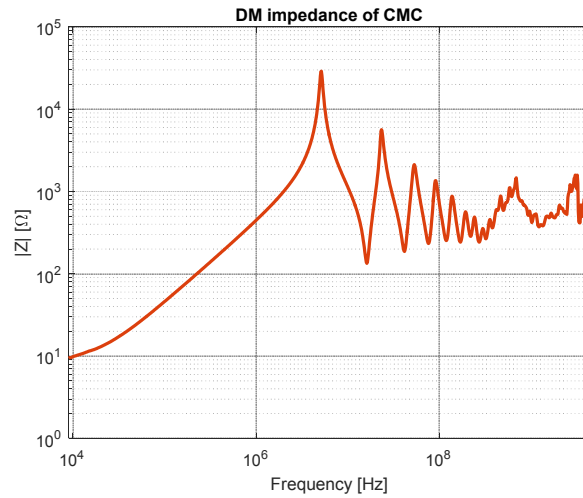
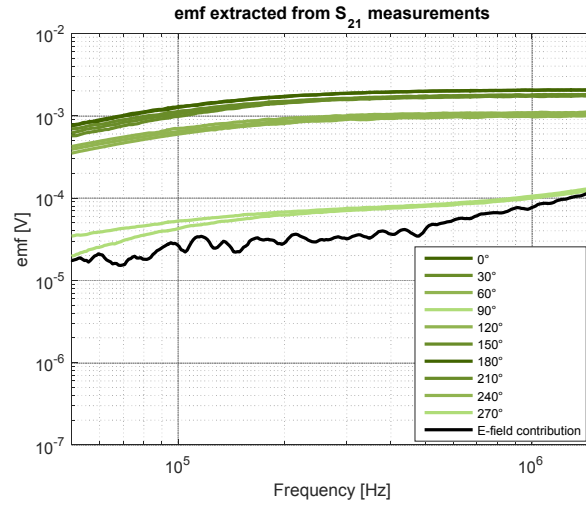


Figure 2.44: DM impedance of CMC

The next step is to calculate electromotive forces from the measured S_{21} parameters and figure out to which extent the magnetic field contributes to these *emfs*.

Figure 2.45: $emfs$ extracted from S_{21} measurements

It can be seen that there are preferred orientations, but the contribution of the electric field is quite high and must be suppressed. Nevertheless, Fig. 2.45 clearly shows that the magnetic field contribution is always higher than the one from the electric field.

This reasoning must be transposed to CM to compare both modes, and finally determine whether there is a dominant mode or not.

2.7.2 Common mode analysis

As far as CM measurement is concerned, the CMC must be connected in CM, as shown in Fig. 2.46.

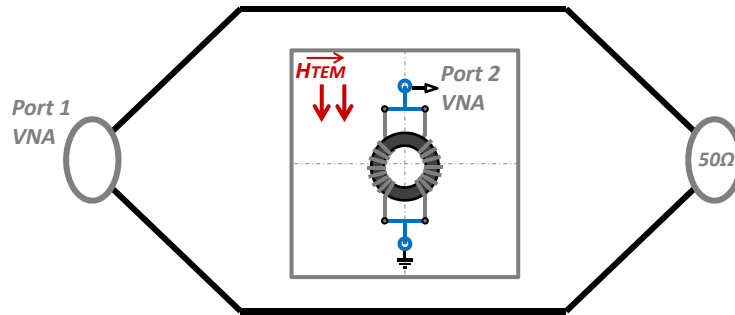


Figure 2.46: CM measurement on a CMC

The aim of this part is the same as for DM, namely to compare electromotive forces generated to the CMC in CM for different orientations of the component. Like for DM measurements, the S parameters are measured every 30° from 0° to 360° and compared to one another.

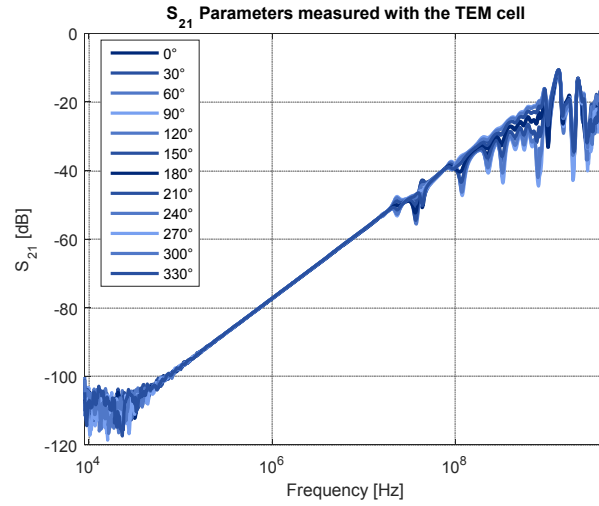
Figure 2.47: S_{21} parameters measured with the TEM cell

Fig. 2.47 highlights that the S_{21} parameters do not depend on the orientation of the CMC; moreover, the level is really low.

As presented in the previous subsection, in order to determine the valid frequency range, the measurement dynamics, the CM impedance and the SWR must all be checked. The valid frequency band where these measurements can be exploited ranges from 50kHz to 300kHz.

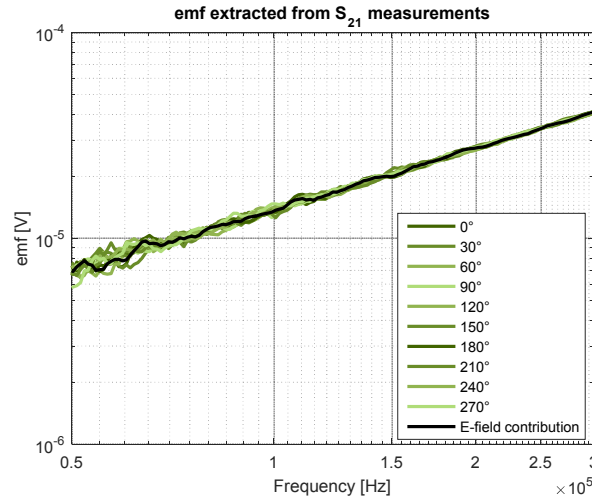
Figure 2.48: emf extracted from S_{21} measurements

Fig. 2.48 clearly shows that the only measured emf is the one generated by the electric field inside the TEM cell. There is no significant magnetic coupling to the CMC in CM.

2.7.3 Comparison between DM and CM analyze

In the previous subsections, an analysis of each mode, DM and CM, was carried out. The first conclusion that can be drawn is that the CM of a CMC does not allow a high level of magnetic

coupling inside the TEM cell compared to DM (Fig. 2.49). Actually, the electromotive force generated to the CMC in CM is in the range of the micro-volt, whereas for DM it is in the range of the milli-volt. Furthermore, the CM measurements does not highlight preferred compared to DM.

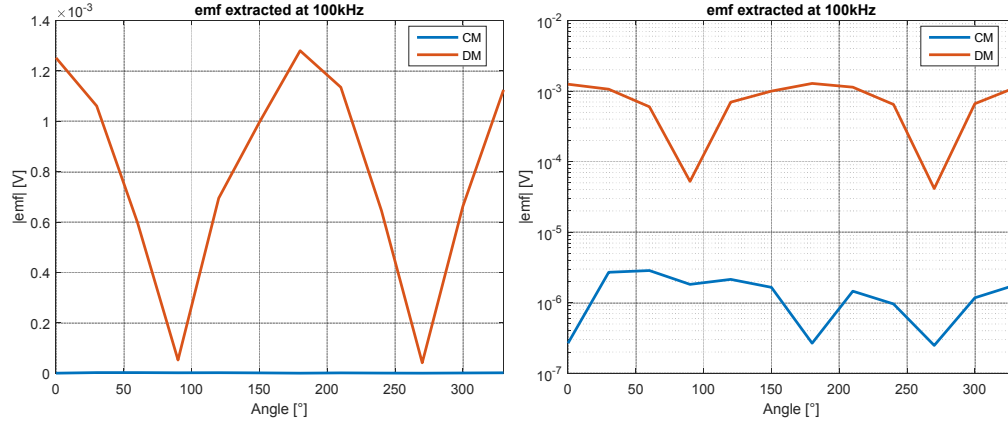


Figure 2.49: Comparison between electromotive forces generated from DM and CM

Actually, it comes from the fact that, when the CMC is connected in CM, it emits very few magnetic field in the air because the majority of the field is concentrated inside the core. However, when it is connected in DM, the magnetic field inside the core is almost canceled and, therefore, all the field goes outside the core and emits more than in CM.

Finally, it can be concluded that only the DM coupling model is necessary to have a good representation of a CMC in its coupling environment.

2.7.4 DM coupling model of a CMC

2.7.4.1 Coupling model definition

The aim of this part is to determine an equivalent model which can reproduce the profile of Fig. 2.49, and which can be deduced from the measurements in the TEM cell. The idea is to approximate the CMC as a succession of loops. Those have a fixed orientation and direction, are located on the mean perimeter of the CMC and are as large as needed to reproduce the magnetic coupling presented in the previous section.

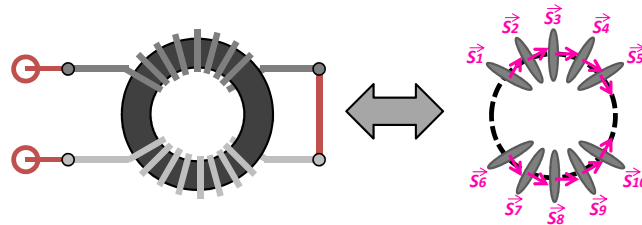


Figure 2.50: DM coupling model of a CMC with 5 loops per winding

Fig. 2.50 depicts an example of a CMC coupling model with five loops per winding, but this model can be extended to more than five loops. The aim of this part is to determine the

ten equivalent coupling surfaces of the coupling model to reproduce the coupling profile of a CMC presented in Fig. 2.49. The case of five loops was chosen because this model was used and validated for several application cases and was sufficient in terms of modeling.

According to Sect. 2.4.2, the electromotive forces extracted from the measured S_{21} must be corrected by the impedance of the DUT to extract the real contribution of the magnetic field to the DUT. Finally, by re-using Eq. 2.13, it is possible to calculate an equivalent coupling surface, which is, in the case of the CMC, a total equivalent coupling model including all coupling surfaces. Eq. 2.18 presents how to extract this equivalent coupling model considering that β is the orientation of the coupling surfaces with respect to the direction of the uniform magnetic field.

$$\|\vec{S}\| = \frac{emf_H}{-j2\pi f\mu_0\mu_r\|\vec{H}_{TEM}\|\cos\beta} \quad (2.18)$$

For each measurement, the ten surfaces have an influence on the generation of each electromotive force. The orientation of the loops constituting the coupling model is called θ and is fixed, like in Sect. 2.3.2. For example, the ten orientations of each loop can be considered in Eq. 2.19 considering that θ_i is the orientation of the surface S_i according to Fig. 2.50.

$$[\theta_i] = [60^\circ \ 30^\circ \ 0^\circ \ -30^\circ \ -60^\circ \ -60^\circ \ -30^\circ \ 0^\circ \ 30^\circ \ 60^\circ] \quad (2.19)$$

The surfaces can be oriented differently. Actually, it depends on the real aperture angle of the windings. This repartition is a good compromise but can induce some errors if the aperture angle of the modeled CMC is very low. This parameter must be adapted depending on the studied CMC.

For the example of Fig. 2.51, the aperture angle is of 120° and, therefore, the best way to represent that CMC is to use a model with θ going from -60° to 60° . Nevertheless, for a CMC with an aperture angle of 30° , θ should go from -15° to 15° .

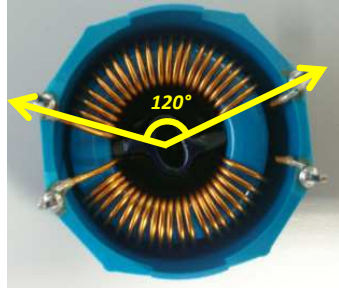


Figure 2.51: Aperture angle of the studied CMC

Then, to calculate the ten surfaces, ten S_{21} measurements are needed in order to build up a square matrix (to ensure the possibility of matrix inversion). The orientation of the CMC inside the TEM cell is called α . For example, the ten orientations in Eq. 2.20 can be taken into account to build the coupling model, considering that the element α_j is the orientation of the CMC in DM inside the TEM cell according to Fig. 2.49.

$$[\alpha_j] = [0^\circ \ 30^\circ \ 60^\circ \ 90^\circ \ 120^\circ \ 150^\circ \ 180^\circ \ 210^\circ \ 240^\circ \ 270^\circ] \quad (2.20)$$

Finally, β_{ij} , the orientation of each loop at each measurement is a 10-by-10 matrix such as:

$$[\beta_{ij}] = [\theta_i] - [\alpha_j] \quad (2.21)$$

It is now possible to express Eq. 2.18 by taking into account the whole coupling model and not only one equivalent coupling surface. Therefore, by inverting the $[\cos(\beta_{ij})]$ in Eq. 2.22, it is now possible to calculate the equivalent coupling surfaces building up the coupling model.

$$[|\vec{S}_j|] = \frac{[emf_{H_i}]}{-j2\pi f \mu_0 \mu_{DM} ||\vec{H}_{TEM}||} [\cos(\beta_{ij})]^{-1} \quad (2.22)$$

Another point that must be taken into account, is the remaining permeability μ_{DM} of the magnetic material when the magnetic flux inside is canceled.

2.7.4.2 Extraction of the DM permeability of a toroidal core

The principle is based on the same methodology as for simple inductor: estimate the DM air core coil L_{DMair} , and use the DM measured inductance L_{DM} like $\mu_{DM} = L_{DM}/L_{DMair}$. To calculate the air core coil, the methodology described in Sect. 3.4.3 is based on the consideration of internal couplings between the turns of the coil and is very accurate.

Then, the L_{DMair} can be calculated and $L_{DMair} = 3\mu\text{H}$ and so gives a value of $\mu_{DM} = 25$.

For mutual inductance calculations that are going to be presented in the following Chapter, it is not necessary to separate the surfaces and the magnetic permeability. Actually, all surfaces, including the influence of the material are used. Indeed, the calculations are simplified.

2.7.4.3 Extraction of the coupling model at a fixed frequency

For this calculation, it is mandatory to determine the frequency where it would be wise to extract the coupling model. According to Sect. 2.7.1, electromotive forces are valid in the frequency range going from 50kHz to 1.5MHz; the coupling model can thus be computed at an intermediate frequency such as 500kHz for example. The coupling model is finally composed as follows, by considering the magnetic material:

$$\mu_{DM}[S] = \mu_{DM} \begin{bmatrix} S_1 \\ S_2 \\ S_3 \\ S_4 \\ S_5 \\ S_6 \\ S_7 \\ S_8 \\ S_9 \\ S_{10} \end{bmatrix} = \begin{bmatrix} 4.6e^{-3} \\ 8.2e^{-3} \\ 9.6e^{-3} \\ 8.5e^{-3} \\ 5.1e^{-3} \\ 5.1e^{-3} \\ 8.5e^{-3} \\ 9.6e^{-3} \\ 8.2e^{-3} \\ 4.6e^{-3} \end{bmatrix} \quad (2.23)$$

2.7.4.4 Extraction of the coupling model over frequency

The extraction of the coupling model can be achieved in the whole frequency range where the measurements are valid. Fig. 2.52 presents this evolution, and it must be noticed that the variation is acceptable. For the ten different surfaces considering the magnetic material, the variation does not exceed 8%. It must be noticed that the surfaces S_6 to S_{10} coincide respectively with surfaces S_5 to S_1 (thanks to their orientations).

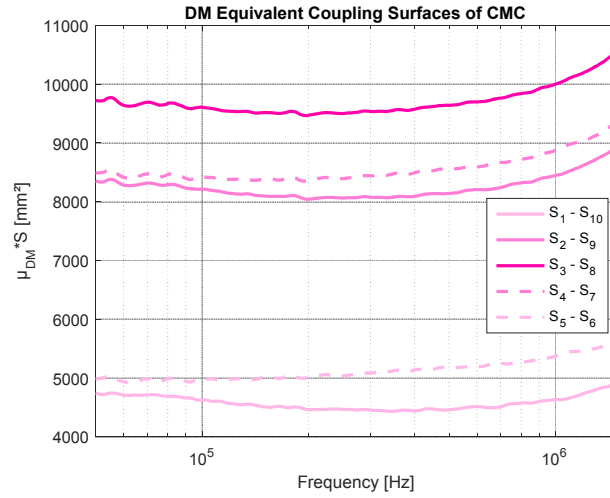


Figure 2.52: DM equivalent coupling model of CMC

2.7.5 Validation of the coupling model with a uniform magnetic field

The aim of this section is to validate the coupling model using a uniform field and by calculating the electromotive force to be compared with measurements. The example in Fig. 2.53 can be considered, which corresponds to a measurement with $\alpha = 30^\circ$.

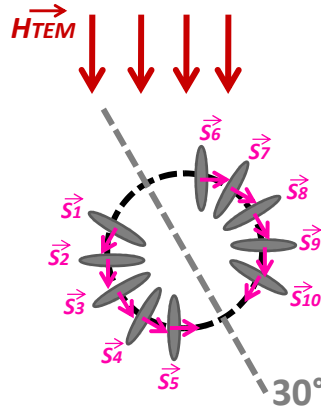


Figure 2.53: Coupling model validation

Eq. 2.21 can be recalled and applied to this case. The angle β is the one presented in Eq. 2.24 as the angle between the magnetic field and the coupling surfaces.

$$[\beta] = \begin{bmatrix} 30^\circ & 0^\circ & -30^\circ & -60^\circ & -90^\circ & -90^\circ & -60^\circ & -30^\circ & 0^\circ & 30^\circ \end{bmatrix}^T \quad (2.24)$$

Finally Eq. 2.25 presents the calculation to estimate the electromotive force when the CMC is oriented at 30° compared to the uniform magnetic field.

$$emf_{H_{30^\circ}} = -j2\pi f\mu_0\mu_{DM}||\overrightarrow{H_{TEM}}|| \sum_{j=1}^{10} (||\overrightarrow{S_j}|| \cdot \cos(\beta_j)) \quad (2.25)$$

considering that $||\overrightarrow{H_{TEM}}||$ is the magnetic measured inside the cell (Sect. 2.2.2) and $||\overrightarrow{S_j}||$ the surfaces constituting the equivalent coupling model of the CMC in DM extracted from measurements in the TEM cell (Sect. 2.7.4.3).

For the coupling surfaces, the fixed values presented in Eq. 2.23 are used. Finally, Fig. 2.54 depicts the electromotive force calculated from the coupling model and the measurement carried out and presented in Sect. 2.7.1. It can be concluded that the model really fits with the electromotive force extracted from measurements. The relative error does not exceed 2%.

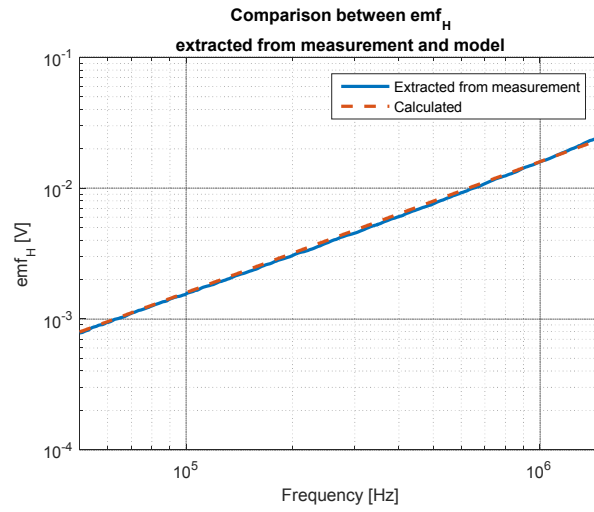


Figure 2.54: Comparison between emf_H extracted from measurement and model

2.7.6 Vertical common mode choke

For the vertical CMC (Fig. 2.55), the principle is exactly the same but the component must be characterized by turning the component on its side, so that the surfaces of the vertical CMC are oriented like an horizontal CMC inside the TEM cell.

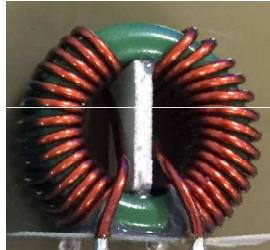


Figure 2.55: 2mH vertical CMC

2.8 Conclusion

In this chapter, the developed methodology in order to determine an equivalent coupling model of passive components was presented. The different steps of calculation to extract an equivalent coupling model from TEM cell measurements were also detailed.

Capacitors and inductors can thus be modeled as a simple surface from two measurements in the TEM cell. For inductors and CMCs, the extracted surfaces take into account the magnetic material influence. Finally, for CMCs, several surfaces are required to have a good representation of its magnetic sensitivity.

The whole methodology has been accrued in a tool, named Equivalent Surface Extractor (ESE tool) as presented in Fig. 2.56. The developed tool and its associated test bench are detailed in Appendix A.1.

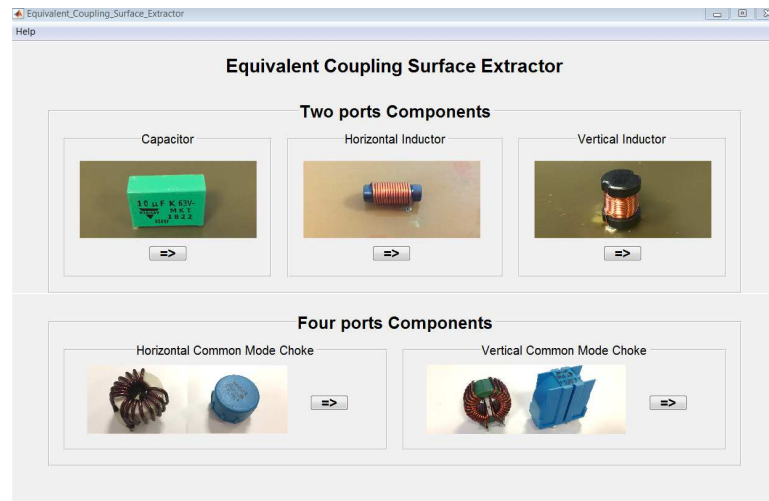
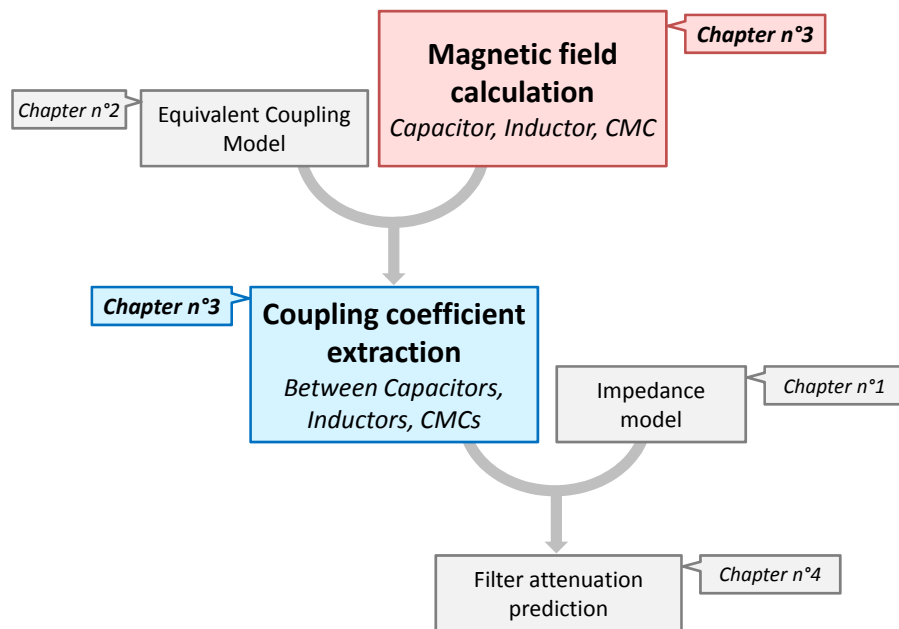


Figure 2.56: ESE tool

Chapter 3

Estimation of the mutual inductance between two passive components



3.1 Introduction to the mutual inductance estimation

In order to determine a mutual inductance between two passive components, the methodology is based on two main formulas (Eq. 3.1 and 3.2) considering that ϕ is the flux of the magnetic field B crossing the surface S , M the mutual inductance and p is the complex variable coming from the Laplace transform.

Actually, the principle is that when a current i flows through a component, a magnetic field B is generated. This magnetic field is coupled to the second component through its equivalent coupling surface S . Finally, the link that exists between the two components is called a mutual inductance M or more generally a coupling coefficient k .

$$d\phi = \vec{B} \cdot d\vec{S} \implies \phi = \vec{B} \cdot \vec{S} \quad (3.1)$$

$$\frac{d\phi}{dt} = M \frac{di}{dt} \implies \phi \cdot p = M \cdot i \cdot p \quad (3.2)$$

$$\vec{B} \cdot \vec{S} = M \cdot i \quad (3.3)$$

In Chapter 2, the methodology to determine an equivalent coupling model was presented. This methodology is applicable to capacitors, inductors and CMCs. In the following section, the magnetic field calculation is explained. Actually, this calculation can be studied by different approach such as the simulation, like in [56, 57] or by models developed from measurement with a near-field scan [58, 59]. The objective here, is to re-use the measurement that are already done for coupling model in order to calculate a magnetic field, without performing additional measurement and based on analytical calculation.

Then, using those two methods (coupling model and magnetic field), the extractions of a mutual inductance between two passive components will be presented.

Finally, a last point about self-inductance prediction is presented. Actually, the principle for mutual inductance calculation can be extended to self-inductance calculation for straight coils and toroid coils.

3.2 Magnetic field calculation principle

3.2.1 Biot & Savart Law

The Biot and Savart law is one of the fundamental laws of magnetostatics, that formulates the magnetic field at any point of space generated by a steady-state line current. Actually, when a current flows through an electric conductor, the magnetic field at any point of space can be calculated as the sum of the contributions $d\vec{B}$ created from a current element $I d\vec{S}$.

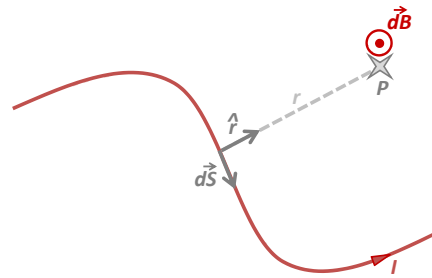


Figure 3.1: Contribution \vec{dB} at point P created by a current element $I\vec{dS}$

$$\vec{dB} = \frac{\mu}{4\pi} \frac{\hat{r}}{r^2} I \vec{dS} \quad (3.4)$$

The Biot and Savart law is valid since the current is considered steady in the circuit. Consequently, the frequency must not be too high to consider a constant current (in order to stay in the quasi-static approximation). The distance to point P must be sufficient to consider the section of the conductor thin enough to be negligible.

3.2.2 Reciprocity principle

The reciprocity principle, applied to circuits, states that : “In any physical linear network, the positions of an ideal voltage source and an ideal ammeter can be interchanged without affecting their readings” [60, 61, 62, 63, 64, 35]. In other terms, let us consider the two coupled inductors in Fig. 3.2. If a current i_1 is considered through the first inductor L_1 , an electromotive force V_2 is generated to L_2 thanks to the mutual inductance M between the two inductors. Inversely, if a current i_2 is considered through the second inductor L_2 , an electromotive force V_1 is generated to L_1 thanks to the mutual inductance M between the two inductors. Both reasonings are the same and so respect the reciprocity principle.

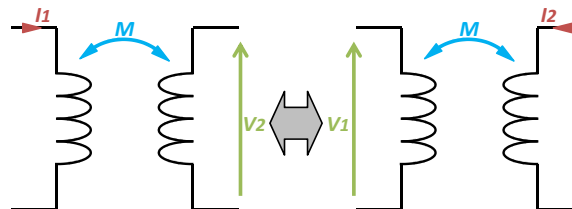


Figure 3.2: Reciprocity principle applied to circuits

In other terms, the reciprocity principle can be applied to electromagnetism. Actually, it was demonstrated in [65] that, when there are two antennas A_1 and A_2 , located at O_1 and O_2 respectively, the magnetic field measured by A_1 if A_2 emits and the one measured by A_2 if A_1 emits are the same in level and in phase (Fig. 3.3). Indeed, the emission surface and the coupling surface are equivalent.

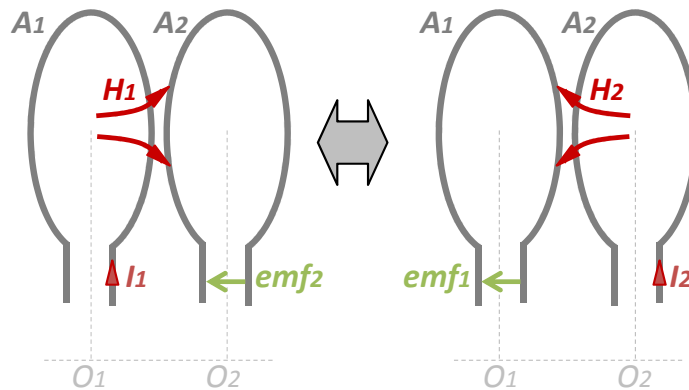


Figure 3.3: Reciprocity principle applied to antennas

In our research work, the reciprocity principle is widely used. Actually, it is considered for mutual inductances: mutual inductances calculated from the first component to the second and inversely are considered equivalent. Then, it can also be considered that the equivalent coupling surface and the equivalent emission surface are equivalent.

3.2.3 Image theory

The image theory comes from field behavior in the presence of an obstacle and for the present case, the magnetic field behavior in the presence of a ground plane. This theory assumes that, if there is a perfect electric conductor, flat and infinite in extent [66, 61, 63, 64, 35], the magnetic field which is reflected from the ground plane must be taken into account to have a better representation of the total magnetic field. The field reflected from the ground plane can be estimated by taking into account the image of the real source with respect to the ground plane [62]. Fig. 3.4-a and Fig. 3.4-b present the image theory for vertical source and horizontal sources.

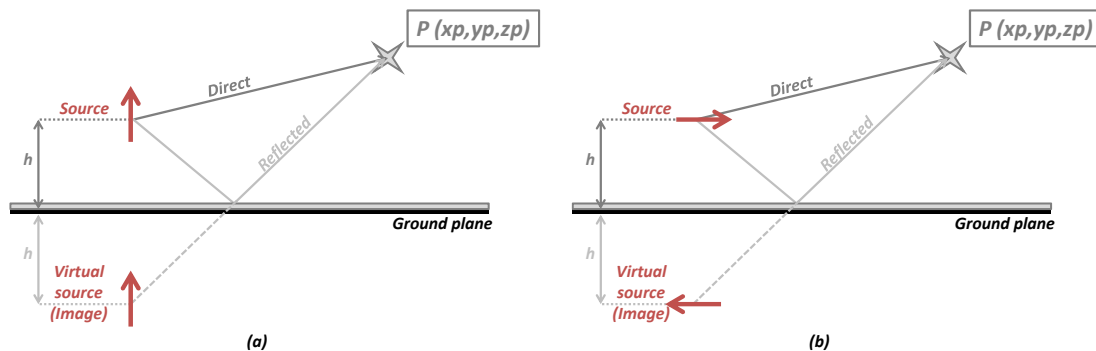


Figure 3.4: a - Vertical b - Horizontal sources and their images considering an infinite ground plane

It must be noticed that, in practice, the ground plane cannot be considered infinite. Nevertheless, since the ground plane is large enough compared to the size and position of the source and the point of calculation, the image theory will be applied.

Furthermore, this theory induces that, in the presence of a ground plane, not only the equivalent emission surface must be duplicated, but also the equivalent coupling surface, thanks to the

reciprocity principle (Sect. 3.2.2).

Finally, it must be noticed that, on power electronics, the filter components are sometimes connected by lead frame and not on a PCB. Therefore, in the case where there is no ground plane, the image theory should not be applied.

3.2.4 Scope of application

The Biot and Savart law is applicable only for the magnetostatic domain. It means that the current is considered constant on its whole path. Indeed, the length of the path must be very small compared to the wave length. The objective here is to have a good representation of the magnetic field generated by passive components for the conducted emission frequency band from 150kHz until 108MHz. Indeed, the length of the current path must be very small with respect to the smallest wavelength associated to this frequency band, which gives $\lambda_{min} = c/f_{max} = 2.78m$ considering that the medium is the air. Actually, the speed depends on the permittivity and the permeability:

$$v = \frac{1}{\sqrt{\mu\epsilon}} = \frac{1}{\sqrt{\mu_0\mu_r\epsilon_0\epsilon_r}} \quad (3.5)$$

Indeed, whether for capacitors, inductors or CMCs, the medium cannot be considered to be only the air. For the capacitor, the surface is located between the two pins, the internal structure and the ground plane. Therefore, the medium at the surface location is the air and the FR4 material of the printed circuit board (PCB). As far as inductors and CMC are concerned, the medium that must be considered is the magnetic material building up the turns.

Therefore, in order to determine the upper frequency of the validity domain, the current path l_{path} must be ten times lower than the minimum wave length: $l_{path} < \lambda_{min}/10$. This condition was determined through near-field scan measurements on different components. Actually, the emission profile does not change since this condition is met.

In order to illustrate this frequency limit, the example of the CMC presented in Sect. 2.7 and Sect. 3.2.7.1 is used. Actually, the current path is calculated from the equivalent coupling surfaces determined with the TEM cell and so $l_{path} = 421mm$. Then, the minimum wavelength must be of $\lambda_{min} = 4.21m$. Furthermore, the medium is the one of the magnetic material building up the CMC in DM. The relative permeability is $\mu_r = 25$ (Sect. 2.7.4.2). Then, the speed is calculated as $v = 6.10^7 m/s$ and a maximum frequency defining the limit of magnetostatic calculation for this CMC is $f_{max} = 8.3MHz$.

Therefore, the emission profile of this component should be the same until that maximum frequency and hereafter, the emission profile should become to change. Fig. 3.5 presents the emission profile of the CMC for three different frequencies in the magnetostatic domain, for 500kHz, 1MHz and 3MHz. The black lines are placed in the same place in order to define the low field zones. Those zones will help to determine if the emission profile changes or not. Actually, the blue zones are behind the black lines and do not move.

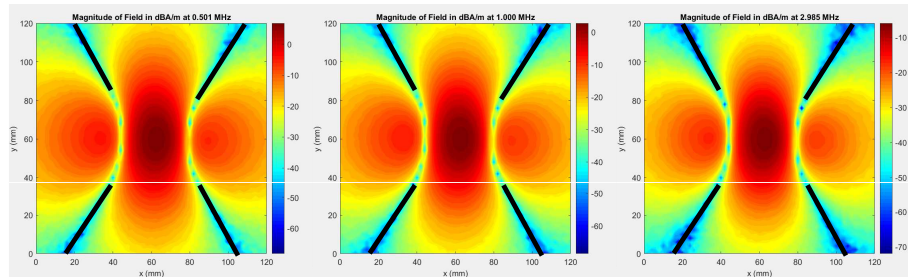


Figure 3.5: Magnetic field generated from CMC measured at 500kHz, 1MHz and 3MHz with a near field scan

Now, for higher frequencies as in Fig. 3.6, for 8MHz, 10MHz, 12MHz and 15MHz, it appears that the blue zone becomes to move regarding the black lines that are the references for low field zone. Therefore, it can be concluded that the frequency limit of 8.3MHz coming from the criteria $l_{path} < \lambda_{min}/10$ is appropriate. It must be noticed that this limitation is also visible on the phase cartography.

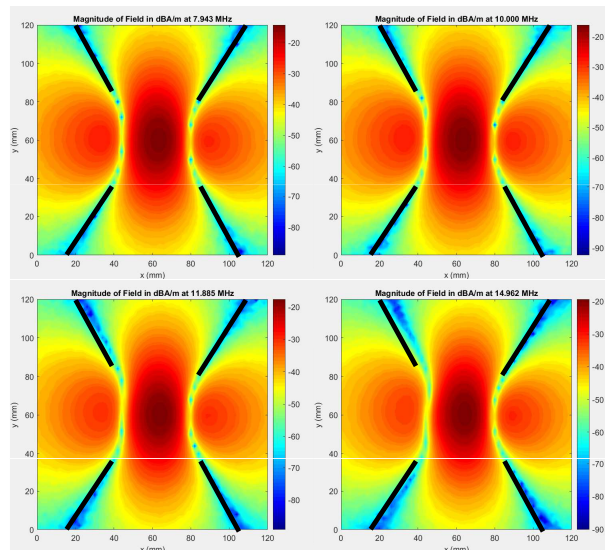


Figure 3.6: Magnetic field generated from CMC measured at 8MHz, 10MHz, 12MHz and 15MHz with a near field scan

Finally, this point must be checked for all magnetic field calculations, in order to determine the valid frequency range. Furthermore, that limit gives also the frequency limit of mutual inductance calculation. Actually, once that frequency limit is exceeded, the magnetic field profile changes and the calculation cannot be simplified as presented in Sect. 3.1.

3.2.5 Application case: the capacitor

In order to calculate the magnetic field generated by a capacitor, the surface determined with the TEM cell in Chapter 2 can be re-used. Indeed, using the reciprocity theorem, the equivalent coupling surface is also the equivalent emission surface. Moreover, the ground plane must be taken into account thanks to the image theory.

In order to determine the dimensions of the rectangular surface, corresponding to the emission surface of the capacitor, the two needed parameters are the distance between the two pins, called d_{pins} , and the height of the pins, named h_{pins} . The parameter d_{pins} is easily measurable from the component and to determine the h_{pins} parameter, the formula $h_{pins} = |\vec{S}_{ec}|/d_{pins}$ can be used.

Finally, Fig. 3.7 can be considered to build up the Biot and Savart law for this application case.

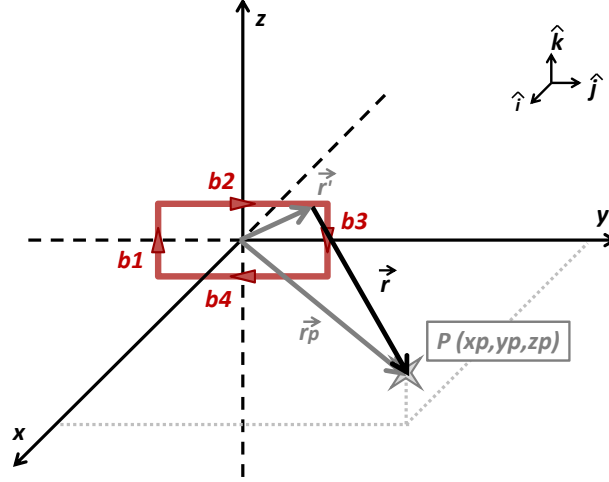


Figure 3.7: Biot & Savart Law applied to a capacitor

From Fig. 3.7, the calculation can be divided into four steps, one for each segment building up the radiation surface. The calculation is described for the four segments beginning with b_1 to b_4 .

- For b_1 , $\vec{dB}_{b_1} = \frac{\mu_0 I}{4\pi} \frac{1}{r^3} \begin{pmatrix} y_p + \frac{d_{pins}}{2} \\ -x_p \\ 0 \end{pmatrix} \cdot \begin{pmatrix} \hat{i} \\ \hat{j} \\ \hat{k} \end{pmatrix} d_{integ_z}$,

where $integ_z = [-h_{pins} : h_{pins}]$,

- For b_2 , $\vec{dB}_{b_2} = \frac{\mu_0 I}{4\pi} \frac{1}{r^3} \begin{pmatrix} h_{pins} - z_p \\ 0 \\ x_p \end{pmatrix} \cdot \begin{pmatrix} \hat{i} \\ \hat{j} \\ \hat{k} \end{pmatrix} d_{integ_y}$,

where $integ_y = [-\frac{d_{pins}}{2} : \frac{d_{pins}}{2}]$,

- For b_3 , $\vec{dB}_{b_3} = \frac{\mu_0 I}{4\pi} \frac{1}{r^3} \begin{pmatrix} \frac{d_{pins}}{2} - y_p \\ x_p \\ 0 \end{pmatrix} \cdot \begin{pmatrix} \hat{i} \\ \hat{j} \\ \hat{k} \end{pmatrix} d_{integ_z}$,

- For b_4 , $\vec{dB}_{b_4} = \frac{\mu_0 I}{4\pi} \frac{1}{r^3} \begin{pmatrix} h_{pins} + z_p \\ 0 \\ -x_p \end{pmatrix} \cdot \begin{pmatrix} \hat{i} \\ \hat{j} \\ \hat{k} \end{pmatrix} d_{integ_y}$.

All the calculations are detailed in Appendix B.1. Finally, the magnetic field generated by the capacitor can be expressed as the sum of the four contributions mentioned above.

The objective is then to apply it to a real capacitor. The used capacitor is the same as the one characterized in the TEM cell (Sect. 2.5).

Two geometrical parameters of the capacitor must be measured; using calipers, the distance between the two pins $d_{pins} = 28.4mm$ is measured and using the equivalent coupling surface, $h_{pins} = |\vec{S}_{ec}|/d_{pins} = 4mm$ can be calculated.

For this capacitor, the current path is about $l_{path} = 64.8mm$ (that corresponds to the perimeter of the surface) and so the minimum wavelength must be of $\lambda_{min} = 648mm$. Furthermore, the medium to be FR4 and the maximum relative permittivity is $\epsilon_r = 4.7$. Then, the speed can be calculated as $v = 1.38 \cdot 10^8 m/s$ and a maximum frequency defining the limit of magnetostatic calculations for this capacitor is $f_{max} = 213MHz$.

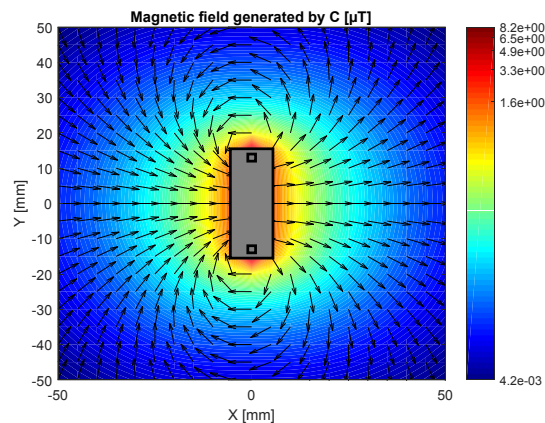


Figure 3.8: Magnetic field generated from C calculated Biot & Savart Law

Fig. 3.8 presents the magnetic field calculated from the Biot and Savart law for the $10\mu F$ capacitor at the ground plane level. Furthermore, the vectors represent the direction of the magnetic field in the (X,Y) plane.

3.2.6 Application case: the inductor

The magnetic field calculation for the inductor is divided into different steps. To calculate the field generated by an inductor, the equivalent coupling surface must be reused as the equivalent emission surface. In order to obtain the right emission profile, the surface must be divided into as many loops as turns. The surface determined in Sect. 2.6 takes into account the influence of the magnetic material. Therefore, each surface is reduced to the surface of one turn and the current is re-calculated to compensate for this surface reduction. This gives the possibility to perform all calculations without considering precisely the geometrical parameters.

3.2.6.1 Horizontal inductor

Concerning the horizontal inductor, the Fig. 3.9 can be used for a unique loop and the principle is the same for several loops.

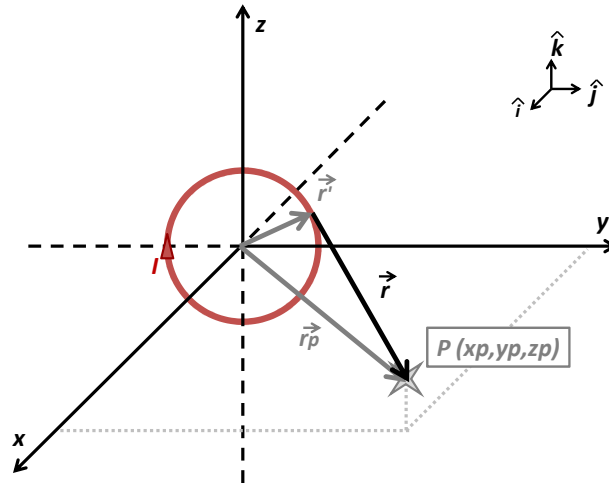


Figure 3.9: Biot & Savart Law applied to a loop in (Y,Z) plane

The objective is to consider each turn as one loop to calculate the direct magnetic field generated to any point P and also the magnetic field reflected on the ground plane, if the latter exists (Fig. 3.10).

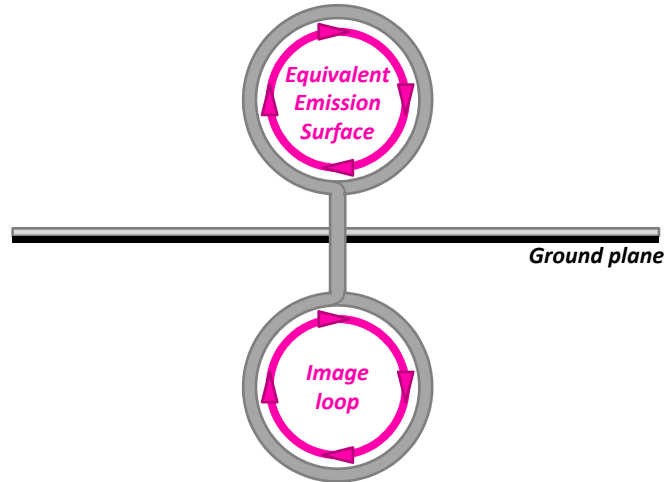


Figure 3.10: Image loop for horizontal inductor

First of all, let us consider the following formula, extracted from Fig. 3.9, to calculate the magnetic field generated by one loop. Details are presented in Appendix B.2.

$$\vec{dB} = \frac{\mu_0 \mu_r I R}{4\pi} \frac{1}{r^3} \begin{pmatrix} Y \cos \phi + Z \sin \phi - R \\ -X \cos \phi \\ -X \sin \phi \end{pmatrix} \cdot \begin{pmatrix} \hat{i} \\ \hat{j} \\ \hat{k} \end{pmatrix} d\phi \quad (3.6)$$

considering that $d\phi = [0 : 2\pi]$ and that X , Y , and Z are the distances to the point P for each turn and its image. Finally, the sum of all contributions gives an estimation of the magnetic field

generated by an inductor, as presented in Fig. 3.11 for a $2\mu\text{H}$ inductor (the same inductor as the one characterized in the TEM cell in Sect. 2.6).

For this inductor, the current path is about $l_{path} = 177\text{mm}$ and so the minimum wavelength must be $\lambda_{min} = 1.77\text{m}$. Furthermore, the medium is considered to be the magnetic material building up the inductor. The relative permeability is $\mu_r = 8.54$. This value of the magnetic permeability is calculated as $\mu_r = \frac{S_{TEM}}{N \cdot S_{loop}}$ considering that S_{TEM} is the surface measured in the TEM cell. Then, the speed can be calculated as $v = 1.03 \cdot 10^8 \text{m/s}$ and a maximum frequency defining the limit of magnetostatic calculation for this inductor is $f_{max} = 58\text{MHz}$.

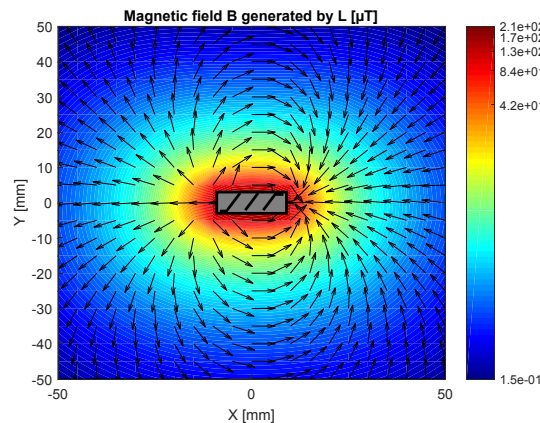


Figure 3.11: Magnetic field generated from L calculated with Biot & Savart Law

3.2.6.2 Vertical inductor

For the vertical inductor, the principle is exactly the same as for horizontal inductor but by considering the loop in the (X,Y) plane (Fig. 3.12).

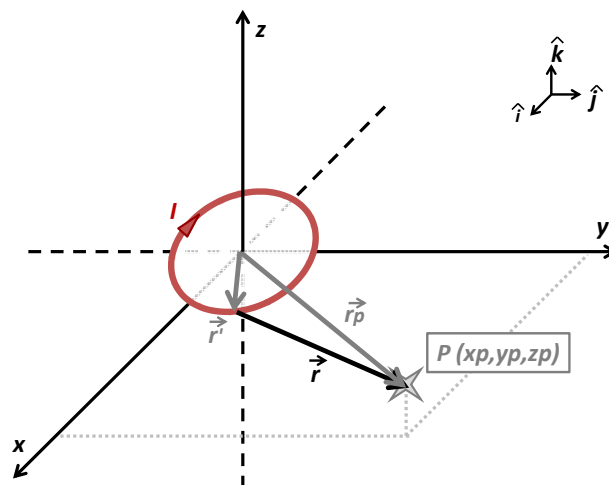


Figure 3.12: Biot & Savart Law applied to a vertical inductor

Furthermore, considering the orientations of turns with respect to the ground plane, the image is not the same as for horizontal inductor and is presented in Fig. 3.13.

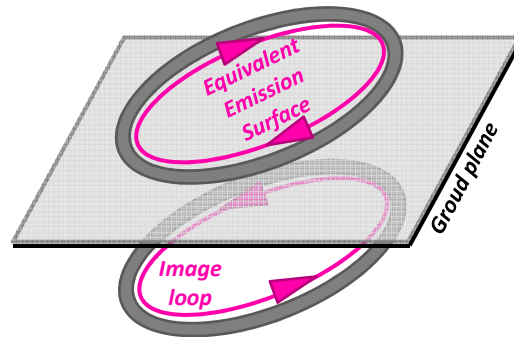


Figure 3.13: Image loop for a vertical inductor

This way, the following formula comes from the application of the Biot and Savart law to this application case. The details are presented in the Appendix B.3.

$$\vec{dB} = \frac{\mu_0 \mu_r I R}{4\pi} \frac{1}{r^3} \begin{pmatrix} -Z \cos \phi \\ -Z \sin \phi \\ X \cos \phi + Y \sin \phi - R \end{pmatrix} \cdot \begin{pmatrix} \hat{i} \\ \hat{j} \\ \hat{k} \end{pmatrix} d\phi \quad (3.7)$$

Finally, by considering as many loops as turns and their images, it is possible to calculate the magnetic field generated by a vertical inductor in the (X,Y) plane (Fig. 3.14). The used inductor is the same as the one characterized in the TEM cell (Sect. 2.6.6).

This calculation is valid until 41.6 MHz regarding the size of the inductor and the magnetic material properties.

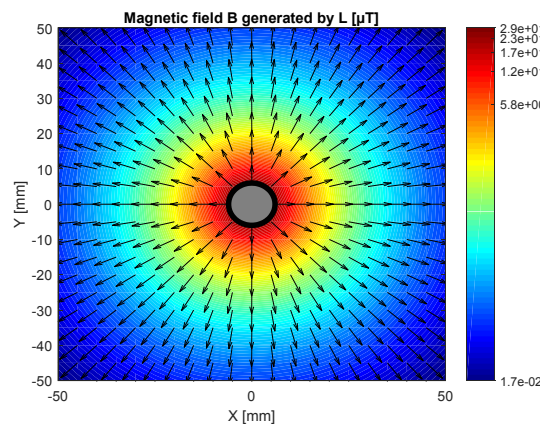


Figure 3.14: Magnetic field generated from L calculated with Biot & Savart Law

3.2.7 Application case: the common mode choke

As presented in Sect. 2.7, a CMC connected in CM does not allow a high magnetic coupling compared to DM. Indeed, thanks to the reciprocity theorem, it can be concluded that the CMC in CM does not generate a high level of magnetic field compared to DM. Therefore, only the magnetic field generated by the CMC in DM is calculated.

In order to calculate that magnetic field, the equivalent coupling model from Sect. 2.7 can be re-used as for capacitor or inductor. Actually, the total magnetic field generated by the CMC is the sum of the contribution of each surface building up the model. However, in order to obtain the right emission profile, the surfaces and the current flowing into them must be corrected. The point is that the measured surfaces S_{ec} are equivalent surfaces and not physical surfaces; they are increased by the influence of the magnetic material. Indeed, the emitting radius is considered as the physical radius $R = \sqrt{\frac{S_{core}}{\pi}}$ (with S_{core} the surface of the core section) and the current is corrected by the surface ratio as $I = I_{injected} \frac{S_{ec}}{S_{core}}$. Therefore, by performing this correction, the products $R \cdot I$ and $R_{sec} \cdot I_{injected}$ are still the same (considering that R_{sec} is the associated radius to S_{ec}).

3.2.7.1 Horizontal common mode choke

To calculate the magnetic field generated by a CMC in DM, the equivalent coupling model is reused as an emission model. The CMC, characterized in the TEM cell (Sect. 2.7), is going to be used for the magnetic field calculation. The following formula can thus be used to calculate the magnetic field considering that θ is the orientation of each surface

$$\vec{dB} = \frac{\mu_0 \mu_{DM} I R}{4\pi} \frac{1}{r^3} \begin{pmatrix} Y \cos\phi + Z \sin\phi \cos\theta - R \cos\theta \\ -X \cos\phi - Z \sin\phi \sin\theta + R \sin\theta \\ -X \sin\phi \cos\theta + Y \sin\phi \sin\theta \end{pmatrix} \cdot \begin{pmatrix} \hat{i} \\ \hat{j} \\ \hat{k} \end{pmatrix} d\phi \quad (3.8)$$

The validity domain of that magnetic field calculation is detailed in Sect. 3.2.4.

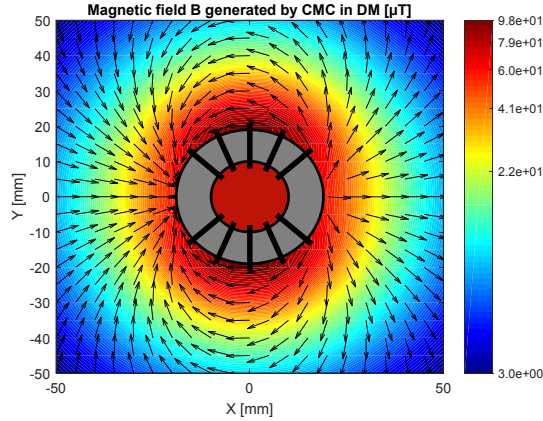


Figure 3.15: Magnetic field generated from CMC in DM calculated with Biot & Savart Law

3.2.7.2 Vertical common mode choke

As far as the vertical CMC is concerned, the calculation principle is the same as for a horizontal CMC. Indeed, the formulas presented in the previous subsection are re-used. A magnetic field calculation generated by a vertical CMC is presented in Fig. 3.16. For this vertical CMC, the upper frequency of the validity domain is $21.3 MHz$.

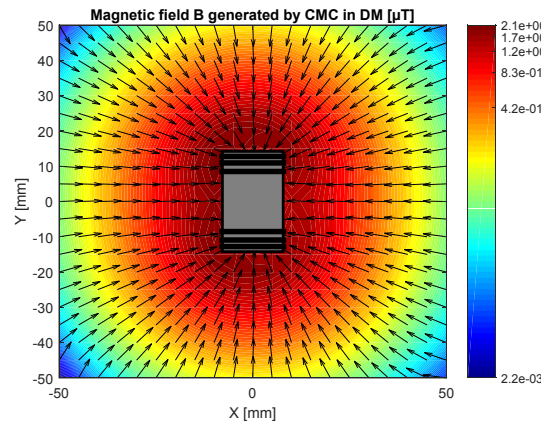


Figure 3.16: Magnetic field generated from CMC in DM calculated with Biot & Savart Law

3.3 Prediction of mutual inductance

Now that the equivalent coupling surface and the magnetic field generated by passive components are known, it is possible to estimate a mutual inductance between two passive components. This kind of calculation will be presented for mutual inductances between two capacitors, two inductors and two CMCs.

3.3.1 Between two capacitors

The first mutual inductance calculation example is dedicated to two $470nF$ capacitors spaced by $10mm$ as presented in Fig. 3.17.

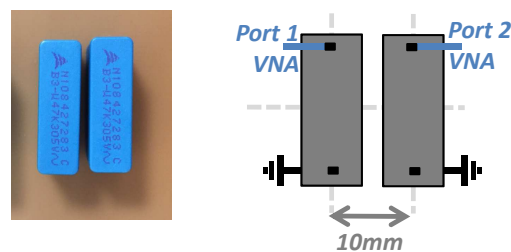


Figure 3.17: Capacitor positioning

The first step is to extract the magnetic field generated by the first capacitor on the second capacitor surface. Indeed, a mean value of the magnetic field crossing the surface can be calculated from Fig. 3.18 that presents the magnetic field level at the surface position.

Different possibilities can be used to extract the magnetic field crossing the surface. A first possibility is to consider the real curve of the surface and perform an integration considering the Neumann formula [67, 68]. However, as long as all coupling surfaces are simplified, thanks to the determination in the TEM cell, the use of the Neumann formula seems to be unnecessary for good prediction. Actually, a mean value of the magnetic field crossing the surface seems to be a good approximation, like it will be presented in the following calculations. Indeed, all calculations are simplified and direct for mutual inductance calculation.

A mean value of the magnetic field $B_{mean} = 0.52\mu T$ and a mean value of the angle between the coupling surface and the field vector $\theta_{mean} = 0^\circ$ are extracted. Then, according to Eq. 3.3, the calculation is direct and gives a mutual inductance value between the two capacitors of $M_{calculated} = 2.71nH$.

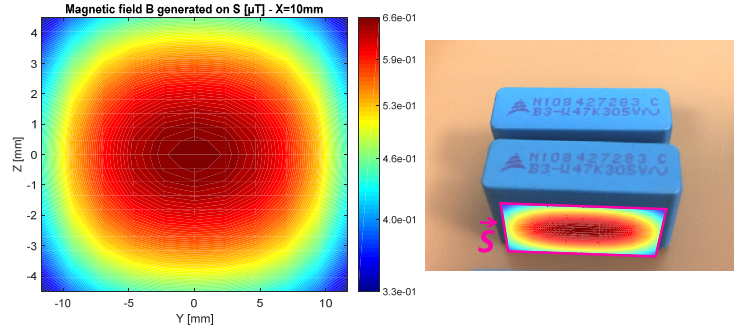


Figure 3.18: Magnetic field generated by the first capacitor on the surface of the second one

To validate this calculation, the best way is to compare it to measurement. In order to do this, Fig. 3.17 presents the measurement to be performed on the components to extract a mutual inductance with a VNA. The S_{21} parameter is extracted and converted to the Z_{21} parameter (Eq.3.9).

$$Z_{21} = 2 \cdot \frac{S_{21}}{(1 - S_{11})(1 - S_{22}) - S_{12}S_{21}} \cdot Z_0 \quad (3.9)$$

Finally, the mutual inductance can be calculated from the measurement, as presented in Eq. 3.10.

$$M = \frac{\text{Imag}(Z_{21})}{2\pi f} \quad (3.10)$$

Fig. 3.19 depicts the comparison between the calculated mutual inductance and the one extracted from measurement.

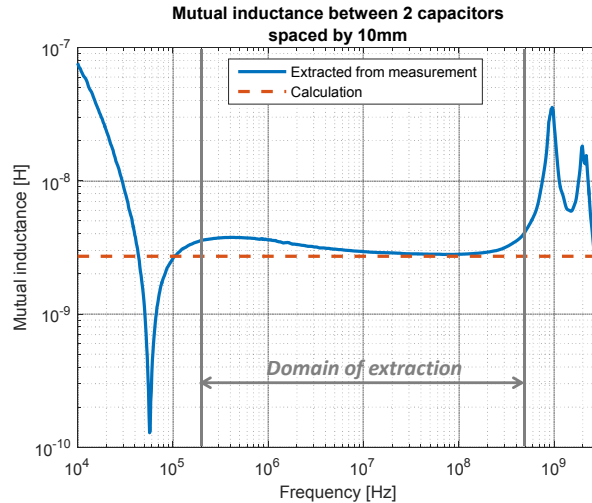


Figure 3.19: Comparison between mutual inductances extracted from measurement and calculation

The calculation really agrees with measurement, and provides a good prediction even for low values of magnetic coupling (in the range of nH).

Nevertheless, the extraction of the mutual inductance cannot be performed on the whole frequency range, as seen in Fig. 3.19. Actually, it depends on the uncertainty coming from the S-parameters measurements [20, 31] and can then be transposed to an uncertainty on Z-parameters, and more particularly an uncertainty on Z_{21} parameter. Therefore, Eq. 3.9 can be expressed in logarithmic expression as in Eq. 3.11.

$$\ln(Z_{21}) = \ln(2) + \ln(S_{21}) - \ln((1 - S_{11})(1 - S_{22}) - S_{12}S_{21}) + \ln(Z_0) \quad (3.11)$$

Therefore, by using the partial derivative, Eq. 3.12 formulates the uncertainty on the Z_{21} parameter from uncertainty and measurements on S-parameters.

$$\frac{dZ_{21}}{Z_{21}} = \frac{dS_{21}}{S_{21}} - \frac{d((1 - S_{11})(1 - S_{22}) - S_{12}S_{21})}{(1 - S_{11})(1 - S_{22}) - S_{12}S_{21}} \quad (3.12)$$

Finally, Eq. 3.13 presents the uncertainty on Z_{21} parameter by considering separately each uncertainty on the S-parameters and by considering that $\Delta S = (1 - S_{11})(1 - S_{22}) - S_{12}S_{21}$.

$$\frac{dZ_{21}}{Z_{21}} = dS_{11} \frac{1 - S_{22}}{\Delta S} + dS_{21} \left(\frac{1}{S_{21}} + \frac{S_{12}}{\Delta S} \right) + dS_{12} \frac{S_{21}}{\Delta S} + dS_{22} \frac{1 - S_{11}}{\Delta S} \quad (3.13)$$

Fig. 3.20 depicts the evolution of the uncertainty on the Z_{21} parameter and, therefore, on the mutual inductance. A maximum uncertainty can be fixed at 10%, which gives an accurate measurement from 130kHz until 800MHz.

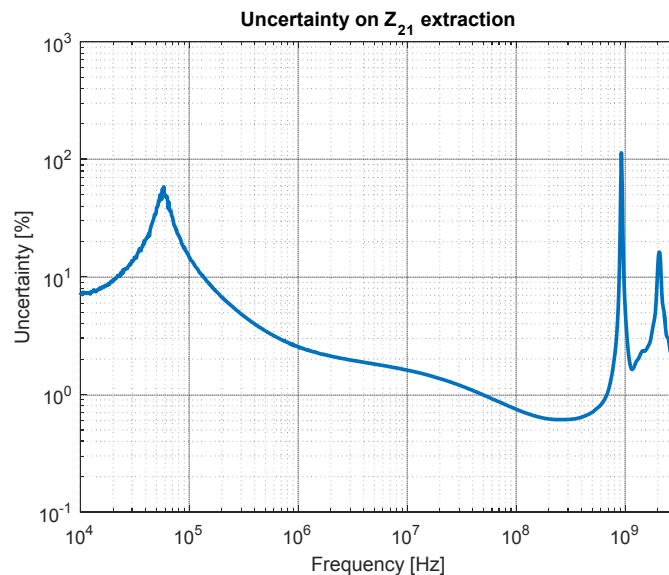


Figure 3.20: Uncertainty on the Z_{21} parameter extracted from S-parameters

Furthermore, the extracted mutual inductance is valid since it is still in magnetostatic domain and, therefore, it reduces the maximum frequency to 500MHz (depending on the current path as presented Sect. 3.2.4). Actually, once the frequency limit of the magnetostatic is exceeded, the magnetic field profile changes and the calculation cannot be simplified as presented.

Finally, for this case, the mutual inductance can be extracted from 130kHz to 500MHz as presented in Fig. 3.19. This analysis of accurate calculation must be performed for all measurements.

3.3.2 Between two inductors

Let us consider the example from Fig. 3.21 for the mutual inductance calculation between two inductors.

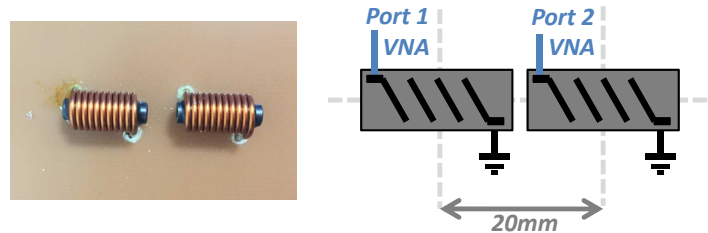


Figure 3.21: Inductor positioning

These two $1.8\mu H$ inductors are spaced by 20mm center to center. As for capacitors, the first step is to calculate the magnetic field generated by the first inductor to the second one. In order to have more accuracy, the calculation is performed by computing the magnetic field at each turn position. Actually, the equivalent coupling surface of the inductor is divided into as many turns as there are and are located at each turn position. Actually, the magnetic field generated to the first turn and the one generated to the last turn are not the same. This way, the variation of magnetic field, along the inductor, is considered.

Fig. 3.22 presents the magnetic field generated by the first inductor on the first surface (the first turn) of the second inductor. This calculation is repeated for all turns.

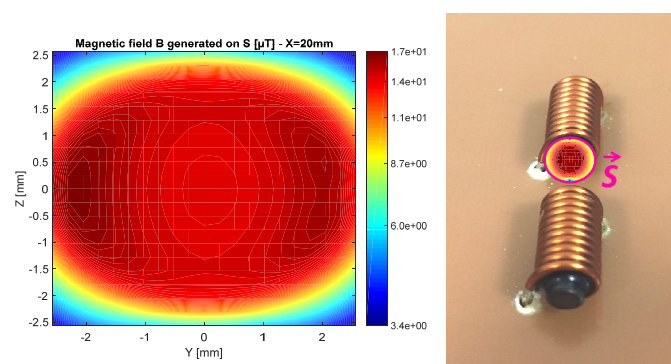


Figure 3.22: Magnetic field generated by the first inductor on the first surface of the second inductor

Therefore, a total mutual inductance value is extracted as the sum of all the mutual inductances generated to each turn of the second inductor. Fig. 3.23 presents the comparison between mutual inductances extracted from measurement and calculation.

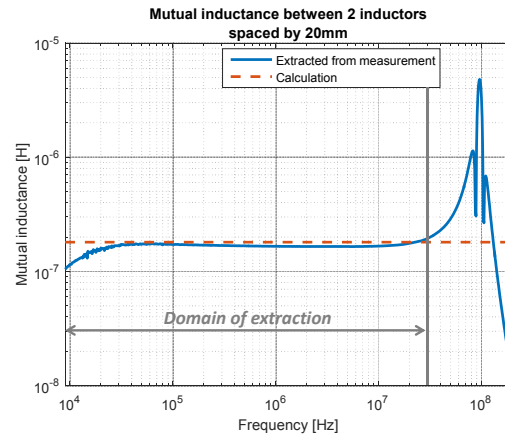


Figure 3.23: Comparison between mutual inductances extracted from measurement and calculation

The magnetic coupling is correctly predicted from 9kHz until 300MHz because of the uncertainty and the limit of the magnetostatic domain.

3.3.3 Between two CMCs in DM

As far as CMCs are concerned, the objective is now to present the mutual inductance calculation between two CMCs, the first one of 6.8mH and the second of 10mH spaced by 40mm (Fig. 3.24).

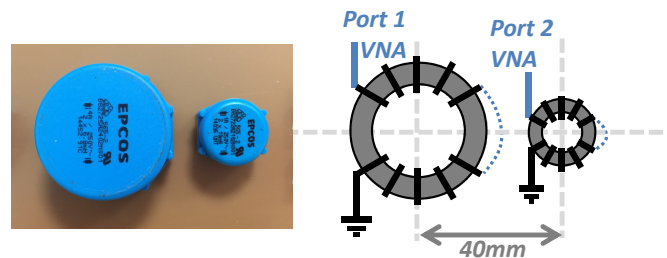


Figure 3.24: CMCs position

The mutual inductance calculation is divided into four steps because there are four different mutual inductances between two CMCs in DM as presented in Fig. 3.25.

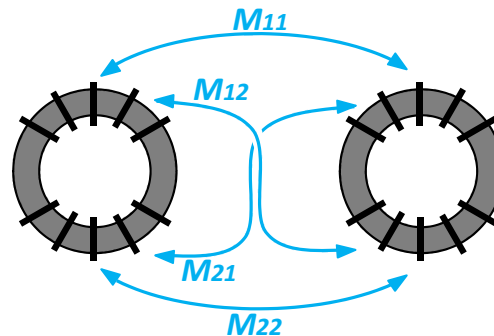


Figure 3.25: Mutual inductances repartition between two CMC

To compare with measurement, the sum of these four mutual inductances must be computed because it is the only one which can be measured. This is a significant drawback because when the two CMCs are not located on their main axes, the mutual inductances are not distributed in an equivalent manner. Therefore, the dissymetry can not be taken into account by measurement. However, by calculation, this distinction can be done. The calculation is then performed one surface at a time and so these four different mutual inductances can be calculated.

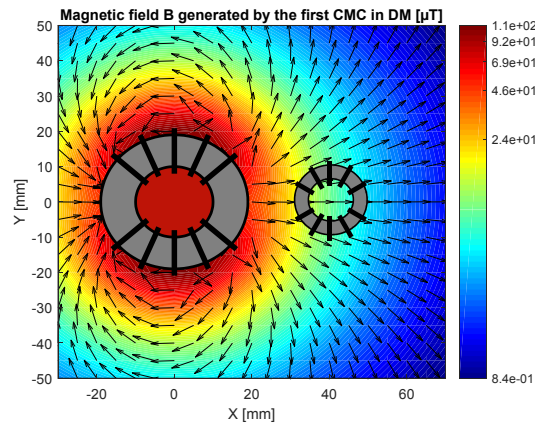


Figure 3.26: Magnetic field generated by the first CMC to the second one

Fig. 3.26 presents the magnetic field generated by the first CMC and the position of the second one. Then, the final result is a ten by ten mutual inductance matrix M_{S_i, S_j} with all the mutual inductances generated by the surface S_i of the first CMC on the surface S_j of the second CMC.

$$M_{11} = \sum_{i=1}^5 \sum_{j=1}^5 M_{S_i, S_j} \quad (3.14)$$

$$M_{12} = \sum_{i=1}^5 \sum_{j=6}^{10} M_{S_i, S_j} \quad (3.15)$$

$$M_{21} = \sum_{i=6}^{10} \sum_{j=1}^5 M_{S_i, S_j} \quad (3.16)$$

$$M_{22} = \sum_{i=6}^{10} \sum_{j=6}^{10} M_{S_i, S_j} \quad (3.17)$$

The mutual inductances $M_{11} = 1.43\mu H$, $M_{12} = 1.24\mu H$, $M_{21} = 1.11\mu H$ and $M_{22} = 1.35\mu H$ are then calculated. A little dissymetry appears and comes from the windings of the CMC which are not totally balanced. Finally, the total mutual inductance, corresponding to the one which can be measured, M_{TOT} can be calculated as in Eq. 3.18.

$$M_{TOT} = M_{11} + M_{12} + M_{21} + M_{22} \quad (3.18)$$

Finally, Fig. 3.27 presents a good agreement between the total mutual inductance measured and the sum of the four mutual inductances calculated. The magnetic coupling is correctly predicted from 100kHz until 1.5MHz because of the uncertainty and the limit of the magnetostatic domain.

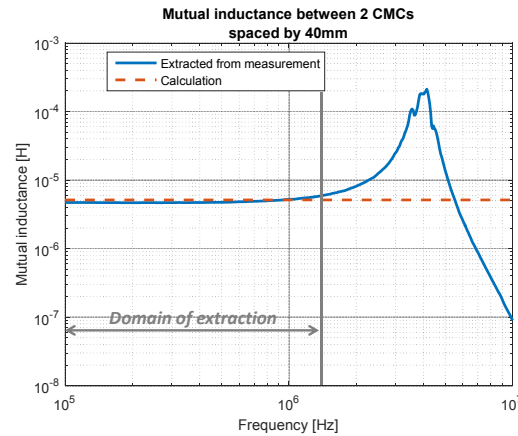


Figure 3.27: Comparison between mutual inductances extracted from measurement and calculation

3.3.4 Conclusion

It was demonstrated here the efficiency of the mutual inductance calculation with Eq. 3.3. The methodology was presented for mutual inductance calculations between two capacitors, two inductors and two CMCs in DM. Other calculations between these passive components are based on the same reasoning and were validated on about sixty mutual inductance measurements.

An analysis of the relative error between mutual inductances calculated and measured was performed in order to validate the methodology.

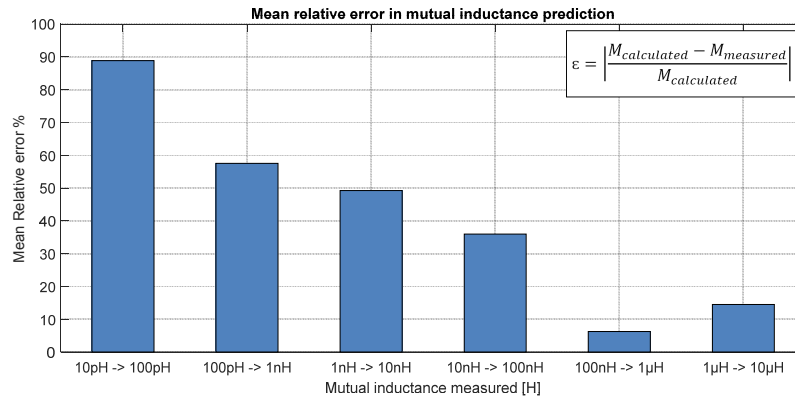


Figure 3.28: Comparison between mutual inductances extracted from measurement and calculation

A point that must be highlighted in this study is the evolution of the relative error between the measured and calculated mutual inductances regarding the magnitude of the mutual inductance. It appears from Fig. 3.28 that, the higher the mutual inductance, the lower the relative error. Therefore, below 1nH of estimated mutual inductance, the relative error would be too high to have confidence on the calculation. Actually, it comes from the uncertainty on the geometry. When the equivalent coupling/emission surfaces are high, or/and the components are very close, a small error on the geometry will not have a high influence on the final results. Actually, a 1nH error on a 1μH inductor will not change the result. However for low equivalent coupling/emission surfaces, or/and

the components are far from each other, the slightest error on the geometry or on the position will have a high influence on the final results.

3.4 Extension of the method to self-inductance prediction

3.4.1 Introduction to the self-inductance prediction

The self-inductance prediction is a key point for equivalent coupling surface estimation when the measurement inside the TEM cell cannot be performed. Actually, it was demonstrated in Sect. 2.6 for inductors and in Sect. 2.7 for CMCs that the permeability of the magnetic material has an influence on their equivalent coupling surface. Actually, the presence of a magnetic material increases those surfaces. Therefore, from TEM cell measurements, there is no need to estimate the self-inductance L_{air} of inductors or CMCs in order to calculate the permeability μ_r (Eq. 3.19) by considering the measured inductance L_{meas} .

$$\mu_r = \frac{L_{meas}}{L_{air}} \quad (3.19)$$

Actually, that value of permeability is directly included in the extracted surface and, therefore, that kind of calculation is not necessary. However, the TEM cell measurements are sometimes impossible to perform, due to a lack of samples for example. Therefore, the estimation of the self-inductance can be mandatory in order to estimate the permeability of the magnetic material and finally the equivalent coupling surface for inductors and CMCs.

Different formulas exist on that topic as it will be presented in the following sections. However, they are often limited and cannot take into account the interaction of both coils for a CMC for example. Therefore, here is presented the methodology we developed for straight and toroidal self-inductance prediction.

3.4.2 Straight coil

A lot of formulas exist in order to determine self-inductance, but the majority of these expressions are valid only under some conditions on dimensions. For example, the best known equation is Eq. 3.20:

$$L = \frac{\mu_0 N^2 S}{l} \quad (3.20)$$

in which L is the self-inductance, $\mu_0 = 4\pi \cdot 10^{-7} H/m$ the permeability of free space, N the number of turns, S the surface of one turn and l the length of the coil (Fig. 3.29). This formula comes from Faraday's law, first introduced in [69], as presented in Eq. 3.21 and Eq. 3.22.

$$emf = L \frac{di}{dt} = N \frac{d\phi}{dt} \implies L \cdot i = N \cdot \phi \quad (3.21)$$

$$\phi = B \cdot S = \mu_0 \cdot H \cdot S = \mu_0 \cdot \frac{NI}{l} \cdot S \quad (3.22)$$

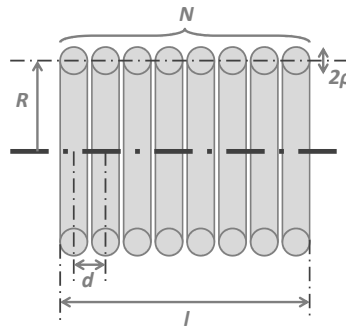


Figure 3.29: Dimensioning parameters for the self-inductance of a straight coil

This equation is very accurate when the solenoid bears a high l/R ratio. However, when this ratio is lower than 1, Eq. 3.20 is no longer valid and other formulas must be used. Indeed, Rayleigh and Niven's formula (Eq. 3.23) is applicable only for short solenoids, when the l/R ratio is low:

$$L = \mu_0 R N^2 \left(\ln\left(\frac{8R}{l}\right) - \frac{1}{2} + \frac{l^2}{32R^2} \left(\ln\left(\frac{8R}{l}\right) - \frac{1}{4} \right) \right) \quad (3.23)$$

Those two equations are just a few examples; there are a lot of other formulas presented in [70]. The main drawback is that the majority of these formulas is based on approximations, or is hard to use because of complexity. However, Eq. 3.24, which is briefly presented in [70] and a little more detailed in [71], computes self-inductance as the sum of the inductances of all turns and all the mutual inductances among turns (Fig. 3.30).

$$L = N.L_T + \sum_{j=1}^{N-1} 2(N-j).M_{1,j+1} \quad (3.24)$$

This formula is considered as very accurate but is generally developed with Maxwell's series which are quite hard to use and time-consuming to establish. In [70], it is concluded that Eq. 3.24 is accurate and convenient when there are only few turns, considering its complexity. The purpose of the following part is to re-use Eq. 3.24 along with the simplified method (Sect. 3.3) to calculate mutual inductances with no limitation on coil dimensions.

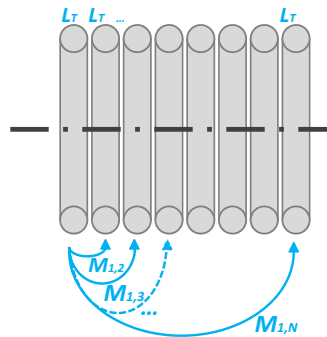


Figure 3.30: Principle of self-inductance calculation

3.4.2.1 Analytical formulation

In order to calculate mutual inductance, the principle presented in Sect. 3.3 will be used. Therefore, the first step in the determination of mutual inductances among all turns consists in computing the magnetic field generated by one turn on another. Indeed, the magnetic field calculation performed using the Biot and Savart law can be resumed as in Sect. 3.2.6.

To simplify the calculation, as the inductor is wound on the x axis, only the x component of the magnetic field can be considered. Therefore, it can be considered that $Y = 0$ and $Z = 0$.

It was demonstrated in Sect. 2.6 that the equivalent coupling surface of a simple loop is basically its physical surface. Moreover, the total value of the magnetic field crossing the surface can be reduced to the one crossing the center of the surface. For better accuracy, the magnetic field can be integrated on the surface but, as presented later, the results are accurate enough without this integration.

Finally, it can be considered that ϕ is going from 0 to 2π in order to cover the whole loop. Eq. 3.25 presents the formula used to calculate the magnetic field generated by a loop:

$$B_{loop,j} = \frac{\mu_0 I R^2}{2.(X_j^2 + R^2)^{3/2}} \quad (3.25)$$

The X_j parameter depends on the distance between the turns of the coil. Therefore, X_j can be expressed as in Eq. 3.26 :

$$X_j = \frac{j.l}{N-1} \quad (3.26)$$

Finally, using Eq. 3.3, mutual inductances can be expressed as follows:

$$M_{1,j+1} = \frac{\mu_0 R^2 S (N-1)^3}{2.((jl)^2 + (R(N-1))^2)^{3/2}} \quad (3.27)$$

Therefore, Eq. 3.27 can be substituted in Eq. 3.24 in order to obtain an expression of the total self-inductance of a straight coil. Indeed, we developed Eq. 3.28 for self-inductance prediction of a straight coil.

$$L = N.L_T + \mu_0 R^2 S (N-1)^3 \sum_{j=1}^{N-1} \frac{N-j}{((jl)^2 + (R(N-1))^2)^{3/2}} \quad (3.28)$$

The last step is to estimate the self-inductance of one turn L_T . As far as the self-inductance of a coil is concerned, there are many formulas, most of which are presented in [72]. The formula developed by G. Kirchhoff in [71] and also presented in [72] is accurate enough for this kind of calculation:

$$L_T = \mu_0 R \left(\ln\left(\frac{8R}{\rho}\right) - 1.75 \right) \quad (3.29)$$

This equation is applicable when the ρ/R ratio is small. Furthermore, the current must be uniformly distributed over the cross section of the ring which implies that frequency must not be too high with respect to loop size. Consequently, all the required parameters in order to determine a self-inductance are now determined. This analytical approach must then be validated by measurements.

3.4.2.2 Validation by measurements

Eq. 3.20, 3.23 and 3.24 (the last one using Eq. 3.28) for the prediction of the self-inductance of a straight coil are going to be compared. To do so, a sample coil can be used with the following properties:

- Radius of one turn: $R = 5.7mm$,
- Number of turns: $N = 10$,
- Wire radius: $\rho = 0.3mm$,
- A parametrical analysis on the length of the coil (varying from $7mm$ to $57mm$) is performed in order to illustrate the validity domain of the different formulas (Fig. 3.31).

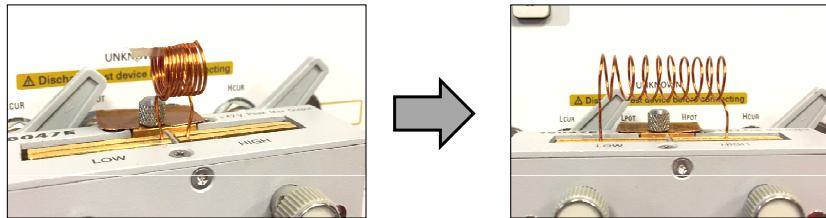


Figure 3.31: Parametrical analysis on self-straight inductance

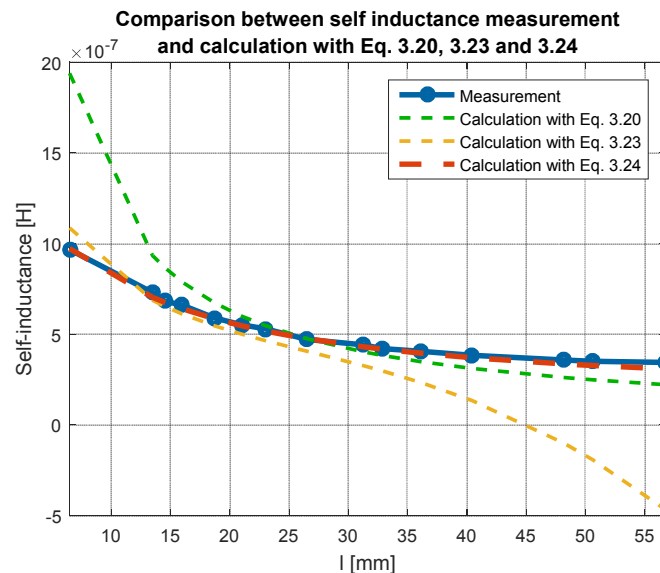


Figure 3.32: Self-inductance prediction for a straight coil

In Fig. 3.32, it appears clearly that Eq. 3.20 is not accurate when the l/R ratio is small. For example, for the smallest coil length, the self-inductance value is overestimated by a factor of 2. However, when the l/R ratio becomes higher, the self-inductance is better predicted but is slightly underestimated.

As far as Eq. 3.23 is concerned, the validity domain is very low because once the l/R ratio exceeds 1; the self-inductance calculation is totally wrong and even becomes negative. For small coil lengths, the self-inductance is predicted quite correctly, but there are still some discrepancies. Finally, the equation we proposed in Eq. 3.24 clearly shows that the method is very accurate, whatever the l/R ratio. Furthermore, this calculation is more accurate than Eq. 3.20 for long coils and more accurate than Eq. 3.23 for short coils. The advantage of that method is that only one equation can be used, which takes into account all the intrinsic parameters of the coil without any limitation on dimensions and turn distribution.

3.4.3 Toroidal coil

The main objective for computing the self-inductance of a toroidal inductor is to predict the leakage inductance of a CMC. Like for straight inductors, different formulas exist for the extraction of the self-inductance of toroidal inductors. It has been presented in [73] that inductance can be calculated from Eq. 3.20 but by considering the associated mean path, with θ the aperture angle of the coil (Fig. 3.33):

$$L = \frac{\mu_0 N^2 S}{l \sqrt{\frac{\theta}{2\pi} + \frac{\sin(\frac{\theta}{2})}{\pi}}} \quad (3.30)$$

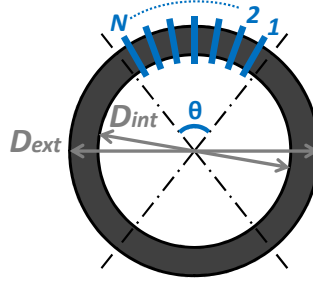


Figure 3.33: Parameters of the self-inductance of a toroidal inductor

However, it is demonstrated in [74] that, when the coil covers less than 40° , the mean path cannot be considered as presented in [73]. Actually, when θ becomes very small, the mean path tends towards zero in Eq. 3.30. Therefore, in [74], a modified mean path is introduced (Eq. 3.31):

$$L = \frac{\mu_0 N^2 S}{\sqrt{\frac{D_{ext}^2}{\sqrt{2}} \left(\frac{\theta}{4} + 1 + \sin\left(\frac{\theta}{2}\right) \right)^2 D_{int}^2 \left(\frac{\theta}{4} - 1 + \sin\left(\frac{\theta}{2}\right) \right)^2}} \quad (3.31)$$

with D_{ext} the external diameter and D_{int} the internal diameter. Those two formulas are described as accurate in [73, 74]: Eq. 3.30 for wide wound coils and Eq. 3.31 for tight wound coils.

A point that must be highlighted with those formulas is that the second coil is not taken into account. Actually, for a CMC, there are two coils and so those two coils must be considered to have the correct results (Fig. 3.34). The internal couplings of one coil have an influence on its self-inductance but the second coil has also an influence on the self-inductance of the first one.

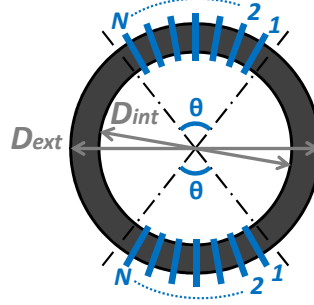


Figure 3.34: Parameters of the self-inductance of a two coils wound on a toroidal core

The purpose of the following section is to use the same principle as for straight inductors (Eq. 3.24) to estimate the self-inductance of a toroidal inductor and compare it to existing formulas.

3.4.3.1 Analytical formulation

In order to calculate self-inductance for toroidal inductors, the inductance of each turn and also the mutual inductances among turns are considered. For the inductance of each turn, Eq. 3.29 is used like for straight coils. For mutual inductance calculation, the magnetic field calculation must be taken into account for x and y components because the windings are in the (x,y) plane. Indeed, we developed Eq. 3.32 and Eq. 3.33:

$$dB_{loop-X_j} = \frac{\mu_0 I}{4\pi} \frac{Y_j \cos\phi - R}{(X_j^2 + Y_j^2 + R^2 - 2RY_j \cos\phi)^{3/2}} d\phi \quad (3.32)$$

$$dB_{loop-Y_j} = \frac{\mu_0 I}{4\pi} \frac{-X_j \cos\phi}{(X_j^2 + Y_j^2 + R^2 - 2RY_j \cos\phi)^{3/2}} d\phi \quad (3.33)$$

with B_{loop-X_j} the x component of the magnetic field, B_{loop-Y_j} the y component of the magnetic field and ϕ going from 0 to 2π in order to cover the whole loop. Parameters X_j and Y_j depend on the distance among turns and, consequently, the radius R of the toroid and also the aperture angle θ . Then, Eq. 3.34 and Eq. 3.35 are considered.

$$X_j = R \sin\left(\frac{j\theta}{N-1}\right) \quad (3.34)$$

$$Y_j = R \left(1 - \cos\left(\frac{j\theta}{N-1}\right)\right) \quad (3.35)$$

Finally, by applying Eq. 3.24 and considering the parameters presented in Eq. 3.32 to Eq. 3.35, it is possible to calculate the self-inductance of the toroidal inductor.

3.4.3.2 Validation by measurements

Eq. 3.30, 3.31 and 3.24 (the last one using Eq. 3.32 to Eq. 3.35) for the prediction of the self-inductance of a toroidal coil are going to be compared. To do so, a sample coil can be used with the following properties:

- External diameter: $D_{ext} = 39.5mm$,

- Internal diameter: $D_{int} = 23.1mm$,
- Wire radius: $\rho = 0.3mm$,

A parametrical analysis on the aperture angle of the coil (from 15° to 180°) and while the number of turns N goes from 3 to 20 turns, is performed (Fig. 3.35).

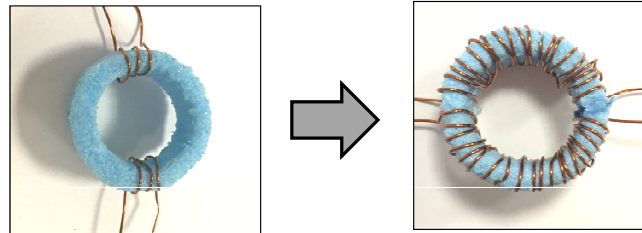


Figure 3.35: Parametrical analysis on self-toroidal inductance

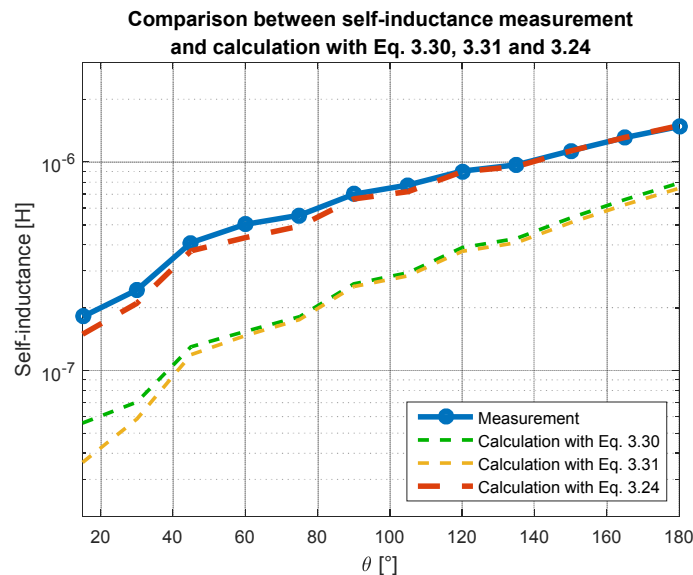


Figure 3.36: Self-inductance prediction for a toroidal coil

Fig. 3.36 clearly shows that Eq. 3.30 and Eq. 3.31 are not accurate enough to predict the self-inductance of a toroidal coil. Furthermore, the difference between both formulas for an aperture angle less than 40° is barely visible. However, Fig. 3.36 demonstrates again the accuracy of Eq. 3.24. The self-inductance is correctly predicted whatever the number of turns or the aperture angle.

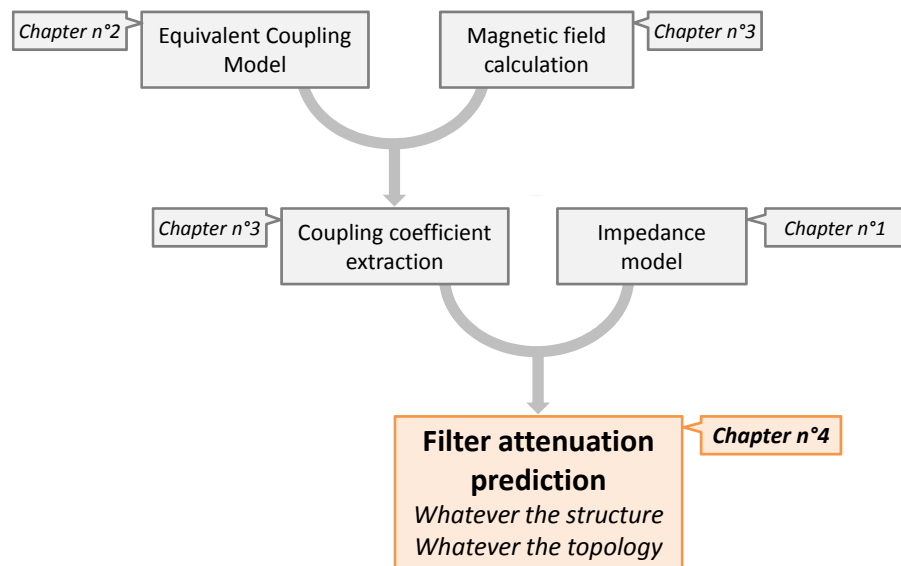
3.5 Conclusion

The mutual inductance calculation is divided into two main steps. The first step, dedicated to the equivalent coupling model, was presented in Chapter 2. The second step was dedicated to

the magnetic field calculation. This kind of calculation can be performed thanks to the equivalent coupling model that is the equivalent emission model (reciprocity principle). Furthermore, as the calculation is performed only for low frequency (magnetostatic domain), the Biot and Savart law can be used for the magnetic field calculation. Then, using those two main steps, the mutual inductance calculation could be achieved and was validated with measurement. Another study that comes from the mutual inductance estimation, is the self-inductance calculation for straight and toroidal inductors. Actually, a lot of formulas exist on this topic. Therefore, a generalization of the self-inductance calculation was developed and validated, without any limit on coil dimensions.

Chapter 4

Prediction of the filter attenuation considering inter-component coupling



4.1 Introduction to the prediction of the filter attenuation considering inter-components coupling

The last step of the methodology is then to bring together the first three chapters that contain the impedance model of passive components, their equivalent coupling models, the magnetic fields that they can generate and finally the magnetic coupling that can exist between them. Therefore, using all those thematics, the objective here is to predict a filter attenuation considering the relative position of the components. As it is presented in the first chapter, there exist a lot of different filter structures and, therefore, a generic approach for filter attenuation calculation must be developed.

To do so, a first part dedicated to the Modified Kron's method applied to EMC (MKME) and its advantages are presented. It goes through the graph construction, the definition of tensors and matrices and finally the resolution. Then, the work performed on the generic Kron's graph development is presented, and for the particular case of filter design. Finally, the whole methodology is illustrated through real world applications.

4.2 Modified Kron's Method applied to EMC (MKME)

The Modified Kron's Method applied to EMC is an appropriate methodology to work on filter design. Actually, this methodology is based on tensorial analysis of networks [75, 76, 77, 78] and is applicable to any system regardless its complexity.

The choice here is to use a modal analysis, instead of a nodal analysis like in SPICE simulation, which is very practical in terms of speed of calculation and generic structure [29]. Furthermore, matrices and tensors are reduced for a modal analysis compared to a nodal analysis. Therefore, calculations are much faster, which is even more visible in a structure that includes hundreds of mutual inductances. It must also be noticed that all the methodology is capitalized in a unique generic tool and, therefore, speed of calculation and generic structure are mandatory.

Another advantage of the MKME is that the intrinsic parameters and the modifiable parameters are clearly separated. For the particular case of filter design considering the inter-components coupling, the intrinsic parameters are the components: their models considering their parasitic elements and the modifiable parameters are the mutual inductances between the components.

4.2.1 Graph construction

A graph is a set of nodes, edges, meshes, chords and networks [28, 26, 27, 79]. The graph (Fig. 4.1) is based on the electrical circuit of the studied system:

- A node is the intersection among two or more edges,
- An edge is a path between two nodes,
- A mesh is a closed path integrating further edges,
- A chord makes the link between two different edges,
- A network is a set of linked nodes, edges and meshes.

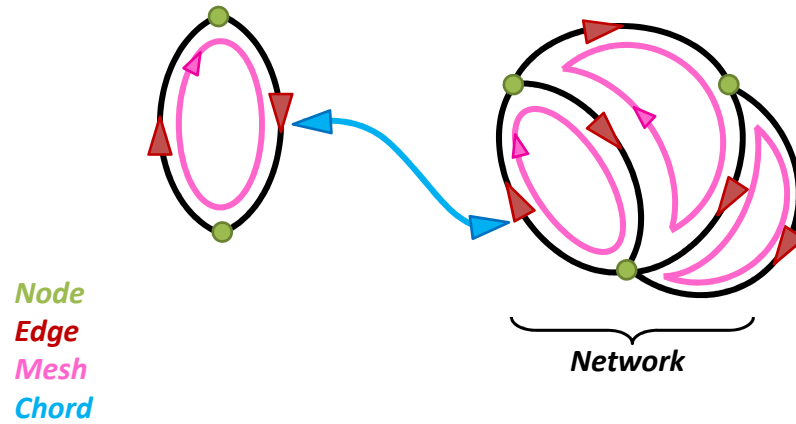


Figure 4.1: Graph example

In concrete terms, in order to better understand these terms, a parallel can be drawn between a SPICE simulation and the MKME. Creating a resistance on a SPICE schematic is the same as defining an edge with the MKME. The creation of a coupling coefficient between two inductors is the same as describing a chord, a coupling interaction with the MKME.

The advantage with a graph is that all the links and the interactions appear clearly. This way it is easy to understand the interactions, the flux and how they interfere together. The mesh notion is quite more abstract but very practical in terms of calculation. Actually, in the mesh space, only the mesh currents are calculated and all the tensors are reduced compared to a nodal analysis.

Actually, there are as many spaces as there are types of element in a graph. There are the node space, the edge space etc. and the objective here is to describe the filter in the edge space and transform it to the mesh space to perform the calculation. This way, the description is simple, thanks to the edge space, and the calculation is practical, thanks to the mesh space. Finally, the system is transformed again to the edge space to interpret the results.

Each element building up a Kron graph, has its own number to distinguish each node, edge etc. To construct a graph, the nodes are defined one by one as intersections (Fig. 4.2).

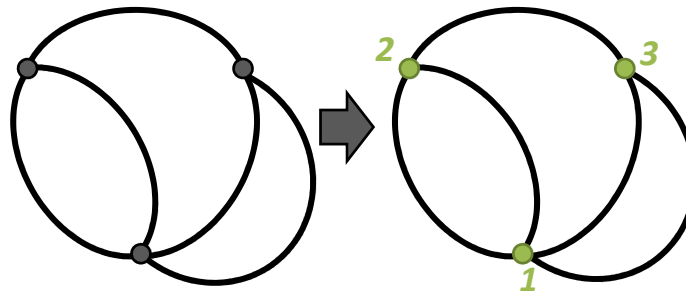


Figure 4.2: Nodes description

The second step is to link all the nodes through paths that are called edges (Fig. 4.3).

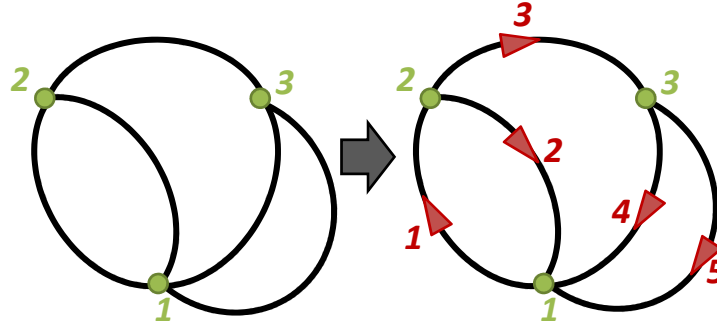


Figure 4.3: Edges description

The next step is dedicated to meshes description. To do so, the required and sufficient number of meshes to describe the graph must be determined. Thus, Eq. 4.1 from [28], is applied considering that N_{nodes} is the number of nodes, N_{edges} is the number of edges, $N_{networks}$ the number of networks and N_{meshes} the number of meshes.

$$N_{meshes} = N_{edges} - N_{nodes} + N_{networks} \quad (4.1)$$

Indeed, it gives a number of meshes $N_{meshes} = 3$ to describe the entire graph. The meshes must describe all edges and ideally they should not be superimposed (Fig. 4.4). The superposition can be problematic particularly for CM attenuation calculation if the ground connection is not correctly taken into account as it will be presented in Sect. 4.3.6.2.

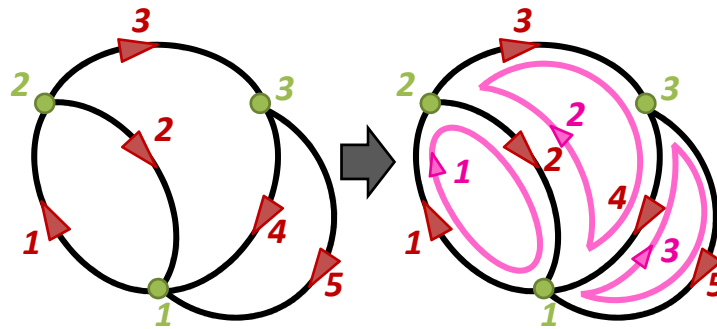


Figure 4.4: Meshes description

Finally the graph is completed by the chords, if there are. For example, a chord between the edges n°3 and n°5 can be considered in the final graph (Fig. 4.5).

The main advantage of that chord definition is that the coupling can be defined as a magnetic coupling, a capacitive coupling or even a radiated near field or far field coupling.

The next step is to build all the matrices that can described the entire graph.

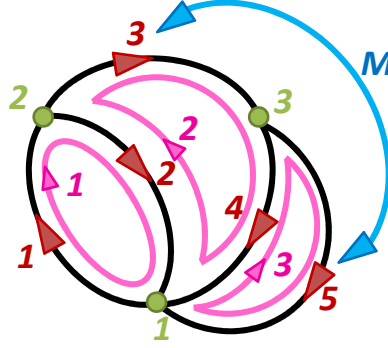


Figure 4.5: Complete graph

4.2.2 Calculation of tensors and matrices

The goal is now to build tensors and matrices to express mathematically the entire graph as in Fig. 4.5. Actually, the graph must be rebuilt from all tensors and matrices and inversely. The first step is to define the impedance tensor in the edge space that describes the impedance of each edge. Let us take the example of Fig. 4.5 and consider that each edge numbered i is weighted by its own impedance Z_i . Indeed, $Z_{intrinsic_E}$ is the tensor including all the intrinsic impedances in the edge space.

$$Z_{intrinsic_E} = \text{mat}(\text{diag}(Z_i)) = \begin{pmatrix} Z_1 & 0 & 0 & 0 & 0 \\ 0 & Z_2 & 0 & 0 & 0 \\ 0 & 0 & Z_3 & 0 & 0 \\ 0 & 0 & 0 & Z_4 & 0 \\ 0 & 0 & 0 & 0 & Z_5 \end{pmatrix} \quad (4.2)$$

It must be noticed that the intrinsic impedances are located on the diagonal because these parameters are only part of their associated edges. Conversely, the coupling tensor integrates the links between edges. This tensor $Z_{coupling_E}$ is the one regrouping the modifiable parameters. In the present case, with the goal of studying inter-component couplings, $Z_{coupling_E}$ will integrate the mutual impedances that exist between edges. For example, the coupling tensor related to the graph in Fig. 4.5 must represent the link between edges n°3 and n°5 and is bidirectional. This link is a mutual inductance M and so the coupling impedance can be expressed as $Z_M = M.p$, where p is the complex variable from the Laplace transform with $p = j\omega = j2\pi f$ considering f the frequency and ω the pulsation.

$$Z_{coupling_E} = \begin{pmatrix} 0 & 0 & 0 & 0 & 0 \\ 0 & 0 & 0 & 0 & 0 \\ 0 & 0 & 0 & 0 & Z_M \\ 0 & 0 & 0 & 0 & 0 \\ 0 & 0 & Z_M & 0 & 0 \end{pmatrix} \quad (4.3)$$

Finally, these two tensors are summed to represent the total impedance network of the system. This tensor is named Z_E : the impedance tensor in the edge space.

$$Z_E = Z_{intrinsic_E} + Z_{coupling_E} \quad (4.4)$$

The following step is to define E_E , the source tensor in the edge space. Sources are located on edges, indeed the source tensor has as many elements as edges (in the edge space). The considered source E can be by default located on the first edge and is an AC source voltage so that $E = 2V$, for attenuation calculation (Sect. 1.3.1.1).

$$E_E = \begin{pmatrix} E \\ 0 \\ 0 \\ 0 \\ 0 \end{pmatrix} \quad (4.5)$$

Now that the impedance and the source tensors are defined, the link between the edge space and the mesh space must be defined. The connectivity matrix $C_{E \rightarrow M}$ fulfills this role by having as many rows as edges and as many columns as meshes. The idea is to specify through that matrix, which edge is part of which mesh. To build this matrix, let's take the example of Fig. 4.5, the first edge is part only of the first mesh, so that the first line of the connectivity matrix is $C_{E \rightarrow M}(1, :) = \begin{pmatrix} 1 & 0 & 0 \end{pmatrix}$. The second edge is part of the first and the second mesh, so that the second line of the connectivity matrix $C_{E \rightarrow M}(2, :) = \begin{pmatrix} 1 & 1 & 0 \end{pmatrix}$ etc. Step by step, considering all edges and all meshes, the connectivity matrix can be built as presented in Eq. 4.6.

$$C_{E \rightarrow M} = \begin{pmatrix} 1 & 0 & 0 \\ 1 & 1 & 0 \\ 0 & 1 & 0 \\ 0 & 1 & 1 \\ 0 & 0 & 1 \end{pmatrix} \quad (4.6)$$

With all those tensors and matrices, it is possible to rebuild the entire graph. Then, the objective is to transform all the tensors to the mesh space to calculate the mesh currents to finally go back to the edge space in order to interpret the results.

4.2.3 Resolution

The objective, in order to calculate the mesh currents, is to transform all the tensors describing the graph in the edge space to the mesh space.

The tensor Z_M can be expressed in the mesh space as follows, considering that $C_{E \rightarrow M}^T$ is the transposed connectivity.

$$Z_M = C_{E \rightarrow M}^T \cdot Z_E \cdot C_{E \rightarrow M} \quad (4.7)$$

Another possibility is to build directly the impedance tensor Z_M in the mesh space. This way, the calculation is even more direct and the first transformation is not necessary. In order to build directly the impedance tensor in the mesh space, it must be noticed that the elements on the diagonal are the ones related to the own impedance of the mesh. For example, the first mesh is only composed of Z_1 and Z_2 and so $Z_M(1, 1) = Z_1 + Z_2$. However, for the extra-diagonal elements, it regroups the common impedance of the two meshes. For instance, the element $Z_M(1, 2)$ which

regroups the common impedances between meshes n°1 and n°2 is only composed of Z_2 . Finally, Eq. 4.8 presents the impedance tensor in the mesh space for the example Fig. 4.5.

$$Z_M = \begin{pmatrix} Z_1 + Z_2 & Z_2 & 0 \\ Z_2 & Z_2 + Z_3 + Z_4 & Z_4 + Z_M \\ 0 & Z_4 + Z_M & Z_4 + Z_5 \end{pmatrix} \quad (4.8)$$

In the same way, the source tensor in the mesh space E_M can be calculated as:

$$E_M = C_{E \rightarrow M}^T \cdot E_E \quad (4.9)$$

Finally, by inverting the mesh impedance tensor Z_M , it is possible to calculate the mesh currents I_M . It must be noticed that this modal analysis is convenient to use because in the mesh space, only the mesh currents are calculated.

$$I_M = (\text{inv}(Z_M) \cdot E_M)^T \quad (4.10)$$

The calculation is direct and allows to extract the voltage at any edge. Each edge voltage can be calculated as in Eq. 4.11, considering that I_M^T is the transposed mesh current.

$$V_E(i) = Z_E(i, i) \cdot C_{E \rightarrow M}(i, :) \cdot I_M^T \quad (4.11)$$

Thanks to the Kron's method, the attenuation calculation is simplified. Furthermore, the objective is to predict a filter attenuation, taking into account the magnetic coupling, whatever the filter structure. Indeed, the reasoning to build a generic graph and all its associated tensors and matrices will be described in the following section.

4.3 Generic Kron's graph development

This reasoning will be illustrated by the construction of a Kron's graph with the filter presented in Fig. 4.6, composed of a DM capacitor, a CMC and two CM capacitors.

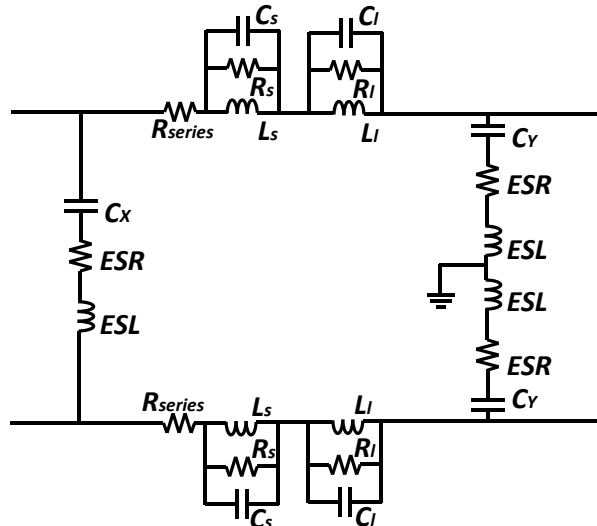


Figure 4.6: Filter example for generic Kron's graph definition

4.3.1 Global parameters

First of all, the global parameters fixed by the user present the given latitude on the filter structure. These parameters are determined to be sufficient in the description and not to overcome the user. Some parameters are essential, such as:

- The number of components building up the filter. This first parameter gives an important information: the complexity of the structure and also the dimension of all tensors and matrices.
- The type of components: inductor, capacitor or CMC. It includes their equivalent electrical circuit and their parasitic elements (Sect. 1.4). This parameter gives the possibility to build all edges.
- Components connections. Using this information, the link between nodes and edges can be determined.
- The magnetic coupling between each component pair, calculated thanks to the methodology presented in Chapter 3.

With those four parameters, it is possible to build the associated graph, the calculation tensors and matrices and finally predict the filter attenuation.

4.3.2 Determination of the number of nodes

As presented in Sect. 1.2, there are two different modes: the differential mode and the common mode.

The first step is then to determine all the number of nodes for all types of elements. Actually, the number of nodes coming from the components or the source is the same in CM or DM, as presented in Fig. 4.7.

It must be noticed that for the capacitor, only one node is defined. Actually, the objective is to have the smallest tensors and matrices, for easier and faster calculations. Therefore, for the case of the capacitor, only the parasitic inductance must be isolated on its own edge (in order to define the magnetic coupling).

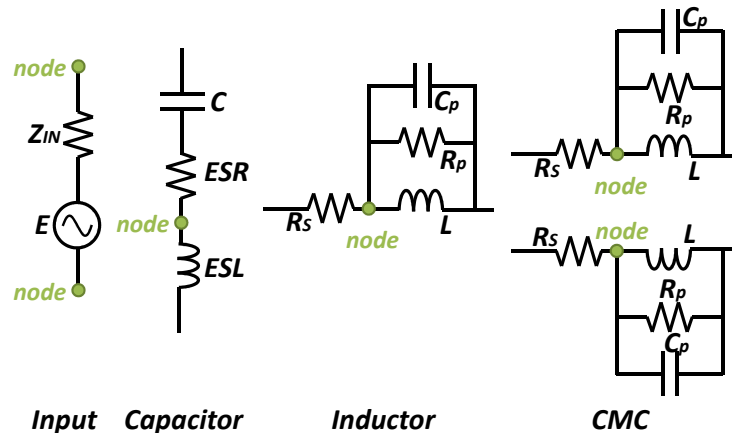


Figure 4.7: Number of nodes description

The source, the components (considering their entire electrical models) and the output are all considered as elements. Therefore, an element in series can be an inductor or a CMC, and an element in parallel is a DM or CM capacitor.

As far as the number of nodes coming from the connections and the output are concerned, those depend on the mode.

4.3.2.1 Number of nodes in DM

The algorithm, in order to determine the number of nodes coming from the connection and from the output, is based on the following reasoning (Fig. 4.8):

- There is one less node than elements in series.
- If there is at least one element in series, there is a node at the output.
- If there is a CMC, an additional node is added.
- For the CM capacitor, an additional node is defined between both capacitors.

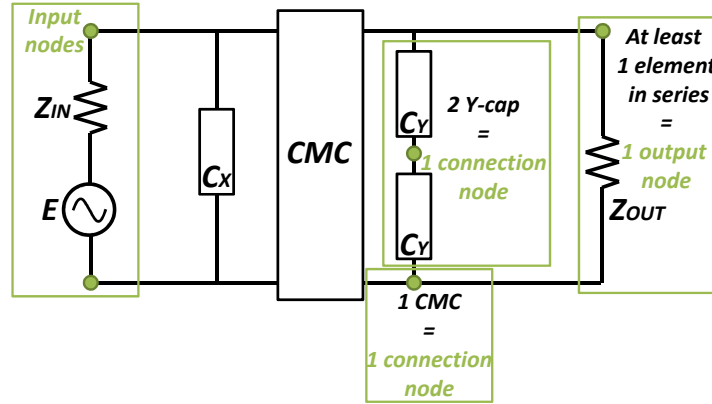


Figure 4.8: Number of nodes in DM

Finally the total number of nodes can be assumed as:

$$N_{nodes} = N_{nodes_{input}} + N_{nodes_{components}} + N_{nodes_{connections}} + N_{nodes_{output}} \quad (4.12)$$

For the example of Fig. 4.6, it gives a DM number of nodes $N_{nodes} = 10$ and is validated with Fig. 4.9.

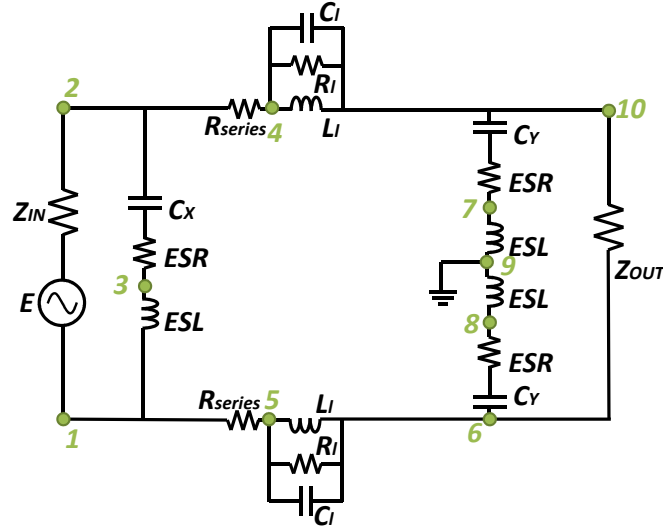


Figure 4.9: Nodes in DM

4.3.2.2 Number of nodes in CM

For the CM, the algorithm is based on the following reasoning (Fig. 4.10):

- If there is at least one element in series, there is a node at the output.
- There are two nodes per CMC, starting from the second CMC.
- There are two nodes per pair of inductors, starting from the second pair of inductors.
- The DM capacitors are not taken into account because they are shorted in CM.
- For CM capacitors, no connection nodes are taken into account because they are connected to the ground and this node is already defined with the source.

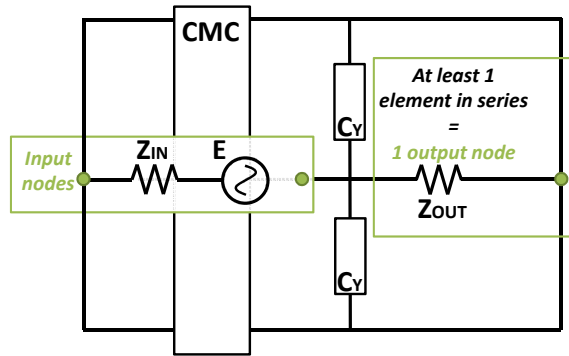


Figure 4.10: Number of nodes in CM

Finally, as for DM, Eq. 4.12 can be used for the calculation of the total number of nodes.

For the example of Fig. 4.6, it gives a CM number of nodes $N_{nodes} = 7$ and is validated with Fig. 4.11.

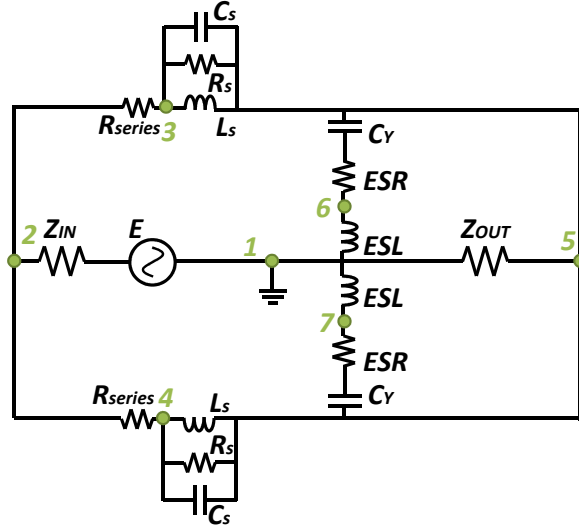


Figure 4.11: Nodes in CM

4.3.3 Determination of the number of edges

For the number of edges, there is no difference between DM and CM (except that DM capacitors are not taken into account in CM). The number of edges only depends on the source, the output and the components, as seen in Fig. 4.12.

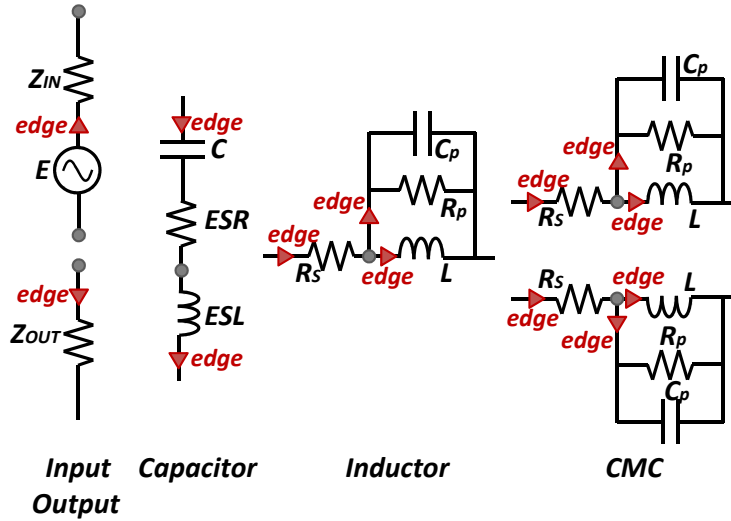


Figure 4.12: Number of edges

As mentioned in the previous subsection, the objective is to isolate each inductance on its own edge and reduce as much as possible the other edges. For instance, for an inductor, the parasitic

parallel resistance and capacitance are on the same edge. Finally, the capacitor is composed of two edges, the inductor of three and the CMC of six edges.

As for the number of nodes, the total number of edges can be expressed as the sum of all the nodes as in Eq. 4.13.

$$N_{edges} = N_{edges_{input}} + N_{edges_{output}} + N_{edges_{components}} \quad (4.13)$$

In order to validate this reasoning, it can be calculated with Eq. 4.13 that $N_{edges} = 14$ for DM and validated with Fig. 4.13 -a. $N_{edges} = 14$ for CM and validated with Fig. 4.13 -b.

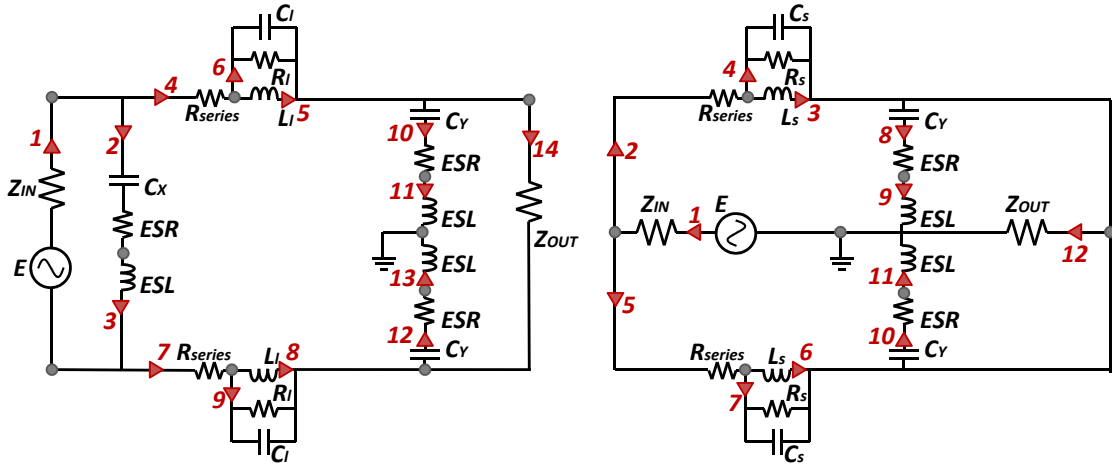


Figure 4.13: Edge definition a- in DM b- in CM

4.3.4 Definition of the impedance tensor

The definition of the impedance tensor is divided into two steps, the first one is dedicated to the intrinsic impedance of each edge (the intrinsic impedance tensor) and the second one dedicated to the integration of all the mutual inductances (the coupling tensor).

4.3.4.1 Intrinsic impedance tensor

This step is direct because everything is already defined. Step by step, $Z_{i-E_{DM}}$ for DM and $Z_{i-E_{CM}}$ for CM are fulfilled by the edge impedances described in Sect. 4.3.3. These two tensors directly come from the determination of edges presented in the previous section (Eq. 4.2). For DM, there are 14 edges, indeed $Z_{i-E_{DM}}$ is a 14 by 14 diagonal tensor in the edge space.

$$\begin{aligned} Z_{i-E_{DM}} = \text{mat}(\text{diag}(& Z_{IN} \quad \frac{1}{C_{X.p}} + ESR \quad ESL.p \quad R_{series} \quad L_l.p \quad \dots \\ & \dots \quad \frac{R_l}{1+R_l C_l.p} \quad R_{series} \quad L_l.p \quad \frac{R_l}{1+R_l C_l.p} \quad \frac{1}{C_{Y.p}} + ESR \quad \dots \\ & \dots \quad ESL.p \quad \frac{1}{C_{Y.p}} + ESR \quad ESL.p \quad Z_{OUT} \quad)) \end{aligned}$$

For CM, it is the same principle as for DM, the graph is followed and $Z_{i-E_{CM}}$ is a 12 by 12 tensor because there are 12 edges in CM.

$$\begin{aligned}
 Z_{i-ECM} = \text{mat}(\text{diag}(& Z_{IN} \quad R_{series} \quad L_s \cdot p \quad \dots \\
 \dots \quad \frac{R_s}{1+R_s C_s \cdot p} \quad & R_{series} \quad L_s \cdot p \quad \frac{R_s}{1+R_s C_s \cdot p} \quad \frac{1}{C_Y \cdot p} + ESR \quad \dots \\
 \dots \quad ESL \cdot p \quad \frac{1}{C_Y \cdot p} + ESR \quad & ESL \cdot p \quad Z_{OUT} \quad))
 \end{aligned}$$

4.3.4.2 Coupling tensor

The coupling tensor comes from all the mutual inductances calculated with the methodology presented in Chapter 3.

The DM coupling tensor Z_{c-EDM} has the same dimension as the intrinsic impedance tensor and so is a 14 by 14 tensor. There are 5 inductances and, consequently, 10 mutual inductances in Z_{c-EDM} . Those mutual inductances are called $M_{i,j}$ with i and j the edge position of each inductance ($i \neq j$).

Let us take the example of the mutual inductance between the parasitic inductance of the DM capacitor and the first leakage inductance of the CMC. These two elements are located on edges n°3 and n°5 respectively. Indeed, $Z_{c-EDM}(3,5) = M_{3,5} \cdot p$ and $Z_{c-EDM}(5,3) = M_{5,3} \cdot p$. As demonstrated in Sect. 3.2.2 it can be noticed that $M_{i,j} = M_{j,i}$ with $i \neq j$ and, therefore, the coupling tensor in the edge space is symmetrical. It must also be noticed that the mutual inductance between the two leakage inductance is fixed and so it can be concluded that $Z_{c-EDM}(5,8) = Z_{c-EDM}(8,5) = -L_l \cdot p$ (according to Sect. 1.4.4). Finally, by doing this reasoning for all the mutual inductances, Z_{c-EDM} can be built.

$$\begin{aligned}
 Z_{c-EDM} &= \dots \\
 \dots & \left(\begin{array}{cccccccccccccccc}
 0 & 0 & 0 & 0 & 0 & 0 & 0 & 0 & 0 & 0 & 0 & 0 & 0 & 0 \\
 0 & 0 & 0 & 0 & 0 & 0 & 0 & 0 & 0 & 0 & 0 & 0 & 0 & 0 \\
 0 & 0 & 0 & 0 & M_{3,5} & 0 & 0 & M_{3,8} & 0 & 0 & M_{3,11} & 0 & M_{3,13} & 0 \\
 0 & 0 & 0 & 0 & 0 & 0 & 0 & 0 & 0 & 0 & 0 & 0 & 0 & 0 \\
 0 & 0 & M_{5,3} & 0 & 0 & 0 & 0 & M_{5,8} & 0 & 0 & M_{5,11} & 0 & M_{5,13} & 0 \\
 0 & 0 & 0 & 0 & 0 & 0 & 0 & 0 & 0 & 0 & 0 & 0 & 0 & 0 \\
 0 & 0 & 0 & 0 & 0 & 0 & 0 & 0 & 0 & 0 & 0 & 0 & 0 & 0 \\
 0 & 0 & M_{8,3} & 0 & M_{8,5} & 0 & 0 & 0 & 0 & 0 & M_{8,11} & 0 & M_{8,13} & 0 \\
 0 & 0 & 0 & 0 & 0 & 0 & 0 & 0 & 0 & 0 & 0 & 0 & 0 & 0 \\
 0 & 0 & 0 & 0 & 0 & 0 & 0 & 0 & 0 & 0 & 0 & 0 & 0 & 0 \\
 0 & 0 & M_{11,3} & 0 & M_{11,5} & 0 & 0 & M_{11,8} & 0 & 0 & 0 & 0 & M_{11,13} & 0 \\
 0 & 0 & 0 & 0 & 0 & 0 & 0 & 0 & 0 & 0 & 0 & 0 & 0 & 0 \\
 0 & 0 & M_{13,3} & 0 & M_{13,5} & 0 & 0 & M_{13,8} & 0 & 0 & M_{13,11} & 0 & 0 & 0 \\
 0 & 0 & 0 & 0 & 0 & 0 & 0 & 0 & 0 & 0 & 0 & 0 & 0 & 0
 \end{array} \right) \cdot p
 \end{aligned}$$

For CM, it is the same principle but this time, there are 4 inductances and so 6 mutual inductances. It must be noticed that, as presented in Sect. 2.7, the CMC in CM cannot couple the magnetic field. This way all couplings with the CMC, $M_{3,9} = M_{9,3}$, $M_{3,11} = M_{11,3}$, $M_{6,9} = M_{9,6}$ and $M_{6,11} = M_{11,6}$ are equal to zero. Furthermore, $M_{3,6} = M_{6,3} = L_s$ because the coupling

coefficient between the two windings of the CMC in CM is +1. Finally, $M_{9,11} = M_{11,9}$, the mutual inductance between the two CM capacitors, remains.

$$Z_{C-ECM} = \begin{pmatrix} 0 & 0 & 0 & 0 & 0 & 0 & 0 & 0 & 0 & 0 & 0 & 0 \\ 0 & 0 & 0 & 0 & 0 & 0 & 0 & 0 & 0 & 0 & 0 & 0 \\ 0 & 0 & 0 & 0 & 0 & M_{3,6} & 0 & 0 & 0 & 0 & 0 & 0 \\ 0 & 0 & 0 & 0 & 0 & 0 & 0 & 0 & 0 & 0 & 0 & 0 \\ 0 & 0 & 0 & 0 & 0 & 0 & 0 & 0 & 0 & 0 & 0 & 0 \\ 0 & 0 & M_{6,3} & 0 & 0 & 0 & 0 & 0 & 0 & 0 & 0 & 0 \\ 0 & 0 & 0 & 0 & 0 & 0 & 0 & 0 & 0 & 0 & 0 & 0 \\ 0 & 0 & 0 & 0 & 0 & 0 & 0 & 0 & 0 & 0 & 0 & 0 \\ 0 & 0 & 0 & 0 & 0 & 0 & 0 & 0 & 0 & 0 & M_{9,11} & 0 \\ 0 & 0 & 0 & 0 & 0 & 0 & 0 & 0 & 0 & 0 & 0 & 0 \\ 0 & 0 & 0 & 0 & 0 & 0 & 0 & 0 & M_{11,9} & 0 & 0 & 0 \\ 0 & 0 & 0 & 0 & 0 & 0 & 0 & 0 & 0 & 0 & 0 & 0 \end{pmatrix} \cdot p$$

4.3.5 Definition of the source tensor

The definition of the source tensor is quite simple. Here, the source edge is fixed at the first edge. Consequently, the source tensor has a unique column and has as many rows as edges with $E = 2V$ located at the first elements and all others equal to zero. This way, E_{EDM} has 14 elements and E_{ECM} contains 12 elements as presented in Eq. 4.14.

$$E_{EDM} = \begin{pmatrix} E \\ 0 \\ 0 \\ 0 \\ 0 \\ 0 \\ 0 \\ 0 \\ 0 \\ 0 \\ 0 \\ 0 \\ 0 \\ 0 \end{pmatrix} / E_{ECM} = \begin{pmatrix} E \\ 0 \\ 0 \\ 0 \\ 0 \\ 0 \\ 0 \\ 0 \\ 0 \\ 0 \\ 0 \\ 0 \end{pmatrix} \quad (4.14)$$

4.3.6 Definition of the connectivity matrix: the transfer matrix between the edge and the mesh space

In the same way as for tensors description, the connectivity matrix depends on the mode. The first step is then to determine the sufficient number of meshes in order to describe the graph, according to Eq. 4.1. The developed methodology is based into two main steps: the first one is dedicated to the assignment of the mesh and the second one to the construction of the connectivity matrix. The two algorithms that are introduced for DM and CM present the mesh assignment by considering M_i as the main mesh #i and M'_i as the secondary mesh #i. A secondary mesh is a mesh that

comes from the equivalent electrical model of components and not from the filter structure. Indeed, by considering those secondary meshes, all main meshes follow one another.

Those reasonings are generic enough to give the possibility to build a graph for any structure and then to calculate an attenuation for all types of passive filters.

4.3.6.1 Determination of meshes and connectivity matrix in DM

According to Eq. 4.1, the number a meshes for DM is $N_{meshes_{DM}} = 5$. Depending on the components and the connection, the reasoning is:

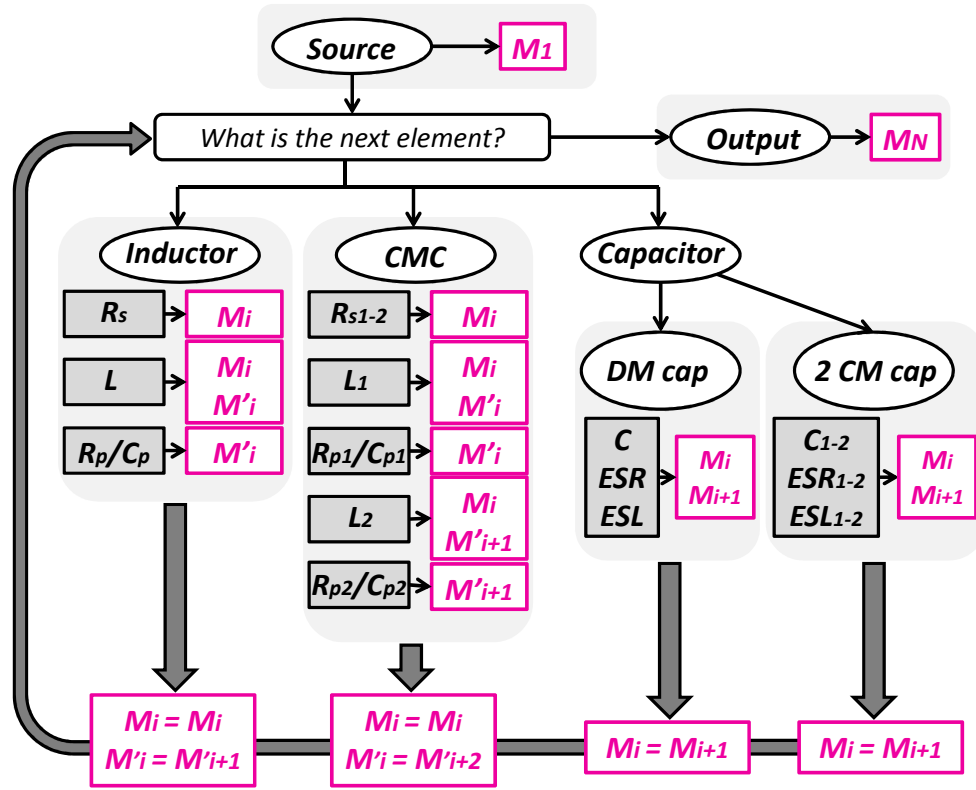


Figure 4.14: Algorithm to determine DM meshes

Fig. 4.14 presents the algorithm in order to determine the relation among all edges and meshes in DM. It can be illustrated with Fig. 4.15 that presents the DM meshes definition for the filter example of Fig. 4.6.

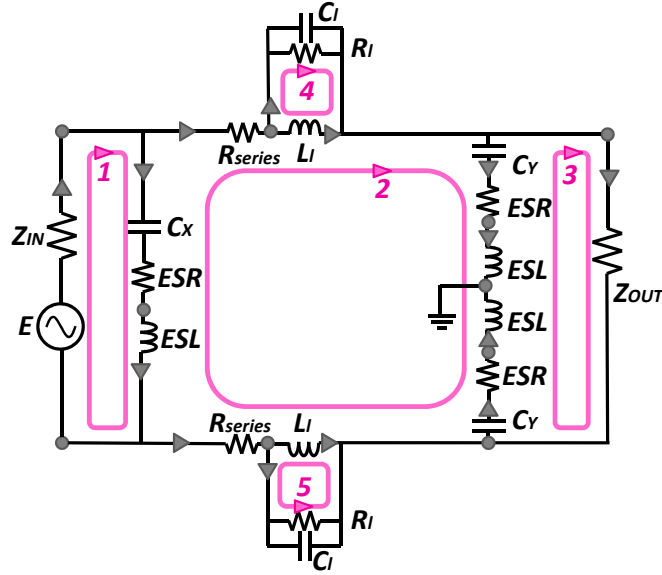


Figure 4.15: Meshes definition in DM

Finally, all that remains is to build the associated connectivity matrix such as presented in Eq. 4.15. Lines refer to edges and columns to meshes.

$$C_{E \rightarrow M_{DM}} = \begin{pmatrix} 1 & 0 & 0 & 0 & 0 \\ 1 & 1 & 0 & 0 & 0 \\ 1 & 1 & 0 & 0 & 0 \\ 0 & 1 & 0 & 0 & 0 \\ 0 & 1 & 0 & 1 & 0 \\ 0 & 0 & 0 & 1 & 0 \\ 0 & 1 & 0 & 0 & 0 \\ 0 & 1 & 0 & 0 & 1 \\ 0 & 0 & 0 & 0 & 1 \\ 0 & 1 & 1 & 0 & 0 \\ 0 & 1 & 1 & 0 & 0 \\ 0 & 1 & 1 & 0 & 0 \\ 0 & 1 & 1 & 0 & 0 \\ 0 & 0 & 1 & 0 & 0 \end{pmatrix} \quad (4.15)$$

4.3.6.2 Determination of meshes and connectivity matrix in CM

As for DM, the first step is to calculate $N_{meshes_{CM}}$ the sufficient number of meshes to describe the CM graph, which gives $N_{meshes_{CM}} = 6$. The methodology is also based on the assignment of meshes.

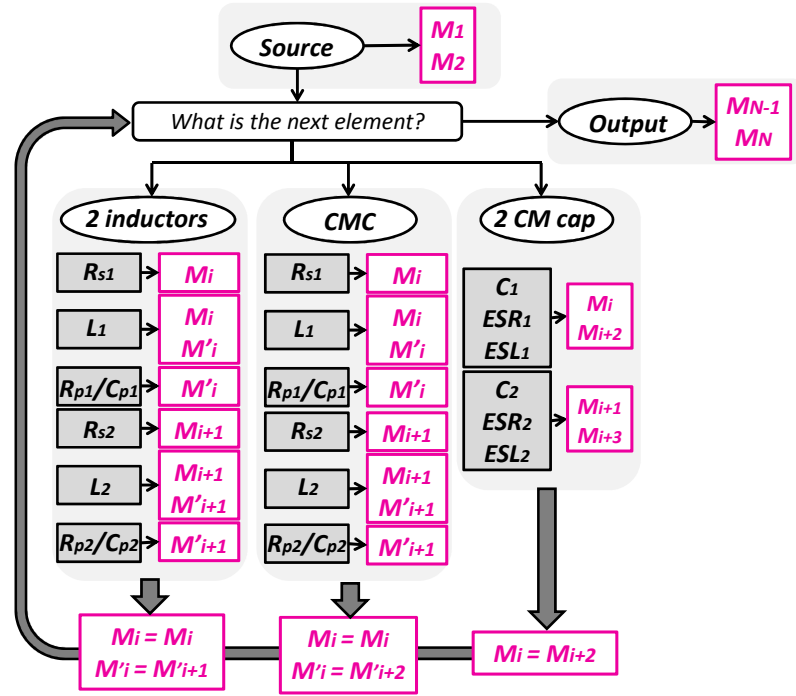


Figure 4.16: Algorithm to determine CM meshes

Likewise, Fig. 4.16 presents the algorithm in order to determine the relation among all edges and meshes in CM. It can be illustrated with Fig. 4.17 that presents the CM meshes definition for the filter example of Fig. 4.6.

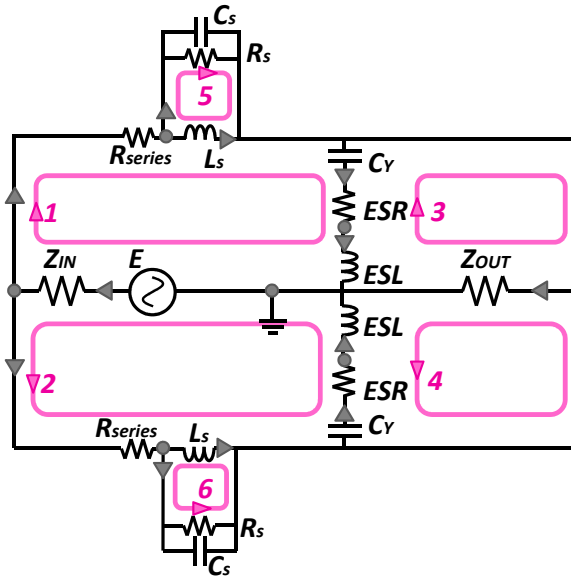


Figure 4.17: Meshes definition in CM

Finally, all that remains is to build the associated connectivity matrix such as presented in Eq. 4.16.

$$C_{E \rightarrow M_{CM}} = \begin{pmatrix} 1 & 1 & 0 & 0 & 0 & 0 \\ 1 & 0 & 0 & 0 & 0 & 0 \\ 1 & 0 & 0 & 0 & 1 & 0 \\ 0 & 0 & 0 & 0 & 1 & 0 \\ 0 & 1 & 0 & 0 & 0 & 0 \\ 0 & 1 & 0 & 0 & 0 & 1 \\ 0 & 0 & 0 & 0 & 0 & 1 \\ 1 & 0 & 1 & 0 & 0 & 0 \\ 1 & 0 & 1 & 0 & 0 & 0 \\ 0 & 1 & 0 & 1 & 0 & 0 \\ 0 & 1 & 0 & 1 & 0 & 0 \\ 0 & 0 & 1 & 1 & 0 & 0 \end{pmatrix} \quad (4.16)$$

4.3.7 Transformation and attenuation calculation

With minimum information about a given filter, it is possible to build its associated graph and all the tensors and matrices that describe this graph mathematically. The methodology of calculation can be followed as presented in Sect. 4.2.3. The first step is then to express all the tensors in the mesh space thanks to the transfer matrix: the connectivity. Then, the impedance tensor in DM: $Z_{M_{DM}}$ (Eq. 4.17), the source in DM: $E_{M_{DM}}$ (Eq. 4.18), the impedance tensor in CM: $Z_{M_{CM}}$ (Eq. 4.19) and the source in CM: $E_{M_{CM}}$ (Eq. 4.20) are calculated.

$$Z_{M_{DM}} = C_{E \rightarrow M_{DM}}^T \cdot (Z_{i-E_{DM}} + Z_{c-E_{DM}}) \cdot C_{E \rightarrow M_{DM}} \quad (4.17)$$

$$E_{M_{DM}} = C_{E \rightarrow M_{DM}}^T \cdot E_{E_{DM}} \quad (4.18)$$

$$Z_{M_{CM}} = C_{E \rightarrow M_{CM}}^T \cdot (Z_{i-E_{CM}} + Z_{c-E_{CM}}) \cdot C_{E \rightarrow M_{CM}} \quad (4.19)$$

$$E_{M_{CM}} = C_{E \rightarrow M_{CM}}^T \cdot E_{E_{CM}} \quad (4.20)$$

The next objective is to calculate the mesh currents in DM: $I_{M_{DM}}$ (Eq. 4.21) and in CM: $I_{M_{CM}}$ (Eq. 4.22).

$$I_{M_{DM}} = (inv(Z_{M_{DM}}) \cdot E_{M_{DM}})^T \quad (4.21)$$

$$I_{M_{CM}} = (inv(Z_{M_{CM}}) \cdot E_{M_{CM}})^T \quad (4.22)$$

Finally, from all those mesh currents, it is possible to estimate the voltages at each edge. The main advantage of performing all calculations in the mesh space is that only the currents are calculated. Actually, thanks to Kirchhoff's voltage law, the mesh voltages are equal to zero. This point represents one the most significant differences between nodal analysis (in the node space) and modal analysis (in the mesh space).

The final objective here is to calculate the voltage at the output edge that represents the filter attenuation (Sect. 1.3.1). For the used case we have followed till now, the voltage that represents

the filter attenuation is the one on edge #14 for DM (Eq. 4.23) and on edge #12 for CM (Eq. 4.24).

$$V_{E_{OUT-DM}} = Z_{OUT}.C_{E \rightarrow M_{DM}}(14, :).I_{M_{DM}}^T \quad (4.23)$$

$$V_{E_{OUT-CM}} = Z_{OUT}.C_{E \rightarrow M_{CM}}(12, :).I_{M_{CM}}^T \quad (4.24)$$

Therefore, thanks to this methodology, it is now possible to estimate any filter attenuation whatever the structure and the topology. Actually, that methodology was included in tool that build up automatically the Kron's graph thanks to Fig. 4.14 and Fig. 4.16.

In order to illustrate the whole reasoning, different application cases will be presented.

4.4 Application case: attenuation of a LC filter and its optimization

The first use case is dedicated to the study of a LC filter, composed of a $2\mu H$ inductor and a $1\mu F$ capacitor spaced by 34mm as presented in Fig. 4.18.

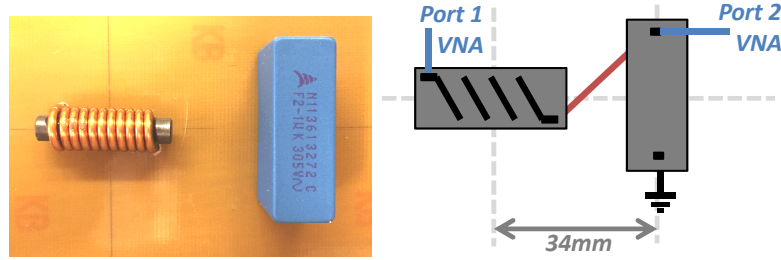


Figure 4.18: LC filter composed of a $2\mu H$ inductor and a $1\mu F$ capacitor

The first step, as described in Chapter 1, was to characterize the components with an impedance analyzer and/or a VNA in order to determine the equivalent electrical model. Fig. 4.19 presents the two characterized components. For the capacitor, only the measurement with the impedance analyzer was sufficient in order to build the model. However, for the inductor, the measurement with the Z-meter was not sufficient because it did not highlight all the different behaviors of the inductor. Therefore, a measurement with the VNA complemented the measurement from the Z-meter in order to build the equivalent electrical model of the inductor.

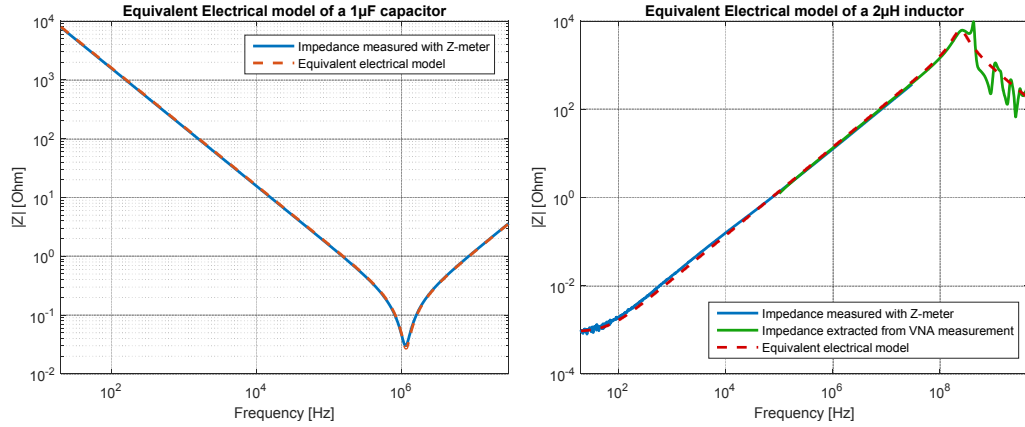


Figure 4.19: Equivalent electrical models of a 1μF capacitor and a 2μH inductor

The second step was then to characterize the two components in the TEM cell in order to determine their equivalent coupling surface. To do so, the methodology presented in Chapter 2 was followed. Fig. 4.20 presents the equivalent coupling surfaces versus frequency for the capacitor and the inductor.

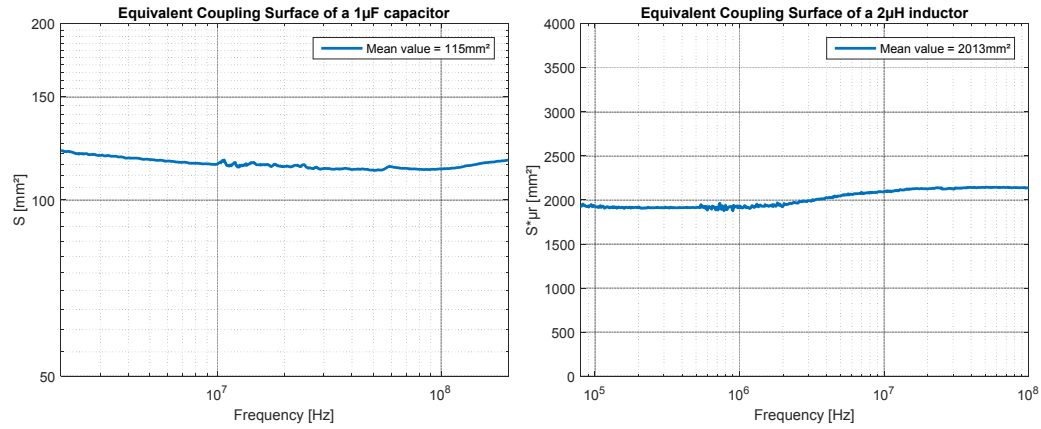


Figure 4.20: Equivalent coupling models of a 1μF capacitor and a 2μH inductor

Thanks to the methodology presented in Chapter 3, the mutual inductance between the two components could be calculated. The advantage of this part is that, once all the formulas are developed and generic enough to be applicable to any case, the calculation is very fast and, therefore, gives the mutual inductance whatever the position of the components.

Actually, for the current position and connection between the components, it gives a mutual inductance of $M = 9nH$. It is important to notice that the mutual inductance is positive and, therefore, it adds more parasitic inductance to the capacitor edge. Finally, it can be concluded that this position leads to a degradation of the filter attenuation as presented in Fig. 4.21, regarding the attenuation considering no coupling.

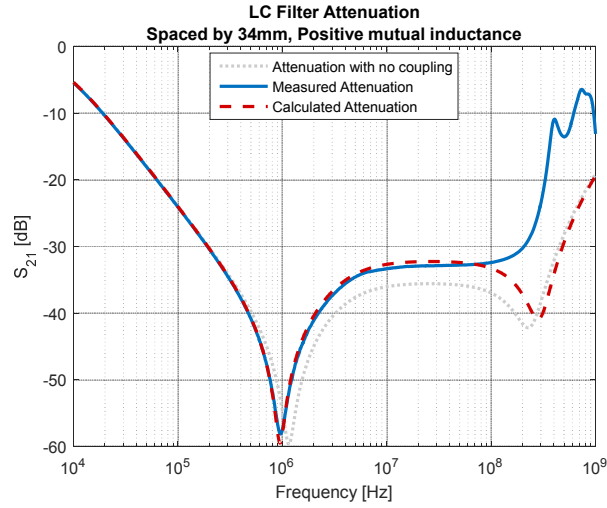


Figure 4.21: LC filter attenuation for placement as defined in Fig. 4.18

Therefore, the first idea in order to avoid the degradation from the magnetic coupling, is to change the sign of the magnetic coupling without moving the components. Indeed, the components connection is changed to induce a negative coupling and not a positive coupling. Actually, with a negative coupling, the parasitic series inductance of the capacitor is reduced and so the attenuation is improved as presented in Fig. 4.22.

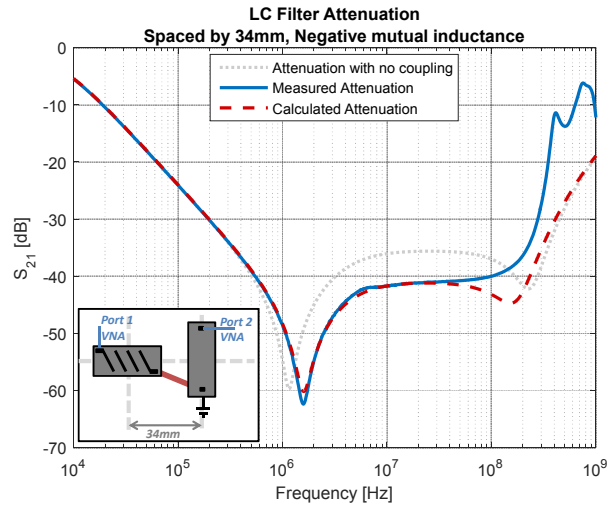


Figure 4.22: LC filter attenuation for a distance of 34mm and negative mutual inductance

This example shows that, just by switching the components connection, an improvement on the filter attenuation can be made. For the current filter, this change induces a 10dB improvement at 10MHz. Nevertheless, it must be noticed that a negative coupling, will improve the filter attenuation, only when the mutual inductance is lower than the parasitic inductance of the capacitor. A negative coupling will not always improve a filter performance.

It has been demonstrated in [4] that the filter response for an LC filter is optimized when the mutual inductance completely cancels the parasitic inductance of the capacitor. Therefore, in

order to obtain the best performance for this LC filter, the mutual inductance between the two components should be equal to $M = -19nH$. Therefore, by fixing the mutual inductance value, an infinite number of positions can be identified as presented in Fig. 4.23. The black arrows represent the correct center positions and orientations of the capacitor with respect to the inductor in order to obtain the best filter attenuation. That calculation is performed automatically with the tool we developed.

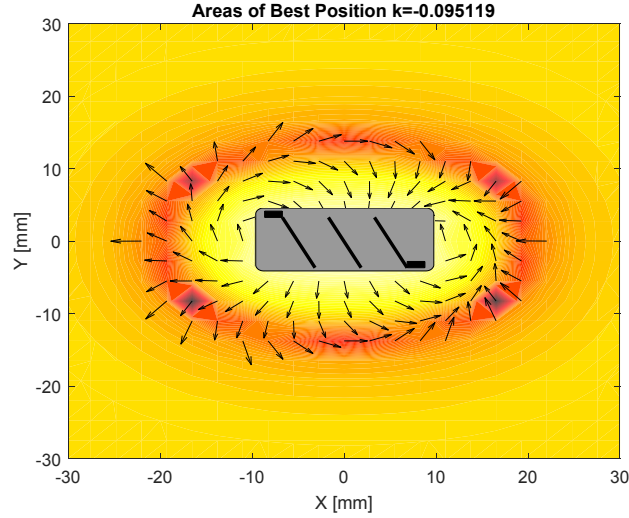


Figure 4.23: Areas of best positions for the capacitor location and orientation

Finally, it was chosen to put the capacitor in the main axi of the inductor and at a distance of 24mm in order to reach the optimized coupling. The components connection is correctly made to obtain a negative coupling between the components. The resulting filter attenuation is presented in Fig. 4.24 and it can be noticed that, regarding the first position of the components, with a minimum of changes, the filter performance is improved by 25dB at 10MHz.

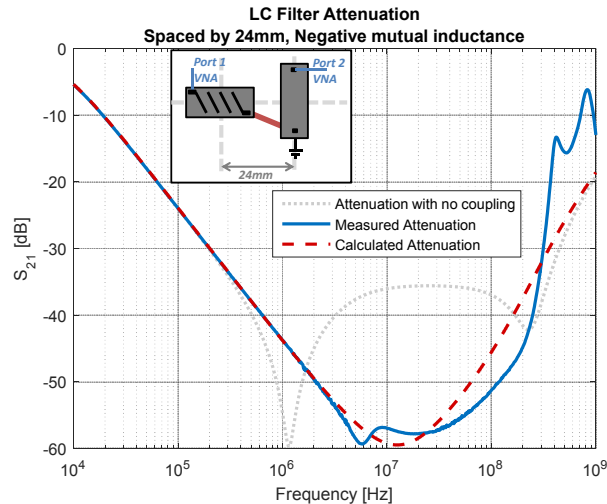


Figure 4.24: Optimized filter attenuation

The resonance that is observed around 10MHz comes from the frequency dependency of the equivalent series resistance as identified and already discussed in [4]. Actually, from Fig. 4.19, the equivalent series resistance of the capacitor is extracted at the resonance frequency around 1MHz. However, that value of ESR evolves over frequency and can be measured with the impedance analyzer. Thus, it can be seen in Fig. 4.25 a value of $20m\Omega$ is correctly extracted at 1MHz but beyond, this value increases and the resonance is visible at 10MHz as in filter attenuation in Fig. 4.24.

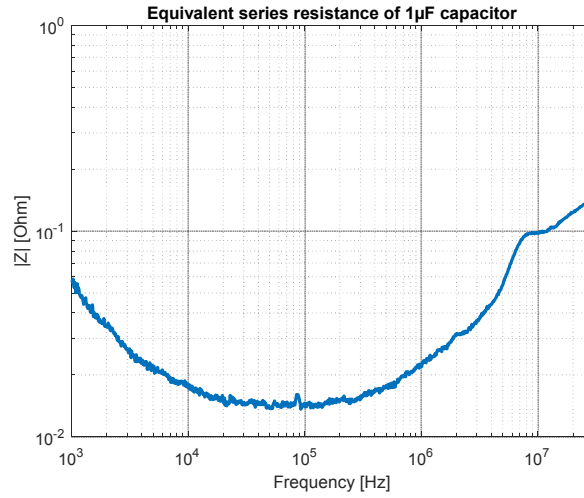


Figure 4.25: ESR of the capacitor

It must be noticed that the optimization is very sensitive. Actually, a simple error of 1mm on the position of the capacitor will induce a degradation. Fig. 4.26 presents the LC filter performance by moving the capacitor 1mm closer to the inductor, and 1mm further.

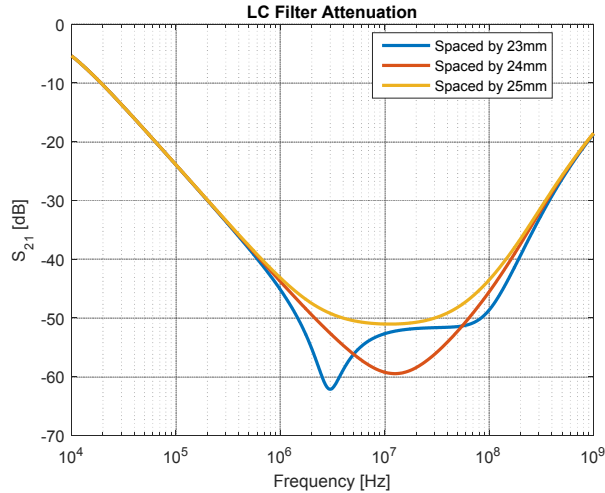


Figure 4.26: Tolerance on the distance between both components

The degradation at 10MHz is of 10dB for the both positions with respect to the optimized one.

Furthermore, that degradation can be even more important if the components are not correctly characterized (impedance used from supplier data sheet, equivalent coupling surface determined from geometrical properties etc.). Actually it will induce even more errors in the calculation and therefore the filter performance won't be accurately predicted. It can be concluded that the methodology of ESL cancellation can be a good approach for optimization, but it is very sensitive.

4.5 Application case: Pi filter on a LED driver for a DC/DC converter

The second application case is dedicated to a Pi filter composed of two $4.7\mu\text{F}$ MLCC 0603 capacitors and a $3.3\mu\text{H}$ inductor (Fig. 4.27). The objective here is to compare different positions of the capacitors.

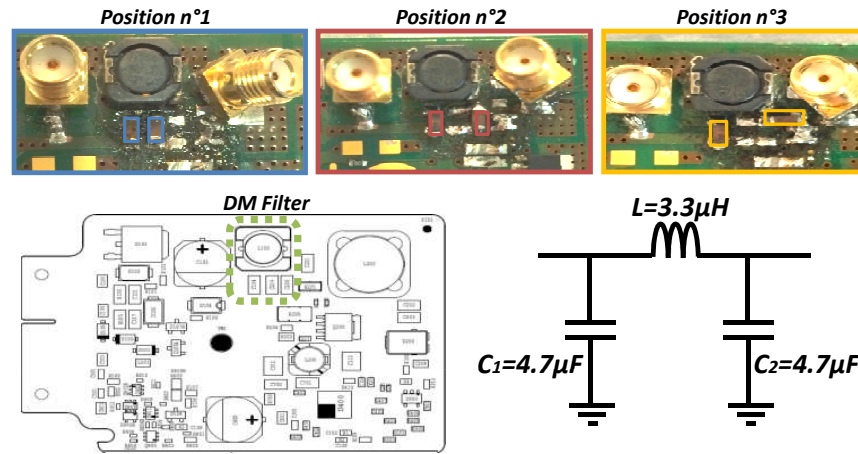


Figure 4.27: Pi filter for three different positions of capacitors

The component models presented in Sect. 2.5.5, dedicated to the study of MLCC capacitors, are re-used. Then, the filter performances for the three different positions can be predicted and are presented in Fig. 4.28.

It is clearly identifiable that the coupling between the two capacitors is destructive and bypass the inductor. Actually, there is a 35dB degradation at 10MHz between position #1 and position #3. This kind of behavior is typical and has been identified through several application cases. Actually, when two capacitors are coupled but not on the same potential, it is very destructive for a filter attenuation. However, when the two coupled capacitors are on the same potential, the coupling has almost no influence on filter performance. It was presented in [80] that the coupling between two capacitors on the same potential can reduce the filter performance. However, it has a very little impact compared to the coupling between two capacitors not on the same potential.

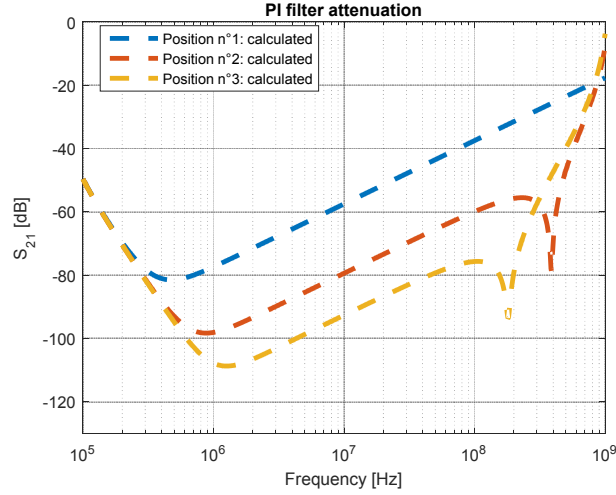


Figure 4.28: Prediction of Pi filter performances for three different positions of capacitors

Finally, the prediction can be validated with measurements as presented in Fig. 4.29.

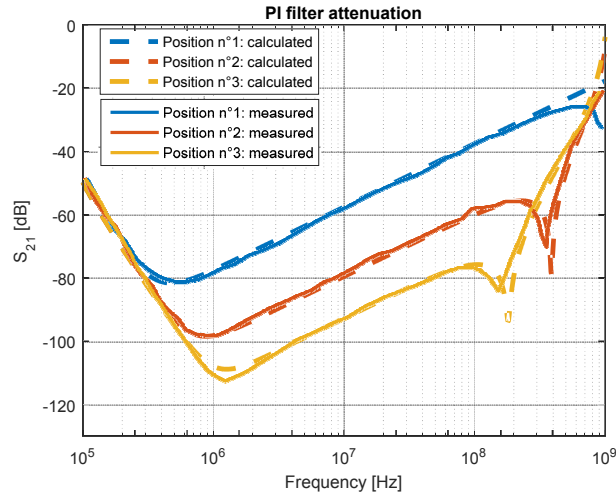


Figure 4.29: Comparison between predicted and measured performances of a Pi filter

From this kind of application case, a design rule can then be identified. When two capacitors are not on the same potential, the magnetic coupling must be reduced to avoid filter performance degradation.

4.6 Application case: OBC (On Board Charger) H filter

The third application case is dedicated to the study of an H filter, composed of two 2.43mH and 2.13mH CMCs and a 2.2μF DM capacitor, as presented in Fig. 4.30.

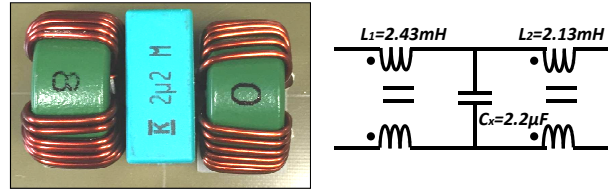


Figure 4.30: H filter composed of two CMCs and a DM capacitor - Initial position

The predicted attenuation for this position of the components is the one presented in Fig. 4.31 and is validated by measurement.

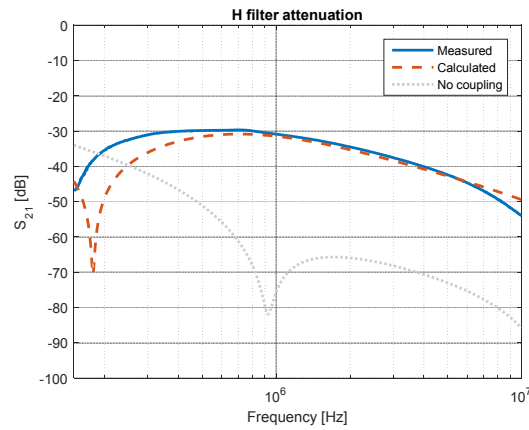


Figure 4.31: H filter performance for initial position

This attenuation is, therefore, the one corresponding to the initial position of the components. The objective is then to improve the filter performance at 1 MHz and so to improve the attenuation. The first idea is then to identify the destructive coupling, the one which degrades the most the filter performance. To do so, the two CMCs are brought closer as presented in Fig. 4.32.

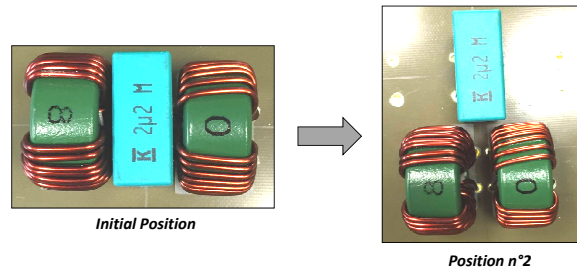


Figure 4.32: Two CMCs brought closer

Therefore, by calculation, it is predicted that this position will degrade the filter performance as presented in Fig. 4.33 -a. This was validated by measurements (Fig. 4.33 -b). It must be noticed that for that topology, the couplings between CMCs and the capacitor are still low, compared to the first one. Actually, by representing the equivalent coupling surfaces of each component, it appears that the surface of the capacitor is always perpendicular to the ones of both CMCs, for

the first position and even the second one. It can then be concluded that the coupling between both CMCs is destructive, regarding Fig. 4.33 and must be reduced.

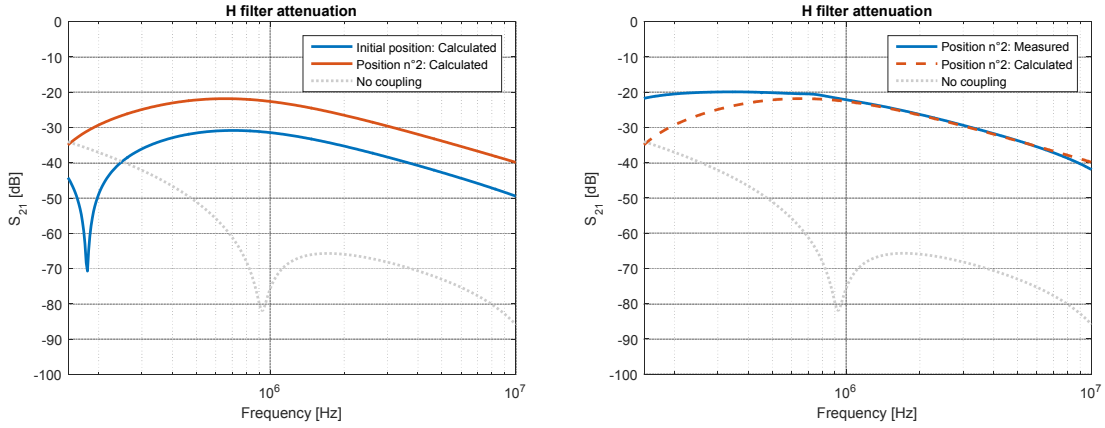


Figure 4.33: Predicted H filter performance for position #2 a- compared to initial position b- compared to measurement

One possibility, in order to reduce the coupling between the two CMCs, is to move them away from each other as it can be seen in Fig. 4.34.

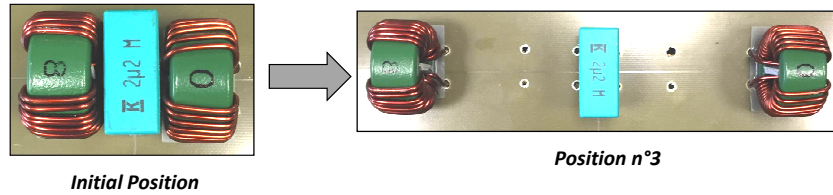


Figure 4.34: Two CMCs moved away from each other

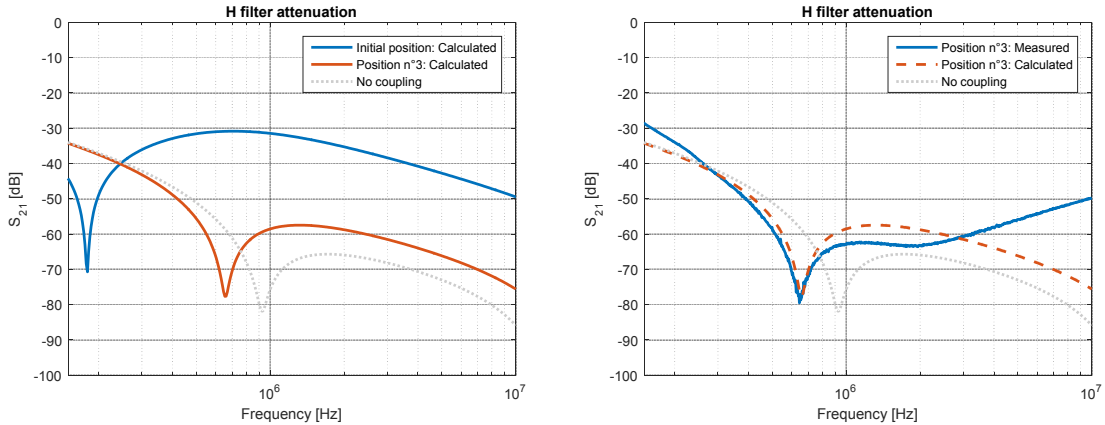


Figure 4.35: Predicted H filter performance for position #3 a- compared to initial position b- compared to measurement

Actually, the predicted attenuation is considerably improved as presented in Fig.4.35 -a. This topology was validated by measurements (Fig.4.35 -b).

An improvement of 30dB at 1MHz is highlighted in that position. However, in a real world application, there is not so much space to put the components as far as in Fig. 4.34. However, there are some discrepancies from 3MHz to 10MHz. That difference was not studied but it can come from the influence of the component connexions. As the components are far from each other, the connexions are long and can have an influence on the filter attenuation. This phenomena is only visible on this measurement because it is the only position where the connexions are long. For other positions, the connexions are very small, as the components are very close.

Therefore, in order to minimize the coupling between the two CMCs, the second one is laid on its side (as a horizontal CMC) and turned by 90° (Fig. 4.36). Actually, by understanding how the components couple, like in Fig. 23, the coupling can be reduced.

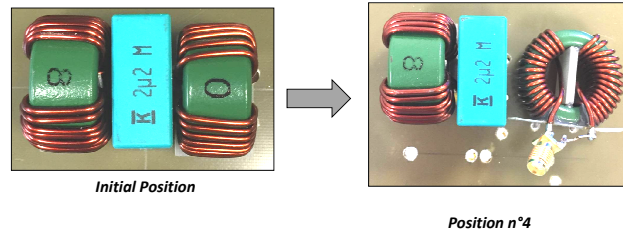


Figure 4.36: Second CMC laying down and turned by 90°

From Fig.4.37 -a, it clearly shows that the filter performance is improved by 20dB at 1MHz and the criteria of minimum of space is respected. This topology was also validated with measurements (Fig.4.37 -b). However, there are still some discrepancies from 3MHz to 10MHz. This difference can come from parasitic capacitances between the components. Actually, they are very close from each other and it could explain the resonance at 6MHz. For the first and the second position that phenomenon is not visible because the magnetic coupling is dominant. For that position, the magnetic coupling is reduced and, therefore, the capacitive coupling could explain that discrepancy.

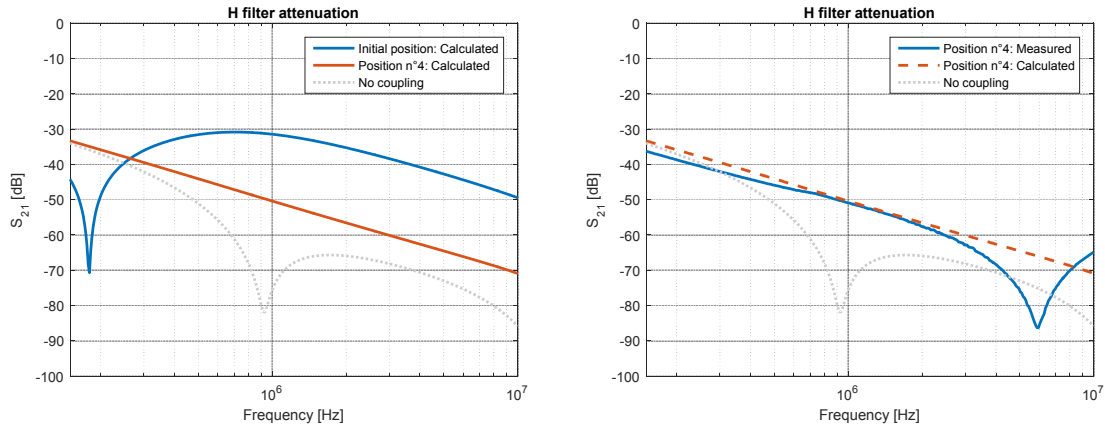


Figure 4.37: Predicted H filter performance for position #4 a- compared to initial position b- compared to measurement

Through this example, a filter topology improvement was presented. It clearly shows that, with a minimum of space and by understanding how components couple together, it is possible to improve filter performance (as introduced in Chapter).

4.7 Application case: Power filter application

The last application case presents one of the advantage of the MKME use for filter design: the simplicity of coupling definition. Therefore, Fig. 4.38 presents the studied filter. It is composed of three cells of filtering for the three phases, same filter for each phase.

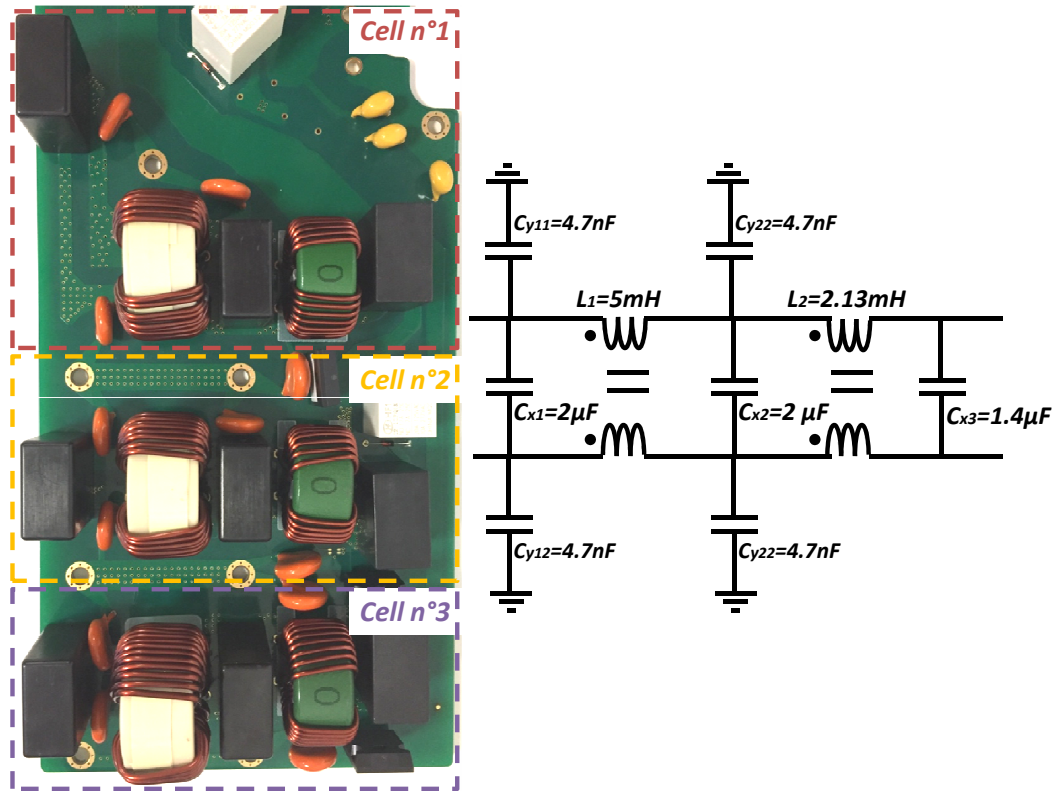


Figure 4.38: Power filter application case

Indeed, there are nine passive components per cells of filtering and two CMCs. Therefore, there are eleven inductances per cells of filtering that can induce magnetic couplings. Finally, by considering the three cells, it induces 528 possible couplings, that is clearly very difficult and long to implement in a SPICE simulation. Actually, all the couplings should be defined manually one by one and it would be time-consuming. Therefore, using the MKME, the analysis is simplified thanks to the tensor description.

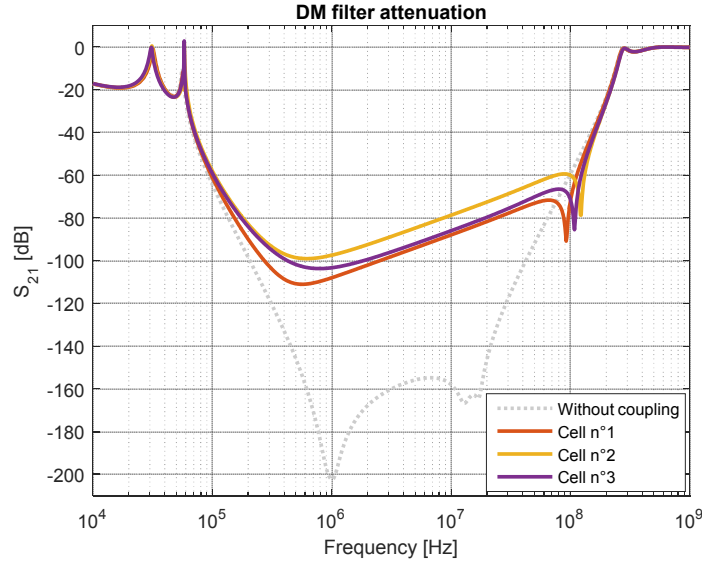


Figure 4.39: Prediction of power filter performance for the three cells

The results for the three different cells are presented in Fig. 4.39. It is clearly identifiable that the degradation is very important regarding the attenuation without considering the coupling. Finally, the calculated attenuation can be compared to measurement, for the first cell for example, like in Fig. 4.40. There are some discrepancies from 10MHz to 100MHz that can come from components electrical models that are not sufficient or other phenomena like layout influence that is not included in this calculation.

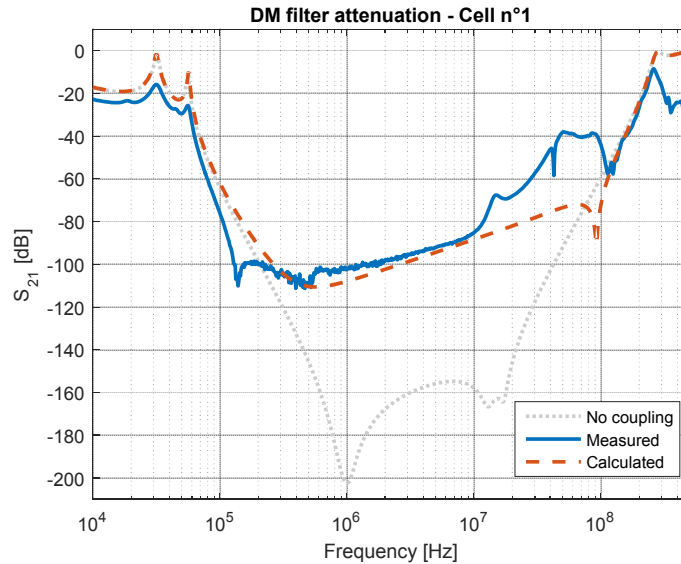


Figure 4.40: Prediction of DM filter performance for cell #1 compared to measurement

4.8 Conclusion

In this chapter, the generic Kron's graph development was presented in order to predict a filter attenuation whatever the filter structure and the filter topology. Here, all the presented topics were gathered: the equivalent coupling model of passive components and the magnetic field generated by those components to predict a mutual inductance and finally a filter attenuation. This methodology presents a major advantage compared to 3D simulation. Actually, for 3D electromagnetic simulation, it takes time to build up the model, but the solving also takes time. With that methodology, the calculation is generic and once the model are build, the calculation is very fast.

Synthesis and conclusions

The main objective of this thesis work was to introduce a methodology for filter design considering component proximity. Actually, it was demonstrated that the proximity has a big influence on the filter performance. Therefore, that coupling phenomenon must be taken into account in order to predict a filter attenuation correctly.

Most of the previous research work performed on that topic was based on numerical study such as 3D electromagnetic simulation. The main drawback of that approach is that a lot of information on components is required in order to build the filter 3D model, such as the exact geometry or the material properties. Furthermore, in addition to being time-consuming for model construction, it is also time-consuming for solving. For each analysis, the simulation must be re-launched and, therefore, it takes too much time for a filter analysis.

The methodology that was developed through this thesis work is based only on measurement and analytical calculation. Therefore, once the models are built, the resolution and the analysis can be performed very quickly.

The methodology is divided into different main steps. The first one gathers component characterization inside the TEM cell. This characterization makes it possible to determine the magnetic sensitivity of each component. Indeed, their equivalent coupling model composed of one or several surfaces can be established. This property is fixed for each component in amplitude and direction. Actually, for capacitors and inductors, there is only one equivalent coupling surface. For capacitors, the surface is oriented like the one delimited between the pins of the components. For inductors, the equivalent coupling surface is oriented like the turns of the component and is increased by the influence of the magnetic material. Finally, for CMCs, only the DM coupling model is necessary because a CMC can only couple a magnetic field when it is connected in DM. Therefore, the DM coupling model is composed of several surfaces (ten in the presented cases) with fixed orientation. All the surfaces presented here are equivalent surfaces and not physical ones. Actually, those surfaces represent a sensitivity to the magnetic field by including all influent parameters such as a magnetic material for example.

The second step is dedicated to the magnetic field calculation. Actually, the equivalent coupling surface is re-used as an equivalent emission surface, thanks to the reciprocity theorem. Therefore, in order to estimate a mutual inductance between two components, the magnetic field generated by the first component on the equivalent coupling surface of the second one is calculated and, therefore, the coupling is calculated.

Thanks to this coupling extraction, the filter performance can then be estimated considering the placement of the components. To do so, the Modified Kron's Method is used and a generic Kron's graph was developed for attenuation calculation. That genericity is very important because, this way, there is not limitation on the filter structure and also in the filter topology.

Finally, in order to build up the global methodology, a tool was developed, named Global Filter Design (GFD). This tool is divided into two main menus. The first one is dedicated to the extraction of the magnetic coupling between two passive components (capacitors, inductors and common mode chokes). The second menu is dedicated to filter performance prediction, considering several fixed structures and the possibility to build a custom structure. Therefore, by considering all the components properties, the filter attenuation can be predicted very accurately. GFD tool is operational and is currently used by design teams for filter design as the examples presented in the last chapter.

The global methodology was applied to several typical filter structures in order to cover a maximum of the possible cases. The comparison between the predicted attenuations and the measured ones presents the high accuracy of the methodology. It can be applied to low order filter (like the example of the LC filter) or for higher order filter (like the example of power filter example), the methodology is still very accurate.

The next steps will be more dedicated to the placement optimization of filters. Actually, it was presented that, using those inter-component couplings, it was possible to improve filter performance. For LC filter, it is quite simple because there is only two components. However, in the last application case on a power filter, a structure with 528 possible couplings was presented and it clearly appears that the optimization is not obvious compared to LC filter. A first step can be to determine the destructive couplings and the ones which have no influence. This is what has been done in the second application case. Through a practical example, a design rule was identified: the coupling between two capacitors, not on the same potential, must be as low as possible. Those examples are first clues for filter design optimization. Another possibility could be to base the optimization process as for LC filter. Actually, for LC filter, the objective was to reduce the parasitic elements using the mutual inductances. That could be applicable to higher order filter but is still complicated when there are several components. Furthermore, as the constraint in terms of space is high, but also considering mechanical structures, this solution cannot be applied for all couplings. Therefore, the two proposed solutions can be mixed for optimization placement.

Finally, another step will be dedicated to the integration of the layout influence. Here, only the magnetic coupling between the components were presented and it was highlighted that those couplings have a major influence on DM attenuations and very few in CM. Actually, the filter performance in CM is more affected by the layout: the coupling between traces but also between traces and the components. Some works using 3D electromagnetic simulations were already developed as presented in the introduction. Therefore, in order to improve the existing methodology, this point could be added to the current methodology, for accurate prediction of filter performance in differential mode but also in common mode. A perspective is to include in the generic tool, Global Filter Design, the influence of the layout. This step could be performed with the MKME, which can easily formulates coupling between meshes, whereas with a usual SPICE simulator, it is not possible.

Bibliography

- [1] CISPR25, “CISPR25 - 3rd Edition - Vehicles boats and internal combustion engines - Radio disturbance characteristics - Limits and methods of measurement for the protection of on-board receivers,” 2008.
- [2] T. De Oliveira, “Optimisation du routage d’un filtre CEM,” Ph.D. dissertation, Université de Grenoble, 2006.
- [3] J. Bernal, M. J. Freire, and S. Ramiro, “Use of mutual coupling to decrease parasitic inductance of shunt capacitor filters,” *IEEE Transactions on electromagnetic compatibility*, vol. 57, pp. 1408 – 1415, 2015.
- [4] A. Zhou, “Modèles de composants passifs et couplage électromagnétique pour filtres HF de puissance - optimisation du placement,” Ph.D. dissertation, Université Claude Bernard, Lyon 1, 2012.
- [5] P. Fernandez-Lopez, F. Ajebbar, F. Lafon, and A. Ramanujan, “EMC filter optimization based on inter-component coupling,” in *17ème colloque international & exposition sur la compatibilité électromagnétique*, 2014.
- [6] A. Zhou, C. Joubert, M. Bensetti, and F. de Daran, “Study and modeling of inter-component coupling to optimize EMC filter,” in *EMC Europe 2011 York*, Sept 2011, pp. 518–522.
- [7] S. Wang and F. C. Lee, “Effects of mutual inductance between inductors and capacitors on LC filter performance,” in *IEEE Power Electronics Specialists Conference*, 2008.
- [8] S. Schumacher, A. Klaedtke, C. Keller, W. Ackermann, and H. De Gersem, “Optimizing the inductance cancellation behavior in an EMI filter design with the help of a sensitivity analysis,” in *EMC Europe, International Symposium and Exhibition on Electromagnetic Compatibility*, 2017.
- [9] N. Moonen, G. Buesink, and F. Leferink, “Optimizing capacitor placement in EMI filter using back annotation of 3D field coupling parameters in circuit models,” in *EMC Europe, International Symposium and Exhibition on Electromagnetic Compatibility*, 2016.
- [10] I. Kovacevic, A. Musing, T. Friedli, and J. W. Kolar, “Electromagnetic modeling of EMI input filters,” in *7th International Conference Integrated Power Electronics Systems*, 2012.
- [11] B. Zhang and S. Wang, “Analysis and reduction of the near magnetic field radiation from magnetic inductors,” in *Applied Power Electronics Conference and Exposition*, 2017.

- [12] G. Asmanis, D. Stepins, A. Asmanis, and L. Ribickis, "Capacitors mutual inductance modeling and reduction," in *International Symposium on Electromagnetic Compatibility*, 2014.
- [13] G. Asmanis, L. Ribickis, D. Stepins, and A. Asmanis, "Differential mode pi-type of EMI filter modeling using CST MWS," in *56th International Scientific Conference on Power and Electrical Engineering*, 2015.
- [14] G. Asmanis, D. Stepins, A. Asmanis, and L. Ribickis, "Mutual couplings between EMI filter components," in *IEEE International Symposium on Electromagnetic Compatibility*, 2015.
- [15] A. Asmanis, G. Asmanis, D. Stepins, and L. Ribickis, "High frequency modeling of EMI filters considering parasitic mutual couplings," in *ESA Workshop on Aerospace EMC*, 2016.
- [16] G. Asmanis, D. Stepins, L. Ribickis, and A. Asmanis, "Modeling of mutual coupling between inductors," in *IEEE Symposium on Electromagnetic Compatibility and Signal Integrity*, 2015.
- [17] A. Asmanis, G. Asmanis, D. Stepins, and L. Ribickis, "Modeling of EMI filters with shields placed between the filter components," in *International Symposium on Electromagnetic Compatibility*, 2016.
- [18] P. Gonzalez-Vizuet, A. Fernandez-Prieto, M. J. Freire, and J. Bernal, "Calculation of parasitic self and mutual inductances of thin film capacitors for power line filters," in *IEEE Transactions on power electronics*, 2018.
- [19] E. Hoene, "Passive filter design," in *ECPE Tutorial EMC*.
- [20] F. Lafon, "Développement de techniques et de méthodologies pour la prise en compte des contraintes CEM dans la conception d'équipements du domaine automobile. Étude de l'immunité, du composant à l'équipement," Ph.D. dissertation, INSA de Rennes, 2011.
- [21] C. Saber, D. Labrousse, B. Revol, and A. Gascher, "A combined CM and DM conducted EMI modeling approach," in *International Symposium on Electromagnetic Compatibility*, 2017.
- [22] M. J. Nave, "Prediction of conducted emissions in switched mode power supplies," in *IEEE International Symposium on Electromagnetic Compatibility*, 1986.
- [23] A. Farhadi and A. Jalilian, "Modeling and simulation of electromagnetic conducted emission due to power electronics converters," in *International Conference on Power Electronic*, 2006.
- [24] J. G. Zola, P. M. Belcaguy, and F. D'Angiolo, "Analysis of common mode conducted emissions applied to switching power supplies," in *Global Electromagnetic Compatibility Conference*, 2016.
- [25] K. Takahashi, T. Ibuchi, and T. Funaki, "Frequency domain simulation of conducted EMI in power electronic converters considering internal near field couplings by FEM," in *International Symposium on Electromagnetic Compatibility*, 2017.
- [26] O. Maurice, "Theoretical application of the tensorial analysis of network for EMC at the system level," 2007.
- [27] O. Maurice, P. Durand, and A. Reineix, "Methodology of networks analysis using xTAN," 2015.

- [28] O. Maurice, *xTAN par la pratique (eXtended Tensorial Ananlysis of Networks)* <http://olivier.maurice.pagesperso-orange.fr/topologieAppliquee/ExTANforStudentsbat.pdf>.
- [29] M. Maurice, "Caractères remarquables de la méthode de Kron," 2016.
- [30] D. Stipanicev, "Damping of resonances in RFI filters with RC members," in *3rd symposium and technical exhibition on electromagnetic compatibility*, 1979.
- [31] Agilent, "Application Note - Agilent, ENA 2 and 4 Port RF Network Analyzers Data Sheet," Agilent, Tech. Rep., 2007.
- [32] —, "Application Note 5989-5935EN - Ultra-Low Impedance Measurements Using 2 - Port Measurements," Agilent, Tech. Rep., 2007.
- [33] I. Novak, "Measuring MilliOhms and PicoHenrys in Power - Distribution Networks," in *DesignCon 2000*, 2000.
- [34] *Keysight Technologie, Impedance Measurement Handbook*.
- [35] R. C. Paul, Ed., *Introduction to electromagnetic compatibility*. Wiley-Interscience, 2006.
- [36] H. Zumbahlen and Engineering staff of Analog Device, *Linear Circuit Design Handbook*. Newnes, 2008.
- [37] M. Togashi, "ESR Controlled MLCCs and decoupling Capacitor Network Design," in *Design-Con 2007*, 2007.
- [38] S. G. Parler, "Improved SPICE models of aluminum electrolytic capacitors for inverter applications," *IEEE Industry Applications Society Conference*, Oct 2002.
- [39] H. Zenker, A. Gerfer, and B. Rall, *Trilogy of inductors - Design Guide for inductors and filters*, 2nd ed. Wurth Elektronik GmbH, 2001.
- [40] I. Stevanovic, S. Skibin, M. Masti, and M. Laitinen, "Behavioral modeling of chokes for EMI simulations in power electronics," *IEEE Transactions on Power Electronics*, vol. 28, pp. 695–705, 2013.
- [41] M. Al-Hamid, R. Vick, M. Kruger, and T. Rinkleff, "Determination of equivalent circuit parameters of current compensated chokes and their use in filters with an application example," in *Proc. EMC Europe, Bruges, Belgium*, 2013.
- [42] A. Roc'h, "Behavioural models for common mode EMI filters," in *Ph.D. dissertation, University of Twente*, 2012.
- [43] A. Mittal, "Data sheet nanocrystalline cores nanophy," in *Stainless and Nicekls Alloys compo-nents*.
- [44] Z. Li, D. Pommerenke, and Shimoshio, "Common mode and diffrential mode analysis of common mode chokes," *IEEE international symposium on EMC*, vol. 1, pp. 384–387, 2003.
- [45] M. L. Crawford and J. L. Workman, *Using a TEM cell for EMC measurements of electronic equipment*, U. D. of commerce, Ed. National Bureau of Standards, 1979.

- [46] M. L. Crawford, "Techniques for measurement of electromagnetic radiation and susceptibility of electronic equipment," in *1st symposium and technical exhibition on electromagnetic compatibility*, 1975.
- [47] G. H. Koepke and M. T. Ma, "A new method for determining the emission characteristics of an unknown interference source," in *5th symposium and technical exhibition on electromagnetic compatibility*, 1983.
- [48] *IEC62132-2 - Integrated circuits Measurement of electromagnetic immunity 150 kHz to 1 GHz Part 2: Measurement of electromagnetic immunity - TEM cell and wideband TEM cell method*, International Electrotechnical Commission Std.
- [49] A. El Abbazi, "Etude et réalisation d'une nouvelle cellule TEM à support rotatif pour des mesures CEM des circuits intégrés: Application du modèle ICEM," Ph.D. dissertation, Institut National des Sciences Appliquées de Rennes, 2006.
- [50] M. L. Crawford, "Generation of standard EM fields using TEM transmission cells," in *IEEE Transactions on electromagnetic compatibility*, 1974.
- [51] E. Grudzinski and H. Trzaska, "The TEM cell in EMC investigations," in *5th Symposium and technical exhibition on electromagnetic compatibility*, 1983.
- [52] N. S. Nahman, M. Kanda, E. Larsen, and M. L. Crawford, "Methodology for standards electromagnetic field measurements," in *IEEE Transactions on instrumentation and measurement*, 1985.
- [53] M. T. Ma, E. B. Larsen, and M. L. Crawford, "Electromagnetic fields with arbitrary wave impedances generated inside the TEM cell," in *IEEE Transactions on Electromagnetic compatibility*, 1991.
- [54] S. Kashyap, "Field distortions in a TEM cell," in *6th Symposium and technical exhibition on electromagnetic compatibility*, 1985.
- [55] *IEC62132-4 - Integrated circuits Measurement of electromagnetic immunity 150 kHz to 1 GHz Part 4: Direct RF power injection method*, International Electrotechnical Commission Std., 2006.
- [56] P. E. Levy, "Modélisation du champ électromagnétique rayonnée par une inductance à noyau ferromagnétique torique," in *Symposium de Génie électrique*, 2014.
- [57] —, "Modélisation du rayonnement électromagnétique quasi-statique des composants magnétiques de puissance - application à la compatibilité EM," Ph.D. dissertation, Ecole Normale Supérieure de Cachan, 2015.
- [58] A. Ramanujan, Z. Riah, A. Louis, and M. B., "Modeling the electromagnetic radiation of passive microwave components using a near-field scanning method," in *IEEE Transactions on Electromagnetic compatibility*, 2010.
- [59] P. Fernandez-Lopez, C. Arcambal, D. Baudry, S. Verdeyme, and B. Mazari, "Simple electromagnetic modeling procedure: from near-field measurements to commercial electromagnetic simulation tool," in *IEEE transactions on instrumentation and measurement*, 2010.

- [60] W. H. Hayt and J. E. Kemmerly, "Engineering circuit analysis, second edition," M.-H. B. Company, Ed., 1962.
- [61] R. Bansal, "Fundamentals of engineering eletromagnetics." Taylor & Francis, 2006.
- [62] R. C. Johnson, "Antenna engineering handbook." McGraw Hill, 1993.
- [63] R. P. Feynman, "The feynman lectures on physics." Addison-Wesley, 1963.
- [64] T. A. Milligan, "Modern antenna design." Willey-Interscience, 2005.
- [65] C. T. Tai, "Complementary reciprocity theorems in electromagnetic theory," *IEEE Transactions on Antennas and Propagation*, vol. 40 No. 6, pp. 675–681, 1992.
- [66] C. A. Balanis, "Advanced engineering electromagnetics," Wiley, Ed., 2012.
- [67] A. Schramm and D. Gerling, "Analytical calculation of the end winding leakage inductance based on the solution of Neumann integrals," in *IEEE ISIE*, 2005.
- [68] J. L. Guermond, "Eléments finis: théorie, applications, mise en oeuvre," A. Ern, Ed. Springer, 2000.
- [69] M. Faraday, "Experimental researches in electricity," in *Philosophical Transactions of the Royal Society of London*, 1832.
- [70] E. B. Rosa and L. Cohen, *Formulas and tables for the calculation of mutual and self-inductance*, W. D. of commerce and labor, Eds. Bulletin of the Bureau of Standards, 1907-8.
- [71] J. C. Poggendorff, *Zur Theorie der Entaldung einer Leydener Flasche; von G. Kirchhoff*. Annalen der Physik und Chemie, 1864.
- [72] E. B. Rosa and L. Cohen, *On the self-inductance of circles*, W. D. of commerce and labor, Eds. Bulletin of the Bureau of Standards, 1907-8.
- [73] M. J. Nave, "On modeling the common mode inductor," *IEEE International Symposium on Eletromagnetic Compatibility*, 1991.
- [74] M. L. Heldwein, L. Dalessandro, and J. W. Kolar, "The three-phase common-mode inductor: Modeling and design issue," *IEEE Transactions on Industrial Electronics*, vol. 58, 2011.
- [75] G. Kron, *Tensors for circuits*. Dover Publications, 1959.
- [76] P. Durand, O. Maurice, and A. Reineix, "The Kron formalism of tensor analysis, applied to graphs, networks and antennas," in *IAENG Transactions on Engineering Sciences*, 2014.
- [77] R. A. Bruns, "Introduction to the tensor analysis of electrical networks," Ph.D. dissertation, Oregon state college, 1943.
- [78] G. Coen and D. De Zutter, "Reduction of circuit complexity by elimination of internal nodes in the circuit modeling of planar interconnection structures," in *Proceedings of the 12th International Zürich Symposium and Technical Exhibition on Electromagnetic Compatibility*, 1997.
- [79] O. Maurice, F. Lafon, and F. de Daran, "Determination of the EMC risk of a complex system using the tensorial analysis of network," in *2EMC - Rouen*, 2005.

-
- [80] T. M. Zeef, T. H. Hubing, T. P. Van Doren, and D. Pommerenke, "Analysis of simple two-capacitor low-pass filters," in *IEEE Transactions on electromagnetic compatibility*, 2003.

Appendix A

Tools development

A.1 Equivalent Surface Extractor - Measurement bench

Equivalent Surface Extractor (ESE) (Fig. A.1) is a tool for extracting an equivalent coupling model of a passive component from TEM cell measurements. Once the equivalent coupling model is extracted, the surface (for capacitors and inductors) or surfaces (for CMCs) can be used in Global Filter Design tool (Sect. A.2) for coupling coefficient calculation and filter performance prediction.

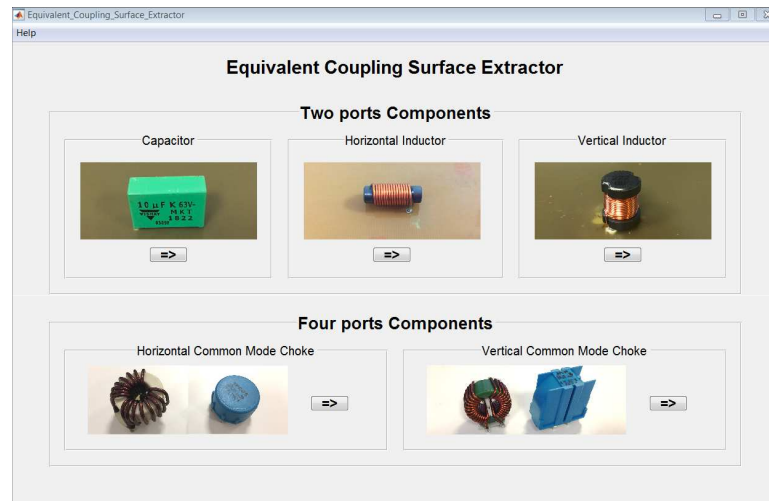


Figure A.1: ESE tool main interface

There is one menu per component: for capacitors, horizontal and vertical inductors and horizontal and verticals CMCs. This tool is linked to its test bench as presented in Fig. A.2. The test bench is useful, in terms of precision and regularity, to perform both measurements for capacitors and inductors, and also the twelve measurements for CMCs.

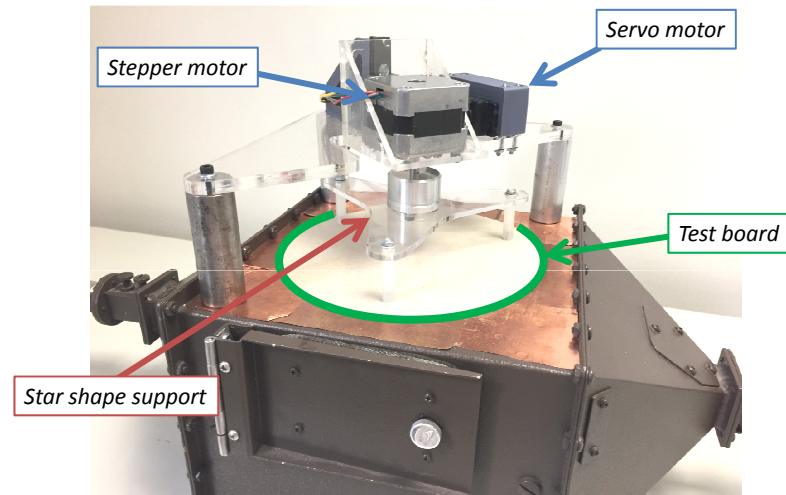


Figure A.2: ESE test bench

The process is the same for all the components. Actually, once the tool is launched, the user choose the menu dedicated to the component he wants to characterize and then, a new interface opens (Fig. A.3) and the initialization begins. The laptop connected to the test bench checks that the Arduino module is correctly connected, that the VNA also and that the associated calibration is recalled.

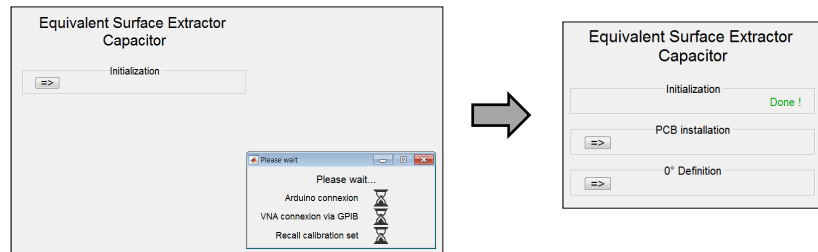


Figure A.3: ESE tool - Initialization

Then, the user can access to the PCB installation menu. In that menu, the different steps for PCB installation are described. When the step is finished the user can validate it and go further as presented in Fig. A.4.

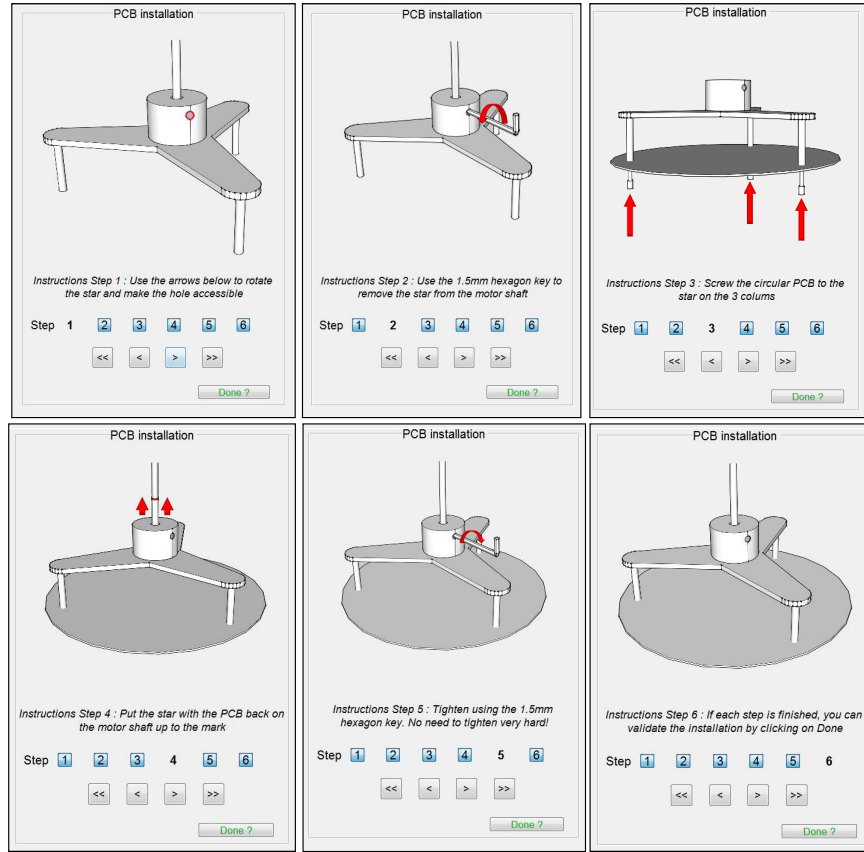


Figure A.4: ESE tool - PCB installation

The installation is divided into 6 steps:

- Step #1: the servo motor lift the star to give the possibility to the user to rotate it with the stepper motor. The objective is to make accessible the hole to remove the star.
- Step #2: the user can remove the star from stepper motor shaft.
- Step #3: the circular PCB can be screwed by the user.
- Step #4 and #5: the star can be put back to its place.
- Step #6: Validate the installation.

Then, the 0° definition menu must be done. In that menu (Fig. A.5), the user can rotate the star until the coupling surface and the magnetic field are collinear.

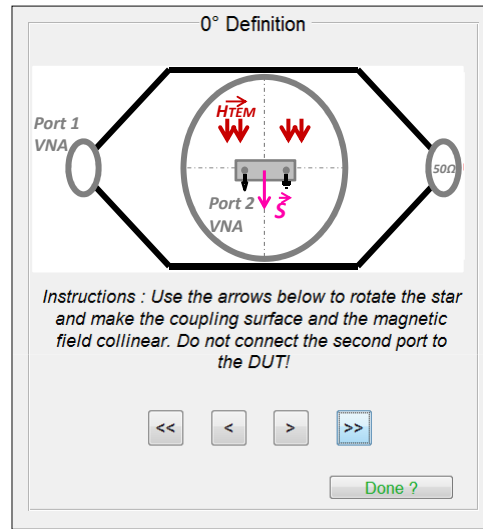


Figure A.5: ESE tool - 0° Definition

The menu dedicated to measurements can be used as presented in Fig. A.6. Once the PCB is connected to the second port of the VNA the user can press the “start measurements” button and, thus, both measurements for the capacitors are performed and saved. For inductors, two measurements are performed also whereas for CMCs, there are twelve measurements every 30°. During the measurements, the user can attend the progression with the picture is updated at each step of the measurements (fixed position, rotation etc.).

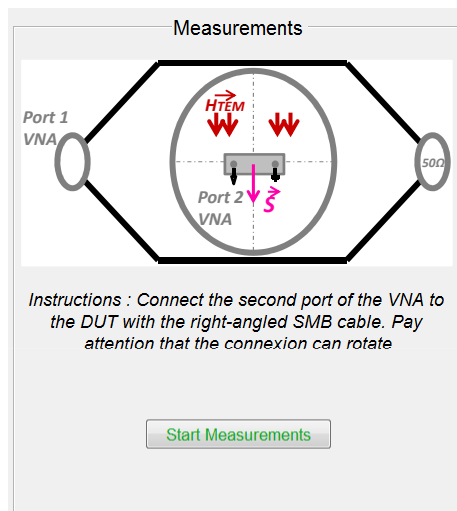


Figure A.6: ESE tool - Measurements

Once the measurements are performed, only the electrical equivalent model remains to be fulfilled to extract the model. Finally, Fig. A.7 presents an example of the fulfilled interface for the characterization of a 470nF-capacitor.

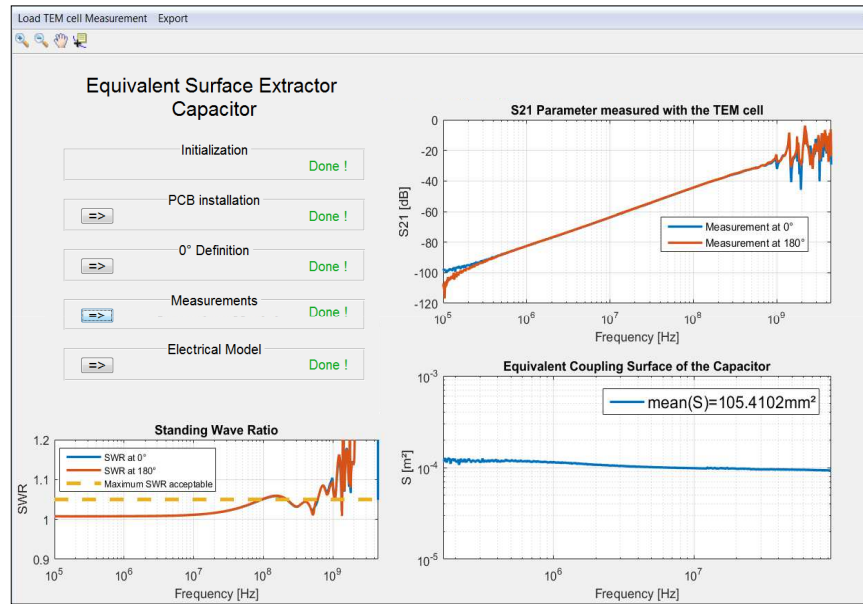


Figure A.7: ESE tool - Capacitor example

A.2 Global Filter Design

One of the major objective of the thesis work was to develop a generic and automatic tool for filter design. Actually, that tool is necessary for filter performance prediction whatever the structure and whatever the topology.

Therefore, Global Filter Design (GFD) is a tool for extracting coupling coefficient between two components or extracting a filter attenuation for different structure. Once the equivalent model (with the couplings) is extracted, the netlist file (.lib) of the filter can be generated. Indeed, the model can be used in a global product simulation as shown in Sect. 1.2 in order to use the filter in its real environment.

The tool is divided into two parts (Fig. A.8):

- Extraction of coupling coefficients between capacitors, inductors and common mode chokes.
- Prediction of filter performance considering inter-component coupling for five fixed structures (LC, Pi, T, Cascade and complete filter structures) and a custom structure which can be built up by the user from basic elements.

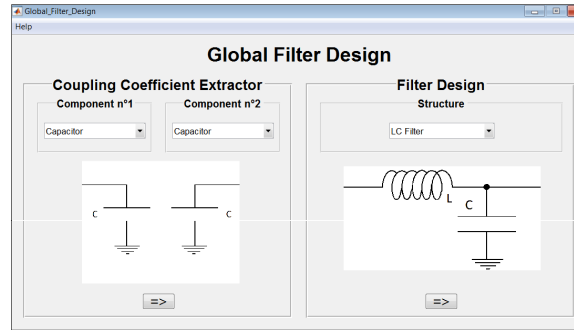


Figure A.8: GFD tool main interface

A.2.1 Component menus

GFD tool is organized with one menu per component. Actually, inside those menus, the user must fill in all the required parameters for mutual inductance calculation.

Capacitor menu:

The capacitor menu is divided into different topics. The first one is dedicated to the geometrical properties of the component, the capacitor width, length and the distance between pins. Then, the equivalent electrical model is required, including the capacitance value, the equivalent series inductance and the equivalent series resistance. Finally, the center position must be specified, considering that the first component is always fixed at the origin. The final point is to fill in the equivalent coupling surface value. This parameter is extracted from TEM cell measurements (or from geometrical parameters as seen in Sect. 2.5.3) and the tool dedicated to this surface extraction is described in A.1.

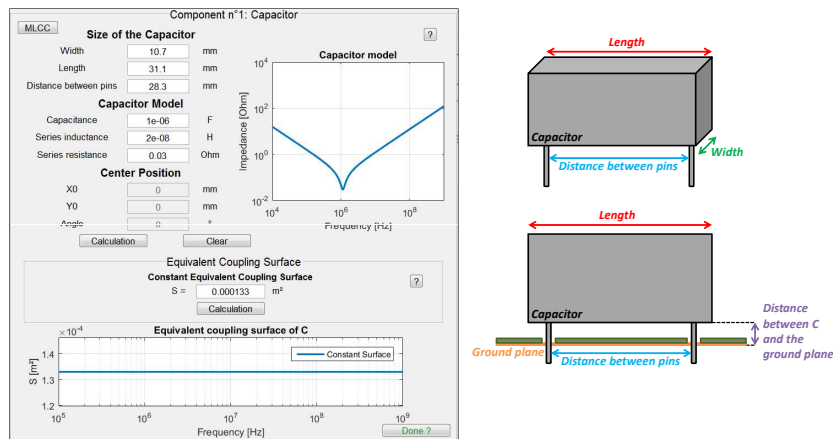


Figure A.9: Capacitor menu and its associated caption

For MLCC capacitors, the menu is simplified because the geometrical properties, the equivalent electrical model and the equivalent coupling surface only depend on the technology, the package and the capacitance value. Therefore, Fig. A.10 presents this simplified menu.

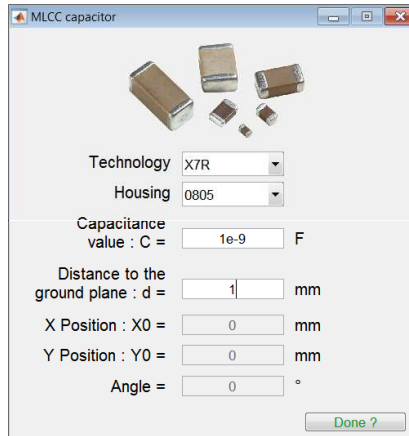


Figure A.10: Capacitor menu and its associated caption

Inductor menu:

The inductor menu depends on inductor nature. Actually, there are horizontal and vertical inductor and, therefore, there are two different menus as presented in Fig. A.11 and Fig. A.12. However, whether it is for horizontal or vertical inductors, the menus are organized in the same way. The geometrical properties are required, the equivalent electrical model and then, the center position of the component. Finally, the equivalent coupling surface extracted from ESE tool is entered. This surface includes the influence of the magnetic material building up the coil.

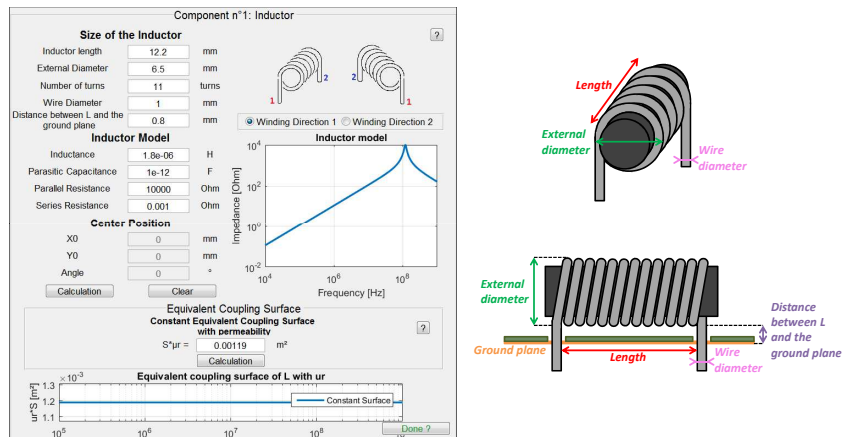


Figure A.11: Horizontal inductor menu and its associated caption

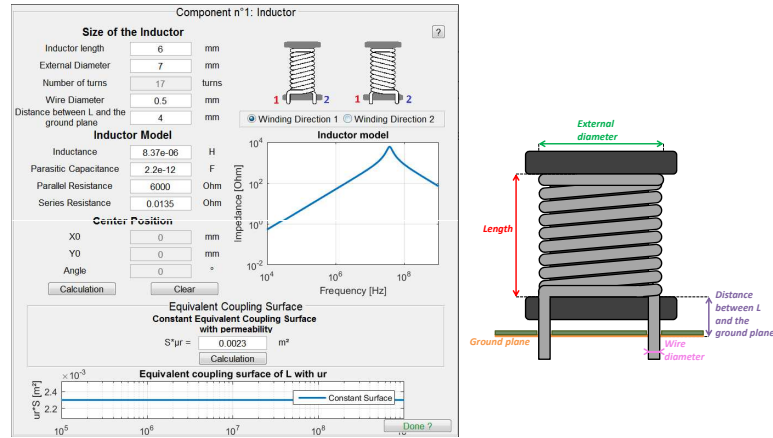


Figure A.12: Vertical inductor menu and its associated caption

Common Mode Choke menu:

Like for inductors, there are also two different menus for CMCs, one for horizontal CMCs (Fig. A.13) and the other for vertical CMCs (Fig. A.14). Geometries are described for both types of CMC. Then the DM and CM model and the center position must be entered. Finally, the ten surfaces that describe the equivalent coupling model of the CMC are specified. Those values are directly extracted from the ESE tool.

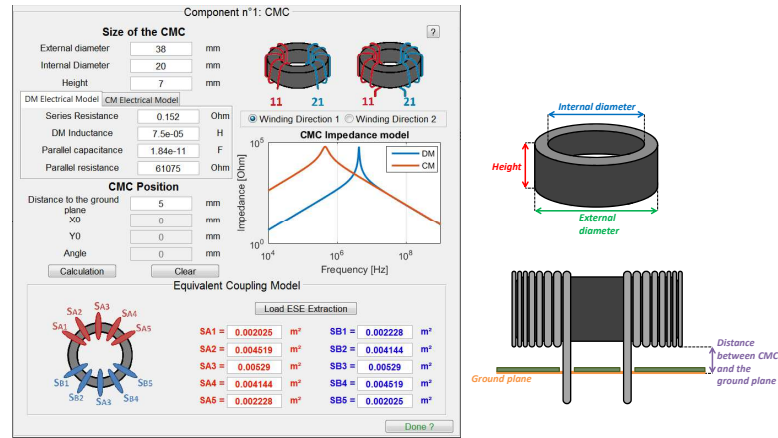


Figure A.13: Horizontal CMC menu and its associated caption

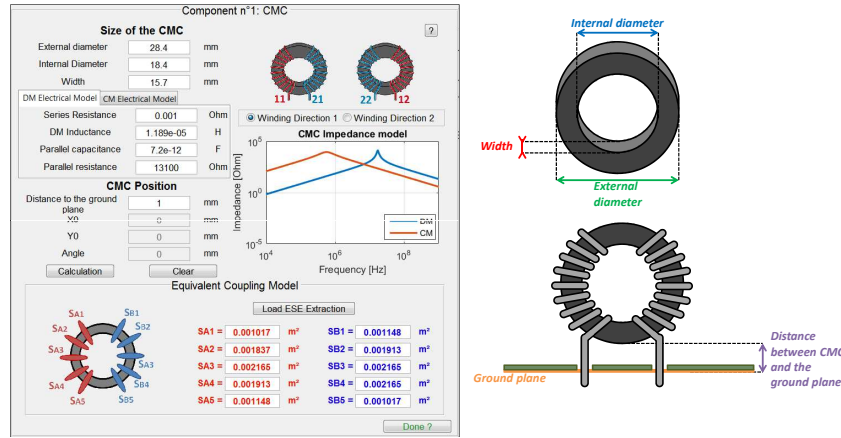


Figure A.14: Vertical CMC menu and its associated caption

A.2.2 Component connections

Component connections are very important because they set the sign of the mutual inductances between the components. Fig. A.15 provides an example is given for components connections for a filter composed of a DM capacitor, a CMC, another DM capacitor and two CM capacitors.

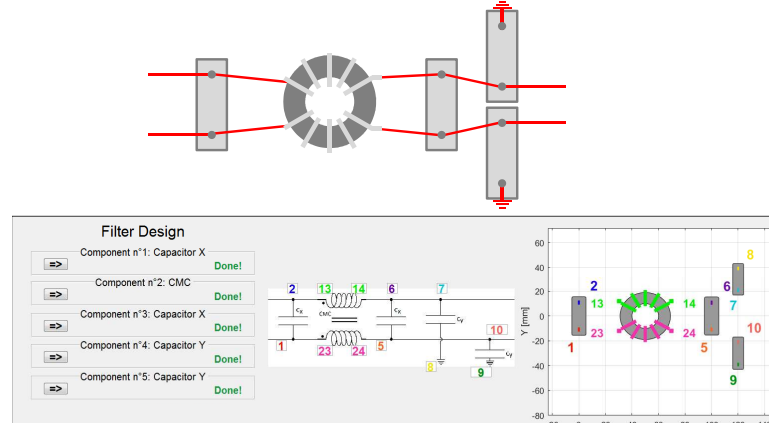


Figure A.15: Example of component connections

A.2.3 Calculation of filter performance

Once the component menus are filled in and the component connections specified, a new menu appears for attenuation calculation. All that remains is to click on the corresponding arrow in order to launch the calculation (very little time). Finally, it is possible to compare several topologies (for different positions of the components). It is also possible to enable and disable one or more couplings in order to identify which ones are destructive.

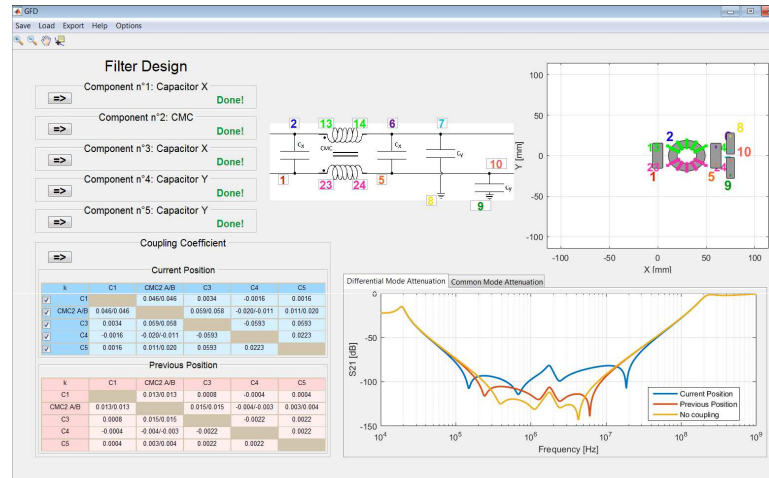


Figure A.16: Example of GFD calculation

Appendix B

Magnetostatic field calculation

B.1 Application case: Capacitor

The objective of this part is to detail the calculation of the magnetic field generated by a capacitor considering the four segments as presented in Fig. 3.7. Thus, the calculation is divided into four steps:

- For b_1 , it can be considered that $\vec{r} = \vec{r}_p - \vec{r}^{\hat{j}}$ with $\vec{r}_p = \begin{pmatrix} x_p \\ y_p \\ z_p \end{pmatrix} \cdot \begin{pmatrix} \hat{i} \\ \hat{j} \\ \hat{k} \end{pmatrix}$

$$\text{and } \vec{r}^{\hat{j}} = \begin{pmatrix} 0 \\ -\frac{d_{pins}}{2} \\ integ_z \end{pmatrix} \cdot \begin{pmatrix} \hat{i} \\ \hat{j} \\ \hat{k} \end{pmatrix}.$$

Furthermore, $integ_z = [-h_{pins} : h_{pins}]$ is the integration domain on which the calculation is made

$$\text{for segment } b_1. \vec{r} \text{ can be calculated with } \vec{r} = \vec{r}_p - \vec{r}^{\hat{j}} = \begin{pmatrix} x_p \\ y_p + \frac{d_{pins}}{2} \\ z_p - integ_z \end{pmatrix} \cdot \begin{pmatrix} \hat{i} \\ \hat{j} \\ \hat{k} \end{pmatrix}.$$

$$\text{Thus } r = \sqrt{x_p^2 + y_p^2 + z_p^2 + \frac{d_{pins}^2}{4} + integ_z^2 + y_p d_{pins} - 2z_p integ_z}.$$

$$\text{It is also possible to calculate } \vec{dS} = \left(\frac{d\vec{r}}{dinteg_z} \right) dinteg_z = \begin{pmatrix} 0 \\ 0 \\ 1 \end{pmatrix} \cdot \begin{pmatrix} \hat{i} \\ \hat{j} \\ \hat{k} \end{pmatrix} dinteg_z.$$

$$\text{Finally, } \overrightarrow{dB_{b_1}} = \frac{\mu I}{4\pi} \frac{\hat{r} \times \vec{dS}}{r^2} = \frac{\mu_0 I}{4\pi} \frac{1}{r^3} \begin{pmatrix} y_p + \frac{d_{pins}}{2} \\ -x_p \\ 0 \end{pmatrix} \cdot \begin{pmatrix} \hat{i} \\ \hat{j} \\ \hat{k} \end{pmatrix} dinteg_z$$

- For b_2 , it can be considered that $\vec{r} = \vec{r}_p - \vec{r}^{\hat{j}}$ with $\vec{r}_p = \begin{pmatrix} x_p \\ y_p \\ z_p \end{pmatrix} \cdot \begin{pmatrix} \hat{i} \\ \hat{j} \\ \hat{k} \end{pmatrix}$

$$\text{and } \vec{r}^{\hat{j}} = \begin{pmatrix} 0 \\ integ_y \\ h_{pins} \end{pmatrix} \cdot \begin{pmatrix} \hat{i} \\ \hat{j} \\ \hat{k} \end{pmatrix}.$$

$$\vec{r} \text{ can be calculated with } \vec{r} = \vec{r}_p - \vec{r}^j = \begin{pmatrix} x_p \\ y_p - \text{integ}_y \\ z_p - h_{pins} \end{pmatrix} \cdot \begin{pmatrix} \hat{i} \\ \hat{j} \\ \hat{k} \end{pmatrix}.$$

$$\text{Thus } r = \sqrt{x_p^2 + y_p^2 + z_p^2 + h_{pins}^2 + \text{integ}_y^2 - 2.(y_p \text{integ}_y + z_p h_{pins})}.$$

$$\text{It is also possible to calculate } \vec{dS} = \left(\frac{d\vec{r}}{d\text{integ}_y} \right) d\text{integ}_y = \begin{pmatrix} 0 \\ 1 \\ 0 \end{pmatrix} \cdot \begin{pmatrix} \hat{i} \\ \hat{j} \\ \hat{k} \end{pmatrix} d\text{integ}_y.$$

$$\text{Finally, } \vec{dB}_{b_2} = \frac{\mu I}{4\pi} \frac{\hat{r} \times \vec{dS}}{r^2} = \frac{\mu_0 I}{4\pi} \frac{1}{r^3} \begin{pmatrix} h_{pins} - z_p \\ 0 \\ x_p \end{pmatrix} \cdot \begin{pmatrix} \hat{i} \\ \hat{j} \\ \hat{k} \end{pmatrix} d\text{integ}_y$$

- For b_3 , it can be considered that $\vec{r} = \vec{r}_p - \vec{r}^j$ with $\vec{r}_p = \begin{pmatrix} x_p \\ y_p \\ z_p \end{pmatrix} \cdot \begin{pmatrix} \hat{i} \\ \hat{j} \\ \hat{k} \end{pmatrix}$

$$\text{and } \vec{r}^j = \begin{pmatrix} 0 \\ \frac{d_{pins}}{2} \\ -\text{integ}_z \end{pmatrix} \cdot \begin{pmatrix} \hat{i} \\ \hat{j} \\ \hat{k} \end{pmatrix}.$$

$$\vec{r} \text{ can be calculated with } \vec{r} = \vec{r}_p - \vec{r}^j = \begin{pmatrix} x_p \\ y_p - \frac{d_{pins}}{2} \\ z_p + \text{integ}_z \end{pmatrix} \cdot \begin{pmatrix} \hat{i} \\ \hat{j} \\ \hat{k} \end{pmatrix}.$$

$$\text{Thus } r = \sqrt{x_p^2 + y_p^2 + z_p^2 + \frac{d_{pins}^2}{4} + \text{integ}_z^2 - y_p d_{pins} + 2z_p \text{integ}_z}.$$

$$\text{It is also possible to calculate } \vec{dS} = \left(\frac{d\vec{r}}{d\text{integ}_z} \right) d\text{integ}_z = \begin{pmatrix} 0 \\ 0 \\ -1 \end{pmatrix} \cdot \begin{pmatrix} \hat{i} \\ \hat{j} \\ \hat{k} \end{pmatrix} d\text{integ}_z.$$

$$\text{Finally, } \vec{dB}_{b_3} = \frac{\mu I}{4\pi} \frac{\hat{r} \times \vec{dS}}{r^2} = \frac{\mu_0 I}{4\pi} \frac{1}{r^3} \begin{pmatrix} \frac{d_{pins}}{2} - y_p \\ x_p \\ 0 \end{pmatrix} \cdot \begin{pmatrix} \hat{i} \\ \hat{j} \\ \hat{k} \end{pmatrix} d\text{integ}_z$$

- For b_4 , it can be considered that $\vec{r} = \vec{r}_p - \vec{r}^j$ with $\vec{r}_p = \begin{pmatrix} x_p \\ y_p \\ z_p \end{pmatrix} \cdot \begin{pmatrix} \hat{i} \\ \hat{j} \\ \hat{k} \end{pmatrix}$

$$\text{and } \vec{r}^j = \begin{pmatrix} 0 \\ -\text{integ}_y \\ -h_{pins} \end{pmatrix} \cdot \begin{pmatrix} \hat{i} \\ \hat{j} \\ \hat{k} \end{pmatrix}.$$

Furthermore, $\text{integ}_y = [-\frac{d_{pins}}{2} : \frac{d_{pins}}{2}]$ is the integration domain on which the calculation is made for segment b_4 .

$$\vec{r} \text{ can be calculated with } \vec{r} = \vec{r}_p - \vec{r}^j = \begin{pmatrix} x_p \\ y_p + \text{integ}_y \\ z_p + h_{pins} \end{pmatrix} \cdot \begin{pmatrix} \hat{i} \\ \hat{j} \\ \hat{k} \end{pmatrix}.$$

$$\text{Thus } r = \sqrt{x_p^2 + y_p^2 + z_p^2 + h_{pins}^2 + \text{integ}_y^2 + 2.(y_p \text{integ}_y + z_p h_{pins})}.$$

$$\text{It is also possible to calculate } \vec{dS} = \left(\frac{d\vec{r}}{d\text{integ}_y} \right) d\text{integ}_y = \begin{pmatrix} 0 \\ -1 \\ 0 \end{pmatrix} \cdot \begin{pmatrix} \hat{i} \\ \hat{j} \\ \hat{k} \end{pmatrix} d\text{integ}_y.$$

Finally, $\overrightarrow{dB_{b_4}} = \frac{\mu I}{4\pi} \frac{\hat{r} \times \overrightarrow{dS}}{r^2} = \frac{\mu_0 I}{4\pi} \frac{1}{r^3} \begin{pmatrix} h_{pins} + z_p \\ 0 \\ -x_p \end{pmatrix} \cdot \begin{pmatrix} \hat{i} \\ \hat{j} \\ \hat{k} \end{pmatrix} d\text{integ}_y$

Finally, by integrating the four contributions along the current path, the level and the direction of the magnetic field generated by a capacitor can be estimated.

B.2 Application case: horizontal inductor

For the horizontal inductor, the calculation must be divided into two steps. The first one is to calculate the direct magnetic field generated by the inductor, by considering each turn as a single loop. The second step is to consider the ground plane by taking into account the reflected field on it and, therefore, the image of each loop.

The loops are located in the (Y,Z) plane and the loops are spaced along X by the distance between adjacent turns.

Let us consider the Fig. B.1 to determine X_n , Y_n , and Z_n , the distances between the center of the loop n and the point P.

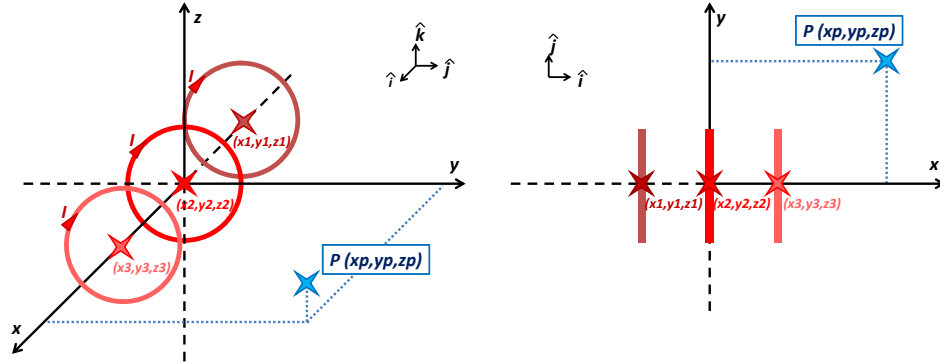


Figure B.1: Example of field calculation for three loops - 3D - Projection on XY plane

Thus, the Biot and Savart law can be applied. The first step is to consider $\overrightarrow{r'} = \overrightarrow{r_p} - \overrightarrow{r^i}$ with $\overrightarrow{r_p} = \begin{pmatrix} X_n \\ Y_n \\ Z_n \end{pmatrix} \cdot \begin{pmatrix} \hat{i} \\ \hat{j} \\ \hat{k} \end{pmatrix}$ and $\overrightarrow{r^i} = \begin{pmatrix} 0 \\ R \cos \phi \\ R \sin \phi \end{pmatrix} \cdot \begin{pmatrix} \hat{i} \\ \hat{j} \\ \hat{k} \end{pmatrix}$.

Furthermore, $\phi = [0 : 2\pi]$ is the integration domain and so:

$$\overrightarrow{r'} = \overrightarrow{r_p} - \overrightarrow{r^i} = \begin{pmatrix} X_n \\ Y_n - R \cos \phi \\ Z_n - R \sin \phi \end{pmatrix} \cdot \begin{pmatrix} \hat{i} \\ \hat{j} \\ \hat{k} \end{pmatrix}.$$

Thus $r = \sqrt{X_n^2 + Y_n^2 + Z_n^2 + R^2 - 2R \cdot (Y_n \cos \phi + Z_n \sin \phi)}$.

It is also possible to calculate $\overrightarrow{dS} = \left(\frac{d\overrightarrow{r'}}{d\phi} \right) d\phi = R \begin{pmatrix} 0 \\ -\sin \phi \\ \cos \phi \end{pmatrix} \cdot \begin{pmatrix} \hat{i} \\ \hat{j} \\ \hat{k} \end{pmatrix} d\phi$.

Finally:

$$\overrightarrow{dB} = \frac{\mu I}{4\pi} \frac{\hat{r} \times \overrightarrow{dS}}{r^2} = \frac{\mu_0 \mu_r I R}{4\pi} \frac{1}{r^3} \begin{pmatrix} Y_n \cos \phi + Z_n \sin \phi - R \\ -X_n \cos \phi \\ -X_n \sin \phi \end{pmatrix} \cdot \begin{pmatrix} \hat{i} \\ \hat{j} \\ \hat{k} \end{pmatrix} d\phi$$

By integrating the contributions of all turns and their images, the level and the direction of the magnetic field generated by a horizontal inductor can be calculated.

B.3 Application case: vertical inductor

As far as the vertical inductor is concerned, the principle is the same as for horizontal inductor but, this time, the loops are located in the (X,Y) plane and the loops are spaced along Z by the distance between adjacent turns (Fig. B.2).

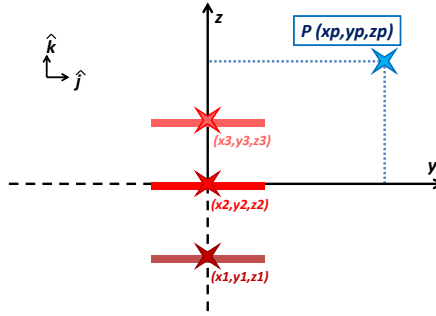


Figure B.2: Example of field calculation for three loops - Projection on YZ plane

Then the Biot and Savart calculation performed for horizontal inductor is re-used and, therefore,

$$\vec{r} = \vec{r}_p - \vec{r}^j \text{ with } \vec{r}_p = \begin{pmatrix} X_n \\ Y_n \\ Z_n \end{pmatrix} \cdot \begin{pmatrix} \hat{i} \\ \hat{j} \\ \hat{k} \end{pmatrix} \text{ and } \vec{r}^j = \begin{pmatrix} R \cos \phi \\ R \sin \phi \\ 0 \end{pmatrix} \cdot \begin{pmatrix} \hat{i} \\ \hat{j} \\ \hat{k} \end{pmatrix}$$

Furthermore, $\phi = [0 : 2\pi]$ is the integration domain and so:

$$\vec{r} = \vec{r}_p - \vec{r}^j = \begin{pmatrix} X_n - R \cos \phi \\ Y_n - R \sin \phi \\ Z_n \end{pmatrix} \cdot \begin{pmatrix} \hat{i} \\ \hat{j} \\ \hat{k} \end{pmatrix}.$$

$$\text{Thus } r = \sqrt{X_n^2 + Y_n^2 + Z_n^2 + R^2 - 2R(X_n \cos \phi + Y_n \sin \phi)}.$$

$$\text{It is also possible to calculate } d\vec{S} = \left(\frac{d\vec{r}^j}{d\phi} \right) d\phi = R \begin{pmatrix} -\sin \phi \\ \cos \phi \\ 0 \end{pmatrix} \cdot \begin{pmatrix} \hat{i} \\ \hat{j} \\ \hat{k} \end{pmatrix} d\phi.$$

Then:

$$d\vec{B} = \frac{\mu I}{4\pi} \frac{\hat{r} \times d\vec{S}}{r^2} = \frac{\mu_0 \mu_r I R}{4\pi} \frac{1}{r^3} \begin{pmatrix} -Z_n \cos \phi \\ -Z_n \sin \phi \\ X_n \cos \phi + Y_n \sin \phi - R \end{pmatrix} \cdot \begin{pmatrix} \hat{i} \\ \hat{j} \\ \hat{k} \end{pmatrix} d\phi$$

considering that X_n , Y_n , and Z_n are the distances between the center of the loop n to the point P.

Finally, by integrating the contributions of all turns and their images, the level and the direction of the magnetic field generated by a vertical inductor can be calculated.

B.4 Application case: horizontal common mode choke

For the horizontal CMC, the equivalent emission surfaces are represented as in Fig. B.3. Actually, in the models that are developed with the TEM cell, the ten surfaces have a fixed orientation and depend on the equivalent coupling model.

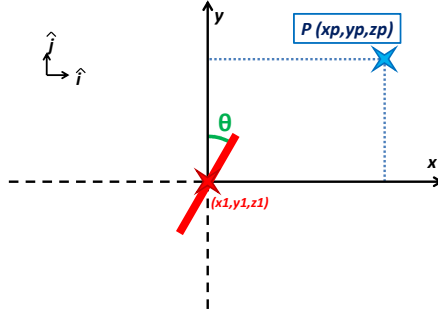


Figure B.3: Example of field calculation for one loop - Projection on XY plane

Therefore, by the same reasoning as for inductor, it gives $\vec{r}_p = \begin{pmatrix} X_n \\ Y_n \\ Z_n \end{pmatrix} \cdot \begin{pmatrix} \hat{i} \\ \hat{j} \\ \hat{k} \end{pmatrix}$ and $\vec{r} = \begin{pmatrix} R \cos \phi \sin \theta \\ R \cos \phi \cos \theta \\ R \sin \phi \end{pmatrix} \cdot \begin{pmatrix} \hat{i} \\ \hat{j} \\ \hat{k} \end{pmatrix}$ considering that θ is the orientation of the current loop regarding the y axes.

Therefore, for the ten surfaces, as extracted in ESE tool, those orientations are fixed and $\theta = [-60^\circ \quad -30^\circ \quad 0^\circ \quad 30^\circ \quad 60^\circ \quad 60^\circ \quad 30^\circ \quad 0^\circ \quad -30^\circ \quad -60^\circ]$.

Furthermore, $\phi = [0 : 2\pi]$ is the integration domain and so:

$$\vec{r} = \vec{r}_p - \vec{r} = \begin{pmatrix} X_n - R \cos \phi \sin \theta \\ Y_n - R \cos \phi \cos \theta \\ Z_n - R \sin \phi \end{pmatrix} \cdot \begin{pmatrix} \hat{i} \\ \hat{j} \\ \hat{k} \end{pmatrix}.$$

Thus $r = \sqrt{X_n^2 + Y_n^2 + Z_n^2 + R^2 - 2R.(X_n \cos \phi \sin \theta + Y_n \cos \phi \cos \theta + Z_n \sin \phi)}$.

It is also possible to calculate $d\vec{S} = \left(\frac{d\vec{r}}{d\phi}\right)d\phi = R \begin{pmatrix} -\sin \phi \sin \theta \\ -\sin \phi \cos \theta \\ \cos \phi \end{pmatrix} \cdot \begin{pmatrix} \hat{i} \\ \hat{j} \\ \hat{k} \end{pmatrix} d\phi$.

Then:

$$\vec{dB} = \frac{\mu I}{4\pi} \frac{\hat{r} \times d\vec{S}}{r^2} = \frac{\mu_0 \mu_{DM} I R}{4\pi} \frac{1}{r^3} \begin{pmatrix} Y_n \cos \phi + Z_n \sin \phi \cos \theta - R \cos \theta \\ -X_n \cos \phi - Z_n \sin \phi \sin \theta + R \sin \theta \\ -X_n \sin \phi \cos \theta + Y_n \sin \phi \sin \theta \end{pmatrix} \cdot \begin{pmatrix} \hat{i} \\ \hat{j} \\ \hat{k} \end{pmatrix} d\phi$$

It must be noticed that, when $\theta = 0^\circ$, the formula for the straight horizontal inductor is recovered.

Finally, by integrating the contributions of all turns and their images, the level and the direction of the magnetic field generated by a horizontal CMC can be calculated.

B.5 Application case: vertical common mode choke

As far as vertical CMC is concerned, it is based on the same principle as for horizontal CMC but this time, the equivalent emission surfaces are represented as in Fig. B.4. Actually, in the models that are developed with the TEM cell, the ten surfaces have a fixed orientation and depend on the equivalent coupling model.

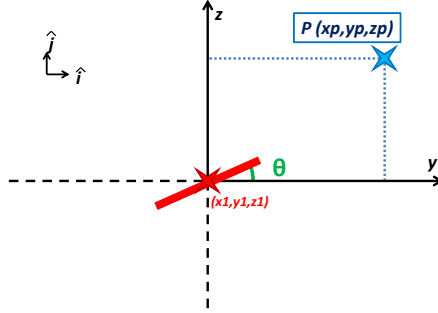


Figure B.4: Example of field calculation for one loop - Projection on YZ plane

Therefore, it gives $\vec{r}_p = \begin{pmatrix} X_n \\ Y_n \\ Z_n \end{pmatrix} \cdot \begin{pmatrix} \hat{i} \\ \hat{j} \\ \hat{k} \end{pmatrix}$ and $\vec{r} = \begin{pmatrix} R\cos\phi \\ R\sin\phi\cos\theta \\ R\sin\phi\sin\theta \end{pmatrix} \cdot \begin{pmatrix} \hat{i} \\ \hat{j} \\ \hat{k} \end{pmatrix}$ considering

that θ is the orientation of the current loop regarding the y axes.

Therefore, for the ten surfaces, as extracted in ESE tool, those orientations are fixed and $\theta = [-60^\circ \ -30^\circ \ 0^\circ \ 30^\circ \ 60^\circ \ 60^\circ \ 30^\circ \ 0^\circ \ -30^\circ \ -60^\circ]$.

Furthermore, $\phi = [0 : 2\pi]$ is the integration domain and so:

$$\vec{r}' = \vec{r}_p - \vec{r} = \begin{pmatrix} X_n - R\cos\phi \\ Y_n - R\sin\phi\cos\theta \\ Z_n - R\sin\phi\sin\theta \end{pmatrix} \cdot \begin{pmatrix} \hat{i} \\ \hat{j} \\ \hat{k} \end{pmatrix}.$$

Thus $r = \sqrt{X_n^2 + Y_n^2 + Z_n^2 + R^2 - 2R.(X_n\cos\phi + Y_n\sin\phi\cos\theta + Z_n\sin\phi\sin\theta)}$.

It is also possible to calculate $\vec{dS} = (\frac{d\vec{r}'}{d\phi})d\phi = R \begin{pmatrix} -\sin\phi \\ \cos\phi\cos\theta \\ \cos\phi\sin\theta \end{pmatrix} \cdot \begin{pmatrix} \hat{i} \\ \hat{j} \\ \hat{k} \end{pmatrix} d\phi$.

Then:

$$\vec{dB} = \frac{\mu I}{4\pi} \frac{\hat{r} \times \vec{dS}}{r^2} = \frac{\mu_0 \mu_{DM} I R}{4\pi} \frac{1}{r^3} \begin{pmatrix} Y_n\cos\phi\sin\theta - Z_n\cos\phi\cos\theta \\ -X_n\cos\phi\sin\theta - Z_n\sin\phi + R\sin\theta \\ X_n\cos\phi\cos\theta + Y_n\sin\phi - R\cos\theta \end{pmatrix} \cdot \begin{pmatrix} \hat{i} \\ \hat{j} \\ \hat{k} \end{pmatrix} d\phi$$

It must be noticed that, when $\theta = 0^\circ$, the formula for the straight vertical inductor is recovered.

Finally, by integrating the contributions of all turns and their images, the level and the direction of the magnetic field generated by a vertical CMC can be calculated.

List of Publications during PhD

Contributions to international peer-reviewed journals

- [1] M. Stojanovic, F. Lafon, S. Op't Land, R. Perdriau and M. Ramdani, "Determination of Equivalent Coupling Surface of Passive Components Using the TEM Cell", *IEEE Transactions on Electromagnetic Compatibility*, vol. 60, pp. 298-309, July 2017.
- [2] M. Stojanovic, F. Lafon, R. Perdriau and M. Ramdani, "Accurate Analytical Prediction of EMI Filter Attenuation Considering Inter-Component Coupling Phenomena", *IEEE Transactions on Electromagnetic Compatibility*, Accepted on 24 June.

Contribution to national peer-reviewed journals

- [3] M. Stojanovic, "Filtrage Antiparasite dans les circuits électroniques", *Techniques de l'Ingénieur*, E3580, August 2018.

Contribution to research book

- [4] P. Durand, S. Leman, O. Maurice, B. Ravelo, A. Reineix, Y. Sohor, M. Stojanovic, "Application de la méthode de Kron à la résolution de problèmes de CEM: exercices corrigés", *Bookelis*, October 2017.

Articles in international conferences

- [5] M. Stojanovic, F. Lafon, P. Fernandez-Lopez, S. Op't Land and R. Perdriau, "Modified Kron's Method (MKME) applied for EMC Optimization, applied to an EMC filter", *7th Asia-Pacific International Symposium on Electromagnetic Compatibility (APEMC)*, 2016.
- [6] M. Stojanovic, F. Lafon, R. Perdriau and M. Ramdani, "Determination of the Coupling Model of Common Mode Chokes using a TEM cell", *International Symposium and Exhibition on Electromagnetic Compatibility (EMC Europe)*, 2017.

Articles in national conferences

- [7] M. Stojanovic, T. D. Pham, T. Q. V. Hoang, P. Fernandez-Lopez and F. Lafon, "Common Mode Choke modeling taking into account Dispersive Material for Conducted Emission Simulations", *18ème Colloque International et Exposition sur la Compatibilité ElectroMagnétique (CEM)*, 2016.
- [8] M. Stojanovic, F. Lafon, R. Perdriau and M. Ramdani, "Self-inductance Prediction for Straight and Toroidal Air Core Coils", *19ème Colloque International et Exposition sur la Compatibilité ElectroMagnétique (CEM)*, 2018.
- [9] K. Loudière, F. Lafon, P. Fernandez-Lopez, M. Stojanovic, "Capacitor robustness prediction in ESD design", *19ème Colloque International et Exposition sur la Compatibilité ElectroMagnétique (CEM)*, 2018.

AVIS DU JURY SUR LA REPRODUCTION DE LA THESE SOUTENUE

Titre de la thèse:

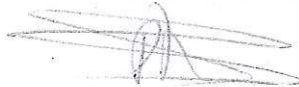
Etude et modélisation des couplages inter-composants pour la conception des filtres - Application aux filtres du domaine automobile

Nom Prénom de l'auteur : STOJANOVIC MARINE

Membres du jury :

- Monsieur BESNIER Philippe
- Madame DUCHAMP Geneviève
- Monsieur REINEIX Alain
- Monsieur VOLLAIRE Christian
- Monsieur RAMDANI Mohamed
- Monsieur PERDRIAU Richard
- Monsieur MAURICE Olivier
- Monsieur LAFON Frédéric

Président du jury :



Philippe BESNIER

Date de la soutenance : 14 Septembre 2018

Reproduction de la these soutenue

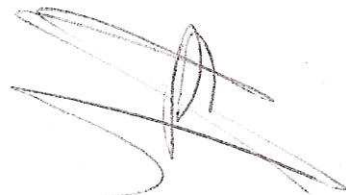
- ☒ Thèse pouvant être reproduite en l'état
☐ Thèse pouvant être reproduite après corrections suggérées

Fait à Rennes, le 14 Septembre 2018

Signature du président de jury

Le Directeur,

M'hamed DRISSI



Titre : Etude et Modélisation des Couplages Inter-Composants pour la Conception de Filtres : Application aux filtres contre les interférences électromagnétiques du domaine automobile

Mots clés: Compatibilité Electromagnétique, Filtre, Couplage, Composant Passif, Modélisation

Résumé: La CEM (Compatibilité ElectroMagnétique) est de plus en plus importante dans la conception des systèmes électroniques et plus particulièrement dans le domaine automobile. En effet, avec la densification de l'électronique dans les véhicules, les problèmes liés à la CEM sont de plus en plus fréquents. Ainsi, afin de limiter ces interférences électromagnétiques, des filtres correctement dimensionnés et implémentés doivent être utilisés. Chaque filtre est dimensionné en tenant compte de l'environnement dans lequel il va être introduit. Cependant, de nombreux facteurs peuvent altérer ses performances, tel que le routage, la structure mécanique ou bien les couplages internes au filtre, entre les composants eux-mêmes. Cette thèse traite de l'étude de l'influence des couplages inter-composants sur les performances d'un filtre pour la CEM.

En effet, les méthodes existantes sont basées uniquement sur des simulations électromagnétiques 3D qui sont coûteuses en terme de temps et requiert également un trop grand nombre d'informations sur les composants (propriétés géométriques, des matériaux etc.). Ainsi, une méthode uniquement basée sur des calculs analytiques et exploitations de mesures a été développée. Cette méthode simplifiée est très efficace car elle permet la prédiction des performances d'un filtre, quelle que soit sa topologie et quelle que soit sa structure. Cette méthode a été validée via de nombreux cas d'applications de filtres implémentés sur des systèmes d'électronique de puissance du domaine automobile. Finalement, cette méthode a été capitalisée au travers d'un outil pour le design et la prédiction des performances de filtre pour la CEM en tenant compte de la proximité des composants.

Title : Study and Modeling of Inter-Component Coupling for Filter Design Application to Automotive EMI Filters

Keywords: Electromagnetic Compatibility, EMI Filter, Coupling, Passive Component, Modeling

Abstract: EMC (ElectroMagnetic Compatibility) is increasingly important in electronic and electrical systems and more particularly in the automotive domain. Actually, there are more and more power electronics equipments in a vehicle and, therefore, EMC issues are more recurrent. In order to limit EMI (ElectroMagnetic Interferences), well designed filters are needed. Each filter is designed corresponding to a system and the required attenuation. However, different parameters can have influence on the filter performances, such as the layout, the mechanical structure or the inter-components coupling of the filter. Therefore, the thesis work is based on the study of the filter performance considering inter-components coupling.

Some methods exist on that topic but are generally based on 3D electromagnetic simulation, which is time-consuming and requires a lot of information on components (geometrical properties, material properties etc.). Therefore, our work is based on a methodology only based on analytical calculation and measurements. That simplified methodology is very accurate because it can predict a filter performance, whatever the filter topology, whatever the structure. That method was validated under several application cases on power electronics systems for automotive domain. Finally, the whole methodology has been accrued in a tool for filter design that can predict a filter attenuation by considering the components proximity.